

UNCLASSIFIED

AD 264 266

*Reproduced
by the*

ARMED SERVICES TECHNICAL INFORMATION AGENCY
ARLINGTON HALL STATION
ARLINGTON 12, VIRGINIA



UNCLASSIFIED

NOTICE: When government or other drawings, specifications or other data are used for any purpose other than in connection with a definitely related government procurement operation, the U. S. Government thereby incurs no responsibility, nor any obligation whatsoever; and the fact that the Government may have formulated, furnished, or in any way supplied the said drawings, specifications, or other data is not to be regarded by implication or otherwise as in any manner licensing the holder or any other person or corporation, or conveying any rights or permission to manufacture, use or sell any patented invention that may in any way be related thereto.

264266

REPORT NO.
TDR-594(1206-02)STR

High Mach Number and Materials Research Program

Phase I, Aerophysics Research Studies

SEMIANNUAL TECHNICAL REPORT

1 JANUARY-30 JUNE 1961

Compiled by R. J. WHALEN

Aeromechanics Department

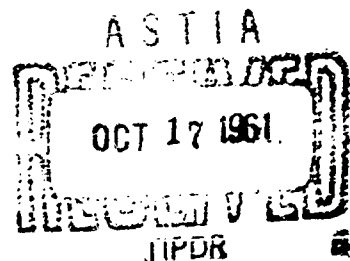
Aerodynamics and Propulsion Research Laboratory

Prepared for DEPUTY COMMANDER AEROSPACE SYSTEMS

AIR FORCE SYSTEMS COMMAND

UNITED STATES AIR FORCE

Inglewood, California



LABORATORIES DIVISION • AERONAUTICAL CORPORATION

CONTRACT NO. AF 04(647)-594

HIGH MACH NUMBER AND
MATERIALS RESEARCH PROGRAM
Phase I, Aerophysics Research Studies

Semiannual Technical Report

1 January - 30 June 1961

Compiled by
R. J. Whalen
Aeromechanics Department
Aerodynamics and Propulsion Research Laboratory

AEROSPACE CORPORATION
El Segundo, California

Contract No. AF 04(647)-594

Prepared for
DEPUTY COMMANDER AEROSPACE SYSTEMS
AIR FORCE SYSTEMS COMMAND
UNITED STATES AIR FORCE
Inglewood, California

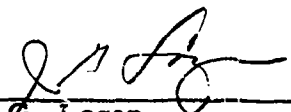
HIGH MACH NUMBER AND MATERIALS RESEARCH PROGRAM
Phase I, Aerophysics Research Studies

SEMIANNUAL TECHNICAL REPORT
1 January - 30 June 1961

Compiled


R. J. Whalen
Aeromechanics Department

Approved


J. G. Logan
Director, Aerodynamics
and Propulsion Research
Laboratory

AEROSPACE CORPORATION
El Segundo, California

ABSTRACT

During the last program period, September 1960 to 1 July 1961, theoretical and experimental investigations of high speed gas dynamics were carried out under this program.

The experimental investigations included stagnation point heat transfer measurements in low Reynolds number flows in the existing helium-driven shock tunnel. Electron beam densitometer studies were continued. Modification of the existing hypersonic shock tunnel to incorporate a combustion driver and a six-foot diameter nozzle was initiated. This modification will allow an increased performance up to a Mach number equal to 30 and density altitudes to 300,000 feet. This modification will be completed by January 1962.

The theoretical investigations included a study of viscous and inviscid non-equilibrium hypersonic flows about blunt and sharp leading edge slender bodies. A numerical program to determine the non-equilibrium flow about a blunt body in the vicinity of the stagnation region was also initiated. A study of the hypersonic wake about blunt re-entry bodies was completed.

CONTENTS

	Page
I. INTRODUCTION (R. J. Whalen)	1
II. THEORETICAL INVESTIGATIONS	4
A. Viscous and Inviscid Non-equilibrium Gas Flows (R. J. Whalen)	4
B. Non-equilibrium Blunt Body Problem (S. T. Chu) . . .	63
C. Hypersonic Wake Flow Studies (A. M. Rodriguez)	82
III. EXPERIMENTAL INVESTIGATIONS	96
A. Stagnation Point Heat Transfer Measurements in Hypersonic Low Reynolds Number Flows (R. L. Varwig)	96
B. Electron Beam Densitometer Studies (E. W. Hewitt)	109
C. High Enthalpy Combustion-Driven Shock Tunnel Design	123
1) General Requirements (R. J. Whalen)	123
2) Combustion-Driven Shock Tunnel Performance (L. Y. Lamb)	132
3) Description of Modified Facility (R. L. Varwig and L. Y. Lamb)	155
4) Combustion Experiments (L. Y. Lamb)	164
D. Advanced Instrumentation (L. Rosenman)	178
IV. FUTURE PROGRAM	188
V. REFERENCES	190

LIST OF FIGURES

	Page
1 Non-equilibrium Flow Regimes	6
2 Degree of Dissociation Behind Oblique Shocks in Air	12
3 Variation of Pressure and Velocity in Shock Layer	15
4 Energy Distribution Behind Oblique Shock	20
5 Energy Distribution Behind Normal Shock	21
6 Nose Drag and Dissociation Energy Distribution	24
7 Characteristics Diagram for "Frozen" Flow	25
8 Difference Between Nose Drag and Dissociation Energy	27
9 Pressure Distribution About Blunt Body in Hypersonic Flow	29
10 Temperature Distribution About Blunt Body in Hypersonic Flow	30
11 Electron Concentration Distribution at the Outer Edge of the Boundary Layer	31
12 Local Skin Friction and Heat Transfer Distribution About Blunt Body in Hypersonic Flow	32
13 "Displacement Thickness Integral" for a "Non-Catalytic" Surface	41
14 Flow Field Description	42
15 Frozen Boundary Layer Interaction on a "Blunt" and "Sharp" Flat Plate	45
16 " M " vs A/A^*	48
17 Energy Distribution in Hypersonic Nozzle as a Function of Stagnation Pressure	49
18 "Controlled Non-equilibrium Expansions"	50
19 Pressure "Similitude"	52
20 Lift Curve "Similitude"	53
21 Heat Transfer and Skin Friction "Similitude"	54
22 Controlled Non-equilibrium Expansion "Simulation"	56
23 "Simulation" of Blunt and Sharp Leading Edge Boundary Layer Interaction	57
24 Shock-Oriented Curvilinear Coordinates	66
25 Control Surfaces for Flow Inside the Shock Layer	77

LIST OF FIGURES (continued)

	Page
26a Schematic of Flow Past a Blunt Body	83
26b Schematic of Flow Past a Sharp Body	83
27 Wake Temperature Decay for Blunt Body in Hypersonic Flow	93
28 Wake Temperature Decay for Slender Body in Hypersonic Flow	95
29 View of Shock Tunnel Showing 12-inch Test Section	98
30a Heat Transfer Rate to Cylinders Normal to the Flow as a Function of Stagnation Point Reynolds Number	99
30b Heat Transfer Rate to Spheres as a Function of Stagnation Point Reynolds Number	100
31 20mm Diameter Cylindrical Model Showing the Two Thin Film Resistance Thermometers Along the Surface which Becomes the Stagnation Line of the Cylinder	102
32 Mounting of the Spherical Model in the Tunnel Showing also the Pitot Tube for Measuring Test Section Total Pressure	103
33 Typical Temperature History for the Stagnation Point of a Cylindrical Model	106
34 Current Ratio of a Function of Pressure for Constant Path Length	112
35 Current Ratio as a Function of Path Length for Constant Pressure-Voltage Ratio	113
36 Coordinate System--Axially Symmetric Flow Calculation	114
37 Electron Gun, Assembled View	119
38 Electron Gun, Exploded View	120
39 Electron Beam Gun and Tilting Mechanism	121
40 General View of the Apparatus	122
41 Hypervelocity Simulation Requirements (Slender Body)	124
42 Hypervelocity Simulation Requirements (Blunt Body)	131
43 Variation of α_f with Stagnation Conditions: Air	133
44 Combustion-Driven Shock Tube Performance as a Function of Percent Helium Diluent in the Stoichiometric Mixture of Hydrogen and Oxygen (plot of Eq. 152)	137

LIST OF FIGURES (continued)

	Page
45 Reservoir Conditions as a Function of Shock Mach Number	138
46 Reservoir Conditions as a Function of Varying Shock Tube Initial Conditions	139
47 Variation of α_f with Stagnation Conditions for Air Showing Region of Coverage with Shock Mach Numbers Attainable in the Shock Tube	140
48 Variation of α_f with Stagnation Conditions for Air Showing Limit of Combustion-Driven Shock Tunnel	141
49 Variation of α_f with Stagnation Conditions for Air. Region of Coverage Using Pure Hydrogen as the Driver Gas is Indicated	143
50 Schematic Diagram of Shock Tunnel with a Converging Divergent Diaphragm Section	144
51 Gain Factor vs Driver Diameter, for Fixed Throat and Driver Tube Diameter (Existing Shock Tunnel)	146
52 Testing Time for Non-tailored Combustion- Driven Shock Tube, 70% Helium	147
53 Tailored Interface Operation for the Combustion- Driven Shock Tunnel (P_g T_g)	148
54 Tailored Interface Operation for the Combustion- Driven Shock Tunnel (P_4 M_g)	149
55 Reservoir Conditions as a Function of Varying Shock Tube Initial Conditions with Tailored Region Superimposed	151
56 Tailored Shock Tube Test Time, Combustion Driver, 70% Helium	152
57 Mach Number vs Area Ratio for Equilibrium and Non-equilibrium Expansion	153
58 View of Shock Tunnel Showing 12-inch Test Section	156
59 Driver Section Assembly Showing Diaphragm Latch Mechanism, Fill-Circulating Tube and Initiating Wire	158
60 Gas Handling System for Charging the Driver Section	159
61 Diaphragm and Diaphragm Package	161
62 Tunnel and Test Section Arranged in Vacuum Tank	163
63 Combustion Driver Spark Plug	166

LIST OF FIGURES (continued)

	Page
64 High Pressure Spark Plug	167
65 Schematic of Exploding Wire System	169
66 Experimental Threshold Potential for Complete Energy Discharge through Exploding Wire. C = 1.5 μ fd. Wire is Copper Alloy of .0015- inch Diameter	171
67 Explosion of Three Wires in Parallel	172
68 Explosion of Three Parallel Wires with Less than Threshold Energy	173
69 Modification of Spark Plug for "Exploding Wire" Type Initiation of Combustible Gas Mixture	174
70 Schematic of Pilot Combustion Test Facility	176
71 Functional Arrangement of Pressure Transducer Using the Piezoelectric Bender Element	180
72 Equivalent Circuit for Figure 71	180
73 Low Frequency Equivalent for Figure 71	181
74 Functional Arrangement of Pressure Transducer with Axial Elements	181
75 Force and Displacement Relationships in the Axial Element Drive System	183
76 Equivalent Circuit for Axial Element Transducer	183
77 Increase in Sensitivity for Optimum Angle ϕ as a Function of C_C/C_D	186

I. INTRODUCTION

In October of 1960, the Aerodynamics and Propulsion Laboratory assumed responsibility for conducting research operations in the hypersonic shock tunnel and arc-driven shock tube. The experimental program being conducted at that time under STL contract no. AF 04(647)-309 was continued in an uninterrupted fashion by Aerospace personnel, since this effort was applicable to the scope and objectives of the High Mach Number and Materials Research Program, Phase I, planned for performance under Aerospace contract no. AF 04(647)-930.

Under Aerospace management, the High Mach Number and Aerophysics Research Program was increased in scope to include a more extensive theoretical effort and advanced planning for future experimental investigations and facilities requirements to meet Air Force research objectives for advanced missile and space systems.

Theoretical work conducted under the High Mach Program during this reporting period includes extension of the hypersonic wake flow studies to fulfill the requirements of the Penetration Aids Program, viscous and inviscid non-equilibrium gas flows, and investigations of the flow field around a blunt body considering finite chemical reaction rates. The viscous and inviscid non-equilibrium flow investigations for blunt and sharp leading edges, and slender body power law geometries were extensive in nature, and conclusive results were reached which are detailed in this report. The investigations of the non-equilibrium flow field about a blunt body include a five-component reacting gas, using the best known values of chemical reaction rates. Ionization non-equilibrium effects are not presently included, but provision has been made for their integration into the program at a later date. The program is presently in the check-out process on the IBM 7090 computer. A major application of this study will be in the area of re-entry plasma interactions with microwave radiation in support of re-entry communications problems.

The experimental studies of arc heating as a means of increasing shock tube performance were completed and a final report submitted. The limitations of this technique for producing high enthalpy flows were clearly defined in the study and detailed in the report. Future effort was discontinued, since this technique was not optimum for providing the flow simulation capability required to meet the objectives of the High Mach Program. The one-inch shock tube used in these studies is presently being used for instrumentation calibration.

Performance analysis studies were performed on various techniques for generating high-enthalpy, high-velocity flows. These studies include arc heated driver methods, spark discharge heated driver methods, and combustion driver techniques. As a result of these studies, it was conclusively shown that the combustion driver technique was the most practical method of generating the required flow in a research-type facility. As a consequence, a modified design of the present hypersonic shock tunnel was completed and plans initiated to convert the present facility to incorporate a combustion driver. The expected performance of the modified facility is enthalpy simulation up to approximately 20,000 ft/sec. The expected date of completion of the modification is December 1961.

During the transition period to combustion-driven operation, the experimental investigations on stagnation point heat transfer in hypersonic low Reynolds number flows have been completed and investigations initiated on control surface effectiveness at high-altitude hypersonic speeds.

Future plans include the incorporation of a six-foot diameter test section into the combustion-driven facility in order to permit larger model size and extend present instrumentation capability for low pressure measurement. Experimental investigations will be conducted in "controlled non-equilibrium expansions" correlated with free stream conditions existing in flight at the corresponding Mach number. Configuration tests will be conducted in the hypersonic flow regime for lifting body configurations characteristic of orbital and super-orbital re-entry flight. Additional

theoretical investigations will be conducted in inviscid three-dimensional hypersonic flows and the Boltzman integral method will be investigated for hypersonic low density flows over a flat plate. Incorporation of a six-component force balance into the lifting body hypersonic investigations is planned for the next six-month period.

II. THEORETICAL INVESTIGATIONS

A. Viscous and Inviscid Non-equilibrium Gas Flows

1. Introduction

The effects of leading edge or nose bluntness and boundary layer displacement have received considerable theoretical and experimental investigation for the case of an equilibrium dissociating gas or a perfect gas with constant specific heats. The most comprehensive theoretical and experimental treatment of this problem has been made recently by Cheng, Hall, Golian, and Hertzberg.¹ Since these effects are most significant for high altitudes and hypersonic speeds, the equilibrium assumption must be examined in terms of the flight spectrum pertaining to hypervelocity vehicles. While an estimate of non-equilibrium flow regimes has been made by previous investigators in rather similar form, a cursory examination of this problem will be included here for purposes of orientation and completeness.

The species conservation equation for steady boundary layer flow may be written

$$\rho u \frac{\partial a_i}{\partial x} + \rho v \frac{\partial a_i}{\partial y} - \frac{\partial}{\partial y} (\rho a_i \nabla_i) = \omega_i \quad (1)$$

where a_i = mass fraction concentration of the species i , ∇_i = diffusion velocity of species i , and ω_i = net gas-phase reaction rate. An estimate of the degree of departure from chemical equilibrium may, therefore, be determined by the ratio of either the convection or diffusion rate to that for recombination. This ratio is written, for convection,

$$\frac{\omega_i}{\rho u \frac{\partial a_i}{\partial x}} \equiv C_i \quad (2)$$

Therefore, within the order of magnitude considered we can take this estimate as

$$\frac{\omega_i}{\rho \frac{u}{x} a_i} \gg 1 \quad (\text{equilibrium})$$

$$\frac{\omega_i}{\rho \frac{u}{x} a_i} \sim 0 \quad (1) \quad (\text{non-equilibrium}) \quad (3)$$

$$\frac{\omega_i}{\rho \frac{u}{x} a_i} \ll 1 \quad (\text{"frozen"})$$

As pointed out by Cheng, the diffusion term can also be shown to be governed by C_i , by noting that $(\delta^*/x)^2 \sim \mathcal{O}_{12}/ux$ and $V_i = \mathcal{O}_{12} \partial/\partial y \ln a_i$. The numerical solutions of Fay and Riddell,² for the stagnation point problem, confirm the order-of-magnitude relation (3).

An estimate of the possible extent of the non-equilibrium flow regime may be observed in Figure 1. Here, the recombination rate parameter for "air" has been evaluated at the stagnation point assuming a rate law for oxygen recombination as proposed by Byron.³ Conclusions regarding the degree of departure from equilibrium downstream of the stagnation point may be indicated by the ratio of the local recombination rate parameter to that at the stagnation point, namely

$$\frac{C_1}{(C_1)_s} = \left(\frac{p_1}{p_s}\right)^2 \left(\frac{T_1}{T_s}\right)^{\omega-2} \frac{(du_b/dx)_s}{U_\infty/x} \quad (4)$$

where it is assumed $R \approx R_s$, $u_b \approx U_\infty$ (hypersonic small-disturbance assumption) and $\omega = 0$ for the Byron rate law. Equation (4) may be written

$$\frac{C_1}{(C_1)_s} = \left(\frac{p_1}{p_s}\right) \left(\frac{T_s}{T_1}\right)^2 \frac{1}{r} \frac{\sqrt{2R_s T_s}}{U_\infty/x} \quad (5)$$

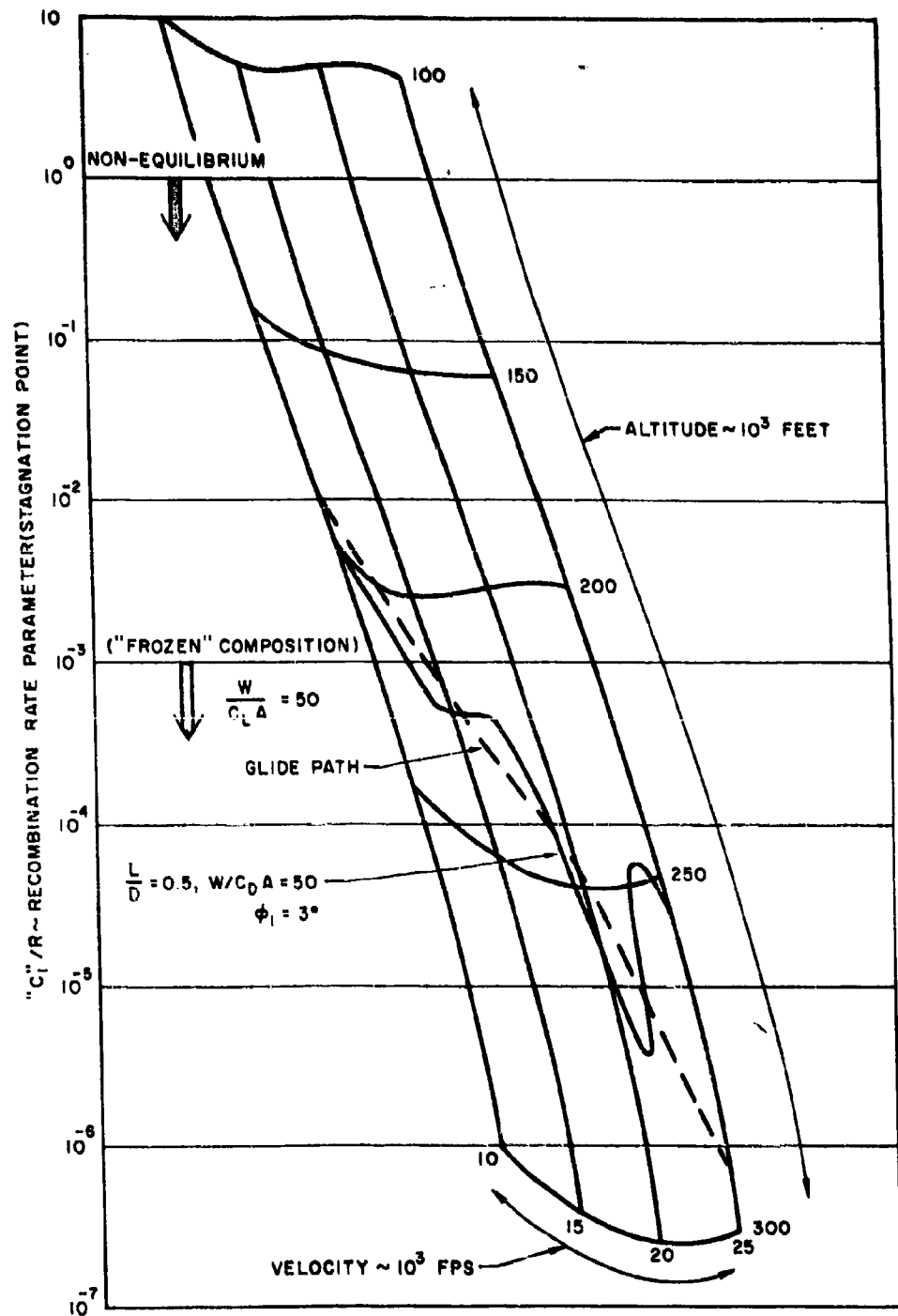


Figure 1. Non-Equilibrium Flow Regimes

where r = radius of the leading edge. Under a predominant inviscid leading edge flow field, (5) becomes

$$\frac{C_1}{(C_1)_s} \sim k^{4/3} \left(\frac{d}{x}\right)^{1/3} \left(\frac{T_s}{T_1}\right)^2 \frac{(R_s T_s)^{1/2}}{U_\infty} \quad (6)$$

In general, the blast-wave local shock slope may be written $d\delta/dx \sim (k d/x)^{1/3}$. Since $k \approx 1$, we may write (certainly within the order of magnitude considered here) $k^{4/3} (d/x)^{1/3} \approx d\delta/dx$ which, within the error of the small-disturbance assumption, is estimated as $d\delta/dx \sim M_\infty^{-1}$. Therefore, (6) may be written

$$\frac{C_1}{(C_1)_s} \sim \frac{1}{M_\infty^{3/2}} \left(\frac{T_s}{T_1}\right)^2 \quad (7)$$

For the inviscid leading edge dominated flow field, it can be readily shown $T_s/T_1 \lesssim M_\infty$. Thus, for hypersonic speeds, criterion (7) is taken as

$$\frac{C_1}{(C_1)_s} \lesssim M_\infty^{1/2} \quad (8)$$

Therefore, according to (8), if the flow in the vicinity of the stagnation point is not in chemical equilibrium, then the flow field downstream of the leading edge will also exhibit a non-equilibrium characteristic.

Similarly, if the boundary layer interaction mechanism is dominant, (4) may be written

$$\frac{C_1}{(C_1)_s} \sim \left(\frac{x_\infty}{M_\infty^2}\right)^2 M_\infty^2 M_\infty^{1/2} \frac{x}{M_\infty} \quad (9)$$

where x_∞ = value of the interaction parameter based on a 1-foot length. In the altitude range of 200,000 to 300,000 ft, $40 \leq x_\infty \leq 400$. Thus, for

hypersonic speeds, $M_\infty \leq X_\infty \leq M_\infty^2$, criterion (9) is taken as

$$M_\infty^{-1/2} \lesssim \frac{C_1}{(C_1)_s} \lesssim M_\infty^{3/2}$$

Therefore, except for extreme altitudes,* if the flow in the vicinity of the stagnation point is not in chemical equilibrium, then the flow field downstream of the leading edge will also exhibit a non-equilibrium characteristic. Therefore, Figure 1 may be taken as an indication of the degree of departure from equilibrium at any point on a sharp or blunt leading edge geometry in hypersonic flow.

Figure 1 presents the recombination rate parameter C_1 , based on stagnation point conditions, for a 1-foot nose or leading edge radius. Thus, for smaller radii, the same velocity-altitude conditions would be expected to show a larger departure from equilibrium. This would be anticipated since the smaller the radius, the shorter the local residence time for a particle. By way of reference, a typical boost-glide vehicle (wing loading = 25 psf, $C_L = 0.5$) and a skip re-entry vehicle ($L/D = 0.5$, initial entry angle = 3 degrees) are indicated. According to this figure, the boost-glide and skip re-entry vehicles indicate a considerable range for which $10^{-7} \leq C_1 \leq 10^{-2}$. Further, it is interesting to note the time duration spent in the "frozen" regime. Specifically, if the frozen composition model is specified by $C_1 \lesssim 10^{-3}$ then the boost-glide vehicle would experience approximately 95 minutes in which the entire flow field is frozen. This represents over 80 per cent of the total glide flight time of this vehicle. Examination of the skip re-entry flight path indicates similar conclusions as to the importance of non-equilibrium phenomena.

* It should be remembered, however, that the stagnation point value of C_1 is extremely small at these altitudes ($C_1 \approx 10^{-7}$ at 300,000 ft), and its subsequent multiplication by $M_\infty^{3/2}$ (in order to consider the state of the flow field downstream of the leading edge) would still indicate a frozen composition and thus should not introduce a large error in the assumption that the degree of departure from equilibrium at any point on the body is indicated by the stagnation point value of C_1 .

With these considerations in mind, viscous and inviscid frozen flow studies of the "blast-wave" and boundary layer interaction mechanism for blunt and sharp leading edge slender bodies are made. These studies are discussed in Sections II. A. 2 and II. A. 3, respectively.

The viscous and inviscid theoretical studies were generalized to consider an arbitrary (frozen) degree of dissociation in the ambient free-stream. This generalization was made to permit analysis of the flow field about geometries placed in wind tunnel nozzles where dissociation non-equilibrium is present within the nozzle itself. Since high "Mach number" gas flows may be readily obtained in wind tunnel nozzles, where dissociation non-equilibrium is present, the "simulation" capabilities, in terms of the previously discussed viscous and inviscid hypersonic flow phenomena of "controlled non-equilibrium expansions" are studied. These studies are discussed in Section II. A. 4.

2. Inviscid Hypersonic Flow

The following assumptions are employed for the inviscid plane and axisymmetric analyses:

- a) The gas composition is constant along a streamline and given by the equilibrium value immediately behind the shock envelope.
- b) The flow process is particle-isentropic, except in crossing the shock envelope.
- c) The translation, rotation, vibrational degrees of freedom are everywhere in equilibrium with the local gas temperature.
- d) The ambient free-stream is uniform in velocity and homogeneous in gas properties.
- e) The free-stream velocity is much greater than the speed of sound in the ambient free-stream atmosphere.
- f) The local flow deflection angle (in radians), as measured from the undisturbed flow, is much smaller than unity everywhere except in the nose region.

a. Sharp-Nosed Slender Bodies

The differential equations describing the one-dimensional particle-isentropic flow for a plane or axisymmetric flow may be written

$$\left(\frac{\partial}{\partial t} + v \frac{\partial}{\partial y} \right) v = - \frac{1}{\rho} \frac{\partial p}{\partial y} \quad (10)$$

$$\left(\frac{\partial}{\partial t} + v \frac{\partial}{\partial y} \right) \rho = - \rho \left(\frac{\partial v}{\partial y} + v \frac{v}{y} \right) \quad (11)$$

$$\left(\frac{\partial}{\partial t} + v \frac{\partial}{\partial y} \right) \mathcal{J} = 0 \quad (12)$$

Since neither the momentum or continuity relations are influenced by the gas model chosen, we need only direct our attention to the entropy transport equation. The specific entropy, \mathcal{J} , may be obtained from the relation

$$d\mathcal{J} = \frac{de + pd(p^{-1})}{T} = \frac{d \left[R (\beta + T \frac{d\beta}{dT} - 1) (1 + \alpha) T \right]}{T} + \frac{\rho R (1 + \alpha) T d(p^{-1})}{T} \quad (13)$$

where

$$\beta = \frac{1 - \alpha}{1 + \alpha} \beta_M + \frac{\alpha}{1 + \alpha} \left\{ \frac{D}{RT} + 2\beta_A \right\}$$

and β_M , β_A are the coefficients of energy content for the molecular and the atomic gas at the given temperature. For the present hypersonic flow investigations, we can take $\beta_A = 5/2$; and β_M , the vibrational energy content, is taken as that for a quantized linear oscillator.

Relation (13), for frozen flow, can be simplified by noting that, for air, we can take $(1 - \alpha/1 + \alpha)(d\beta_M/dT) \ll (\alpha/1 + \alpha)(D/RT^2)$ which reduces (13) to

$$\frac{d}{dx} = \left[(1 - \alpha) \beta_M + 4\alpha - 1 \right] \ln p - \left[(1 - \alpha) \beta_M + 5\alpha \right] \ln p + (\text{constant}) \quad (14)$$

Therefore, the entropy transport Eq. (12) may be written

$$\left(\frac{\partial}{\partial t} + v \frac{\partial}{\partial y} \right) p \rho - \frac{\left[(1 - \alpha) \beta_M + 5\alpha \right]}{\left[(1 - \alpha) \beta_M + 4\alpha - 1 \right]} = 0 \quad (15)$$

The exponent $(1 - \alpha) \beta_M + 5\alpha / (1 - \alpha) \beta_M + 4\alpha - 1$ can be identified as the specific heat ratio, γ , for a given streamline. Thus for the frozen flow over a sharp-nosed slender body, we notice the variation of the shock layer properties are bounded by the $7/5 \leq \gamma \leq 5/3$ ($\alpha = 0, 1$, respectively) solutions.

The solutions of Eqs. (10), (11), and (15) can be readily obtained for $\alpha = \text{constant}$, since assumption (f) allows us to take $\beta_M = 7/2$. The utility of such a solution must, therefore, be examined. The variation of α with flow deflection angle as a function of altitude and free-stream velocity is shown in Figure 2. The results presented in this figure are for a nondissociated free-stream, but an arbitrary degree of dissociation in the ambient free-stream will have a negligible influence on these results. Assumption (f) and Figure 1 indicate that for sharp-nosed slender bodies we can take, to good approximation, $(1 - \alpha) \beta_M + 5\alpha / (1 - \alpha) \beta_M + 4\alpha - 1 \approx 7/5$. The solution of Eqs. (10), (11), and (15) in terms of a family of

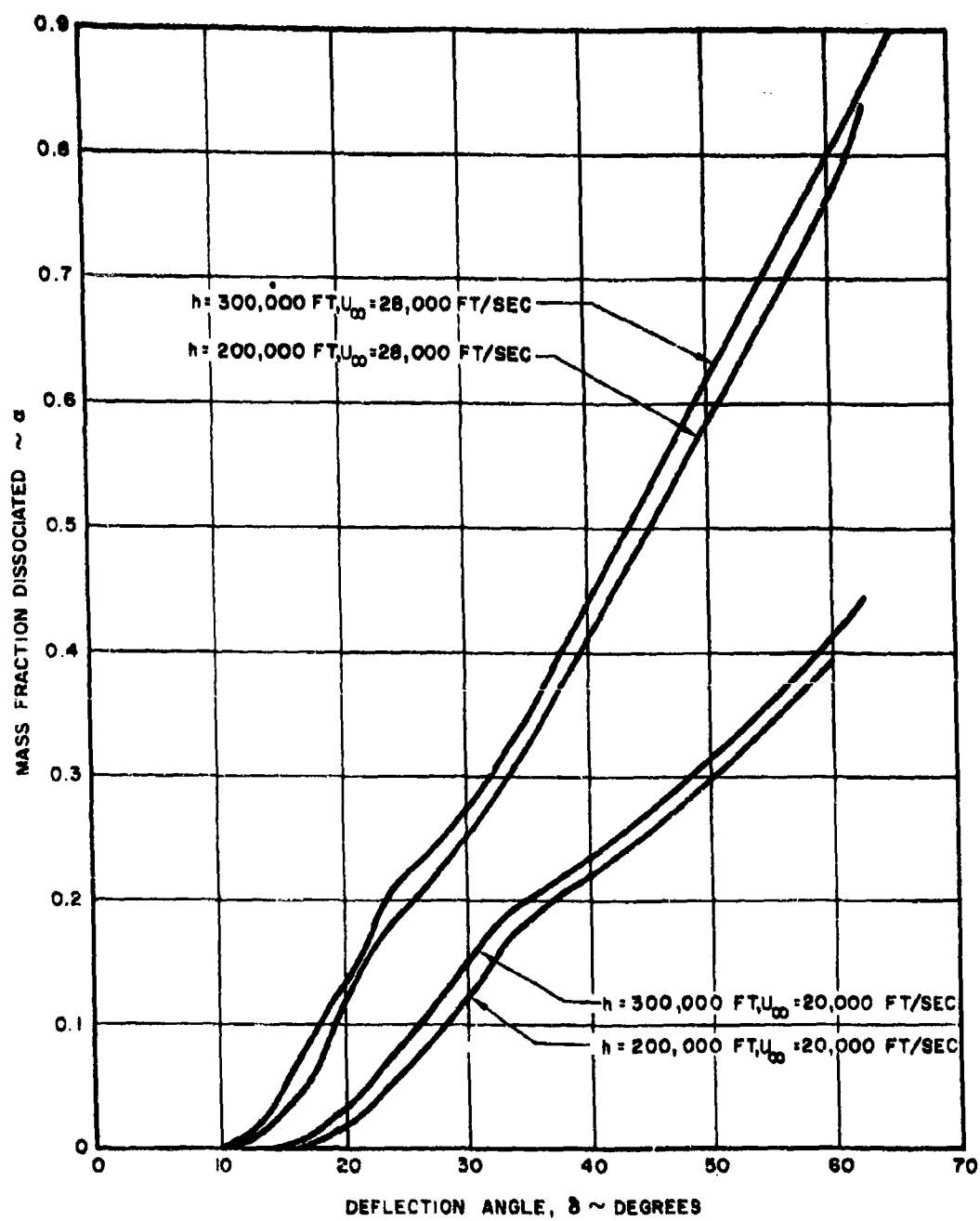


Figure 2. Degree of Dissociation Behind Oblique Shocks in Air

similar solutions, is readily obtained by means of the transformation⁴
 $\eta = y/\delta(t)$, viz:

$$\begin{aligned}\frac{p}{p_{\infty}} &= \left(\frac{p_1}{p_{\infty}}\right) P(\eta) \\ \frac{\rho}{\rho_{\infty}} &= \left(\frac{\rho_1}{\rho_{\infty}}\right) R(\eta) \\ \frac{v}{\delta} &= \frac{v_1}{\delta} V(\eta)\end{aligned}\tag{16}$$

together with the Hugoniot relations for strong shocks, $(\dot{\delta}/a_{\infty})^2 \gg 1$,
 $(\dot{\delta} = d\delta/dt)$.

$$\begin{aligned}\frac{p_1}{p_{\infty}} &= \frac{2\gamma}{\gamma+1} \left(\frac{\dot{\delta}}{a_{\infty}}\right)^2 \\ \frac{p_1}{\rho_{\infty}} &= \frac{\gamma+1}{\gamma-1} \\ \frac{v_1}{\delta} &= \frac{2}{\gamma+1}\end{aligned}\tag{17}$$

Relations (16) and (17) reduce the system of Eqs. (10), (11), and (15) to a system of ordinary differential equations involving P , R , V . Since this system of equations involves the ratio of specific heats, as a result of the boundary conditions (17), the influence of a dissociated free-stream must be considered for the value to be employed in the boundary condition (17). Certainly, for a nondissociated ambient free-stream, the $\gamma = 7/5$ value will be applicable. Consideration of the influence of a

dissociated free-stream on the Hugoniot relations, over a wide range of chemical and thermodynamic variables in air, has been made.⁵ These results indicate, as would be anticipated, that we can bound the specific heat ratio by $7/5 \lesssim \gamma \lesssim 5/3$. Numerical solutions for $P(\eta)$, $R(\eta)$, $V(\eta)$ have been obtained for various conditions by several authors,^{4,6-9} and some of these results are presented in Figure 3. The $\sigma = 2/3$, $3/4$ represent, respectively, the two-dimensional blunt leading edge flat plate and boundary layer interaction mechanisms. Since the surface pressure is dependent on the values of $P(0)$ and $V(0)$, the relatively small influence of the boundary conditions, even for the limiting cases ($\gamma = 7/5$, $5/3$), can be observed.

With the solutions for $P(0)$ and $V(0)$ determined, the local pressure distribution is determined upon transformation of (16) to the steady flow plane. To do this, we make use of energy conservation in the following form:

$$a_{\infty} D + \frac{U_{\infty}^2}{2} \approx a D + \frac{U^2}{2} \quad (18)$$

Therefore, except for a highly dissociated ambient gas stream ($a \sim 1$), the ratio of the frozen pressure distribution (p_f) on a sharp-nosed slender body and the corresponding perfect gas value ($p_{7/5}$) should be given, for the same free-stream velocity, to good approximation by

$$\frac{p_f}{p_{7/5}} \approx \frac{7}{5} \left[(1 - a_{\infty}) \frac{7}{2} + 4a_{\infty} - 1 \right] \left[\frac{1 + \frac{a_{\infty} D}{U_{\infty}^2/2}}{(1 - a_{\infty})^{7/2} + 5a_{\infty}} \right] \frac{T_{\infty p.g.}}{T_{\infty f}} \quad (19)$$

where $T_{\infty p.g.}$ and $T_{\infty f}$ are the ambient free-stream temperature for a nondissociated and dissociated gas, respectively. Correspondingly, if we

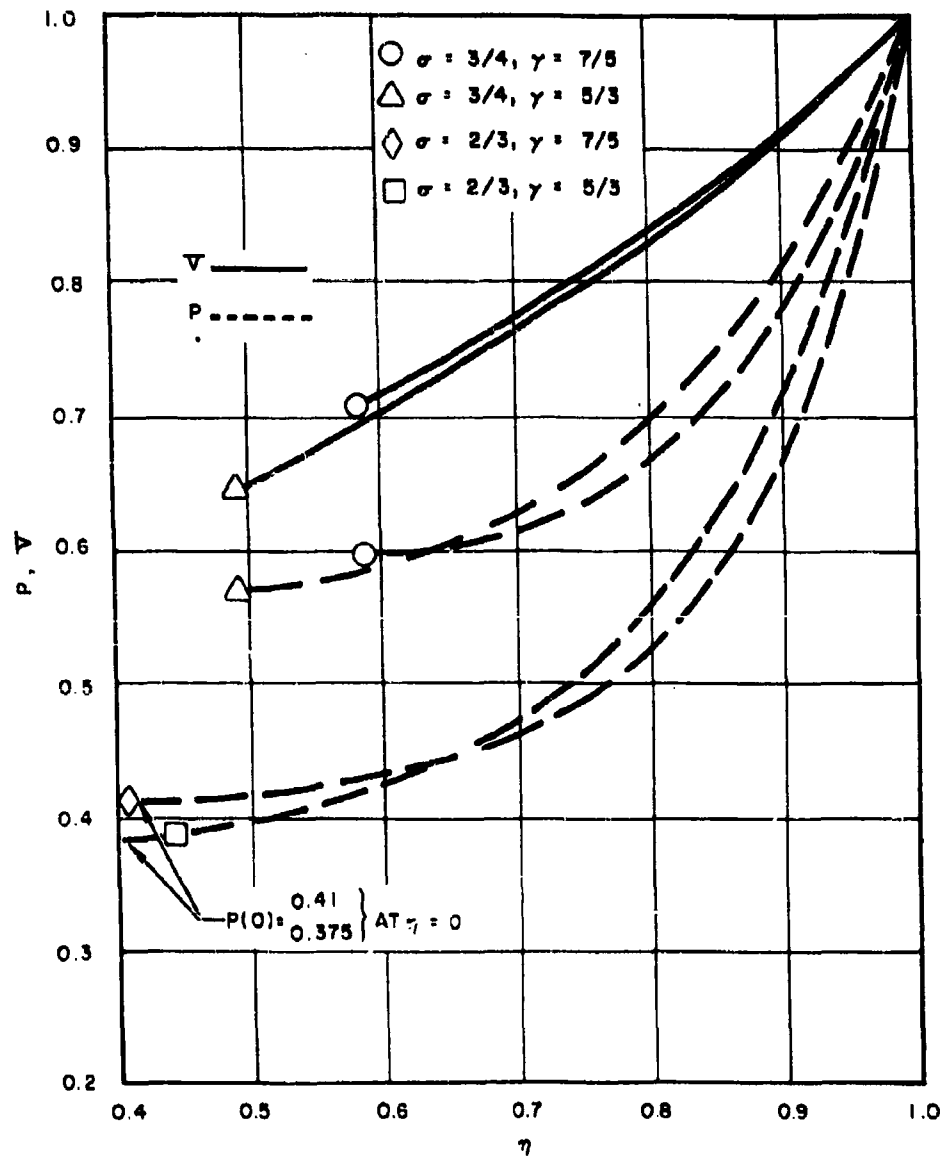


Figure 3. Variation of Pressure and Velocity in Shock Layer

consider wind tunnel application, we can examine the ratio (19) for the same "Mach number."* In this case, the ratio (19) becomes

$$\frac{p_\delta}{p_{7/5}} \approx 1 + \frac{a_\infty^2 D}{U_{\infty f}^2 / 2} \quad (20)$$

where $U_{\infty f}$ = frozen free-stream velocity associated with non-equilibrium nozzle expansion.

b. Blunt-Nosed Slender Bodies

The above discussion is directed toward geometries for which the nose drag may be ignored in relation to the drag of the afterbody. We will now turn our attention toward blunt-nosed bodies for which the nose drag contributes a substantial portion of momentum and energy to the flow field downstream of the immediate vicinity of the leading edge. This condition is the one associated with the "blast-wave" analogy problem.^{4,6-8,10} Inclusion of the contribution of a finite leading edge necessitates the introduction of an energy and momentum balance in the transverse flow field. The change of momentum in the axial direction may be written

$$D_N + \int_0^x p_w \frac{dr_b}{dx} (2\pi r_b)^v dx =$$

$$\int_{r_b}^{\delta} \rho \left[(\beta - 1) \frac{p}{\rho} + \frac{1}{2} v^2 \right] (2\pi y)^v dy - \rho_\infty \delta (\pi \delta)^v \left[(\beta_\infty - 1) \frac{p_\infty}{\rho_\infty} \right]$$

$$- \int_{r_b}^{\delta} \rho \left(1 - \frac{u}{U_\infty} \right) \left(\beta \frac{p}{\rho} + \frac{1}{2} u^2 + \frac{1}{2} v^2 - \frac{1}{2} U_\infty^2 \right) (2\pi y)^v dy \quad (21)$$

*The "Mach number" is included in quotes because of its definition in a frozen ambient gas stream. This problem is discussed in detail in Section II. A. 4. For our purpose here, we need only consider it defined as "M" = V/a where $a^2 = (\partial p / \partial \rho)_s$.

where

$$D_N = k \frac{1}{2} \rho_{\infty} U_{\infty}^2 \frac{d}{2} \left(\pi \frac{d}{2} \right)^{\nu}$$

Similarly, mass conservation is written

$$\rho_{\infty} U_{\infty} \delta (\pi \delta)^{\nu} = \int_{r_b}^{\delta} \rho u (2\pi y)^{\nu} dy \quad (22)$$

Substitution of relation (18) into (21) yields

$$\begin{aligned} D_N + \int_0^x \rho_w \frac{dr_b}{dx} (2\pi r_b) dx = \\ \int_{r_b}^{\delta} \rho \left(\frac{1-a}{1+a} \beta_M \frac{p}{\rho} + aD + \frac{2\beta A^a}{1+a} \frac{p}{\rho} - \frac{p}{\rho} + \frac{1}{2} v^2 \right) (2\pi y)^{\nu} dy - \rho_{\infty} \delta (\pi \delta)^{\nu} \\ \left(\frac{1-a_{\infty}}{1+a_{\infty}} \beta_M \frac{p_{\infty}}{\rho_{\infty}} + a_{\infty} D + \frac{2\beta A^a}{1+a_{\infty}} \frac{p_{\infty}}{\rho_{\infty}} - \frac{p_{\infty}}{\rho_{\infty}} \right) \\ - \int_{r_b}^{\delta} \rho \left[1 - \sqrt{1 - \frac{(a-a_{\infty}) D}{U_{\infty}^2/2}} \right] \left(\frac{1-a}{1+a} \beta_M \frac{p}{\rho} + \frac{2\beta A^a}{1+a} + a_{\infty} D + \frac{1}{2} v^2 \right) (2\pi y)^{\nu} dy \quad (23) \end{aligned}$$

We can ignore the last term in Eq. (23) since we can take

$$1 - \sqrt{1 - \frac{(a - a_{\infty})D}{U_{\infty}^2/2}} \ll 1$$

for most cases of interest. In addition, for hypersonic flow we can take

$$a_{\infty} D \gg \left\{ \frac{1 - a_{\infty}}{1 + a_{\infty}} \beta_{M_{\infty}} + 2\beta_A \frac{a_{\infty}}{1 + a_{\infty}} - 1 \right\} \frac{p_{\infty}}{\rho_{\infty}},$$

whereupon (23) can be written

$$\begin{aligned} U_{\infty} D_N + U_{\infty} \int_0^x p_w \frac{dr_b}{dx} (2\pi r_b)^{\nu} dx \approx \\ - \rho_{\infty} U_{\infty} \delta (\pi \delta)^{\nu} a_{\infty} D + \int_{r_b}^{\delta} \frac{\rho u}{\sqrt{1 - \frac{(a - a_{\infty})D}{U_{\infty}^2/2}}} \\ \left\{ \left[\frac{1 - a}{1 + a} \beta_M + \frac{2\beta_A a}{1 + a} - 1 \right] \frac{p}{\rho} + aD + \frac{1}{2} v^2 \right\} (2\pi y)^{\nu} dy \end{aligned} \quad (24)$$

Finally, substitution of the continuity relation yields

$$\begin{aligned} U_{\infty} D_N + U_{\infty} \int_0^x p_w \frac{dr_b}{dx} (2\pi r_b)^{\nu} dx \\ - \int_{r_b}^{\delta} \rho u \left\{ \left[\frac{a}{\sqrt{1 - \frac{(a - a_{\infty})D}{U_{\infty}^2/2}}} - a_{\infty} \right] D \right\} (2\pi y)^{\nu} dy \approx \\ U_{\infty} \int_{r_b}^{\delta} \rho \left\{ \left[\frac{1 - a}{1 + a} \beta_M + \frac{2\beta_A a}{1 + a} - 1 \right] \frac{p}{\rho} + \frac{1}{2} v^2 \right\} (2\pi y)^{\nu} dy \end{aligned} \quad (25)$$

Equation (25) is observed to reduce to the previous perfect gas results^{4, 6-8, 10} for $a = a_\infty = 0$, $\beta_M = 7/2$, $\beta_A = 5/2$.

Before continuing any further, it would appear desirable to obtain an estimate of the parameter $(a - a_\infty)D/(U_\infty^2/2)$, the ratio of the "dissociation energy" to the free-stream kinetic energy, for the range of flight conditions applicable to hypervelocity vehicles. A quantitative discussion of this parameter can be obtained by means of available shock tables.¹¹ These results would, therefore, correspond to the free-flight case where $a_\infty = 0$. The data for the oblique shock case are presented in Figure 4, while data for the normal shock are presented in Figure 5. Thus, examination of Figures 4 and 5 indicates that the numerical evaluation of the third term in Eq. (25) must be made for flow disturbances which violate assumption (f). We conclude, therefore, since relation (25) is dependent on the details in the immediate vicinity of the leading edge, the previous similar solution techniques employed in the perfect gas problem^{4, 6-8, 10} cannot be applicable for the frozen composition model.

Since the "dissociation energy" term in (25) is dependent on the detailed flow field in the immediate vicinity of the leading edge (in particular, the shock wave envelope), a general solution for arbitrary nose geometries is not apparent to the author at the present time. General conclusions as to the importance and interplay between a blunt leading edge and the afterbody can be obtained, however, by examining special cases in terms of relation (25). If, initially, we consider a blunt flat plate, an estimate of the point on the body for which $p_w \approx p_\infty$ is given by

$$U_\infty D_N - \int_{r_b}^b \rho u \left\{ \left[\frac{a}{\sqrt{1 - \frac{(a - a_\infty)D}{U_\infty^2/2}}} - a_\infty \right] D \right\} (2\pi y)^v dy \approx 0 \quad (25a)$$

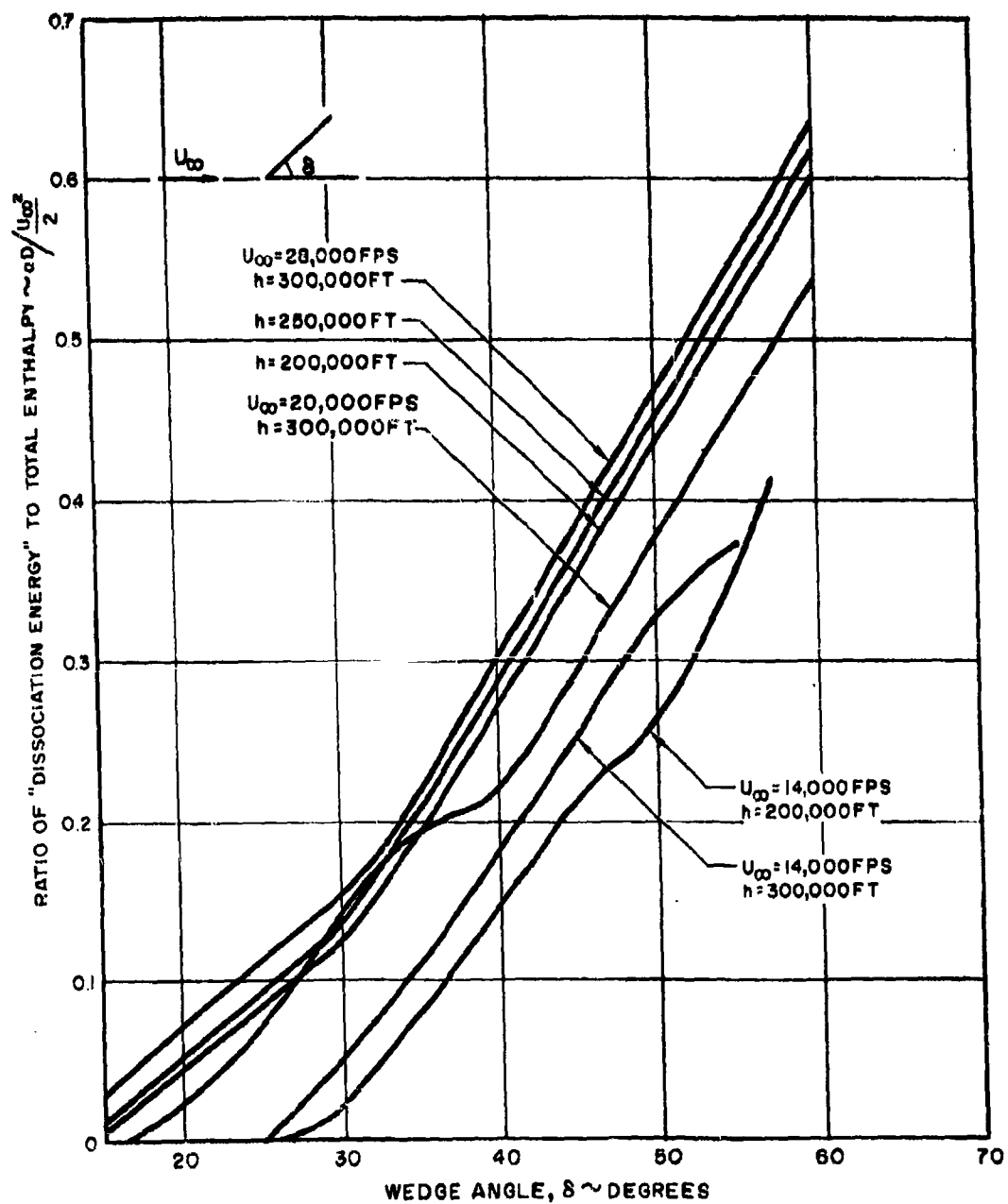


Figure 4. Energy Distribution Behind Oblique Shock

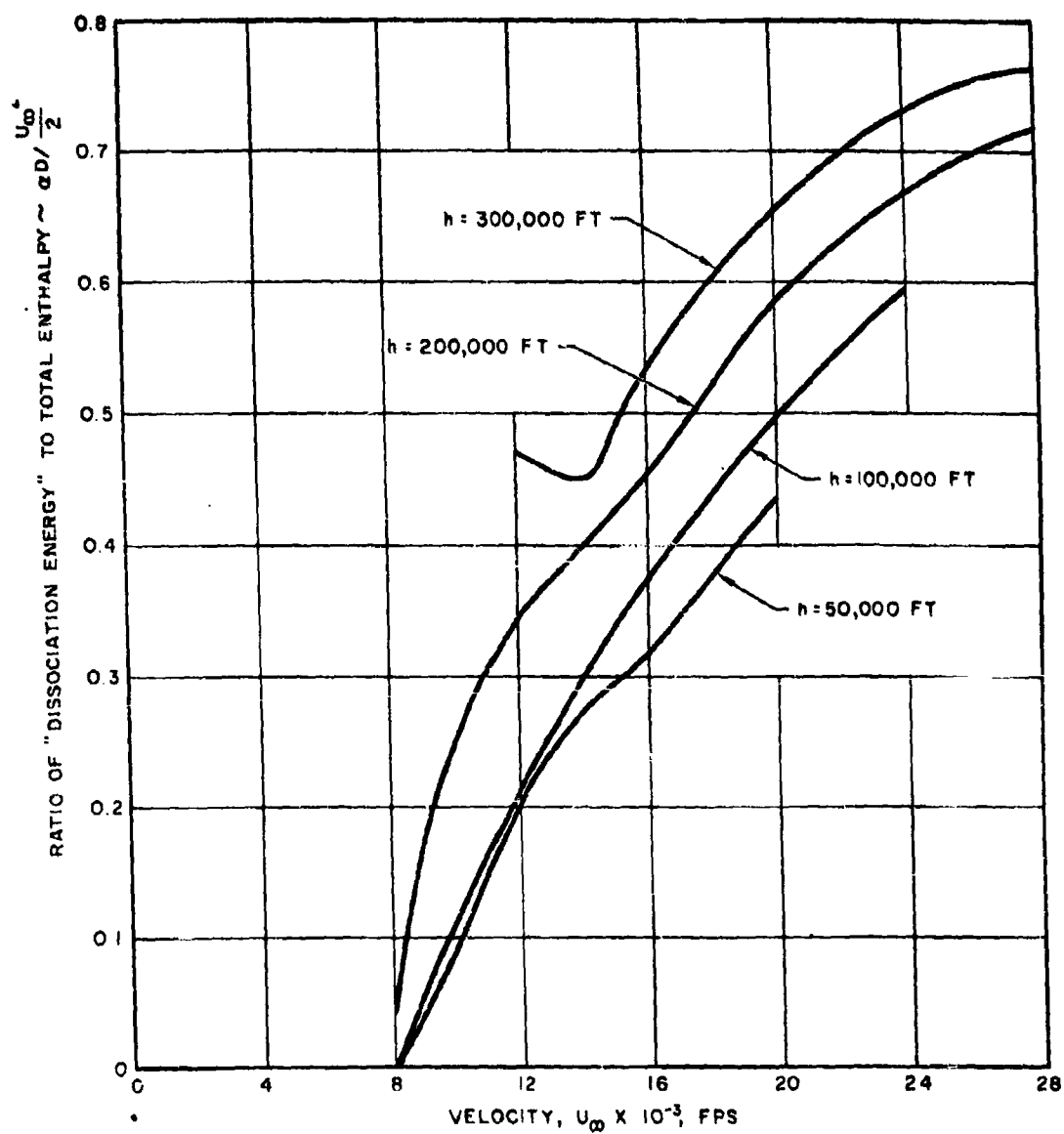


Figure 5. Energy Distribution Behind Normal Shock

The above relation expresses the condition where the energy introduced into the transverse flow field due to the presence of a finite leading edge (nose drag) is just balanced by the dissociation energy which is frozen at the shock wave envelope. Indeed, since the nose drag term is independent of downstream distance, relation (25a) clearly indicates the possibility of obtaining values of $p_w/p_\infty < 1$. Substituting for the nose drag in (25a), we obtain

$$\rho_\infty U_\infty \frac{d}{2} \left(\pi \frac{d}{2} \right)^v k - \int_{r_b}^{\delta} \rho u \left\{ \left[\frac{a}{\sqrt{1 - \frac{(a - a_\infty) D}{U_\infty^2/2}}} - a_\infty \right] \frac{D}{U_\infty^2/2} \right\} (2\pi y)^v dy \approx 0 \quad (25b)$$

If we consider leading edge geometries (e.g., flat, wedge, cone, leading edges) for which $(a - a_\infty)D/(U_\infty^2/2) = \text{constant}$ for dimensions of the order of d , then (25b) can be written

$$\begin{aligned} \rho_\infty U_\infty \frac{d}{2} \left(\pi \frac{d}{2} \right)^v \left\{ k - \left[\frac{a_0}{\sqrt{1 - \frac{(a_0 - a_\infty) D}{U_\infty^2/2}}} - a_\infty \right] \frac{D}{U_\infty^2/2} \right\} \\ - \int_{d/2}^{\delta} \rho u \left\{ \left[\frac{a}{\sqrt{1 - \frac{(a - a_\infty) D}{U_\infty^2/2}}} - a_\infty \right] \frac{D}{U_\infty^2/2} \right\} (2\pi y)^v dy \approx 0 \end{aligned} \quad (25c)$$

where a_0 = mass fraction dissociated behind shock wave in region between $\delta = \pm d/2$. A plot of the term

$$k = \left[\frac{a_0}{\sqrt{1 - \frac{(a_0 - a_\infty) D}{U_\infty^2/2}}} - a_\infty \right] \frac{D}{U_\infty^2/2}$$

the difference between the nose drag and the "dissociation energy" term, is presented as a function of nose geometry, free-flight velocity, and altitude in Figure 6. The results for the circular nose are based upon the normal shock value of the dissociation energy term. According to Figure 6, for flight velocities greater than 20,000 fps, relation (25a) should be satisfied for $\delta/d \gtrsim 1$. Since the "negative running" characteristics from the region $\delta/d \lesssim 1$ will intersect the surface of the body very near the leading edge, the condition $p_w \approx p_\infty$ should occur very close to the leading edge for a flat afterbody. Accordingly, the "blast-wave" mechanism usually associated with blunt nosed slender bodies in hypersonic flow will be considerably reduced for altitudes ($\gtrsim 200,000$ ft) where the "frozen" composition model is applicable. In this case, most leading edge geometries can be considered "sharp" nosed with the boundary layer interaction mechanism determining the downstream flow field for flat afterbody geometries (a detailed discussion of the frozen boundary layer interaction problem is presented in Section II. A. 3).

In order to obtain numerical verification of the preceding conclusions, a characteristics solution of the frozen hypersonic flow about a blunt leading edge slender body was made.⁵ Employing the "sonic-wedge" model of Bertram,¹² the frozen and equilibrium flow models have been numerically examined for $V_\infty = 28,000$ fps, $h = 300,000$ ft. To be sure, viscous effects must be considered in any accurate determination of the flow field at these flight conditions. However, this consideration is not pertinent to the objective of this particular investigation. The characteristics net for the "sonic-wedge" problem is shown in Figure 7. The large region downstream of the leading edge influenced by the gas contained

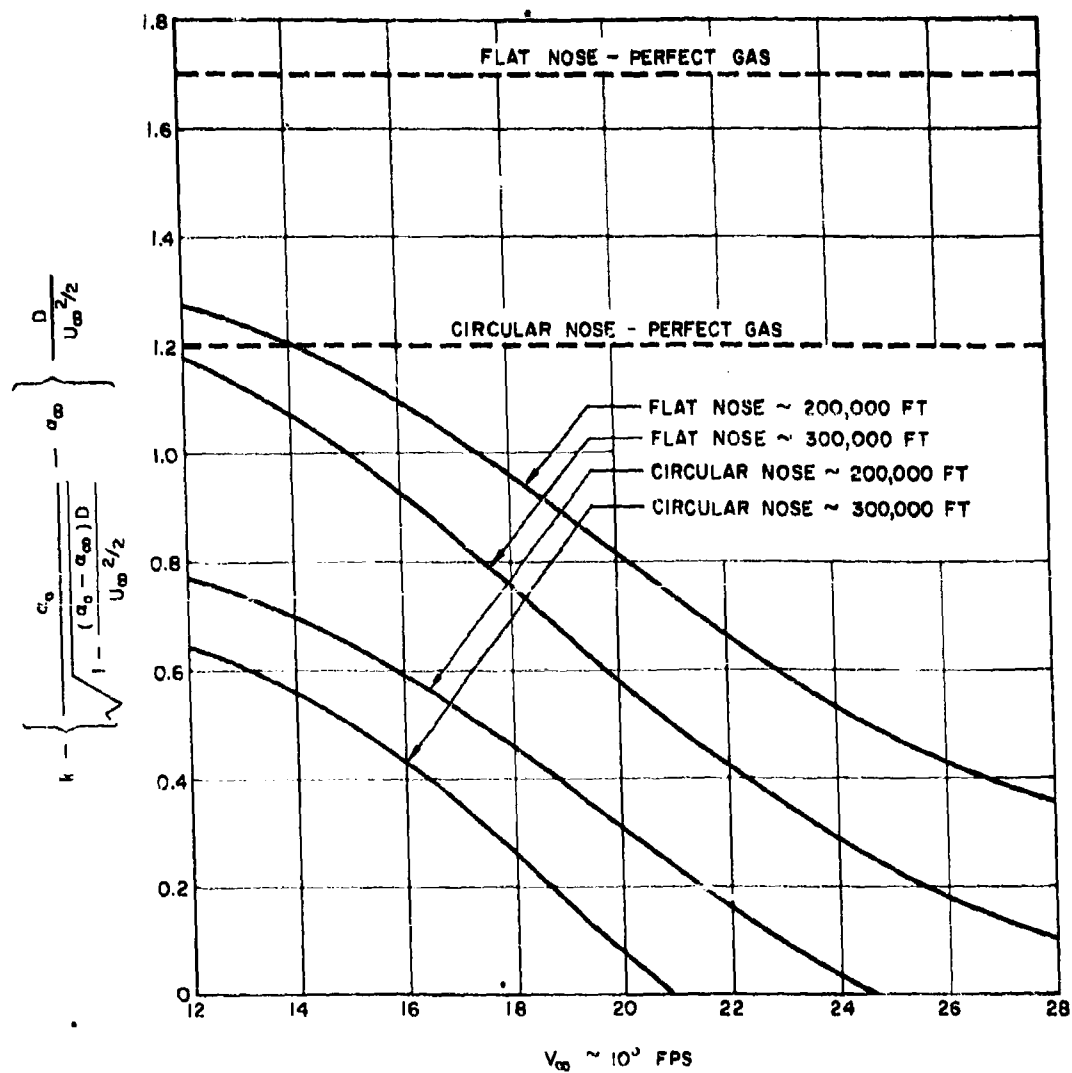


Figure 6. Nose Drag and Dissociation Energy Distribution

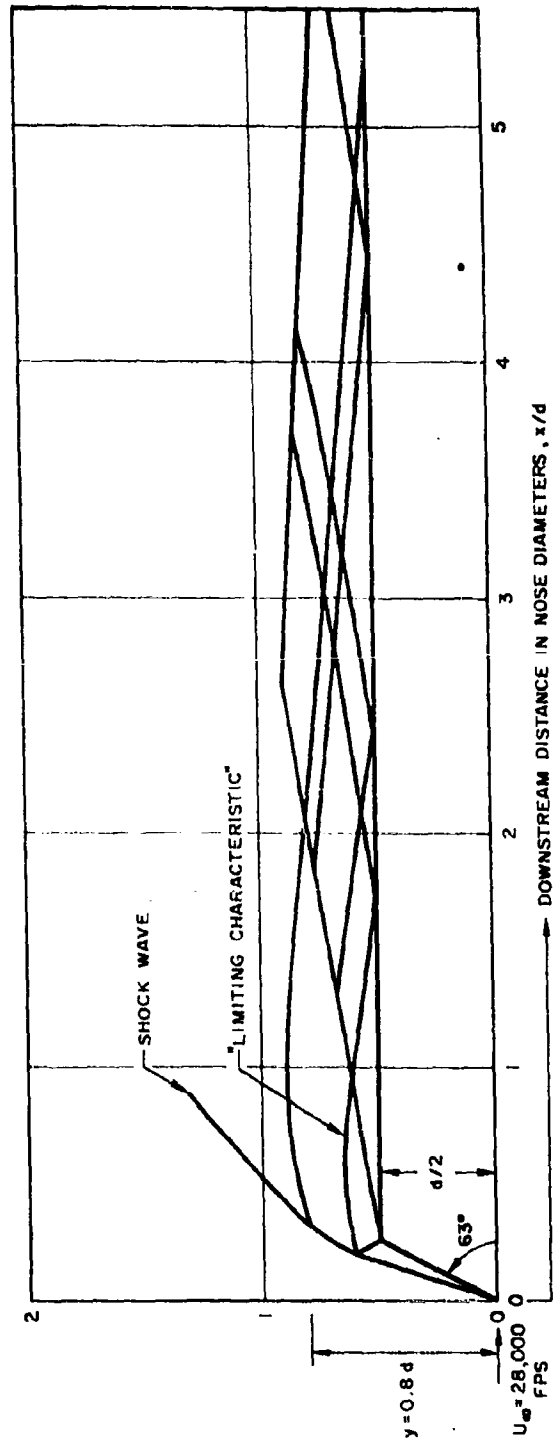


Figure 7. Characteristics Diagram for "Frozen" Flow

between the centerline of the wedge and the "limiting characteristic" can be observed in this figure. This is a result of the "sonic-wedge" geometry which should provide a larger downstream influence than that associated with flat or circular noses.*

For this particular case, .

$$k = \left[\frac{a_0}{\sqrt{1 - \frac{(a_0 - a_\infty) D}{U_\infty^2/2}}} - a_\infty \right] \frac{D}{U_\infty^2/2} = \frac{1}{2},$$

and relation (25c) takes the form

$$\frac{1}{2} p_\infty U_\infty \frac{d}{2} \approx \int_{d/2}^{\delta} p u \left\{ \left[\frac{a}{\sqrt{1 - \frac{(a - a_\infty) D}{U_\infty^2/2}}} - a_\infty \right] \frac{D}{U_\infty^2/2} \right\} dy \quad (26)$$

which, observing the value of $aD/U_\infty^2/2$ (Figure 4) associated with the "sonic-wedge" leading edge region, requires

$$\frac{\delta}{d} \lesssim 1 \quad (27)$$

Numerical integration of the right-hand term in (26) can be obtained from the wave diagram shown in Figure 7. The results of this integration are presented in Figure 8. It can be observed, from this figure, relation (27) is satisfied for $\delta/d \approx 0.8$. The negative characteristic at $\delta/d \approx 0.8$ is observed (wave diagram Figure 7) to intersect the after-body of the "sonic-wedge" at $x/d \approx 5.5$. This downstream distance should, therefore, provide an estimate of the point where $p_w \approx p_\infty$.

*The "sonic-wedge" geometry was chosen, of course, in order to avoid the difficult detached shock problem associated with the flat or circular nose geometries.

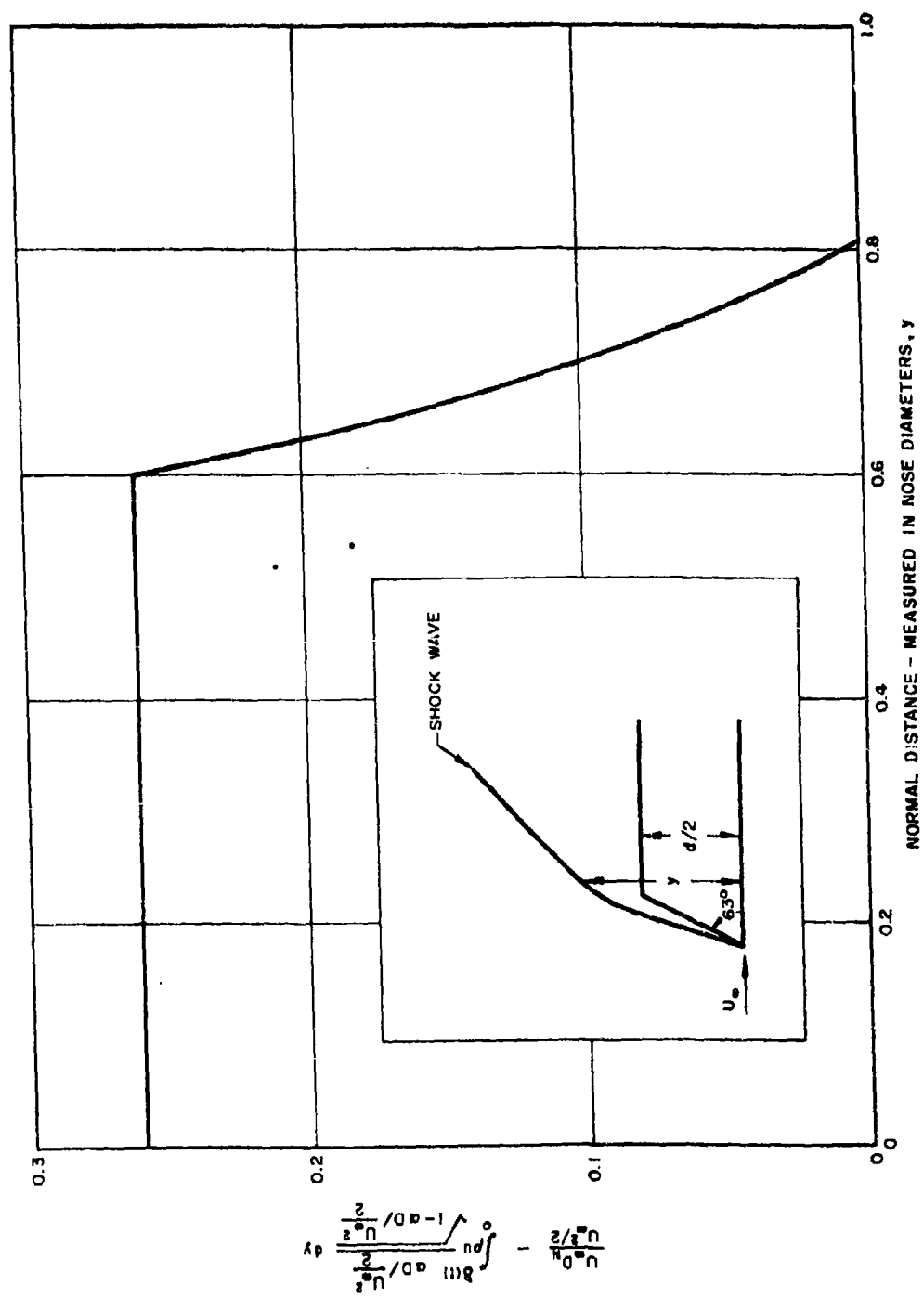


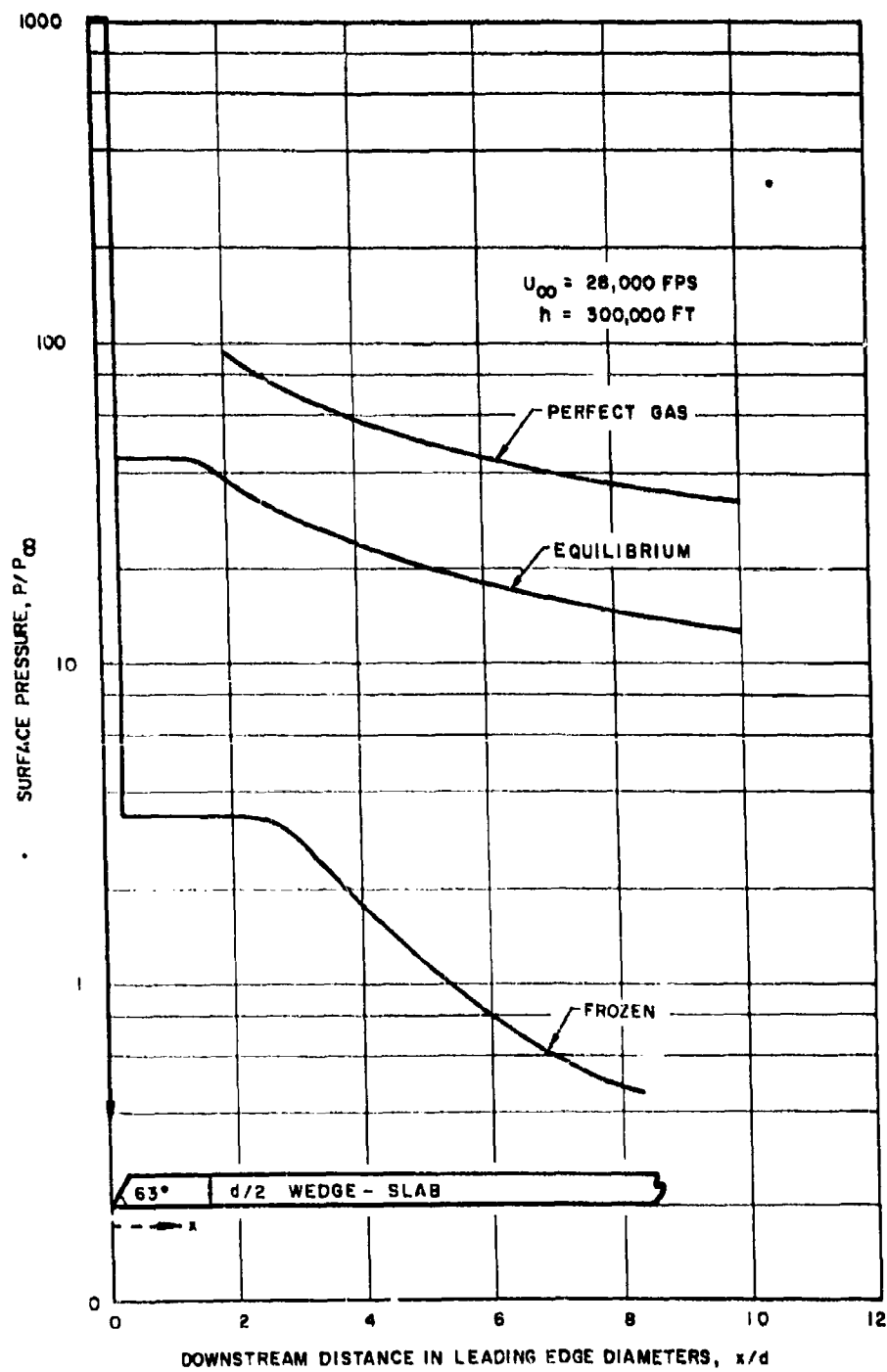
Figure 8. Difference Between Nose Drag and Dissociation Energy

The surface pressure distribution as a function of downstream distance in leading edge diameters, for both the equilibrium and frozen flow models, is presented in Figure 9. The agreement of the estimated point at which $p_w \approx p_\infty$ from relation (26), with the characteristics solution, can be observed in this figure. In addition, the previously discussed possibility of obtaining values of $p_w/p_\infty < 1$ can be observed in this figure. This is a result of the condition

$$U_\infty D_N < \int_{r_b}^{\delta} \rho u \left\{ \left[\frac{a}{\sqrt{1 - \frac{(a - a_\infty)^2 D}{U_\infty^2/2}}} - a_\infty \right] D \right\} dy \quad (28)$$

The large error introduced with the use of an equilibrium pressure distribution can also be readily observed in Figure 9. It should be remembered at this point, as previously discussed, the "sonic-wedge" geometry should provide a maximum downstream influence of the leading edge. Detached shock leading edge geometries, according to (25c), should yield $p_w \approx p_\infty$ closer to the leading edge than that for the "sonic-wedge" geometry, thus, greatly diminishing and eliminating, for most practical purposes, the "blast-wave" mechanism.

The corresponding frozen and equilibrium temperature and electron concentration distribution at the outer edge of the boundary are shown in Figures 10 and 11, respectively. The frozen electron concentration is determined assuming the electrons to be in equilibrium with the local frozen gas temperature. Finally, Figure 12 presents the frozen and equilibrium skin friction and heat transfer coefficients as a function of downstream distance. Both the skin friction and heat transfer parameters are normalized with respect to the wall velocity and enthalpy gradients, respectively, in order to allow incorporation of the influence of finite surface catalysis.



• Figure 9. Pressure Distribution About Blunt Body
 in Hypersonic Flow

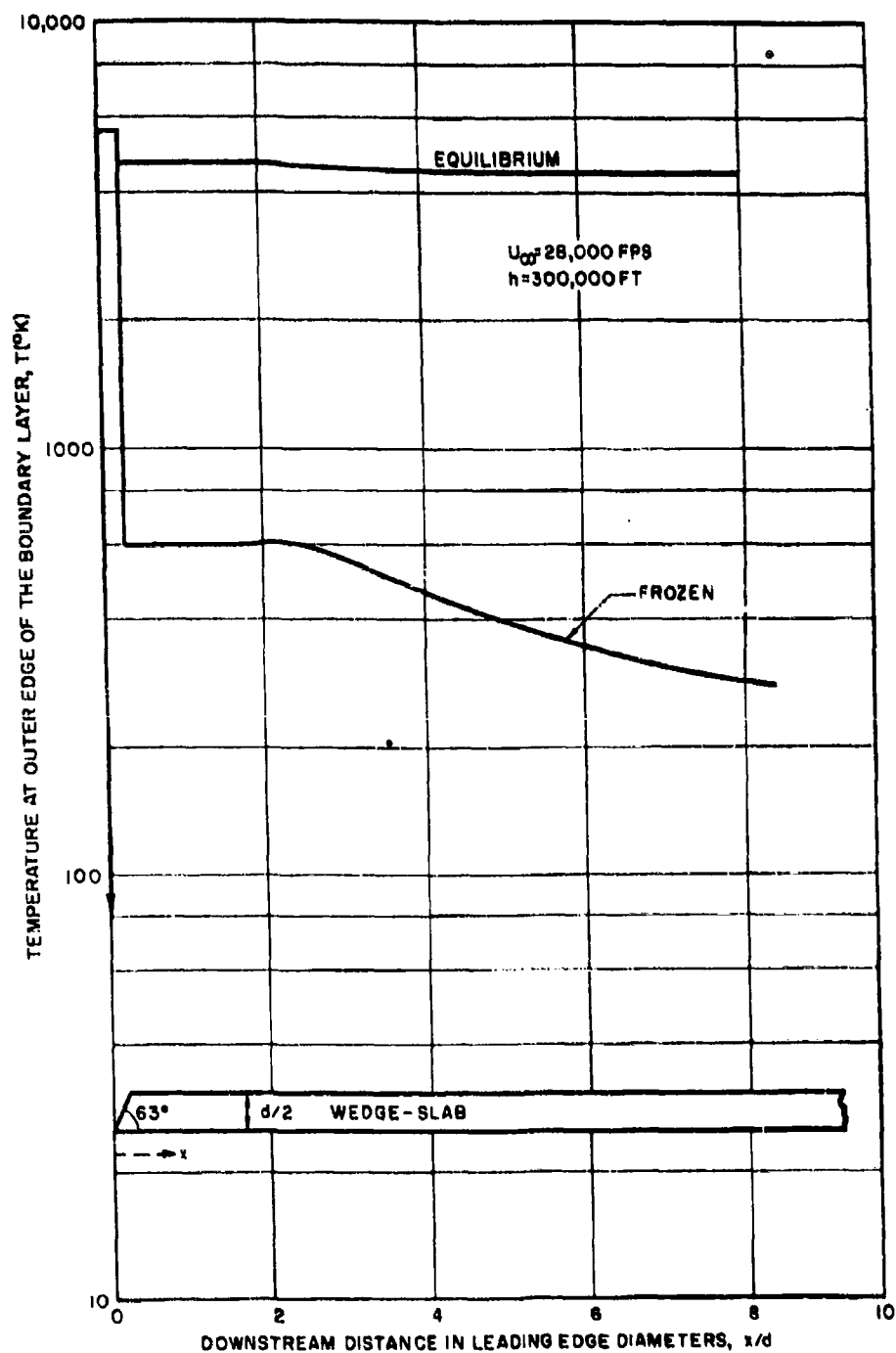


Figure 10. Temperature Distribution About Blunt Body in Hypersonic Flow

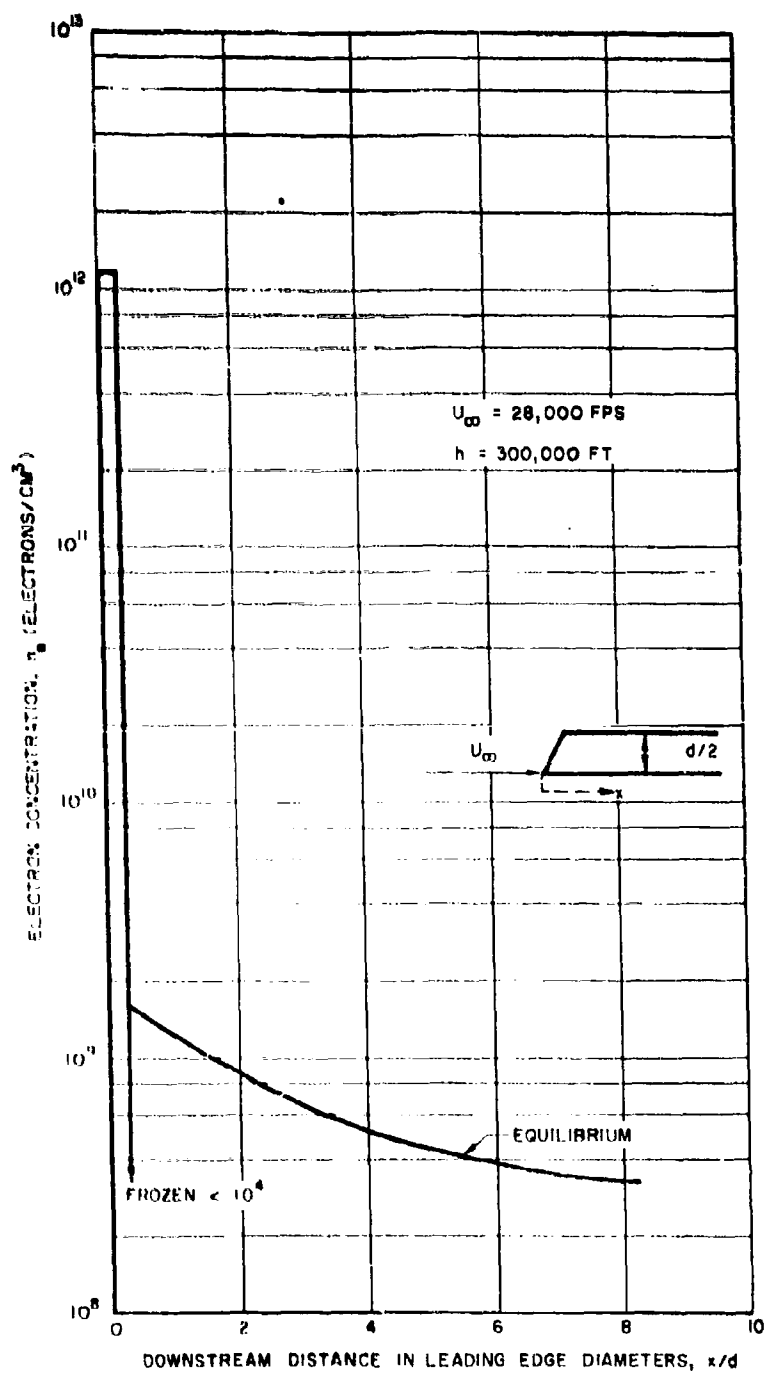


Figure 11. Electron Concentration Distribution at the Outer Edge of the Boundary Layer

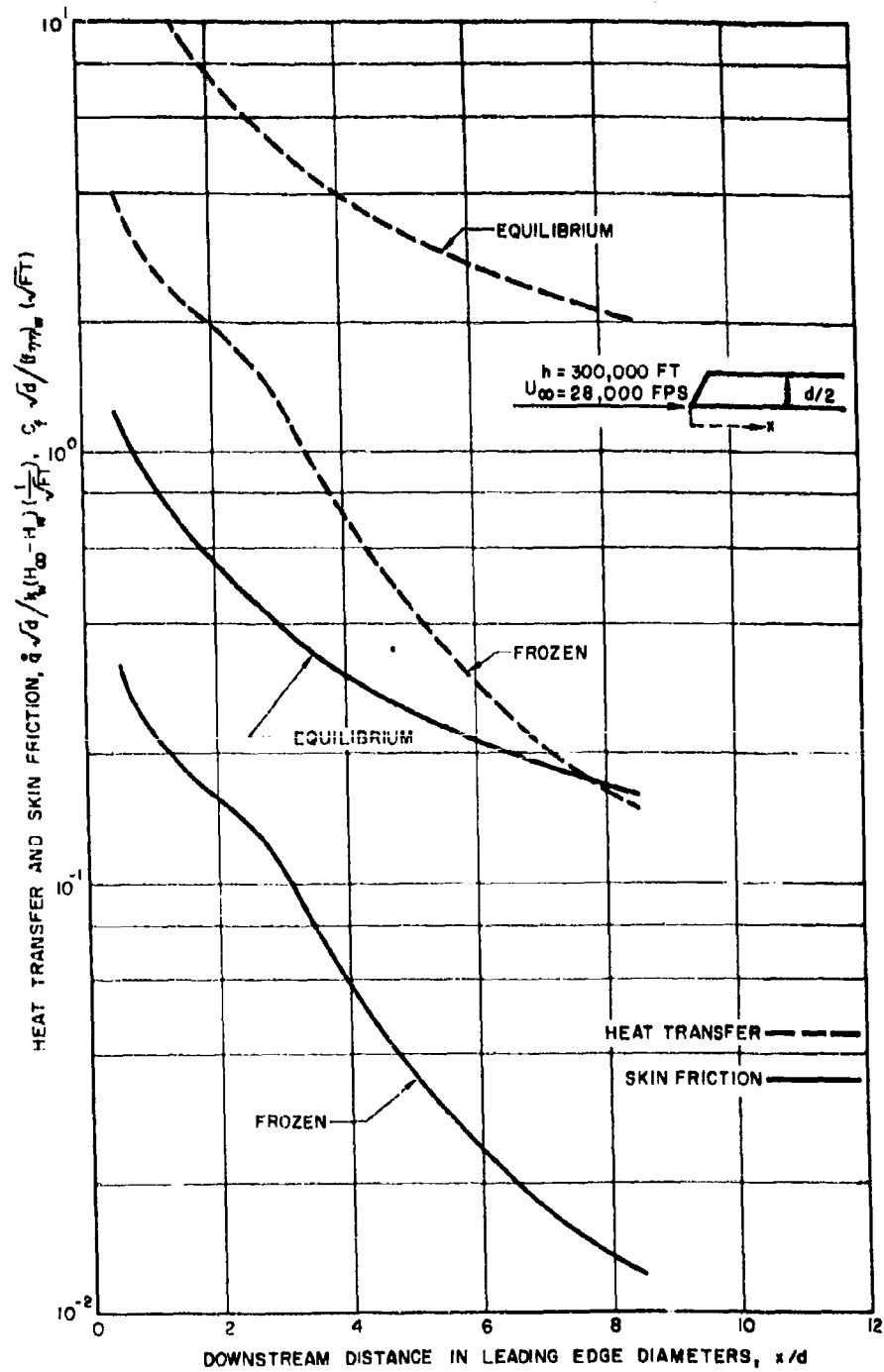


Figure 12. Local Skin Friction and Heat Transfer Distribution About Blunt Body in Hypersonic Flow

The above discussion neglected the presence of an afterbody. According to (25), the afterbody is observed to govern the down-stream flow field when

$$U_{\infty} \int_0^x p_w \frac{dr_b}{dx} (2\pi r_b)^{\nu} dx \gg \left| U_{\infty} D_N - \int_{r_b}^{\delta} \rho u \left\{ \left[\frac{a}{\sqrt{1 - \frac{(u - a_{\infty})^2 D}{U_{\infty}^2/2}}} - a_{\infty} \right] D \right\} (2\pi y)^{\nu} dy \right| \quad (29)$$

The absolute value signs are employed in (29) to include the condition in which case the local pressure on the surface of the body will be less than that associated with a "sharp" nosed geometry with the same afterbody. An estimate of the inequality (29) can be obtained if we consider blunt nosed cones or wedges, namely:

$$\frac{(2\pi)^{\nu}}{\nu+1} \frac{\theta^{3+\nu}}{\gamma} \left(\frac{x}{d} \right)^{\nu+1} \gg \frac{\pi^{\nu}}{2^{\nu+2}} k - \frac{1}{\rho_{\infty} U_{\infty}^3 d^{\nu+1}} \int_{r_b}^{\delta} \rho u \left\{ \left[\frac{a}{\sqrt{1 - \frac{(u - a_{\infty})^2 D}{U_{\infty}^2/2}}} - a_{\infty} \right] D \right\} (2\pi y)^{\nu} dy \quad (30)$$

which, for order-of-magnitude purposes, may be taken as

$$\frac{x}{d} \gg \frac{k^{1/1+\nu}}{\theta^{3+\nu/1+\nu}} \quad (31)$$

Relation (31) indicates that the downstream surface pressure on a blunt nosed cone or wedge can be lower than the corresponding "sharp" nosed value for a considerable distance downstream of the leading edge. The exact downstream distance for which this is the case is, according to (30), dependent on the shock wave envelope and the altitude and velocity [i. e., $(\alpha - \alpha_\infty) D/U_\infty^2/2$] of the vehicle.

3. Viscous Hypersonic Flow

The following assumptions are made for the viscous flow studies:

- a) The flow field in the shock layer is assumed to be divisible into a distinct boundary layer and an inviscid flow external to the boundary layer.
- b) The inviscid flow field is assumed to be governed by the inviscid flow assumptions listed in Section II. A. 2, (a) through (f).

With these assumptions in mind, we will now direct our attention to the "frozen" hypersonic boundary layer interaction problem.

a. "Sharp" Leading Edge Flat Plate

Employing the Howarth transformation, the boundary layer displacement thickness, δ^* , may be written

$$\delta^* = \frac{(2\tilde{s})^{1/2}}{\rho_\delta u_\delta} \int_0^\infty \left(\frac{\rho_\delta}{\rho} - \frac{u}{u_\delta} \right) d\eta \quad (32)$$

where $\tilde{s} = \int_0^s \rho_\delta \mu_\delta u_\delta ds$. Since the gas composition in the boundary layer is frozen at the value at the outer edge of the boundary layer, we can write

$$\frac{\rho_\delta}{\rho} = \frac{T}{T_\delta} = \frac{\beta_\delta (1 + \alpha_\delta)}{[(1 - \alpha_\delta) \beta_M + 2\beta_A \alpha_\delta]} \frac{H_\infty}{h_\delta} \left(g - \frac{u_\delta^2}{2H_\infty} f_1^2 - \frac{\alpha_\delta D}{H_\infty} \right) \quad (33)$$

where $H/H_\infty = g$, $f' = u/u_\delta$. We can further write

$$\frac{T}{T_\delta} - \frac{u}{u_\delta} = \frac{H_\infty}{[(1 - a_\delta) \beta_M + 2\beta_A a_\delta R T_\delta]} \left\{ g - \frac{u_\delta^2}{2H_\infty} f'^2 - \frac{a_\delta D}{H_\infty} - \frac{[(1 - a_\delta) \beta_M + 2\beta_A a_\delta] R T_\delta}{H_\infty} f' \right\} \quad (34)$$

but

$$[(1 - a_\delta) \beta_M + 2\beta_A a_\delta R T_\delta] = H_\infty - a_\delta D + u_\delta^2/2 \quad (35)$$

Therefore,

$$\frac{T}{T_\delta} - \frac{u}{u_\delta} = \frac{H_\infty}{[(1 - a_\delta) \beta_M + 2\beta_A a_\delta R T_\delta]} \left[g - \frac{u_\delta^2}{2H_\infty} f'^2 - \frac{a_\delta D}{H_\infty} + \left(\frac{a_\delta D}{H_\infty} + \frac{u_\delta^2}{2H_\infty} - 1 \right) f' \right] \quad (36)$$

Downstream of the leading edge, the temperature is sufficiently low so that we may take

$$H_\infty = \frac{u_\delta^2}{2} + a_\delta D \quad (37)$$

Therefore, the integral in (32) may be written

$$\int_0^\infty \left(\frac{\rho_\delta}{\rho} - \frac{u}{u_\delta} \right) d\eta \approx \frac{H_\infty}{[(1 - a_\delta) \beta_M + 2\beta_A a_\delta R T_\delta]} \int_0^\infty \left[g - f'^2 - \frac{a_\delta D}{H_\infty} (1 - f'^2) \right] d\eta \quad (38)$$

For the lower temperatures associated with downstream of the leading edge, we can take

$$\frac{\mu_\delta}{\mu_\infty} = \lambda \frac{T_\delta}{T_\infty} \quad (39)$$

Therefore, relation (32) can be written

$$\delta^* = \left(\frac{2\lambda}{Re_\infty} \right)^{1/2} \frac{\left(\int_0^s \frac{p_\delta}{p_\infty} \frac{1+a_\infty}{1+a_\delta} ds \right)^{1/2}}{\frac{p_\delta}{p_\infty}} - \left(\frac{U_\infty}{u_\delta} \right)^{1/2} \frac{1+a_\delta}{1+a_\infty} \frac{H_\infty}{\left[(1-a_\delta)\beta_M + 2\beta_A a_\delta RT_\delta \right]} I(\beta, S_w, a) \quad (40)$$

where

$$Re_\infty = \rho_\infty \frac{U_\infty}{\mu_\infty}, \quad I(\beta, S_w, a) = \int_0^\infty \left[g-f'^2 - \frac{a_\delta D}{H_\infty} (1-f'^2) \right] d\eta$$

If we assume inviscid pressure distributions of the form of relations (16) and (17) and note that for the boundary layer interaction problem, we can write

$$v_w = \frac{d}{dt} \left[r_b(t) \right] = \sigma B t^{\sigma-1} = v_1 V(0) \quad (41)$$

and, substituting for v_1 , we obtain

$$A = \frac{\gamma+1}{2} \frac{B}{V(0)} \quad (42)$$

where we have taken $\delta = At^\sigma$ and $r_b = Bt^\sigma$. Identifying the boundary layer displacement thickness with $r_b(t)$ we can write (40) as

$$\delta^* = \left(\frac{2\lambda}{Re_\infty} \right)^{1/2} \frac{\left[\int_0^s \frac{1+a_\infty}{1+a_\delta} s^{2(\sigma-1)} ds \right]^{1/2}}{\left(\frac{2\gamma}{\gamma+1} \right)^{1/2} \sigma A M_\infty U_\infty^{-\sigma} [P(0)]^{1/2} \sigma^{2(\sigma-1)} \left(\frac{U_\infty}{u_\delta} \right)^{1/2}} \frac{1+a_\delta}{1+a_\infty} \frac{I_\infty}{[(1-a_\delta)\beta_M + 2\beta_A a_\delta RT_\delta]} I(\beta, S_w, a) \quad (43)$$

The above equation can be treated analytically by considering the limiting cases of large and small a_δ (i.e., in order to let $1+a_\delta \approx \text{constant}$). In this case, we may remove the term $(1+a_\delta)$ from the integral. In lieu of this relation, (43) must be solved numerically for a prescribed $a_\delta = a_\delta(s)$ which then introduces additional complication into $I(\beta, S_w, a)$ since $a_\delta D/H_\infty \neq \text{constant}$. Therefore, for $a_\delta \approx \text{constant}$, we can write

$$\delta^* = \left(\frac{2\lambda}{Re_\infty} \right)^{1/2} \frac{U_\infty^\sigma s^{\sigma-1/2}}{\left(\frac{2\gamma}{\gamma+1} \right)^{1/2} \sigma A M_\infty [2(\sigma-1)+1]^{1/2} [P(0)]^{1/2} s^{2(\sigma-1)}} \left(\frac{U_\infty}{u_\delta} \right)^{1/2} \left(\frac{1+a_\delta}{1+a_\infty} \right)^{1/2} \frac{(1-a_\infty)\beta_M RT_\infty + 2\beta_A a_\infty RT_\infty + a_\infty D + \frac{U_\infty^2}{2}}{[(1-a_\delta)\beta_M RT_\infty + 2\beta_A a_\delta RT_\infty]} I(\beta, S_w, a) \quad (44)$$

For either the hypersonic nozzle problem or the free-flight case, we can take

$$(1-a_\infty)\beta_M RT_\infty + 2\beta_A a_\delta RT_\infty \ll a_\infty D + \frac{U_\infty^2}{2} \quad (45)$$

which simplifies (44) to

$$\delta^* = \left(\frac{\lambda}{Re_\infty} \right)^{1/2} \frac{U_\infty^\sigma s^{3/2-\sigma}}{\left(\frac{\gamma}{\gamma+1} \right)^{1/2} \sigma A [2(\sigma-1)+1]^{1/2} [P(0)]^{1/2}} \left(\frac{U_\infty}{u_\delta} \right)^{1/2} \\ \left(\frac{1+a_\delta}{1+a_\infty} \right) \frac{\gamma_\infty (1+a_\infty)}{2} \left\{ \frac{1 + \frac{a_\infty^2 D}{U_\infty^2/2}}{[(1-a_\delta)\beta_M + 2\beta_A a_\delta]} \right\} M_\infty I(\beta, S_w, a) \quad (46)$$

Making use of relation (42) and noting $\sigma = 3/4$ for the boundary layer interaction problem, we can solve for A :

$$A^2 = \frac{\sqrt{2}}{3} (\gamma+1) \frac{U_\infty^{3/4} u_\delta^{3/4}}{\left(\frac{\gamma}{\gamma+1} \right)^{1/2} [P(0)]^{1/2}} \left(\frac{U_\infty}{u_\delta} \right)^{1/2} \left(\frac{1+a_\delta}{1+a_\infty} \right)^{1/2} \frac{\gamma_\infty (1+a_\infty)}{V(0)} \\ \left\{ \frac{1 + \frac{a_\infty^2 D}{U_\infty^2/2}}{[(1-a_\delta)\beta_M + 2\beta_A a_\delta]} \right\} M_\infty \sqrt{\frac{\lambda}{Re_\infty}} I(\beta, S_w, a) \quad (47)$$

Substitution of (47) into (16) yields the surface pressure in the form

$$\frac{p_w}{p_\infty} \approx \frac{3\sqrt{2}}{8} [\gamma(\gamma+1)]^{1/2} \gamma_\infty (1+a_\infty) \left(\frac{u_\delta}{U_\infty} \right)^{1/4} \left(\frac{1+a_\delta}{1+a_\infty} \right)^{1/2} \\ \left\{ \frac{1 + \frac{a_\infty^2 D}{U_\infty^2/2}}{[(1-a_\delta)\beta_M + 2\beta_A a_\delta]} \right\} \frac{[P(0)]^{1/2}}{V(0)} I(\beta, S_w, a) \chi_g \quad (48)$$

where $\chi_s \equiv M_\infty^3 (\lambda/Re_s)^{1/2}$, $Re_s = \rho_\infty U_\infty s / \mu_\infty$. Since we are concerned with the downstream problem, we can take $\gamma = 7/5$, as in the previous study, for all cases except those where $\alpha_\infty \rightarrow 1$. The only other term which would provide any numerical difficulty would be $[P(0)]^{1/2}/V(0)$. Since the previous remarks bound the value of this parameter between the $7/5 \leq \gamma \leq 5/3$ value, an inspection of Figure 3 indicates

$$\frac{[P(0)]^{1/2}}{V(0)} = 1.045 \quad \text{for } \gamma = 7/5 \quad (49)$$

$$\frac{[P(0)]^{1/2}}{V(0)} = 1.18 \quad \text{for } \gamma = 5/3.$$

Therefore, the $\gamma = 7/5$ value should numerically introduce a small error into relation (48). Further, we should also note we can take

$$\left(\frac{U_\delta}{U_\infty} \right)^{1/4} \approx \left[1 + \frac{(\alpha_\infty - \alpha_\delta) D}{U_\infty^2 / 2} \right]^{1/8} \approx 1 \quad (50)$$

For all practical values of $(\alpha_\infty - \alpha_\delta) D / U_\infty^2 / 2$.

Numerical evaluation of $I(\beta, S_w, \alpha)$ will complete the numerical requirements for relation (48). In general, numerical evaluation of $I(\beta, S_w, \alpha)$ can only be made for a given set of altitude-velocity conditions since g and f , among other things, are functions of Prandtl number and thus vary due to the dissipation term in the energy equation according to N. Kemp.* If, however, we ignore this variation for the range of altitude and velocity we are concerned with and, also, consider g and f independent of $\alpha_\delta D / H_\infty$ (an assumption which is certainly open to question for large values of $\alpha_\delta D / H_\infty$), we can then numerically evaluate $I(\beta, S_w, \alpha)$ as a

* Private communication.

0

function of $\alpha_\delta D/H_\infty$. Therefore, $I(\beta, S_w, \alpha)$ is evaluated numerically subject to the following boundary conditions:

$$f(0) = 0, f'(0) = 0, f'(\infty) = 1$$

$$g(0) = \frac{\alpha_\delta D}{H_\infty}, \quad g(\infty) = 1 \quad (51)$$

$$\alpha'(0) = 0$$

where the primed condition denotes $d/d\eta$.

The above conditions imply a highly cooled, "noncatalytic" wall. The numerical results are presented in Figure 13. As would be anticipated, for $\alpha_\delta D/H_\infty = 1$, $I(\beta, S_w, \alpha) = 0$. Namely, if all the energy is frozen in the dissociation mode a viscous dissipation mechanism, the boundary layer, is not required. To be sure, as $\alpha_\delta D/H_\infty \rightarrow 1$, the assumptions (i.e., hypersonic small disturbance, invariance of g and f , neglect of ionization) employed in this analysis are no longer valid; and therefore, the region in the vicinity of $I(\beta, S_w, \alpha) \approx 1$ should not be considered too seriously.

Before any numerical evaluation of (48) is made, one must naturally inquire as to the range of values of α_δ for sharp leading edges which are associated with realistic flight conditions. This consideration can be made in a simple manner; namely, consider the flow field geometry in Figure 14. Mass conservation requires

$$\rho_\infty U_\infty h_1 = \int_0^{\delta^*} \rho u dy \quad (52)$$

which, under the Howarth transformation, can be written

$$\rho_\infty U_\infty h_1 = (2\tilde{x})^{1/2} \int_0^\infty f' d\eta \quad (52a)$$



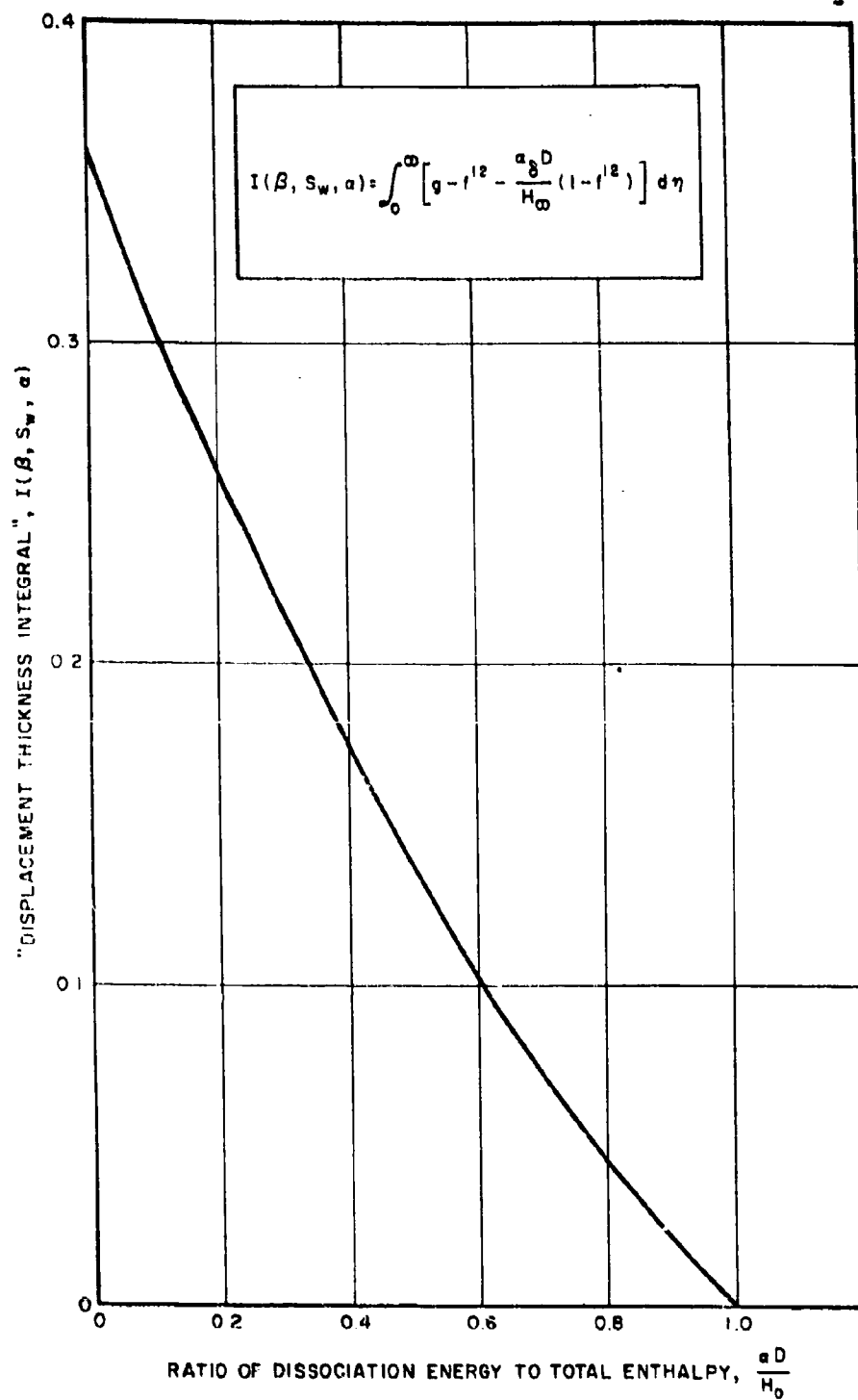


Figure 13. "Displacement Thickness Integral" for a "Non-Catalytic" Surface

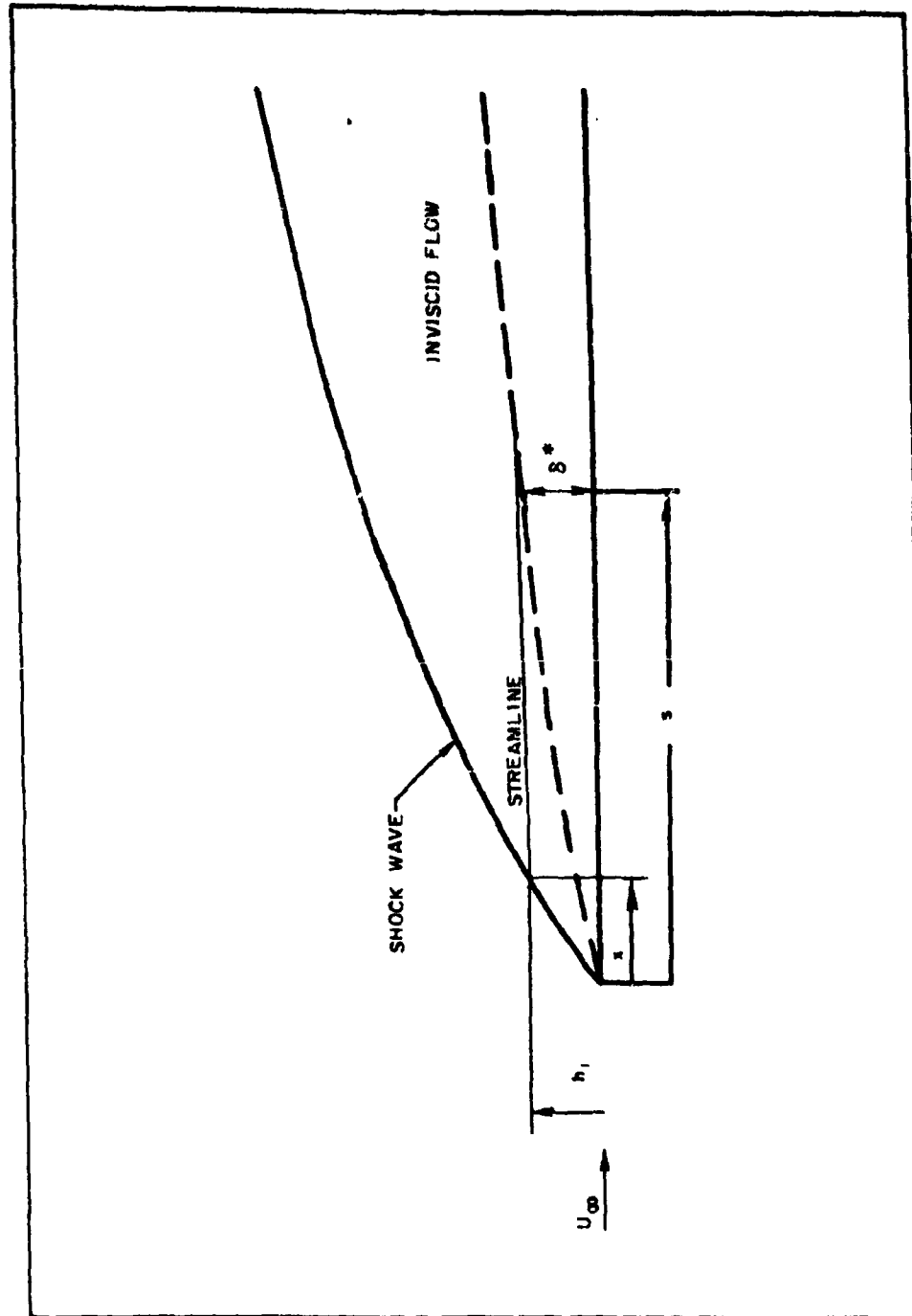


Figure 14. Flow Field Description

where

$$\tilde{s} = (\rho_{\infty} U_{\infty} \lambda \mu_{\infty}) \frac{U_{\delta}}{U_{\infty}} \int_0^s \frac{p_{\delta}}{p_{\infty}} \frac{1 + a_{\infty}}{1 + a_{\delta}} ds$$

Substitution of relation (48) into (52a) and differentiating we obtain

$$\frac{dh_1}{dx} = 0.40 \frac{(\gamma + 1)^{11/12}}{\gamma^{5/12}} \frac{[P(0)]^{5/12}}{[V(0)]^{1/2}} \left(\frac{U_{\infty}}{U_{\delta}} \right)^{1/24} \left(\frac{1 + a_{\delta}}{1 + a_{\infty}} \right)^{5/12} \gamma_{\infty}^{1/2} (1 + a_{\infty})^{1/2} \left\{ \frac{1 + \frac{a_{\infty} D}{U_{\infty}^2/2}}{[1 - a_{\delta} \beta_M + 2\beta_A a_{\delta}]} \right\} \frac{\chi_s}{M_{\infty}^{1/3}} \frac{[1(\beta, S_w, a)]^{1/2}}{\left(\int_0^{\infty} f' d\eta \right)^{1/3}} \quad (53)$$

If we substitute for $a_{\infty} = 0$, $\gamma = 7/5$, we obtain

$$\frac{dh_1}{dx} \approx 0.44 \frac{\chi^{1/6}}{M_{\infty}^{1/3}} \quad (54)$$

For practical flight conditions, for which the division of a distinct boundary layer and inviscid flow is possible, $\chi^{1/6}/M_{\infty}^{1/3} < 1$. According to (54), this condition implies flow deflections of less than 25 degrees which, upon examination of Figure 4, indicate values of $\alpha D/U_{\infty}^2 \leq 0.1$. Therefore, "freezing" of the dissociation energy should have a small influence on the boundary layer interaction problem for a "sharp" flat plate. Specifically, the frozen boundary layer interaction on a "sharp" flat plate should be given, to good approximation, by the perfect gas $\gamma = 7/5$ prediction.

b. "Blunt" Leading Edge Flat Plate

The boundary layer interaction problem for the blunt leading edge flat plate is defined as the condition where the streamlines at the

outer edge of the boundary layer are those which passed through the near-normal shock in the vicinity of the leading edge. In contrast to the investigations in Reference 1, the decreased importance of the frozen blast-wave mechanism, discussed in II. A. 2. b, allows examination of this problem with neglect of the downstream influence of the leading edge. In addition, since we are not concerned here with the low-Reynolds number problem, we will ignore vorticity corrections such as those considered by Lees.¹³

With these remarks in mind, we need simply evaluate the conditions at the outer edge of the boundary layer for incorporation into relation (48). In this case, a_δ is equal to the value behind a normal shock for the given free-stream velocity and altitude. The value of $I(\beta, S_w, a)$ is equal to the value obtained from Figure 13 with $a_\delta D/H_\infty$ equal to that behind a normal shock for the given free-stream velocity and altitude. Finally, the velocity at the outer edge of the boundary layer is obtained by

$$U_\delta \approx U_\infty \sqrt{1 - \frac{(a - a_\infty) D}{U_\infty^2 / 2}} \quad (55)$$

with a = value behind normal shock. With these considerations in mind, the frozen boundary layer-induced pressure for a "blunt" and "sharp" flat plate is presented in Figure 15. The "catalytic" curve is taken as that for which $I(\beta, S_w, a)$ is equal to the value for $a_\delta D/H_\infty = 0$. The large differences which are observed in this figure are due mainly to variations of $I(\beta, S_w, a)$ with $a_\delta D/H_\infty$. The relatively weak dependence on free-stream velocity can also be observed in this figure. As would be anticipated, the "sharp" leading edge-induced pressure is given closely by the perfect gas value (i.e., $p/p_\infty \approx 0.16X$). The "blunt" leading edge "catalytic" wall value is slightly higher as a result of the term $[(1 + a_\delta)/(1 + a_\infty)]^{1/2}$ in relation (48).

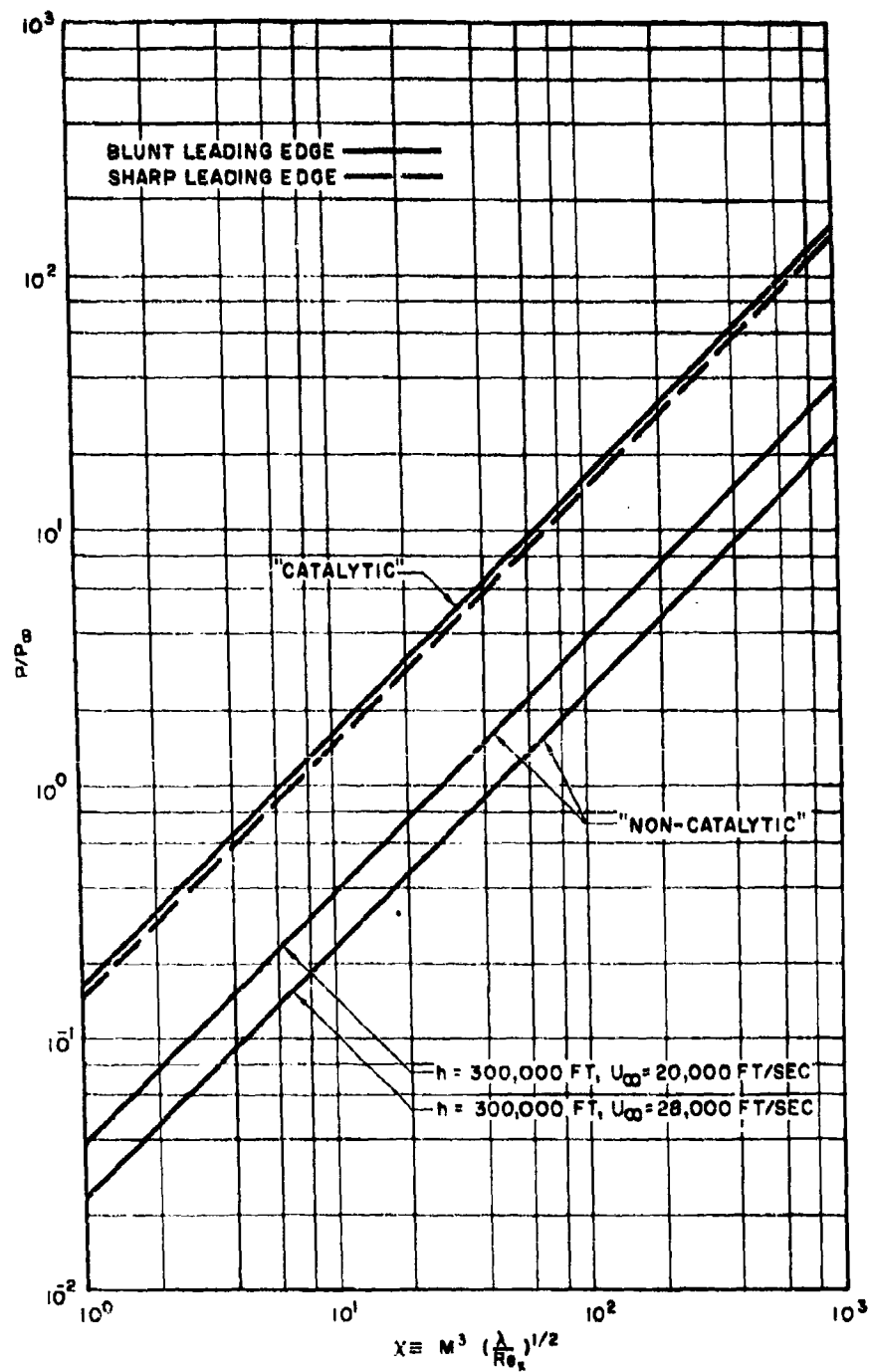


Figure 15. Frozen Boundary Layer Interaction on a "Blunt" and "Sharp" Flat Plate

4. "Controlled Non-Equilibrium Expansions"

One of the most serious problems associated with the development of high enthalpy-low density hypervelocity facilities is the presence of dissociation non-equilibrium within the expansion nozzle. Indeed, the stagnation conditions required for experimentally investigating dissociative non-equilibrium phenomena can give rise to large departures from equilibrium within the nozzle itself. This problem has received considerable theoretical investigation for single component systems.¹⁴⁻¹⁶ In addition, a recent experimental investigation of this problem, for a multi-component system (air), has been made by Nagamatsu, et al.¹⁷ Since the analysis of the non-equilibrium nozzle flow problem has been discussed in detail in References 5, 14-16, we shall not discuss it further. Rather, we shall employ the results in the present discussion.

If we define a Mach number "M" such that

$$"M" = \frac{U}{"a"} = \frac{u}{\sqrt{(\partial p / \partial \rho)_s}} \quad (56)$$

then, for a dissociating gas we can write¹⁸

$$"a"{}^2 = \left(\frac{\beta + T \frac{d\beta}{dT}}{\beta - 1 + T \frac{d\beta}{dT}} \right) R (1 + \alpha) T \quad (57)$$

It can be easily shown that (57), for a constant gas composition, can be written

$$"a"{}^2 = \frac{\frac{1-\alpha}{1+\alpha} \beta_M + 2\beta_A \frac{\alpha}{1+\alpha}}{\frac{1-\alpha}{1+\alpha} \beta_M + 2\beta_A \frac{\alpha}{1+\alpha} - 1} \quad (58)$$

where we have neglected $d\beta_M/dT$ in comparison to the remaining terms. With "Mach number" in a frozen gas stream defined by (56) and (58), we

0
have calculated "M" as a function of a nozzle expansion ratio assuming a rate law for "air" recombination to be given by that proposed by Byron³ for oxygen recombination, namely $k_R(T) = 2.16 \times 10^{17} \text{ cm}^6/\text{mole}^2 \text{ sec.}$ (T in °K).

To be sure, the complex kinetics associated with the coupled reactions in air cannot be represented by a simple temperature dependence; however, the relatively weak influence of $k_R(T)$ on the non-equilibrium nozzle expansion process will lend some degree of generality to the results. In addition, the present results can easily be modified to incorporate more accurate rate data when it becomes available.

Figure 16 presents "M" as a function of nozzle expansion ratio for a stagnation temperature of 8000°K and for stagnation pressures (P_0) of 10, 100, and 1000 atmospheres. The calculations were made for a conical nozzle with a 7.5-degree half-angle and a throat diameter of 0.1 inch. However, since the nozzle dimensions and geometry have a weak influence on the non-equilibrium process,^{5, 15-17} the results can be considered quite general. These stagnation pressures would correspond, respectively, to arc-jet, shock tunnel, spark-heated (hot shot) operation. The difference between the equilibrium and non-equilibrium "Mach number" is due to the large difference in static temperature between the equilibrium and non-equilibrium expansion process. Figure 16, therefore, indicates the attractive possibilities for generating high "Mach number" gas flows by means of "controlled non-equilibrium expansions" (using stagnation pressure variations). The main consideration here, of course, is the utility (in terms of aerodynamic simulation) of this frozen composition high "Mach number" gas stream. A measure of the dissociation energy frozen in the nozzle is shown in Figure 17. In this figure the ratio of the frozen dissociation energy in the nozzle to the stagnation enthalpy is presented as a function of stagnation pressure. The trade-offs between "Mach number" and frozen dissociation energy can, therefore, be observed in Figures 16 and 17. The simulation capabilities, in terms of "M" and χ , for a stagnation pressure of 10 atmospheres are shown in Figure 18. Indeed, the possibility of concurrent "Mach number"

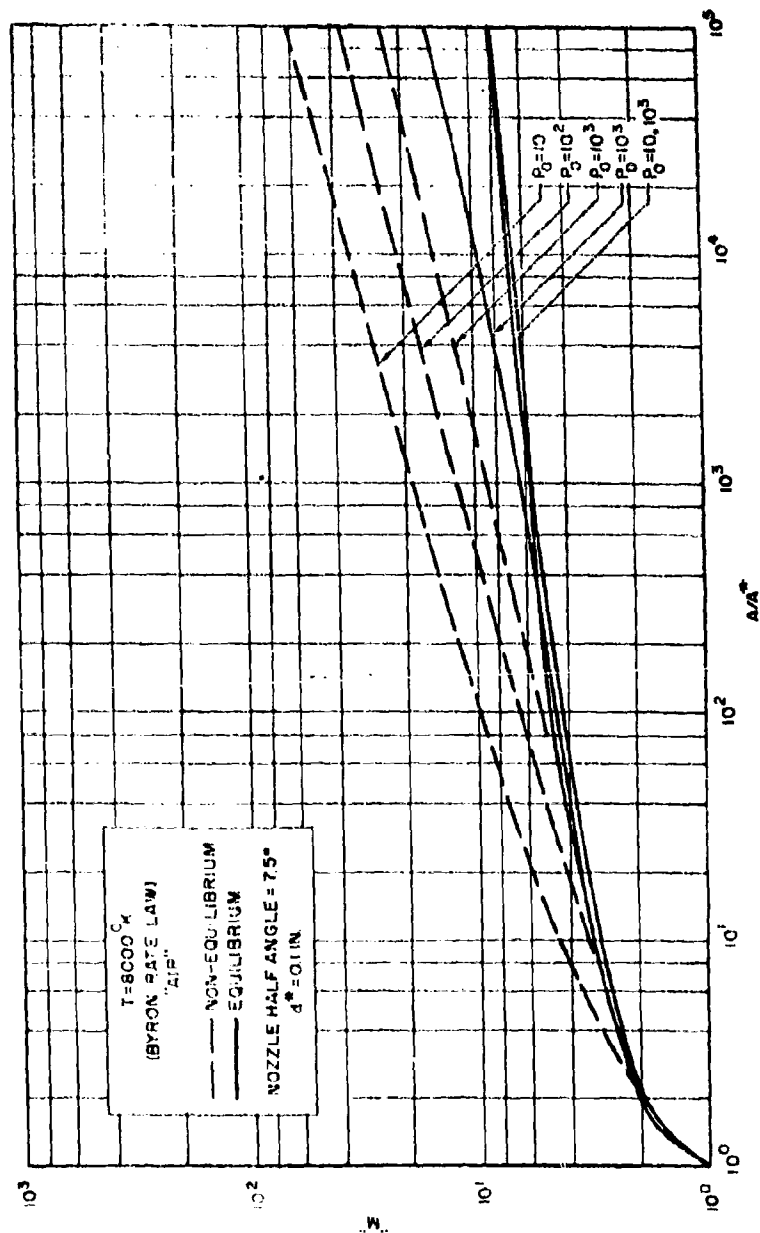


Figure 16. "M" vs A/A^*

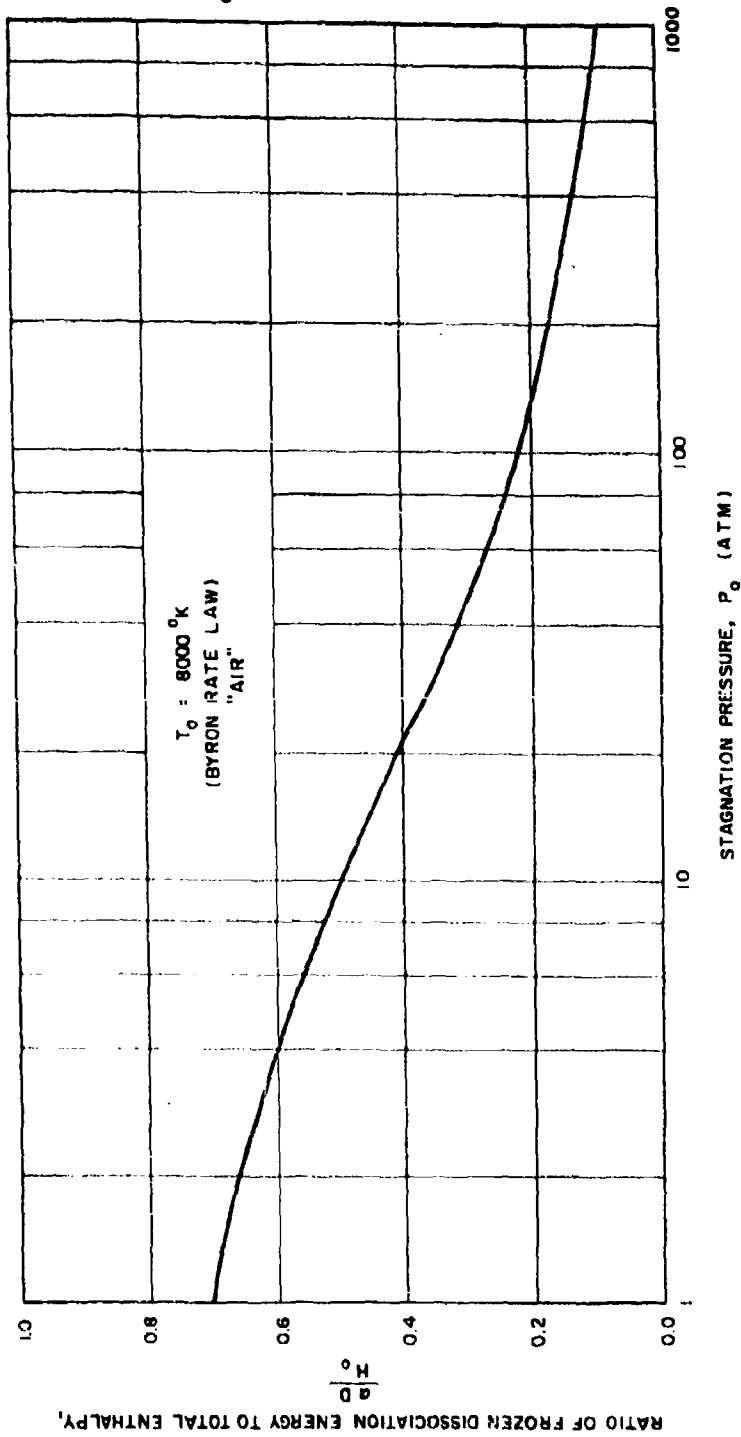


Figure 17. Energy Distribution in Hypersonic Nozzle as a Function of Stagnation Pressure

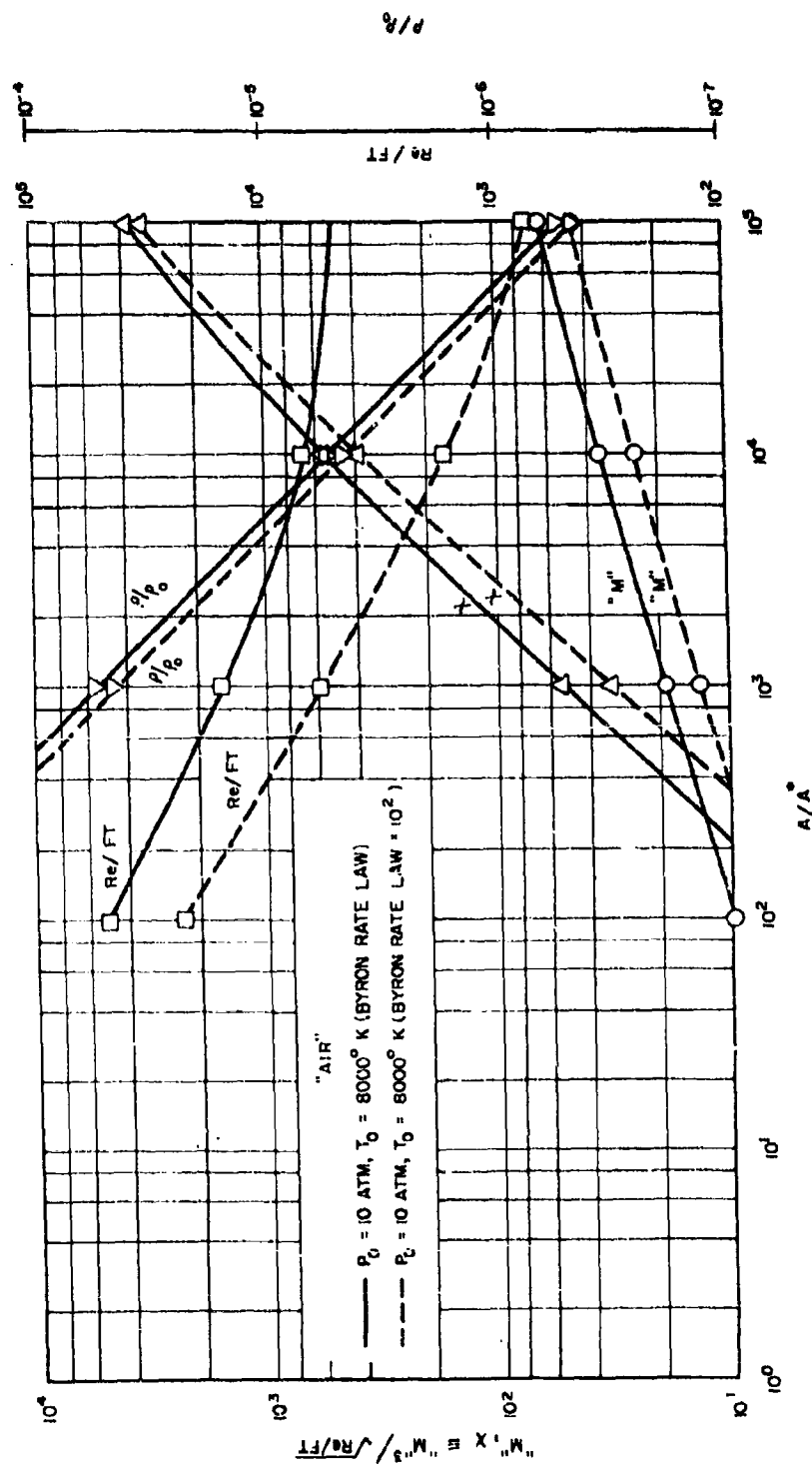


Figure 18. "Controlled Non-Equilibrium Expansions"

and Reynolds number simulation can be observed from this figure. These parameters are indicated for the previously discussed Byron rate law and a rate law two orders of magnitude "faster" (i. e., Byron rate law $\times 10^2$). The previously discussed weak dependence on $k_R(T)$ can be observed in this figure. With these "performance charts" for orientation, we shall now turn our attention toward a discussion of the simulation capabilities of high "Mach number" frozen composition gas flows.

If first we consider the simulation capabilities in terms of the similitude for slender sharp-nosed bodies established by Cheng,¹⁹ we can write the surface pressure similitude as

$$\frac{p}{p_\infty} = \pi(M_\infty, \tau, p_\infty, \rho_\infty, a_\infty) \quad (59)$$

where $p_\infty, \rho_\infty, a_\infty$ expresses the free-stream atmosphere simulation requirement. Since the surface pressure has previously indicated¹⁹ a weak dependence on $p_\infty, \rho_\infty, a_\infty$, we can examine this similitude, in terms of the Hugoniot relations, for the non-equilibrium nozzle flows indicated in Figures 16 to 18 where, indeed, $p_\infty, \rho_\infty, a_\infty$ are not properly simulated. These results are presented in Figure 19. In this figure the pressure ratio across an oblique shock is plotted against the similarity parameter " M " τ (τ = wedge angle) for the "Mach number" range $6.7 \lesssim "M" \lesssim 62.5$. The agreement with the similitude curve for a nondissociated free-stream-atmosphere, given to good approximation by $p/p_\infty = \gamma(\gamma+1)/2 "M"{}^2 \tau^2$, can be observed in this figure. Similar agreement with the lift curve similitude can be observed in Figure 20. Numerical results for the skin friction and heat transfer coefficient are presented in Figure 21. The solid curve labeled "free-flight" represents a correlation of the Hugoniot relations for the range $10,000 \leq V \leq 28,000$ fps at $h = 300,000$ ft. The agreement of the frozen skin friction and heat transfer coefficients with the "free-flight" values from $10 \lesssim "M" \lesssim 25$ can be observed in this figure. The results are presented for both the Byron rate law and the Byron rate $\times 10^2$. The corresponding lack of simulation for " M " = 35.5, 45, 62.5 can also be observed.

0

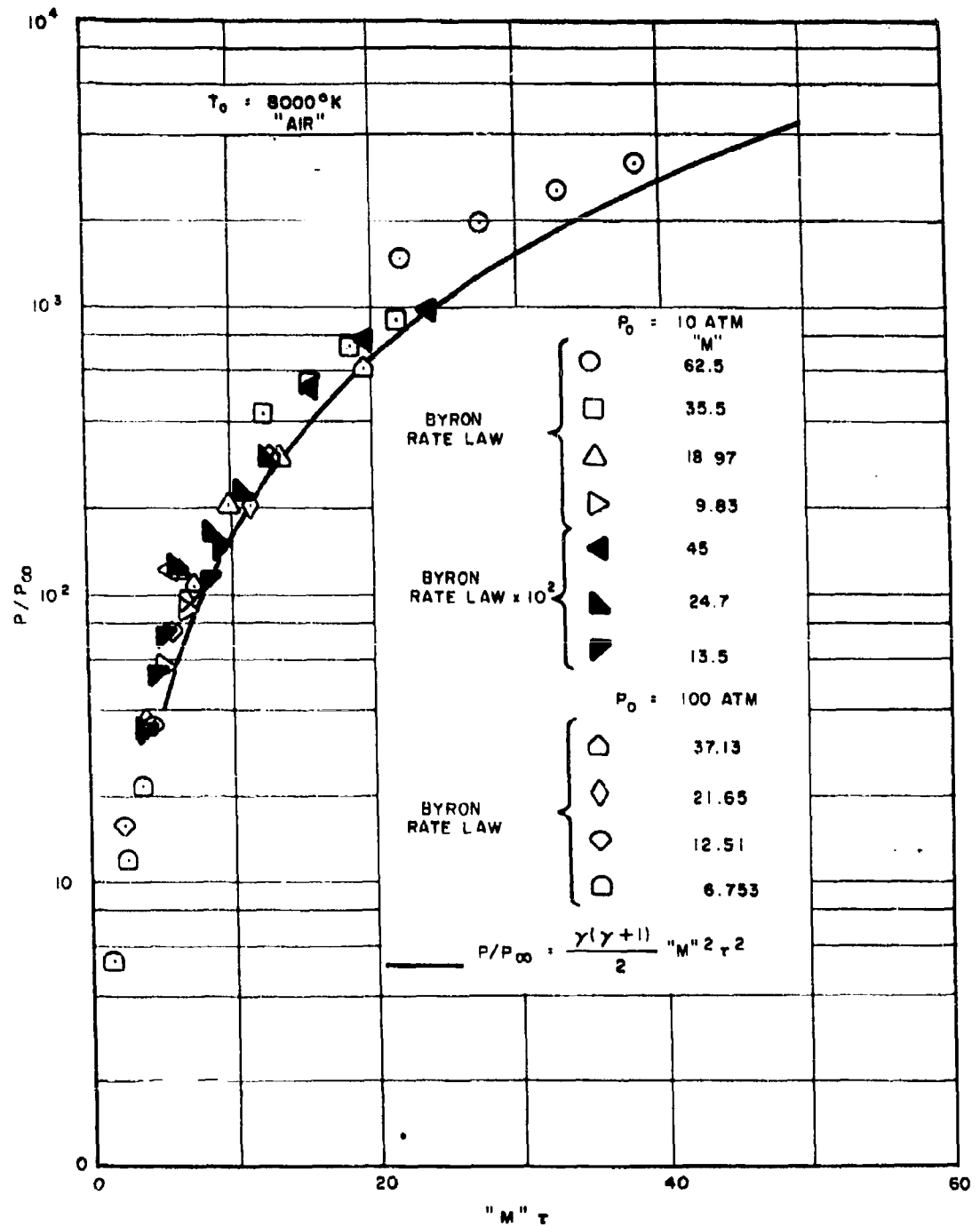


Figure 19. Pressure "Similitude"

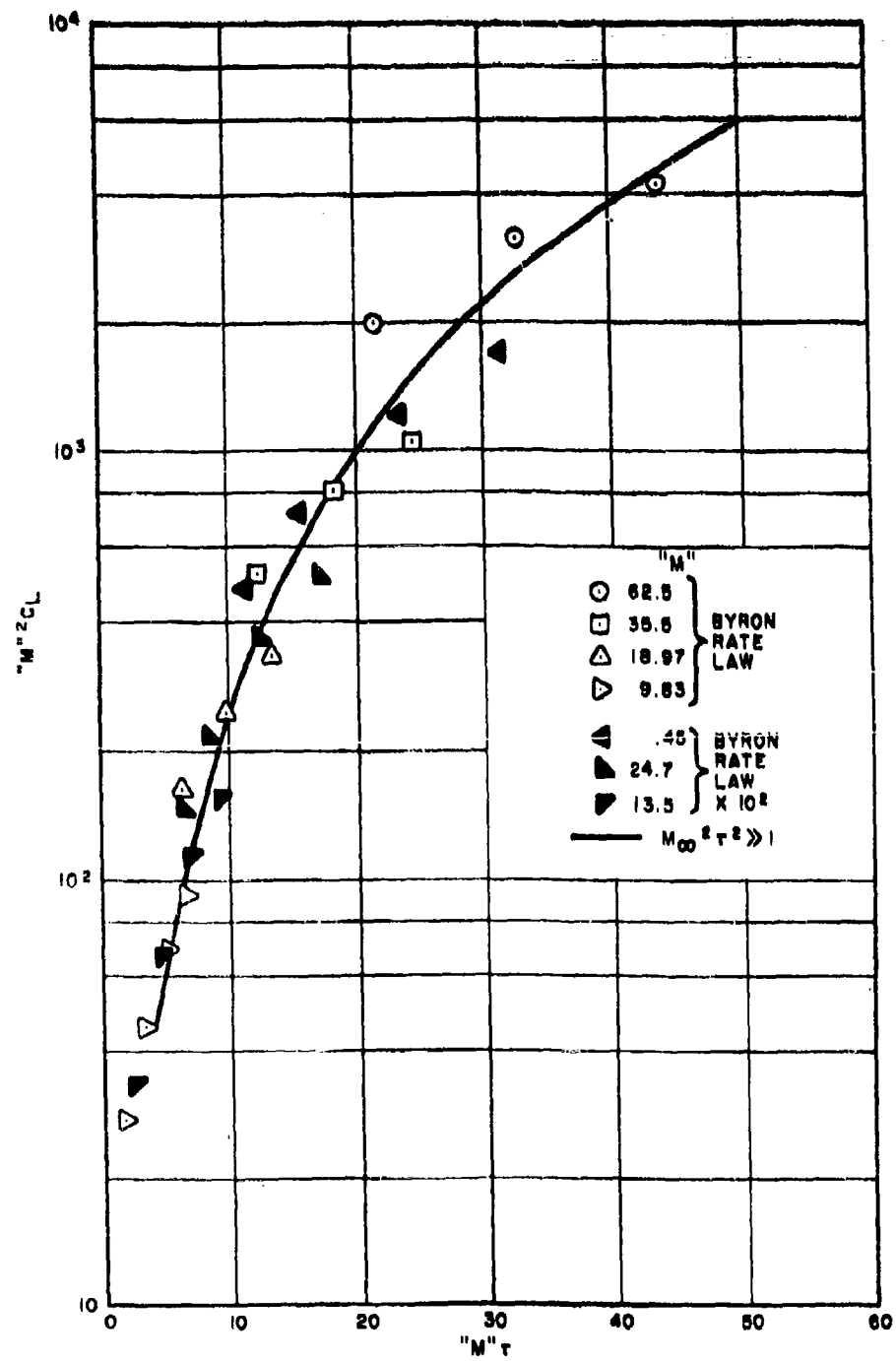


Figure 20. Lift Curve "Similitude"

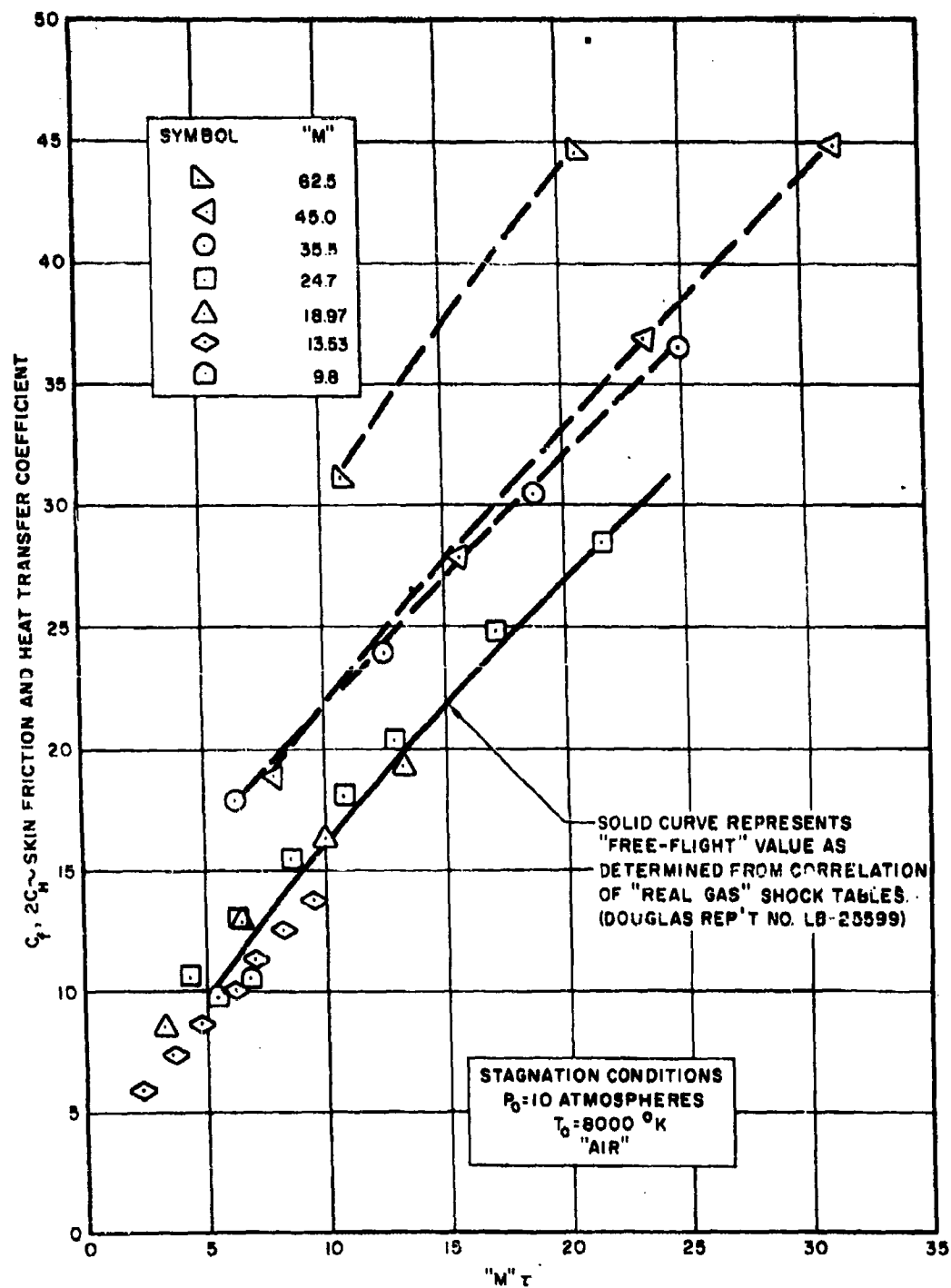


Figure 21. Heat Transfer and Skin Friction "Similitude"

Thus, for the simplified flow mechanism considered, meaningful pressure, lift, skin friction, heat transfer simulation for " $M \approx 25$ " appears possible. We will now turn our attention toward consideration of more "complicated" flow mechanisms.

In order to examine the blunt leading edge slender body problem, numerical solutions of the flow about a "sonic-wedge" model at " $M = 30.3$ " were made. The value of " $M = 30.3$ " was selected in order to allow a comparison with the previous results presented in Figures 9 and 10 for $V = 28,000$ fps and $h = 300,000$ ft, corresponding to " $M = 30.3$ ". Numerical results were obtained for $P_0 = 10$ and 100 atmospheres, $T_0 = 8000^\circ\text{K}$. " $M = 30.3$ " corresponds to an expansion ratio of 4.4×10^4 and 6×10^3 for $P_0 = 10$ and 100 atmospheres, respectively. The wedge angle corresponding to the "sonic-wedge" model for 100 and 10 atmospheres were, respectively, 52 degrees and 57 degrees. The numerical results are presented in Figure 22. The calculations were only carried out for the wedge shock and the expansion around the wedge shoulder because of the computational time involved in continuing the calculation further by characteristics. A comparison of Figure 22 and Figures 9 and 10 indicates the simulation for the stagnation conditions chosen. It is felt the major difference can be ascribed to the lower enthalpy (i. e., lower than that corresponding to 28,000 fps) for the given stagnation conditions with the associated decrease in the parameter $\alpha D/H_\infty$ behind the shock wave envelope. This conjecture is currently being evaluated numerically. While this simulation is far from adequate, it should be examined in terms of that obtained by means of existing facilities. Namely, the differences in pressure and temperature indicated by a comparison of Figure 22 and Figures 9 and 10 should be compared to those differences associated with the corresponding perfect gas values.

The simulation capabilities of high "Mach number" frozen gas flows, in terms of the boundary layer interaction problem, are presented in Figure 23. The free-flight curves are obtained with $\alpha_\infty = 0$ and employing relation (48).

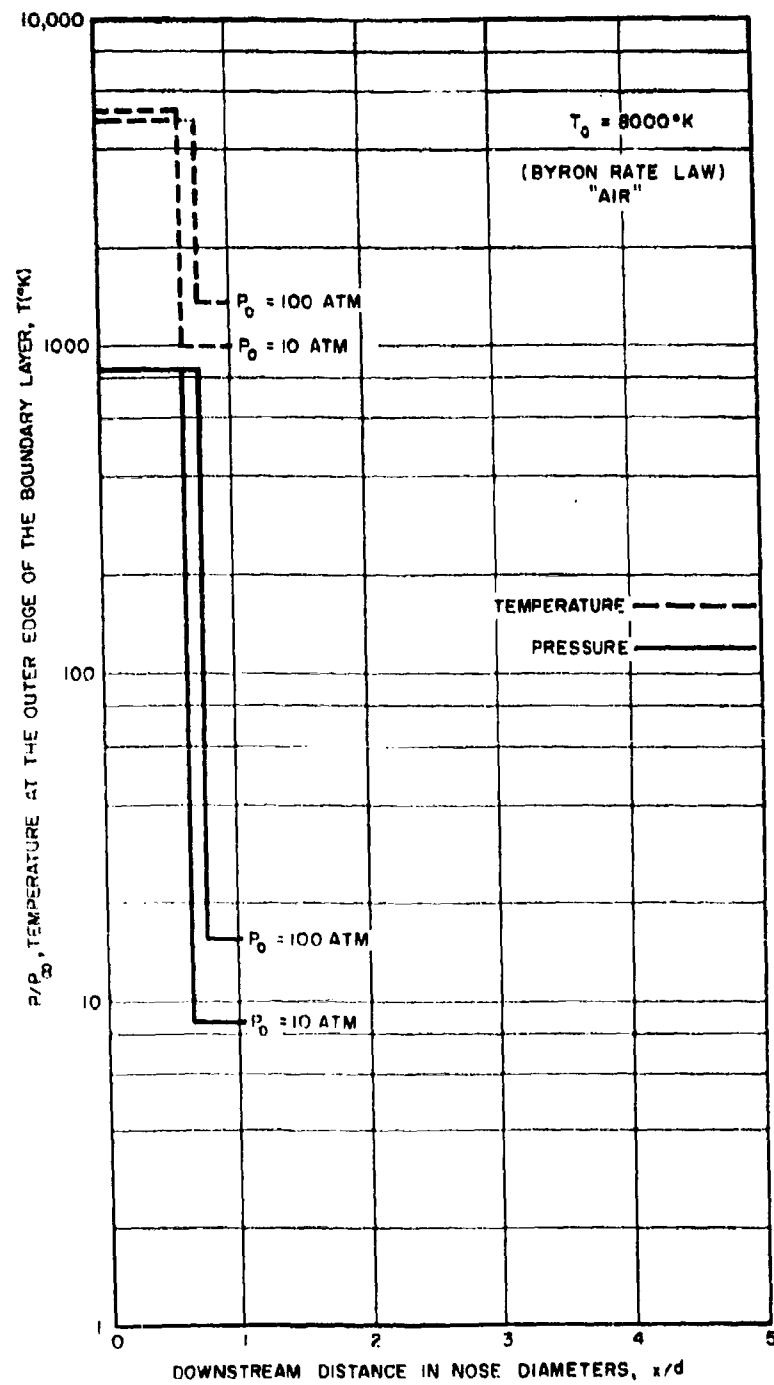


Figure 22. Controlled Non-Equilibrium Expansion "Simulation"

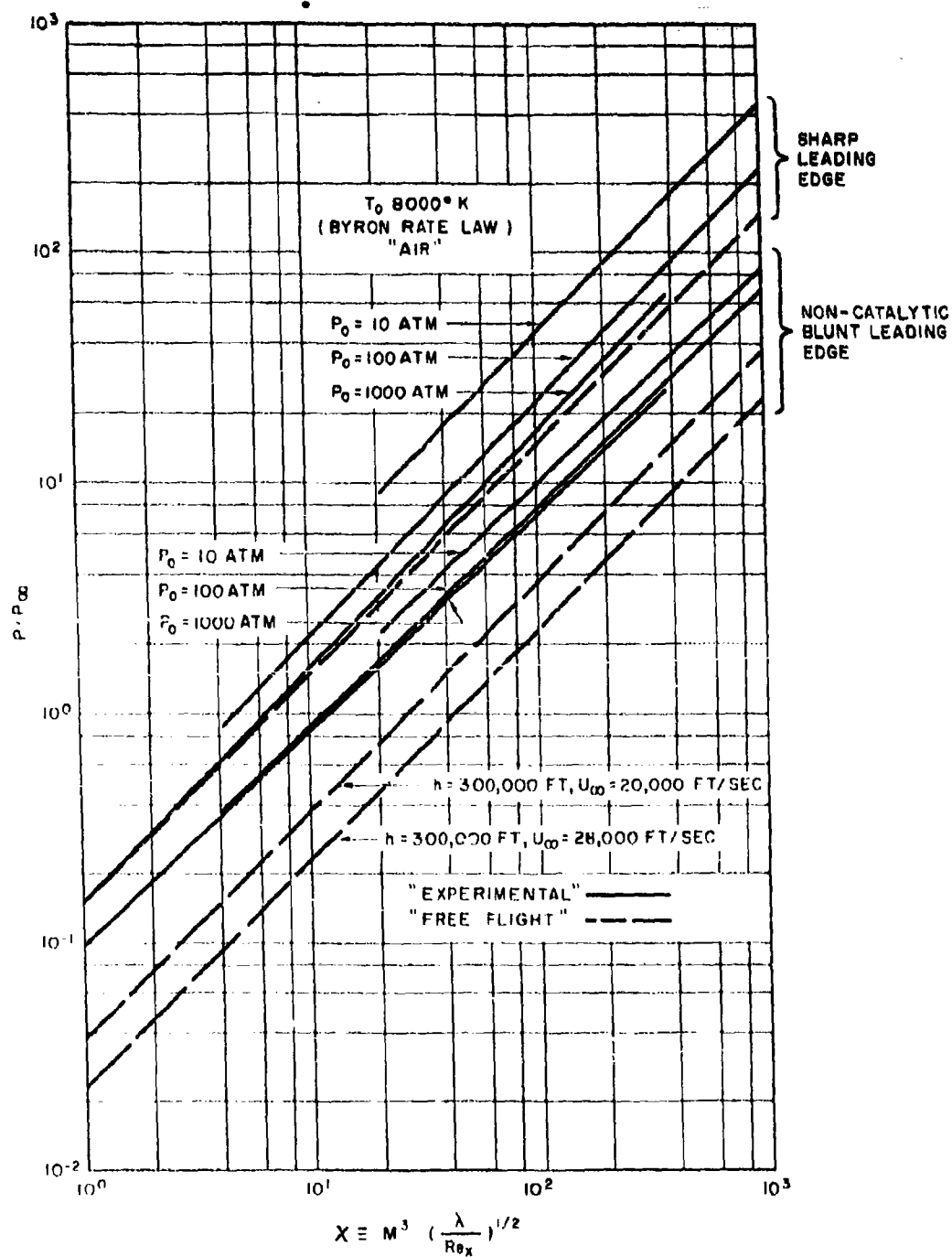


Figure 23. "Simulation" of Blunt and Sharp Leading Edge Boundary Layer Interaction

Finally, it should be noted that this investigation is based upon employing a "frozen" composition model for the region immediately behind the shock wave envelope. It has already been indicated that this model is bounded at lower altitudes by those densities which are high enough so as to yield particle residence times of the same order as those associated with the chemical rates. Certainly, this model is bounded at the higher altitudes by the forward problem, namely, the time to dissociate in the reaction zone behind the shock envelope (cf. Reference 5). In addition, low-Reynolds number effects will also serve to introduce an upper limit in altitude.

5. Concluding Remarks

A theoretical study has been made of the "frozen" viscous and inviscid hypersonic flow about blunt and sharp-nosed slender bodies.

The inviscid investigation indicates, as would be anticipated, "freezing" of the dissociation energy in the region immediately behind the shock wave envelope has a small influence on the sharp-nosed slender body problem. In this case, the flow field should be given, to good approximation, by the perfect gas ($\gamma = 7/5$) prediction.

Conversely, the frozen flow over blunt-nosed slender bodies exhibits large departures from either the equilibrium or perfect gas predictions. An energy balance in the transverse flow field indicates this large difference is primarily due to the condition where the energy introduced into the transverse flow field by the presence of a finite leading edge (nose drag) is offset by the corresponding dissociation energy which is frozen at the shock wave envelope. In addition, since the nose drag term is independent of downstream distance, the energy distribution, (i. e., the large amount of energy frozen in dissociation indicates) the possibility of obtaining surface pressures lower than the ambient free-stream value. These conclusions are verified numerically by a characteristics solution for the frozen and equilibrium hypersonic flow about a "sonic-wedge" slab.

0

The viscous investigations take the form of an investigation of the frozen boundary layer interaction problem. As in the sharp-nosed inviscid studies, the frozen composition model has a small influence on the sharp leading edge problem for values of the hypersonic interaction parameter, χ , less than 1000. The large differences, compared to the $\gamma = 7/5$ value, for the blunt leading edge case are primarily due to the decrease in the "boundary layer displacement integral" for a noncatalytic wall.

The viscous and inviscid theoretical studies were generalized to consider an arbitrary (frozen) degree of dissociation in the ambient free-stream. This generalization was made to permit analysis of the flow field about geometries placed in wind tunnel nozzles where dissociation non-equilibrium is present within the nozzle itself. Since high "Mach number" gas flows may be readily obtained in wind tunnel nozzles where dissociation non-equilibrium is present, the simulation capabilities in terms of the previously discussed viscous and inviscid hypersonic flow phenomena, by means of "controlled non-equilibrium expansions" were studied. The results indicate attractive simulation possibilities which are currently under further theoretical and experimental investigation.

SYMBOLS (Section II, A)

a	speed of sound
A	area
c_f	skin friction coefficient
C	recombination rate parameter
C_D	drag coefficient
C_L	lift coefficient
c_q	heat transfer coefficient
d	leading edge diameter
D	dissociation energy
D_N	nose drag
e	internal energy
f'	boundary layer velocity profile, $f' = u/u_\delta$
g	boundary layer enthalpy profile, $g = H/H_\infty$
h	static enthalpy
H	total enthalpy
k	nose drag coefficient, $k \equiv D_N / 1/2 \rho_\infty U_\infty^2 d/2 (\pi d/2)^v$
k_R	specific rate constant, recombination
M	molecular weight
p	static pressure
P_o	stagnation pressure
Pr	Prandtl number
q	heat transfer rate
R	universal gas constant

SYMBOLS (continued)

r_b	local radius of the body
Re	Reynolds number per length, $Re = \rho u / \mu$
\tilde{s}	defined by, $\tilde{s} = \int_0^s \rho_\delta \mu_\delta u_\delta ds$
s	entropy
t	time
T	static temperature
u	axial velocity component
U_∞	free-stream velocity
v	normal velocity component
V	velocity, $V = \sqrt{u^2 + v^2}$
∇	diffusion velocity
x	axial distance
y	distance normal to surface
α	mass fraction dissociated
β	dimensionless enthalpy defined by $h = \beta p / \rho$
χ	hypersonic interaction parameter, $\chi = M^3 (\lambda / Re_x)^{1/2}$
η	nondimensional distance between shock wave envelope and body surface, $\eta = y / \delta$
δ	shock wave envelope
δ^*	boundary layer displacement thickness
$\dot{\delta}$	$d\delta / dt$
γ	ratio of specific heats
λ	constant in linear viscosity-temperature law
μ	viscosity

SYMBOLS (continued)

ν	0, 1, respectively, for two-dimensional and axisymmetric flow
σ	shock wave power law, $\delta \sim t^\sigma$
ρ	density
τ	fineness ratio
θ	wedge angle
ω	reaction rate

Subscripts

A	atomic species translational energy term
E	conditions at equilibrium
f	frozen composition
i	refers to i^{th} atomic chemical species
M	molecular species energy term
s	evaluated at stagnation point
w	evaluated at the surface
δ	evaluated at the outer edge of the boundary layer
∞	ambient free-stream

B. Non-Equilibrium Flow About a Blunt Body

1. Introduction

An inverse method for analyzing compressible flow about a blunt body was first suggested by Lin and Rubinov.²⁰ This method starts with an assumed form of shock shape. The flow field behind the shock and the body shape are determined by numerical analyses. Further investigations were carried out by Lin and Shen,²¹ Cabannes,²² Van Dyke,²³ Zlotnick and Newman,²⁴ Mangler and Evans.²⁵ Other refined analyses classified as inverse methods were also given by Garabedian and Lieberstein,²⁶ and Vaglio-Laurin and Ferri.²⁷ A detailed review of these analyses may be found in Ref. 28. More recently a comprehensive review of advances in non-equilibrium dissociating gas dynamics was given by Li.²⁹ The case of a reacting and relaxing steady flow around a blunt body was treated by Lick³⁰ who used the inverse method of analysis. Some rather interesting results were presented. However, these results are only of limited qualitative value because of the assumptions used in the analysis. The two important assumptions employed are listed as follows:

- a) Air is considered as a binary mixture composed of atoms and molecules. Therefore, the distinction among NO, O₂, N₂, and the distinction between O and N, are not taken into account.
- b) A parameter, $\chi = (R_0 / \rho_\infty V_\infty)(\omega_2 / \bar{\rho})$, is introduced in the analysis where R_0 is the radius of curvature of the nose at the stagnation point; ω_2 represents the mass rate of production of the molecular species by chemical reactions. Numerical computations were carried out for the flow fields of constant values of χ . When the value of χ is large, for example $\chi = 100$, the solution corresponds closely to that of equilibrium dissociation. When the value of χ is zero, it corresponds to that of frozen dissociation. Case of intermediate values of χ will then provide qualitative information on the non-equilibrium flow phenomena.

0

The first assumption mentioned above represents a hypothesis of using an idealized chemical system in place of the actual one, while the second one is employed mainly for mathematical expedience. It is easy to see that the value of χ should vary instead of remaining constant in the flow field.

In the present analysis, these two restrictive conditions are removed. The method of solution follows the inverse approach previously explored in the literature. It may be argued that since the predicted reaction rates are far from accurate, the first assumption used in Lick's analysis is thus well justified. However, in the continual search for a better solution for the flow field, a more realistic representation of the chemical system will certainly provide additional information of interest. Especially, the relative difference of rates among oxygen, nitrogen, and nitric oxide may have significant effects on the final solution of the flow field.

2. Analysis

For a prescribed shock shape, the conditions immediately behind the shock may be directly determined from the oblique shock relations by assuming that immediately behind the shock, the vibrational degrees of freedom have been fully excited while dissociation has not yet begun. Next, a smoothing technique such as a polynomial fit may be used to establish the partial derivatives of these conditions with respect to a direction tangential to the shock surface. Knowing the values of the variables and their partial derivatives along the shock surface, the values of their partial derivatives normal to the shock surface may be determined from the governing equations of motion and the equation of state when a shock-oriented curvilinear coordinate system is chosen. Linear extrapolation with respect to the direction normal to the shock surface based on difference formula may now be used to calculate the values of the variables along a new boundary located a short distance away from the shock surface. The same smoothing

technique establishes the partial derivatives along this new boundary. In turn, the partial derivatives normal to this boundary are determined from the governing flow equations. Successive applications of this scheme allows the computation to be extended to the unknown body surface which will be established as a part of the solutions based upon the consideration of flow continuity.

The equations of motion, in terms of the shock-oriented curvilinear coordinates may be written (Fig. 24),

$$\frac{u}{1+Ky} \frac{\partial a_i}{\partial x} + v \frac{\partial a_i}{\partial y} = \frac{\omega_i}{\rho} \quad (60)$$

$$\frac{\partial}{\partial x} (\rho u r) + \frac{\partial}{\partial y} [\rho v r (1+Ky)] = 0 \quad (61)$$

$$u \frac{\partial u}{\partial x} + K u v + (1+Ky) v \frac{\partial u}{\partial y} = - \frac{1}{\rho} \frac{\partial p}{\partial x} \quad (62)$$

$$u \frac{\partial v}{\partial x} + (1+Ky) v \frac{\partial v}{\partial y} - K u^2 = - \frac{1+Ky}{\rho} \frac{\partial p}{\partial y} \quad (63)$$

$$d \left(\sum_i h_i d_i \right) + u du + v dv = 0 \quad (64)$$

The equation of state is written as

$$p = (R/\mathcal{M}) \rho T \quad (65)$$

Where R is the universal gas constant, and \mathcal{M} is the molecular weight,

$$\frac{1}{\mathcal{M}} = \sum_{i=1}^n \left(\frac{a_i}{\mathcal{M}_i} \right)$$

n denotes the total number of chemical components in the system. The above system of (n plus 5) equations will be used for the determination of a_i , T , ρ , p , u , and v , which completely describe the flow field.

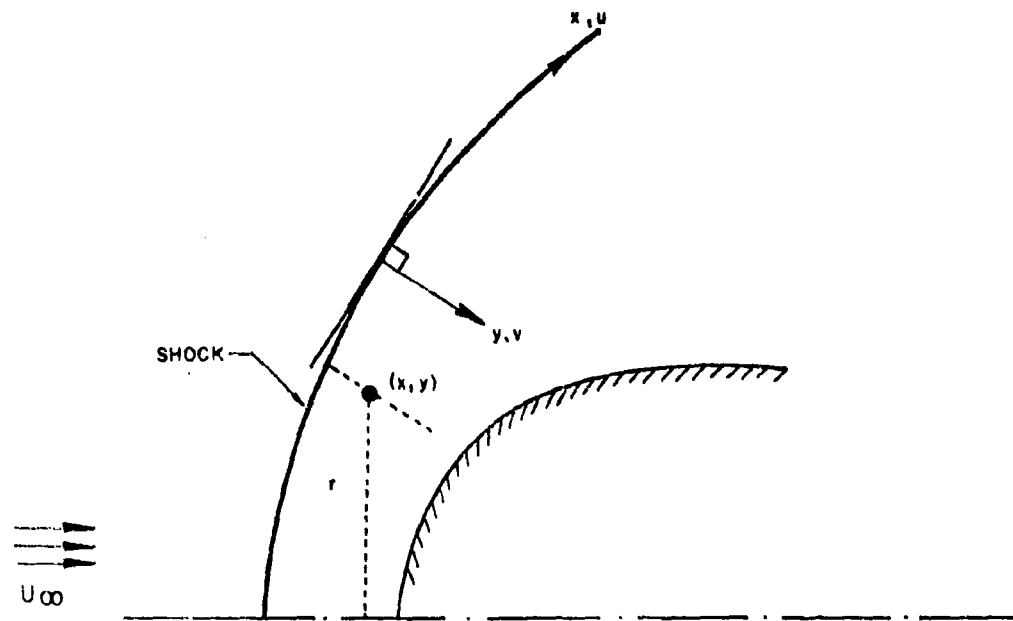


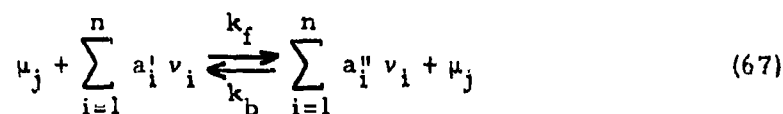
Figure 24. Shock-Oriented Curvilinear Coordinates

In Eq. (60) the mass rate of production of the component by chemical reactions, ω_i , is given by

$$\omega_i = \frac{M_i}{A} \frac{dv_i}{dt} \quad (66)$$

where A is the Avogadro's number, v_i is the number of particles of the i^{th} component per unit volume, (particle/cm³).

In general, chemical reactions can proceed in both forward and backward directions. A set of opposing chemical reactions may be represented by (Ref. 31),



where a_i' and a_i'' are stoichiometric constants.

In these representations, any "third body" chemical species, μ_j , which acts as an energy source or sink in a chemical reaction but is otherwise unchanged, is included.

The net rate of production of i^{th} species is then given by

$$\frac{dv_i}{dt} = (a_i'' - a_i') k_f \prod_{i=1}^n (v_i)^{a_i'} \mu_j + (a_i' - a_i'') k_b \prod_{i=1}^n (v_i)^{a_i''} \mu_j \quad (68)$$

At thermodynamic equilibrium there is no net change in composition, therefore, the rate constants k_b and k_f must be related through the equilibrium constant, \tilde{K} . That is,

$$(k_f/k_b) = \tilde{K} \equiv \prod_{i=1}^n (v_i, e)^{a_i'' - a_i'} \quad (69)$$

When multiple chemical reactions are involved, the net rate production of i th species can be obtained by summing Eq. (68) over all the chemical reactions in the system. Where \bar{K} is the equilibrium constant in the unit of (particle/cm³) while the rate constant, k , has the unit of [cm⁶/(sec particle²)]. In the case of atmospheric air the dominant chemical reactions with their respective rate constants are listed in Table 1.

The rate constants for all the chemical reactions with various "third bodies" used in this analysis are those given by AVCO.³² It should be understood that these numerical values of the reaction constants are to be considered as recommended estimates only. Modifications can readily be introduced when better experimental data become available. Related discussion on chemical kinetics may be found in Ref. 33.

Combining Eqs. (60), (66), (68), and (69) on the basis of chemical reactions and their rate constants given in Table 1, the following set of five equations may be obtained in place of Eq. (60):

$$\begin{aligned} \frac{\partial a_{O_2}}{\partial y} = & \frac{L p_r \bar{m}_{O_2}}{\bar{m}_r u_r} \frac{\bar{p}}{\bar{v}} \left\{ k_D \left[\frac{p_r}{K_{O_2}} \frac{\bar{p}}{\bar{T}} \frac{a_{O_2}^2}{\bar{m}_{O_2}^2} - \frac{a_{O_2}}{\bar{m}_{O_2}} \right] \left[\frac{a_N}{\bar{m}_N} + \frac{a_{N_2}}{\bar{m}_{N_2}} + \frac{a_{NO}}{\bar{m}_{NO}} \right] \right. \\ & + \frac{k_D^2}{k_D} \frac{a_{O_2}}{\bar{m}_{O_2}} + \frac{k_D^3}{k_D} \frac{a_O}{\bar{m}_O} \left. + k_2 \left[\frac{1}{K_{O_2, N}} \frac{a_{NO} a_O}{\bar{m}_{NO} \bar{m}_O} \right. \right. \\ & \left. \left. - \frac{a_{O_2} a_N}{\bar{m}_{O_2} \bar{m}_N} \right] + k_2^3 \left[\frac{a_{NO}^2}{\bar{m}_{NO}^2} - \frac{K_{O_2} K_{p_2}^2}{(K_p^{NO})^2} \frac{a_{N_2} a_{O_2}}{\bar{m}_{N_2} \bar{m}_{O_2}} \right] \right\} \\ & - \frac{\bar{u}}{\bar{v} (1 + \bar{K} \bar{y})} \frac{\partial a_{O_2}}{\partial x} \end{aligned} \quad (70)$$

0

$$\begin{aligned}
 \frac{\partial a_{N_2}}{\partial \bar{y}} = & \frac{L \rho_r^2 \bar{m}_{N_2}}{\bar{m}_r^2 u_r} \frac{\bar{p}}{\bar{v}} \left\{ k_R \left[\frac{a_N^2}{\bar{m}_N^2} \bar{p} - \frac{K_{N_2}^{N_2} a_{N_2}}{p_r \bar{m}_{N_2}} \frac{1}{\bar{T}} \right] \left[\frac{a_O}{\bar{m}_O} + \frac{a_{O_2}}{\bar{m}_{O_2}} \right. \right. \\
 & \left. \left. + \frac{a_{NO}}{\bar{m}_{NO}} + \frac{k_R^2 a_{N_2}}{k_R' \bar{m}_{N_2}} + \frac{k_R^3 a_N}{k_R' \bar{m}_N} \right] \right\} \\
 & + \frac{L \rho_r \bar{m}_{N_2}}{\bar{m}_r u_r} \frac{\bar{p}}{\bar{v}} \left\{ k_2^2 \left[\frac{a_{NO} a_N}{\bar{m}_{NO} \bar{m}_N} - \frac{1}{K_{N_2', O}} \frac{a_{N_2} a_O}{\bar{m}_{N_2} \bar{m}_O} \right] + k_2^3 \left[\frac{a_{NO}^2}{\bar{m}_{NO}^2} \right. \right. \\
 & \left. \left. - \frac{K_{O_2}^{O_2} K_{N_2}^{N_2} a_{O_2} a_{N_2}}{\left[K_P^{NO} \right]^2 \bar{m}_{O_2} \bar{m}_{N_2}} \right] \right\} - \frac{\bar{u}}{\bar{v}(1 + \bar{K}\bar{y})} \frac{\partial a_{N_2}}{\partial \bar{x}} \quad (71)
 \end{aligned}$$

$$\begin{aligned}
 \frac{\partial a_{NO}}{\partial \bar{y}} = & \frac{L \rho_r^2 \bar{m}_{NO}}{\bar{m}_r^2 u_r} \frac{\bar{p}}{\bar{v}} \left\{ k_R^4 \left[\frac{a_N a_O}{\bar{m}_N \bar{m}_O} \bar{p} - \frac{K_P^{NO} a_{NO}}{p_r \bar{m}_{NO}} \frac{1}{\bar{T}} \right] \left[\frac{a_{O_2}}{\bar{m}_{O_2}} + \frac{a_{N_2}}{\bar{m}_{N_2}} \right. \right. \\
 & \left. \left. + \frac{k_R^5}{k_R^4} \left(\frac{a_{NO}}{\bar{m}_{NO}} + \frac{a_O}{\bar{m}_O} + \frac{a_N}{\bar{m}_N} \right) \right] \right\} \\
 & + \frac{L \rho_r \bar{m}_{NO} \bar{p}}{\bar{m}_r u_r \bar{v}} \left\{ k_2 \left[\frac{a_{O_2} a_N}{\bar{m}_{O_2} \bar{m}_N} - \frac{1}{K_{O_2, N}} \frac{a_{NO} a_O}{\bar{m}_{NO} \bar{m}_O} \right] - k_2^2 \left[\frac{a_{NO} a_N}{\bar{m}_{NO} \bar{m}_O} \right. \right. \\
 & \left. \left. - \frac{1}{K_{N_2', O}} \frac{a_{N_2} a_O}{\bar{m}_{N_2} \bar{m}_O} \right] - 2k_2^3 \left[\frac{a_{NO}^2}{\bar{m}_{NO}^2} \right. \right. \\
 & \left. \left. - \frac{K_{O_2}^{O_2} K_{N_2}^{N_2} a_{O_2} a_{N_2}}{\left[K_P^{NO} \right]^2 \bar{m}_{O_2} \bar{m}_{N_2}} \right] \right\} - \frac{\bar{u}}{\bar{v}(1 + \bar{K}\bar{y})} \frac{\partial a_{NO}}{\partial \bar{x}} \quad (72)
 \end{aligned}$$

$$\begin{aligned}
\frac{\partial a_O}{\partial \bar{y}} = & \frac{L p_r \bar{m}_O}{m_r u_r} \frac{\bar{p}}{\bar{v}} \left\{ 2k_D' \left[\frac{a_{O_2}}{\bar{m}_{O_2}} - \frac{p_r}{K_{p_{O_2}}} \frac{a_{O_2}^2}{\bar{m}_{O_2}^2} \right] \left[\frac{a_N}{\bar{m}_N} + \frac{a_{N_2}}{\bar{m}_{N_2}} \right. \right. \\
& \left. \left. + \frac{a_{NO}}{\bar{m}_{NO}} + \frac{k_D^2 a_{O_2}}{k_D' \bar{m}_{O_2}} + \frac{k_D^3 a_O}{k_D' \bar{m}_O} \right] \right\} \\
& + \frac{L p_r^2 \bar{m}_O}{m_r^2 u_r} \frac{\bar{p}}{\bar{v}} \left\{ k_R^4 \left[\frac{K_{p_{NO}}}{p_r} \frac{a_{NO}}{\bar{m}_{NO}} \frac{1}{\bar{T}} - \frac{a_O a_N}{\bar{m}_O \bar{m}_N} \bar{p} \right] \left[\frac{a_{O_2}}{\bar{m}_{O_2}} \frac{a_{N_2}}{\bar{m}_{N_2}} \right. \right. \\
& \left. \left. + \frac{k_R^5}{k_R^4} \left(\frac{a_{NO}}{\bar{m}_{NO}} + \frac{a_O}{\bar{m}_O} + \frac{a_N}{\bar{m}_N} \right) \right] \right\} \\
& + \frac{L p_r \bar{m}_O}{m_r u_r} \frac{\bar{p}}{\bar{v}} \left\{ k_2' \left[\frac{a_{O_2} a_N}{\bar{m}_{O_2} \bar{m}_N} - \frac{1}{K_{O_2, N}} \frac{a_{NO} a_O}{\bar{m}_{NO} \bar{m}_O} \right] + k_2^2 \left[\frac{a_{NO} a_N}{\bar{m}_{NO} \bar{m}_N} \right. \right. \\
& \left. \left. - \frac{1}{K_{N_2, O}} \frac{a_{N_2} a_O}{\bar{m}_{N_2} \bar{m}_O} \right] \right\} - \frac{\bar{u}}{\bar{v}(1 + \bar{K}\bar{y})} \frac{\partial a_O}{\partial \bar{x}} \quad (73)
\end{aligned}$$

$$\begin{aligned}
\frac{\partial a_N}{\partial \bar{y}} = & \frac{L p_r^2 \bar{m}_N}{m_r^2 u_r} \frac{\bar{p}}{\bar{v}} \left\{ 2k_R' \left(\frac{K_{p_{N_2}}}{p_r} \frac{a_{N_2}}{\bar{m}_{N_2}} \frac{1}{\bar{T}} - \frac{a_N^2}{\bar{m}_N^2} \bar{p} \right) \left[\frac{a_O}{\bar{m}_O} + \frac{a_{O_2}}{\bar{m}_{O_2}} \right. \right. \\
& \left. \left. + \frac{a_{NO}}{\bar{m}_{NO}} + \frac{k_R^2 a_{N_2}}{k_R' \bar{m}_{N_2}} + \frac{k_R^3 a_N}{k_R' \bar{m}_N} \right] \right\}
\end{aligned}$$

G

$$\begin{aligned}
 & + \frac{L p_r^2 \bar{m}_N}{\bar{m}_r^2 u_r} \frac{1}{v} \left\{ k_R^4 \left[\frac{K_P^{NO}}{p_r} \frac{a_{NO}}{\bar{m}_{NO}} \frac{1}{T} - \frac{a_O a_N}{\bar{m}_O \bar{m}_N} \right] \left[\frac{a_{O_2}}{\bar{m}_{O_2}} + \frac{a_{N_2}}{\bar{m}_{N_2}} \right] \right. \\
 & \quad \left. + \frac{k_R^3}{k_R^4} \left(\frac{a_{NO}}{\bar{m}_{NO}} + \frac{a_O}{\bar{m}_O} + \frac{a_N}{\bar{m}_N} \right) \right\} \\
 & + \frac{L p_r \bar{m}_N}{\bar{m}_r u_r} \frac{1}{v} \left\{ k_2^1 \left[\frac{1}{K_{O_2, N}} \frac{a_{NO} a_O}{\bar{m}_{NO} \bar{m}_O} - \frac{a_{O_2} a_N}{\bar{m}_{O_2} \bar{m}_N} \right] \right. \\
 & \quad \left. + k_2^2 \left[\frac{1}{K_{N_2, O}} \frac{a_{N_2} a_O}{\bar{m}_{N_2} \bar{m}_O} - \frac{a_{NO} a_N}{\bar{m}_{NO} \bar{m}_N} \right] \right\} \\
 & - \frac{\bar{u}}{v(1 + \bar{K}y)} \frac{\partial a_N}{\partial x}
 \end{aligned} \tag{74}$$

where

$$\begin{aligned}
 p_i &= (\bar{m}_i v_i / A) \\
 K_P^{O_2} &\equiv \frac{(p_O)^2}{p_{O_2}}, \quad K_P^{N_2} \equiv \frac{(p_N)^2}{p_{N_2}}, \quad K_P^{NO} \equiv \frac{p_O p_N}{p_{NO}} \\
 K_{O_2, N} &\equiv \frac{p_{NO} p_O}{p_{O_2} p_N}, \quad K_{N_2, O} \equiv \frac{p_O p_{N_2}}{p_{NO} p_N}
 \end{aligned} \tag{75}$$

In obtaining the above equations, proper care has been taken to convert the rate constants k_f , k_b , in the unit of $(\text{cm}^3/\text{particle sec})$ to k_D^j ,

k_R^j, k_i^j in the units given in Table 1. Furthermore, the following non-dimensional quantities have been introduced:

$$\bar{x} = \frac{x}{L}, \quad \bar{y} = \frac{y}{L}, \quad \bar{p} = \frac{p}{p_r}, \quad \bar{\rho} = \frac{\rho}{\rho_r} \quad (76)$$

$$\bar{T} = \frac{T}{T_r}, \quad \bar{m}_i = \frac{m_i}{m_r}, \quad u = \frac{u}{u_r}, \quad v = \frac{v}{u_r}, \quad \bar{K} = K/L$$

where $L, p_r, \rho_r, T_r, m_r, u_r$ are chosen reference quantities

$$u_r = \sqrt{p_r/\rho_r}, \quad p_r = \rho_r \left(\frac{R}{m_r} \right) T_r \quad (77)$$

In terms of these same non-dimensional quantities, Eq. (62) may be rewritten as:

$$\frac{\partial \bar{u}}{\partial \bar{y}} = \frac{-1}{\bar{v}(1 + \bar{K}\bar{y})} \left[\frac{1}{\bar{\rho}} \frac{\partial \bar{p}}{\partial \bar{x}} + \bar{K} \bar{u} \bar{v} + \bar{u} \frac{\partial \bar{u}}{\partial \bar{x}} \right] \quad (78)$$

Eq. (63) may be rewritten as:

$$\frac{\partial \bar{p}}{\partial \bar{y}} = \frac{-\bar{\rho}}{(1 + \bar{K}\bar{y})} \left[u \frac{\partial \bar{v}}{\partial \bar{x}} + (1 + \bar{K}\bar{y}) \bar{v} \frac{\partial \bar{v}}{\partial \bar{y}} - \bar{K} \bar{u}^2 \right] \quad (79)$$

Eq. (61) may be rewritten as:

$$\begin{aligned} \frac{\partial \bar{p}}{\partial \bar{y}} = \frac{-\bar{\rho}}{\bar{v}(1 + \bar{K}\bar{y})} & \left[(1 + \bar{K}\bar{y}) \frac{\partial \bar{v}}{\partial \bar{y}} + \frac{\partial \bar{u}}{\partial \bar{x}} + \frac{\bar{u}}{\bar{\rho}} \frac{\partial \bar{p}}{\partial \bar{x}} \right. \\ & \left. + (1 + \bar{K}\bar{y}) \frac{\bar{v}}{\bar{r}} \frac{\partial \bar{r}}{\partial \bar{y}} + \bar{v} \bar{K} + \frac{\bar{u}}{\bar{r}} \frac{\partial \bar{r}}{\partial \bar{x}} \right] \quad (80) \end{aligned}$$

Differentiating the equation of state, Eq. (65), with respect to y , we have,

$$\frac{1}{T} \frac{\partial T}{\partial y} = \frac{1}{p} \frac{\partial p}{\partial y} + \frac{1}{M} \frac{\partial M}{\partial y} - \frac{1}{\rho} \frac{\partial \rho}{\partial y} \quad (81)$$

where

$$(\partial M / \partial y) = - \sum_i (1/M_i) (\partial a_i / \partial y)$$

Dividing the partial differential form of the energy equation, Eq. (64), by the absolute temperature, we obtain,

$$\frac{1}{T} \frac{\partial T}{\partial y} \sum_i \left(a_i \frac{dh_i}{dT} \right) + \frac{1}{T} \sum_i \left(h_i \frac{\partial a_i}{\partial y} \right) + \frac{u}{T} \frac{\partial u}{\partial y} + \frac{v}{T} \frac{\partial v}{\partial y} = 0 \quad (82)$$

Substitution of (81) into (82) yields,

$$\sum_i \left(a_i \frac{dh_i}{dT} \right) \left[\frac{1}{p} \frac{\partial p}{\partial y} - M \sum_i \left(\frac{1}{M_i} \frac{\partial a_i}{\partial y} \right) - \frac{1}{\rho} \frac{\partial \rho}{\partial y} \right] + \frac{1}{T} \sum_i \left(h_i \frac{\partial a_i}{\partial y} \right) + \frac{u}{T} \frac{\partial u}{\partial y} + \frac{v}{T} \frac{\partial v}{\partial y} = 0 \quad (83)$$

Eliminating $(\partial p / \partial y)$ and $(\partial \rho / \partial y)$ from Eq. (83) by using Eq. (63) and Eq. (61) respectively, we obtain

$$\begin{aligned} & \left[\sum_i \left(a_i \frac{dh_i}{dT} \right) \left(\frac{M}{RT} v - \frac{1}{v} \right) - \frac{v}{T} \right] \frac{\partial v}{\partial y} = \left\{ \sum_i a_i \frac{dh_i}{dT} \frac{M}{RT(1+Ky)} \left(Ku^2 - u \frac{\partial v}{\partial x} \right) \right. \\ & - \left[\sum_i \left(a_i \frac{dh_i}{dT} \right) M \left[\sum_i \left(\frac{1}{M_i} \frac{\partial a_i}{\partial y} \right) \right] + \frac{1}{T} \sum_i \left(h_i \frac{\partial a_i}{\partial y} \right) + \frac{u}{T} \frac{\partial u}{\partial y} \right. \\ & \left. \left. + \frac{\sum_i \left(a_i \frac{dh_i}{dT} \right)}{v(1+Ky)} \left[\frac{\partial u}{\partial x} + \frac{u}{\rho} \frac{\partial \rho}{\partial x} + (1+Ky) \frac{v}{r} \frac{\partial r}{\partial y} + vK + \frac{u}{r} \frac{\partial r}{\partial x} \right] \right\} \quad (84) \end{aligned}$$

The non-dimensional form of Eq. (84) reads,

$$\begin{aligned} \left[\sum \left(a_i \frac{d\bar{h}_i}{d\bar{T}} \right) \left(\bar{M} \frac{\bar{v}}{\bar{T}} - \frac{1}{\bar{v}} \right) - \frac{\bar{v}}{\bar{T}} \right] \frac{\partial \bar{v}}{\partial \bar{y}} = & \left\{ \sum \left(a_i \frac{d\bar{h}_i}{d\bar{T}} \right) \frac{\bar{M}}{\bar{T}(1 + \bar{K}\bar{y})} \left(\bar{K} \bar{u}^2 - \bar{u} \frac{\partial \bar{v}}{\partial \bar{x}} \right) \right. \\ & - \bar{M} \left[\sum \left(a_i \frac{d\bar{h}_i}{d\bar{T}} \right) \left[\sum \left(\frac{1}{\bar{M}_i} \frac{\partial a_i}{\partial \bar{y}} \right) \right] + \frac{1}{\bar{T}} \sum \left(h_i \frac{\partial a_i}{\partial \bar{y}} \right) + \frac{\bar{u}}{\bar{T}} \frac{\partial \bar{u}}{\partial \bar{y}} \right. \\ & \left. \left. + \frac{1}{\bar{v}(1 + \bar{K}\bar{y})} \left[\sum \left(a_i \frac{d\bar{h}_i}{d\bar{T}} \right) \left[\frac{\partial \bar{u}}{\partial \bar{x}} + \frac{\bar{u}}{\bar{p}} \frac{\partial \bar{p}}{\partial \bar{x}} + (1 + \bar{K}\bar{y}) \frac{\bar{v}}{\bar{r}} \frac{\partial \bar{r}}{\partial \bar{y}} + \bar{K} \bar{v} + \frac{\bar{u}}{\bar{r}} \frac{\partial \bar{r}}{\partial \bar{x}} \right] \right] \right\} \quad (85) \end{aligned}$$

where

$$\bar{h}_i = h_i / u_r^2 = \left[h_i / \left(\frac{p_r}{\rho_r} \right) \right]$$

The equation of state may be rewritten as,

$$\left[\sum \left(\frac{a_i}{\bar{M}_i} \right) \right]^{-1} \bar{p} = \bar{p} \bar{T}$$

that is,

$$\left(\frac{a_O}{\bar{M}_O} + \frac{a_N}{\bar{M}_N} + \frac{a_{NO}}{\bar{M}_{NO}} + \frac{a_{O_2}}{\bar{M}_{O_2}} + \frac{a_{N_2}}{\bar{M}_{N_2}} \right)^{-1} \bar{p} = \bar{p} \bar{T} \quad (86)$$

Now the reacting flow field inside the shock layer is governed by the differential system consisting of Eqs. (70, 71, 72, 73, 74, 78, 79, 80, 85, 81, or 86). There are ten equations for the ten unknown quantities

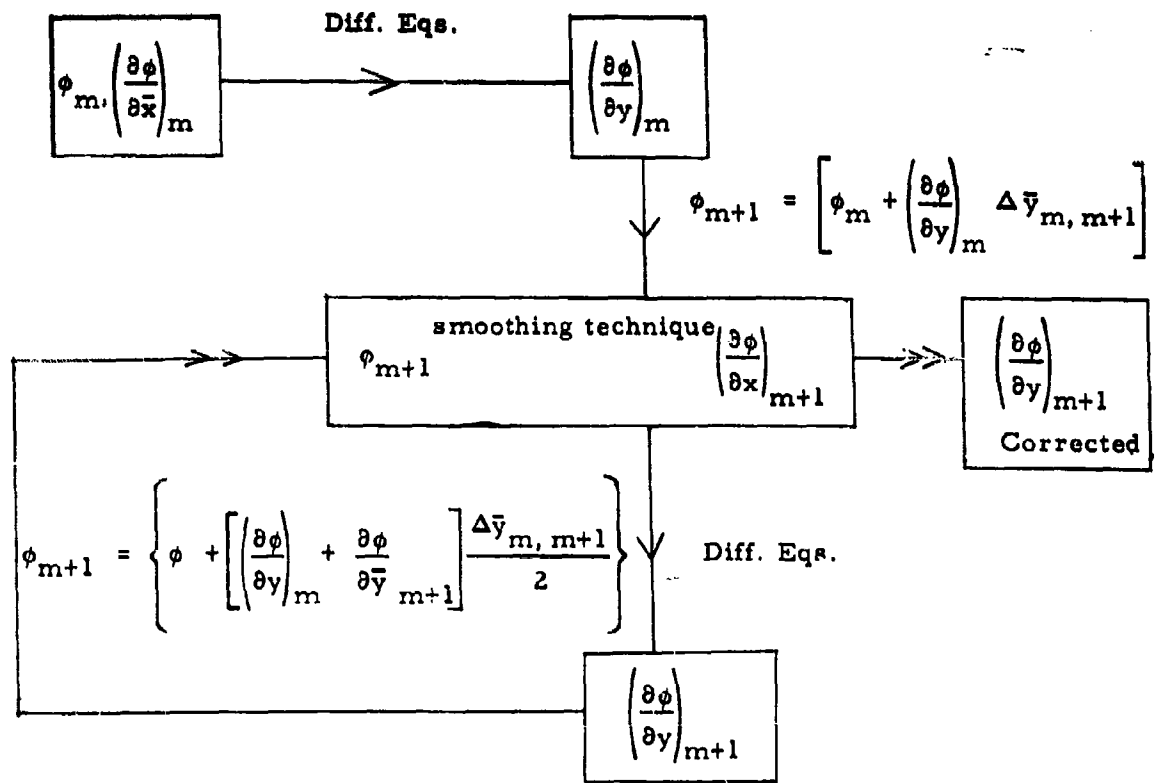
$$a_O, a_N, a_{O_2}, a_{N_2}, a_{NO}, \bar{u}, \bar{v}, \bar{p}, \bar{r}, \bar{T}.$$

0

In this inverse method, the shape of the shock wave is prescribed. The flow conditions immediately behind the shock wave can be determined from the shock wave relations. In turn, the partial derivatives of the flow conditions with respect to x can be numerically calculated because of the shock-oriented coordinates chosen in the analysis. From the governing differential system, we then calculate successively the partial derivatives of the unknown quantities with respect to \bar{y} in the following order:

- 1) Determine $(\partial a_1 / \partial \bar{y})$ individually from Eqs. (70) through (74).
- 2) Determine $(\partial \bar{u} / \partial \bar{y})$ from Eq. (78).
- 3) Determine $(\partial \bar{v} / \partial \bar{y})$ from Eq. (85).
- 4) Determine $(\partial \bar{p} / \partial \bar{y})$ from Eq. (79).
- 5) Determine $(\partial \bar{\rho} / \partial \bar{y})$ from Eq. (80).
- 6) Determine $(\partial \bar{T} / \partial \bar{y})$ from Eq. (81).

Knowing the partial derivatives normal to the shock surface, linear extrapolation based on difference formula will be used to calculate the value of variables along a new boundary located a small \bar{y} distance away from the shock surface. Step (6) may be deleted, and the temperature distribution along the new boundary may be determined directly from the equation of state, Eq. (86), after all the other variables along the new boundary become known. The detail of the computation may best be illustrated by the following block diagram.



Where ϕ denotes any of the dependent variables ϕ_m is the value of ϕ at the m th step. The values of ϕ_0 , $(\partial\phi/\partial\bar{x})_0$ are initially obtained from the oblique shock calculations. The computations are carried out by applying this scheme successively until the body streamline is established from continuity consideration.

Consider a streamline crossing the curved shock at an arbitrary point, B (Fig. 25). The amount of fluid enclosed between this streamline AB and the streamline along the axis of symmetry must be equal to the amount that crosses the section BC inside the shock layer. It should be understood that for the axisymmetric flow, the control surfaces will be obtained by revolving AB and BC about the axis of symmetry. The above mentioned physical condition may be represented by the following equation:

$$\pi r_s^2 \rho_\infty U_\infty = 2\pi \int_0^{y_w} r \rho u dy \quad (87)$$



0

To find the shape of the body surface, we numerically integrate the right hand side of the equation above--a process which can be carried out once the distributions of p and u are determined inside the shock layer--and determine the y_w coordinate at which this equality is satisfied.

After the body streamline shape is established, the mass flow rate is then integrated from the body surface toward the shock to determine various streamline positions.

Numerical computations (IBM7090) for selected geometries and flight conditions are currently being determined.

SYMBOLS (Section II. B)

A	Avogadro number
h	specific enthalpy
\bar{h}	$= h/h_r$, where $h_r = (p_\infty/\rho_\infty)$
k	reaction rate constant, $\text{cm}^6/[\text{sec}(\text{particles})^2]$
k_D^j	dissociation rate constant, $[\text{cm}^3/(\text{mole sec})]$, see Table I
k_R^j	recombination rate constant, $[\text{cm}^6/(\text{mole}^2 \text{ sec})]$, see Table I
k_i^j	reaction rate constant, $[\text{cm}^3/(\text{mole sec})]$, see Table I
K	curvature
\bar{K}	$= K L = K \Omega$.
\tilde{K}	Equilibrium constant, $\text{particles}/\text{cm}^3$
$K_P^{O_2}$	Equilibrium constant, $\equiv (p_O^2/p_{O_2})$
$K_P^{N_2}$	Equilibrium constant, $\equiv (p_N^2/p_{N_2})$
$K_{O_2, N}$	Equilibrium constant, $\equiv [(p_{NO} p_O)/(p_{O_2} p_N)]$
$K_{N_2, O}$	Equilibrium constant, $\equiv [(p_{N_2} p_O)/(p_{NO} p_N)]$
L	reference length, $= \Omega$.
M	Mach number
\mathcal{M}	molecular weight
p	pressure
\bar{p}	$= (p/p_r)$, where $p_r = p_\infty$
r	radial distance from the axis of symmetry
\bar{r}	$= (r/\Omega)$

SYMBOLS (Continued)

R	Universal gas constant
t	time, sec
T	temperature, °K
\bar{T}	$= (T/T_r)$, where $T_r = T_\infty$
u	velocity component along the x direction
\bar{u}	$= u/u_r$, where $u_r = \sqrt{p_\infty/\rho_\infty}$
V_∞	free stream velocity
v	velocity component along the y-direction
\bar{v}	$= v/u_r$, where $u_r = \sqrt{p_\infty/\rho_\infty}$
x	coordinate distance along the shock surface
\bar{x}	$= x/\Omega$
y	coordinate distance normal to the shock surface
\bar{y}	$= y/\Omega$
a_1	$= \rho_1/\rho$
γ	= specific heats ratio for perfect gas
ν	= number density (particle/cm ³)
μ	= number density of "third body" species (particle/cm ³)
ρ	= density
σ	= shock angle
ϕ	= arbitrary function
Ω	= radius of curvature
Ω_s	= radius of curvature of shock wave at stagnation streamline

SYMBOLS (Continued)-

Subscripts:

i	ith species or arbitrary index on rate constants
j	jth species or arbitrary index on rate constants
0	quantities at $x = 0$ or sea level standard conditions
r	reference
s	conditions immediately behind the shock
w	wall conditions
∞	free stream

C. Hypersonic Wake Flow Studies

1. Introduction

As a body, such as a nose cone, enters the earth's atmosphere, it leaves a deposit of energy in the form of a trail. The rate at which energy is deposited is equal to the drag energy DU where D is the aerodynamic drag and U is the flight velocity. Part of this energy goes into heating the air and part goes into giving the air directed motion or momentum in the flight direction. It is the heated air that gives rise to observables in the form of an ionized trail and gas radiation.

After the air has passed through the bow shock, around the body, and through the trailing shock system, as shown in Fig. 26, it returns to ambient pressure at some distance x_0 behind the body. At this station a certain velocity and temperature profile would persist downstream if it were not for laminar diffusion, turbulent mixing, and radiation.

The amount of energy radiated from the wake is extremely small compared to the other controlling processes of energy transfer, and, hence, can be neglected in any wake analysis.

Figures 26a and 26b are schematics of what is qualitatively expected in the trail behind a blunt-nosed body and a slender-pointed body, respectively. Both bodies are assumed to have about the same base area and volume. The skin friction or viscous drags of the two bodies will be roughly the same at the same velocity and altitude. This fact is reflected in the temperature and velocity profiles shown in Figures 26a and 26b, and is represented by the small bumps at the center of the profiles. This is a schematic representation only. In reality the momentum defect associated with the bump should include not only skin friction drag, but nose drag in the case of a sharp body with a small nose radii, and the drag associated with the base recompression at the neck. This bump in the velocity profile constitutes the inner core and its spread will be dominated by viscous processes, either laminar or turbulent, if transition has occurred.

0

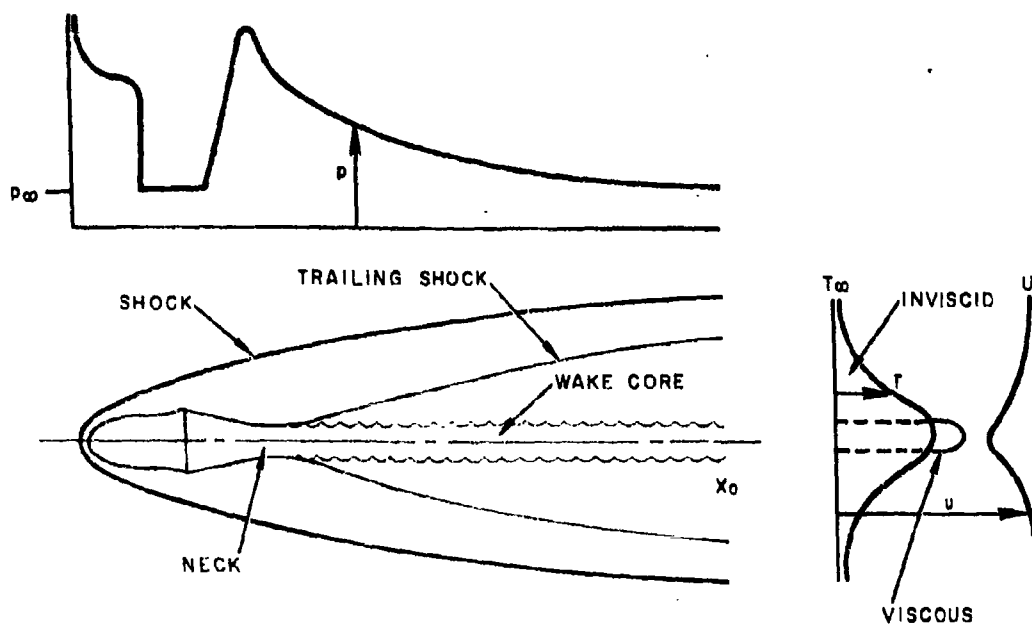


Figure 26a. Schematic of Flow Past a Blunt Body

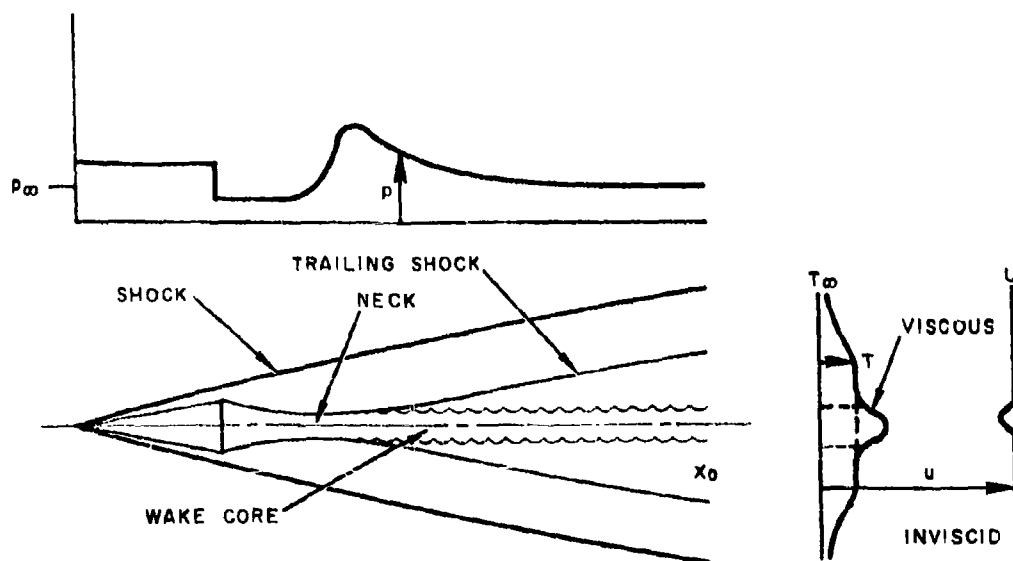


Figure 26b. Schematic of Flow Past a Sharp Body

The associated bump in the temperature or enthalpy profile will reflect, in addition, the heat taken out of the flow by the body, and its peak will, therefore, be much lower than in the case of an insulated body. As will become apparent in the analysis, heat transfer to the body plays a dominant role in erasing observables in the wake of a sharp body which are dependent on the maintenance of a high-temperature environment. Although the heat transfer to the blunt body is of the same order as the heat transfer to the sharp body at the same velocity and altitude, a high-temperature environment is maintained by the high temperature air that has passed through the steep portion of the bow shock and surrounds the viscous core as shown in Fig. 26a, so that in the blunt-body case heat transfer to the body does not play an important role in erasing observables.

2. The Spread of Turbulence in Axisymmetric Wakes

This section presents a simplified analysis of the spread of turbulence in the trail wherein certain simplifying assumptions are made. These assumptions may be summarized:

- a. Equilibrium flow,
- b. Negligible radiation,
- c. Negligible laminar diffusion compared to turbulent mixing,
and
- d. Turbulence originates in the viscous core or on the body and is fully developed and in equilibrium by the time it has reached the 50 radii station.

Turbulence is thus confined to a circular core, the front of which moves out and "swallows up" mass from the outer entropy trail. Eventually the front will have moved out into the outer cool air at the edge of the entropy trail, and the entire trail begins to cool by turbulent mixing. As to how long this process takes (or how far downstream) before the entropy trail produced by the normal portion of the shock of a blunt body is cooled

0

sufficiently to erase any observables such as electron density, will depend upon certain initial parameters at the station x_0 . These parameters are:

- a. Total drag coefficient,
- b. Ratio of drag associated with the turbulent inner core to the total drag,
- c. Width of the entropy trail, and
- d. Width of turbulent inner core.

3. Basic Equations

We will use the stream function ψ and x as independent variables in this analysis. The stream function is related to the physical radial coordinate r through the formula

$$\psi = 2\pi \int_0^r \rho u r dr \quad (88)$$

and r can be found from the inverse relation

$$r^2 = \frac{1}{\pi} \int_0^\psi \frac{d\psi}{\rho u} \quad (89)$$

Thus the radius R of the stream tube ψ in the free stream up to the bow shock is

$$R^2 = \frac{\psi}{\pi \rho_\infty U_\infty} \quad (90)$$

Let ψ_t be the stream tube which enters the effective front of the inner turbulent core at x and let ψ_f be the stream tube that enters at x_0 , the origin of calculation. Then from conservation of momentum in the x -direction we have

$$I = \int_0^{\psi_f} u_t d\psi = \int_0^{\psi_{f_0}} u_{t_0} d\psi + \int_{\psi_{f_0}}^{\psi_f} u_1 d\psi \quad (91)$$

since there is no x-momentum transported through stream tube boundaries in the outer inviscid flow and the pressure is assumed to be constant.

A second relation is found, the integral relation between the kinetic energy and the dissipation in the turbulent core, viz.

$$\frac{d}{dx} \int_0^{\psi_f} \frac{1}{2} u_t^2 d\psi = \frac{1}{2} u_f^2 \frac{d\psi_f}{dx} - 4\pi^2 \int_0^{\psi_f} \epsilon_t r^2 \rho_t u_t \frac{2u_T^2}{\psi} d\psi \quad (92)$$

By substituting the profile

$$u_t = u_a + (u_f - u_a) \frac{\psi}{\psi_f} \quad (93)$$

into the integral relations (91) and (92) one obtains

$$\frac{1}{2} (u_f + u_a) \psi_f = \frac{1}{2} (u_{f_0} + u_{a_0}) \psi_{f_0} + \int_{\psi_{f_0}}^{\psi_f} u_t d\psi \quad (94)$$

$$\frac{1}{6} (u_f - u_a) \frac{du_a}{dx} \psi_f = 4\pi^2 \int_0^{\psi_f} \epsilon_t r^2 \rho_t u_t (u_f - u_a)^2 \frac{1}{\psi^2} d\psi \quad (95)$$

Where both Eq. (94) and its differential form were used in reducing the left hand side in Eq. (92) to that in Eq. (95). ψ_f , u_a , and u_f are assumed to be purely functions of x with initial values of ψ_{f_0} , u_{a_0} , and u_{f_0} at $x = x_0$. Equation (95) can then be further reduced to

$$\frac{du_a}{dx} = 24\pi^2 \frac{u_f - u_a}{\psi_f^3} \int_0^{\psi_f} \epsilon_t r^2 \rho_t u_t d\psi \quad (96)$$

In order to obtain a simple evaluation of the dissipation integral on the right hand side of Eq. (96) we restrict ourselves to the case where the

variations of velocity and density are small across the core. For this case we make the "incompressible" assumption

$$r^2 = \frac{\psi}{\pi \rho_t u_t} = \frac{\psi}{\pi \rho_f u_f} \quad (97)$$

and approximate ϵ_t by

$$\epsilon_t = K \rho_f r_f |u_f - u_a| = \frac{K}{\sqrt{\pi}} \sqrt{\frac{\psi_f \rho_f}{u_f}} |u_f - u_a| \quad (98)$$

Substituting these into (96) we obtain

$$\frac{du_a}{dx} = 12 K \sqrt{\frac{\rho_f}{\psi_f u_f}} |u_f - u_a| (u_f - u_a) \quad (99)$$

Now from the relation (94) we obtain u_a in terms of u_f and an expression for du_a/dx :

$$u_a = \frac{2}{\psi_f} \int_{\psi_{f0}}^{\psi_f} u_i d\psi + \frac{(u_{f0} + u_{a0}) \psi_{f0}}{\psi_f} - u_f \quad (100)$$

$$\frac{du_a}{dx} = \left[\frac{2u_f}{\psi_f} - \frac{du_f}{d\psi_f} - (u_{f0} + u_{a0}) \frac{\psi_{f0}}{\psi_f^2} - \frac{2}{\psi_f^2} \int_{\psi_{f0}}^{\psi_f} u_i d\psi \right] \frac{d\psi_f}{dx} = \frac{du_a}{d\psi_f} \frac{d\psi_f}{dx} \quad (101)$$

Since u_i is assumed to be known as a function of ψ , it is a simple matter to obtain x as a function of ψ_f by numerical integration of Eq. (99).

We have

$$\int_{\psi_{f0}}^{\psi_f} \frac{\frac{du_a}{d\psi_f}}{1 - u_f - u_a} \sqrt{\frac{\psi_f u_f}{\rho_f}} d\psi_f = 12 K \sqrt{\pi} (x - x_0) \quad (102)$$

0

From the graph of x vs ψ_f we can obtain ψ_f vs x and, hence, the flow quantities and equilibrium electron densities as a function of x and ψ and ultimately as a function of x and r through the relation (89).

This formulation is for an arbitrary u_i as a function of ψ . We shall look at the special case where u_i can be approximated by

$$u_i(\psi) = U_\infty (1 - a e^{-b\psi}) \quad (103)$$

This distribution, by the proper choice of a and b , can be made to fit the velocity defect produced by a blunt body fairly well. It gives the bell-shaped nearly Gaussian curve for the outer entropy trail shown in Fig. 26a when plotted in the physical coordinate r . (Note that $\psi \sim r^2$ from Eq. (88).)

At the initial station $x = x_0$ let the drag associated with the inner turbulent core be D_w and let D be the total drag. We then have

$$D_w = \int_0^{\psi_f} (U_\infty - u_i) d\psi = \frac{1}{2} (u_{f_0} - u_{a_0}) \psi_{f_0} \quad (104)$$

$$\begin{aligned} D - D_w &= (U_\infty - u_{f_0}) \psi_{f_0} + \int_{\psi_{f_0}}^{\infty} (U_\infty - u_i) d\psi = (U_\infty - u_{f_0}) \psi_{f_0} \\ &+ \frac{a}{b} U_\infty e^{-b\psi_{f_0}} = \left(\frac{1}{b} + \psi_{f_0} \right) (U_\infty - u_{f_0}) \end{aligned} \quad (105)$$

from which one readily obtains the relation

$$\psi_{f_0} = \frac{2 D_w}{u_{f_0} - u_{a_0}} \quad (106)$$

We shall introduce at this point the dimensionless quantities:

$$u^* = u/U_\infty \quad (107)$$

$$\rho^* = \rho/\rho_\infty \quad (108)$$

$$T^* = T/T_\infty = \rho_\infty/\rho = 1/\rho^* \text{ (since } p = \text{const.} = p_\infty) \quad (109)$$

$$C_D = D/\frac{1}{2} \rho_\infty U_\infty^2 A \quad (110)$$

$$C_{D_w} = D_w/\frac{1}{2} \rho_\infty U_\infty^2 A \quad (111)$$

$$k = C_{D_w}/C_D \quad (112)$$

$$\psi^* = \psi/\psi_b \quad (113)$$

$$\bar{\psi}^* = 1/b \psi_b \quad (114)$$

$$\eta = b \psi_f = \psi_f^*/\bar{\psi}^* \quad (115)$$

$$C_D^* = C_D/\bar{\psi}^* \quad (116)$$

U_∞ = flight speed

ρ_∞ = atmospheric density at flight altitude

T_∞ = absolute temperature at flight altitude

p_∞ = ambient pressure at flight altitude

A = re-entry body maximum x-sectional area = πr_b^2

r_b = maximum body radius

$\psi_b = \rho_\infty U_\infty A$ = stream function value of free-stream tube equal to body x-sectional area

D = total drag

D_w = drag contained in turbulent core at the start of calculation

\dot{Q} = total heat transfer rate to the body

$\dot{Q}^* = \dot{Q}/\frac{1}{2} U_\infty^2 \psi_b \bar{\psi}^*$ = dimensionless heat transfer rate coefficient.

Equation (101) can then be written in non-dimensional form, viz.

$$\int_{\eta_0}^{\eta} \frac{\frac{du_a^*}{d\eta}}{|u_f^* - u_a^*|(u_f^* - u_a^*)} \eta u_f^* T_f^* d\eta = \frac{12K}{\sqrt{\psi^*}} \left(\frac{x - x_0}{r_b} \right) \quad (117)$$

where

$$u_f^* = 1 - \frac{1}{2} C_D^* \frac{1-k}{1+\eta_0} e^{\eta_0} e^{-\eta}, \quad \left(a = \frac{1}{2} C_D^* \frac{1-k}{1-\eta_0} e^{\eta_0} \right) \quad (118)$$

$$u_a^* = \frac{2}{\eta} \int_{\eta_0}^{\eta} u_f^* d\eta + \frac{\eta_0}{\eta} \left(2 - \frac{k C_D^*}{\eta_0} \right) - u_f^* = 1 - \frac{C_D^*}{\eta} + \frac{1}{2} \cdot \frac{1-k}{1+\eta_0} C_D^* e^{\eta_0} \left(1 + \frac{2}{\eta} \right) e^{-\eta} \quad (119)$$

$$u_f^* - u_a^* = \frac{C_D^*}{\eta} \left[1 - \frac{1-k}{1+\eta_0} e^{\eta_0} (1+\eta) e^{-\eta} \right] \quad (120)$$

$$\frac{du_a^*}{d\eta} = \frac{C_D^*}{\eta^2} \left[1 - \frac{1-k}{1+\eta_0} e^{\eta_0} \left(1 + \eta + \frac{\eta^2}{2} \right) e^{-\eta} \right] \quad (121)$$

$$T_f^* = 1 + \frac{\gamma-1}{2} M_{\infty}^2 (1 - u_f^{*2}) \quad (122)$$

$$T_a^* = 1 + \frac{\gamma-1}{2} M_{\infty}^2 \left(1 - u_a^{*2} - Q^* \frac{2}{\eta} \right) \quad (123)$$

$$\eta_0 = \frac{k C_D^*}{u_{f_0}^* - u_{a_0}^*} \quad (124)$$

It can be seen immediately that, if Eqs. (120) and (121) are substituted into Eq. (117), a factor $1/C_D^*$ can be pulled out. Thus multiplying Eq. (117) by C_D^* we obtain

$$\int_{\eta_0}^{\eta} F(\dot{Q}^*, M_{\infty}^2, \gamma, k, \eta_0, C_D^*; \eta) d\eta = \frac{12KC_D^*}{\sqrt{\psi^*}} \frac{x - x_0}{r_b} = \xi \quad (125)$$

with

$$F = \frac{1 - \frac{1-k}{1+\eta_0} e^{\eta_0} \left(1 + \eta + \frac{\gamma^2}{2}\right) e^{-\eta}}{\left|1 - \frac{1-k}{1+\eta_0} e^{\eta_0} (1+\eta) e^{-\eta}\right| \left[1 - \frac{1-k}{1+\eta_0} e^{\eta_0} (1+\eta) e^{-\eta}\right]} \sqrt{\eta u_f^* T_f^*} \quad (126)$$

4. Discussion and Numerical Examples

Examination of Eq. (125) and (126) reveals that the major parameters that control the spreading of the turbulent core occur only in the combinations

$$C_D^*, \frac{1-k}{1+\eta_0} e^{-\eta_0}, \frac{\gamma-1}{2} M_{\infty}^2, \frac{12KC_D^*}{\sqrt{\psi^*}}, \frac{kC_D^*}{u_{f_0}^* - u_{a_0}^*} = \eta_0$$

and that $(x - x_0)/r_b$ can be expressed entirely in terms of these parameters. It can further be shown that these parameters can all be expressed in terms of

$$\gamma, M_{\infty}, K, C_D, k, T_{f_0}^*, u_{f_0}^* - u_{a_0}^*$$

Although the exponential variation of velocity given by Eq. (103) was chosen on the basis of a good fit for a blunt body with a spherical nose, the approximation can still be used for sharp bodies, such as a cone, without losing any of the salient features in describing the turbulent core

spreading and temperature on the axis as a function of $(x - x_0)/r_b$. This is due to the fact that, for a sharp body, the radial distribution of velocity and temperature in the inviscid flow is fairly flat and the gradients at the edges are not important. This is demonstrated in the two numerical calculations discussed in the ensuing paragraphs.

Two numerical calculations at 150,000 ft and Mach 20 are presented: one for a typical blunt body such as that shown in Fig. 26a and one for a typical sharp body shown in Fig. 26b. The drag contained in the turbulent core bucket is assumed to be the same, that is, $C_{Dw} = .06$. This, in both cases, includes the skin friction and base drag, plus nose drag in the case of the sharp body. At 150,000 ft, the skin friction coefficient is about 0.03, and using Reynolds analogy, the heat transfer coefficient is $\dot{Q}/(2 \rho_\infty u_\infty^3 A) = 0.015$. These values were assumed for both cases. Both calculations were started with the assumption that the velocity on the axis was zero at the beginning which would be the case at the effective rear stagnation point. Each case will now be discussed separately.

a. Blunt Body

A typical pressure drag coefficient for a blunt body is 0.54, giving a total drag coefficient of $C_D = 0.6$ with $k = 0.1$. The results are shown in Fig. 27 where η , T_f^* and T_a^* with and without heat transfer are plotted against $(x - x_0)/r_b$. A measure of how far the front has moved laterally in terms of Gaussian widths of the entropy trail is given by η . It can be seen that in the blunt body case, the front must move many Gaussian widths before the center of the turbulent core begins to cool. This distance is of the order of a hundred body radii. The solid curve for T_a^* is the temperature ratio on the axis for an insulated body, while the dashed curve is for the assumed value of the heat transfer rate. It can be seen that the heat transfer rate to the body has little effect in depressing the temperature except at the very beginning where, for $u_a^* = 0$, T_a^* is about 0.56 times the free stream stagnation temperature (strictly speaking T^* is the enthalpy ratio and not the temperature ratio).

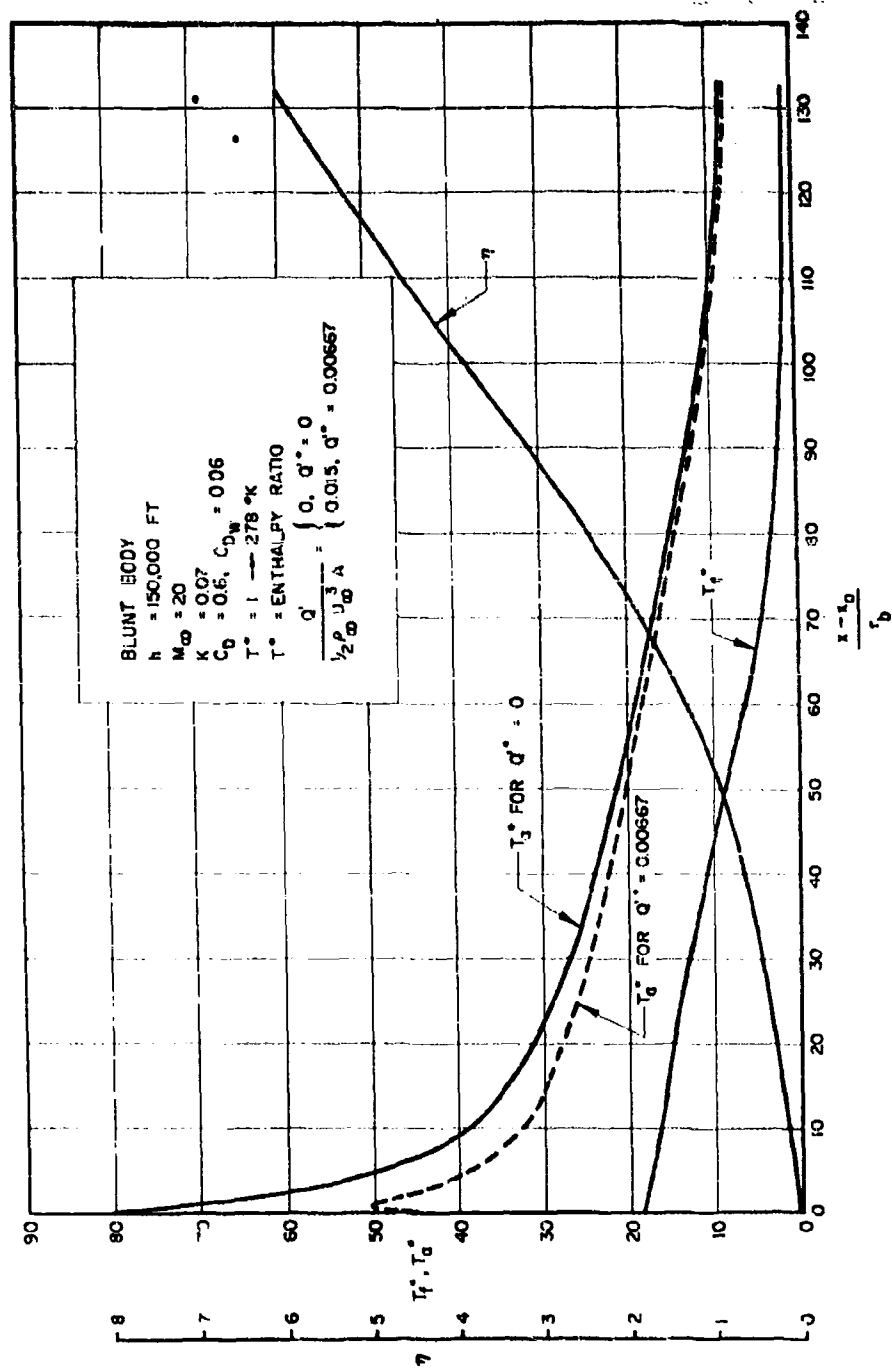


Figure 27. Wake Temperature Decay for Blunt Body in Hypersonic Flow

It can be concluded that for a typical blunt body with a two-foot diameter the temperatures will be sufficiently high to produce large amounts of radiation and sustain high electron concentrations visible to radar. Furthermore, the width of the turbulent core becomes very large for the blunt body case, as evidenced by the large values of η in terms of body radii. When T_a^* has reached roughly half the value of $T_{f_0}^*$, the initial front temperature in the entropy trail, η has the value 5 corresponding to $r_f/r_b = 18.1$ as calculated from Eq. (89), and $(x - x_0)/r_b$ is 117.

b. Sharp Body

A typical pressure drag coefficient for a sharp body, say a 10° half angle cone or an equivalent ogive, is 0.06 giving a total drag coefficient of $C_D = 0.12$ with $k = 0.5$. The results are shown in Fig. 28 where the same quantities are plotted as in the blunt body case. It can be seen that the wake is cooled in a much shorter length than in the blunt body case. The temperature on the axis has reached the value $T_a^* = 9$ at a value of $(x - x_0)/r_b = 33$, with $\eta = 2.1$ for a value of $r_f/r_b = 5.4$.

It can be concluded that for a typical sharp body the dimensions of the high temperature region in the wake are about a factor of three less than for the blunt body case. The heat transfer rate to the body has a more significant effect on the reduction of these dimensions than in the blunt body case.

The values of the parameters chosen for the sharp body are conservative and they tend to make the wake larger than that which might actually be expected at this altitude.

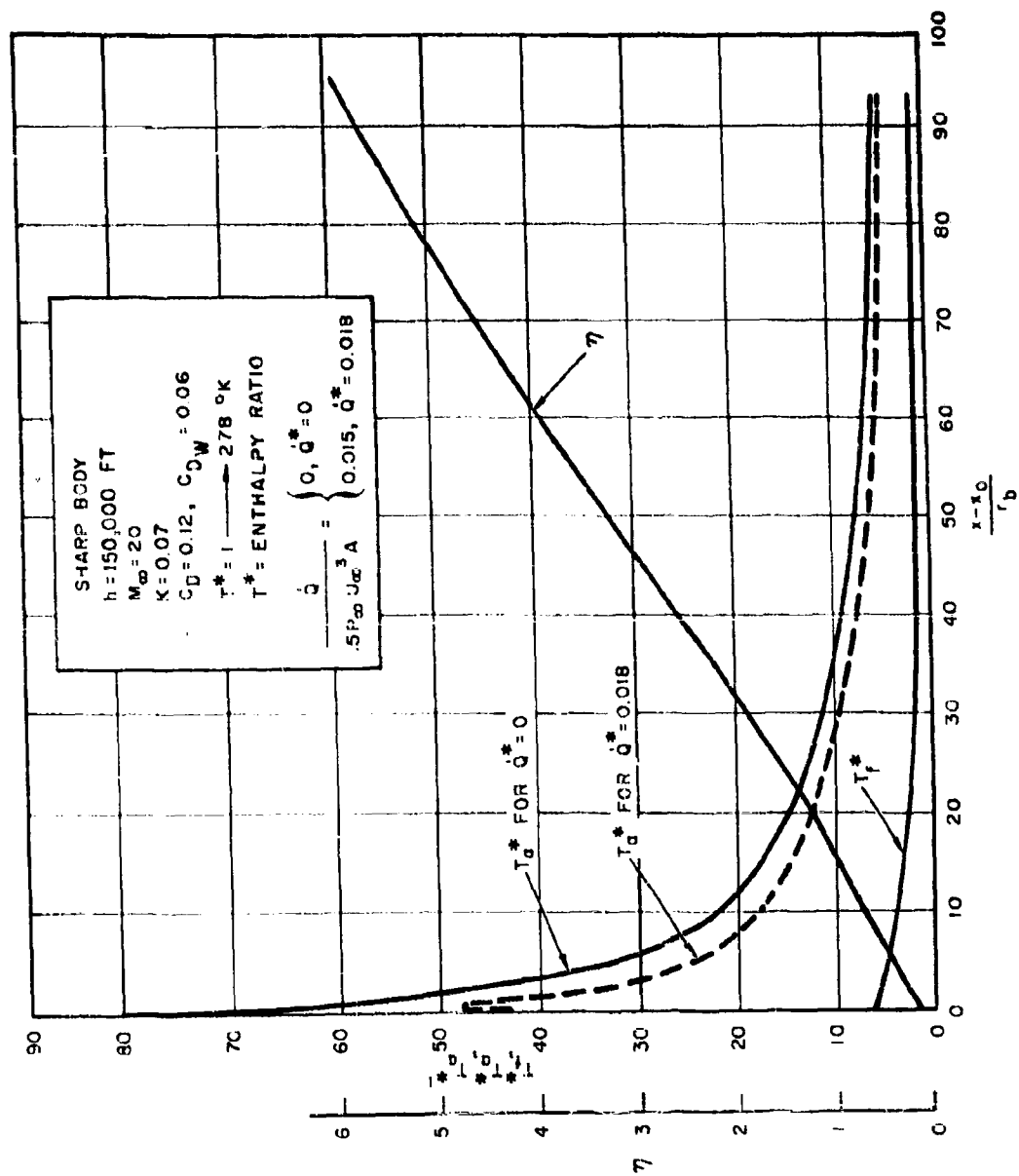


Figure 28. Wake Temperature Decay for Slender Body in Hypersonic Flow

III. EXPERIMENTAL INVESTIGATIONS

A. Stagnation Point Heat Transfer Measurements in Hypersonic Low Reynolds Number Flows

1. Introduction

In determining the point at which protective fairings for delicate payloads should be jettisoned during the launch trajectory of satellites vehicles, free molecule flow heat transfer rates have been assumed. Calculations based on this assumption provide the maximum heat transfer rate predictions, and hence, the maximum payload protective fairing requirements. As a result, the tendency has been to carry the fairings to altitudes which are much beyond optimum because of the uncertainty of the heat transfer rates in the very high atmosphere. These rates were not significant relative to exit and re-entry heat rates and these unknowns were tolerable. Now situations are arising where it is no longer advisable to ignore these uncertainties. Also theoretical analysis³⁴ in the low density regime is, for the most part, unsubstantiated by experiment. It is, therefore, the purpose of this study to attempt to measure the stagnation point heat transfer rates to cylinders and spheres in the hypersonic shock tunnel at flow Mach numbers from 13 to 23. The Reynolds number range to be covered is from 5 to 500, based on leading edge diameter, corresponding to the regime between free molecule flow and the continuum regime.

Because of its high reservoir stagnation temperature, the shock tunnel is an instrument peculiarly suited to making measurements at high Mach numbers and low Reynolds numbers typical of the high altitude portions of the launch trajectory of satellite vehicles. Furthermore, the shock tunnel can yield a variety of stagnation pressures, and hence, Reynolds numbers for a given stagnation temperature. The chief drawback inherent in shock tunnels is the comparatively short time interval during which measurements can be made. As a result, equilibrium conditions between the flow and the measuring instrument usually cannot be obtained and must

be inferred from the transient response of the measuring device. In this report heat transfer rate measurements determined from the transient response of thin film resistance thermometers mounted at the stagnation point of models will be described and the results of the measurements presented. The shock tunnel facility in which these tests were made is shown in Fig. 29.

2. Theoretical Predictions

Probstein and Kemp³⁴ have considered the problem of calculating the aerodynamic heating to be expected in hypersonic rarified gas flows, where the mean free path becomes too large for the use of the inviscid flow-boundary layer approach and too small for the free molecule flow regime to apply. They have solved the Navier stokes equations for two sets of boundary conditions; (1) a "viscous layer" class in which a thin shock wave exists, but the region between the shock and the blunt body is fully viscous, and (2) a "merged layer" class representing a more rarified condition. In the merged layer the shock wave is no longer thin and the Navier stokes equations are used to provide a solution which includes the shock structure and free stream conditions as outer boundary conditions.

From this analysis a deviation is predicted in the stagnation point heat transfer rate from that expected on the basis of extrapolated boundary layer theory. The viscous layer theory predicts higher heat transfer to both spheres and cylinders normal to the flow as the Reynolds number (based on nose diameter) is decreased to the order of 10.

The "incipient merged layer" theory modifies the heat transfer rates to values which are less than in the viscous layer, but greater than in the boundary layer theory. The predicted results for spheres and cylinders are shown in Fig. 30a and 30b. Although an incipient merged layer prediction for the cylinder is not made, it is easy to suppose that it lies between the viscous layer and boundary layer value. These curves were computed on the basis of a density ratio across the shock of 0.1 and a γ for the gas of 11/9.

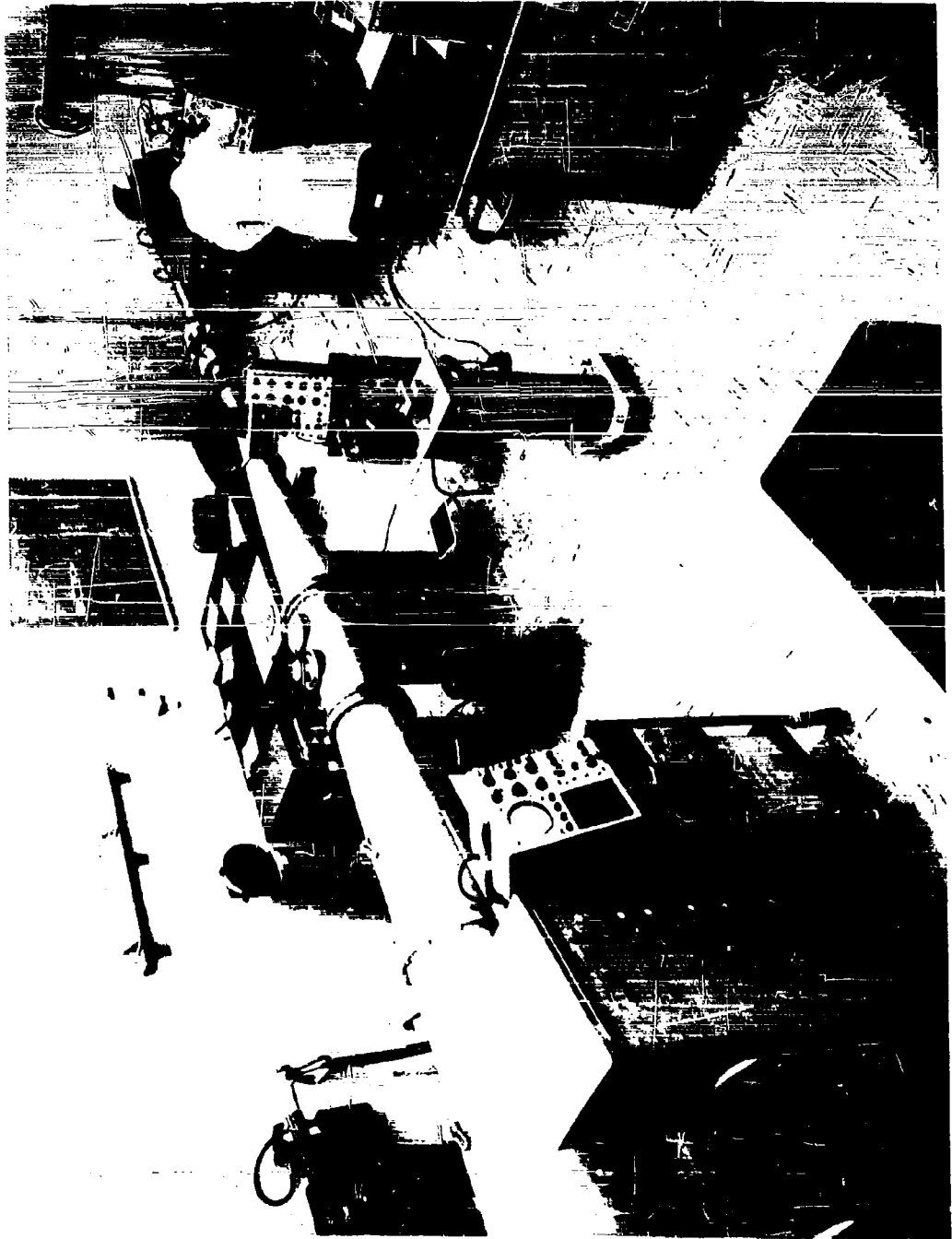


Figure 29. View of Shock Tunnel Showing 12-inch Test Section

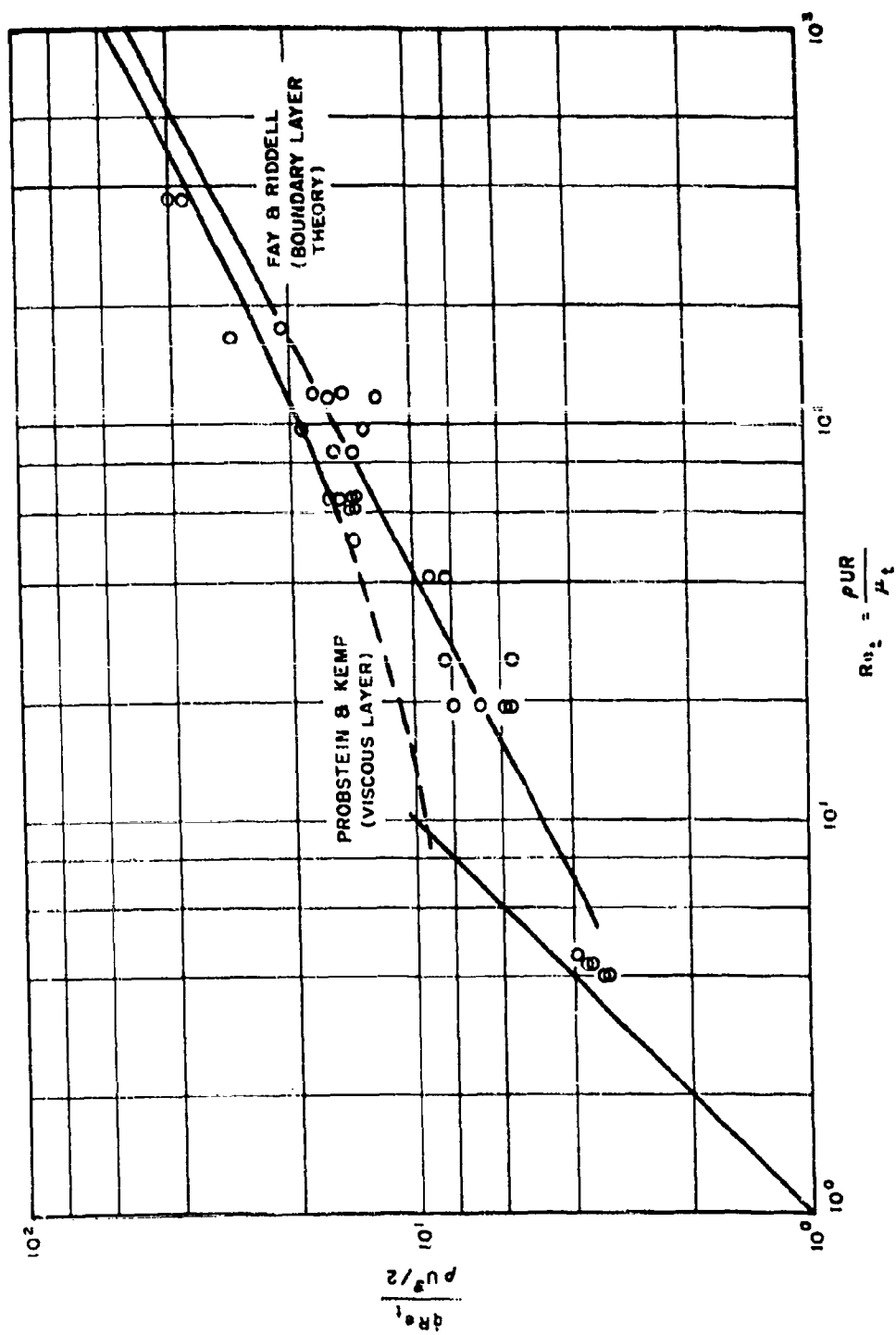


Figure 30a. Heat Transfer Rate to Cylinders Normal to the Flow as a Function of Stagnation Point Reynolds Number

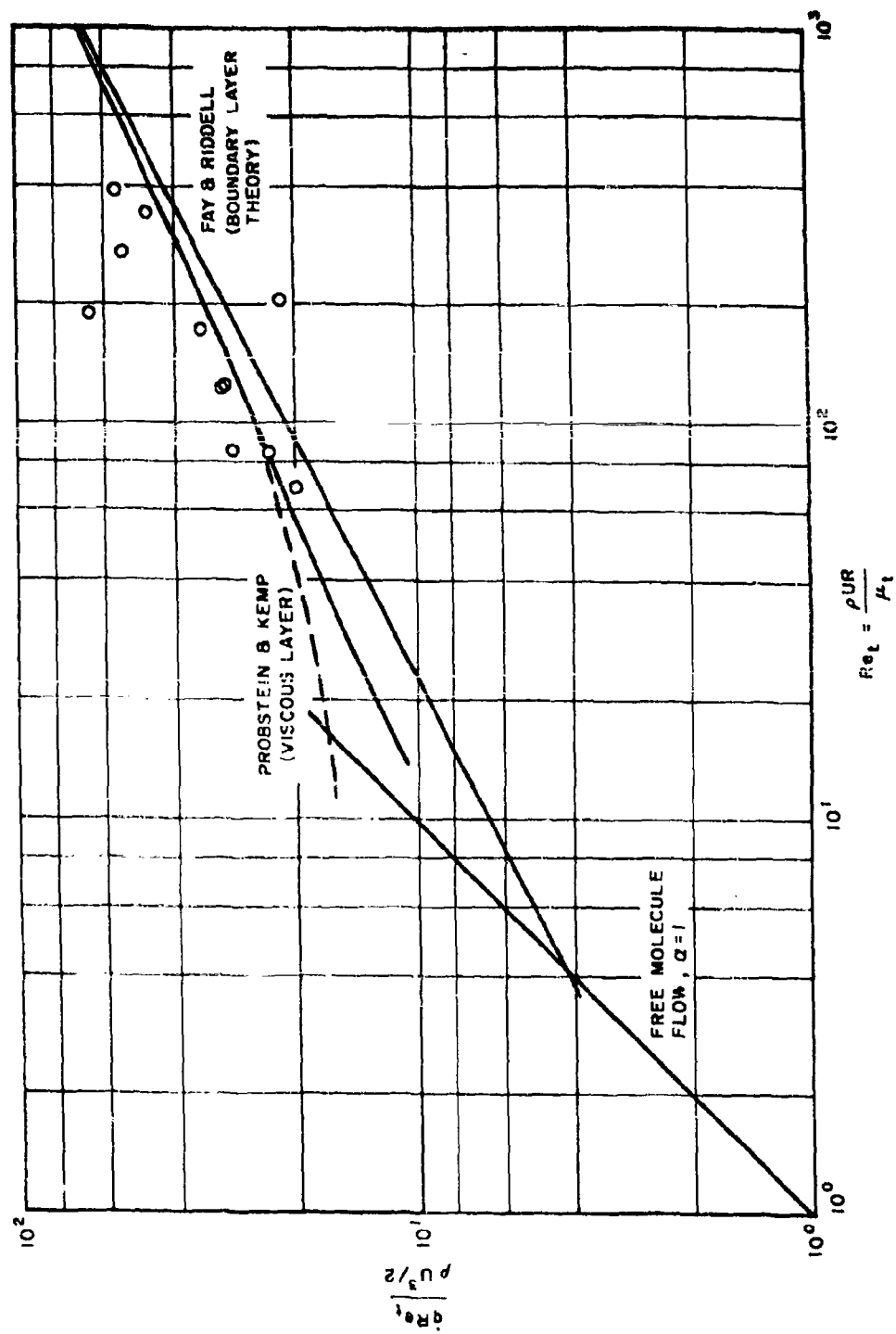


Figure 30b. Heat Transfer Rate to Spheres as a Function of Stagnation Point Reynolds Number

For shock tunnel reservoir conditions of about 240 atmospheres and 2840°K, and test section Mach numbers from 10 to 20, the heat transfer rates, according to Fay and Riddell,² were calculated. These values are plotted in Fig. 30 for comparison with the results of Probst and Kemp. A free molecule flow value for an accommodation coefficient of unity is plotted also.

3. Experiments

In the shock tunnel for shock Mach numbers of 4.5 to 4.7, reservoir test conditions (which remain steady for about 4 millisecon) of about 220 and 240 atm and 2840 and 3000°K are obtained. Using the twelve-inch diameter test section and varying the throat diameter over a range of .04 to .375 inches, Mach numbers from 10 to 23 are achieved. For each test, the shock Mach number (M_g) in the shock tube, and the pitot pressure (P_t) in the test section, are measured. From the shock Mach number, the reservoir conditions (that is, the conditions behind the reflected shock) are ascertained. These conditions, along with the pitot pressure measurement, determine the flow Mach number in the test section.

Spherical and cylindrical shells of Pyrex 7740 glass, ranging in diameter from 3 to 20 mm, were employed as models. Two thin film resistance thermometers were applied at the stagnation point of the cylinder and half an inch on either side of the mid-point of the cylinder. The films were applied by airbrushing Hanovia No. 05X liquid bright platinum paint in a strip 0.5 mm wide and half an inch long and then firing it at 1250°F. Firing silver micro paint in a heavy layer provides low resistance contacts with the measuring circuit. Fig. 31 is a photograph of the cylindrical model. This model was mounted in the test section normal to the flow so that the mid-point of the cylinder corresponded with the axis of the tunnel test section. The cylinder was supported from the wall in cantilever fashion. The spherical model shown in Fig. 32 has a shorter thin film at its stagnation point and is supported from the model stand as illustrated. The pitot pressure gauge location is indicated also in this photograph.

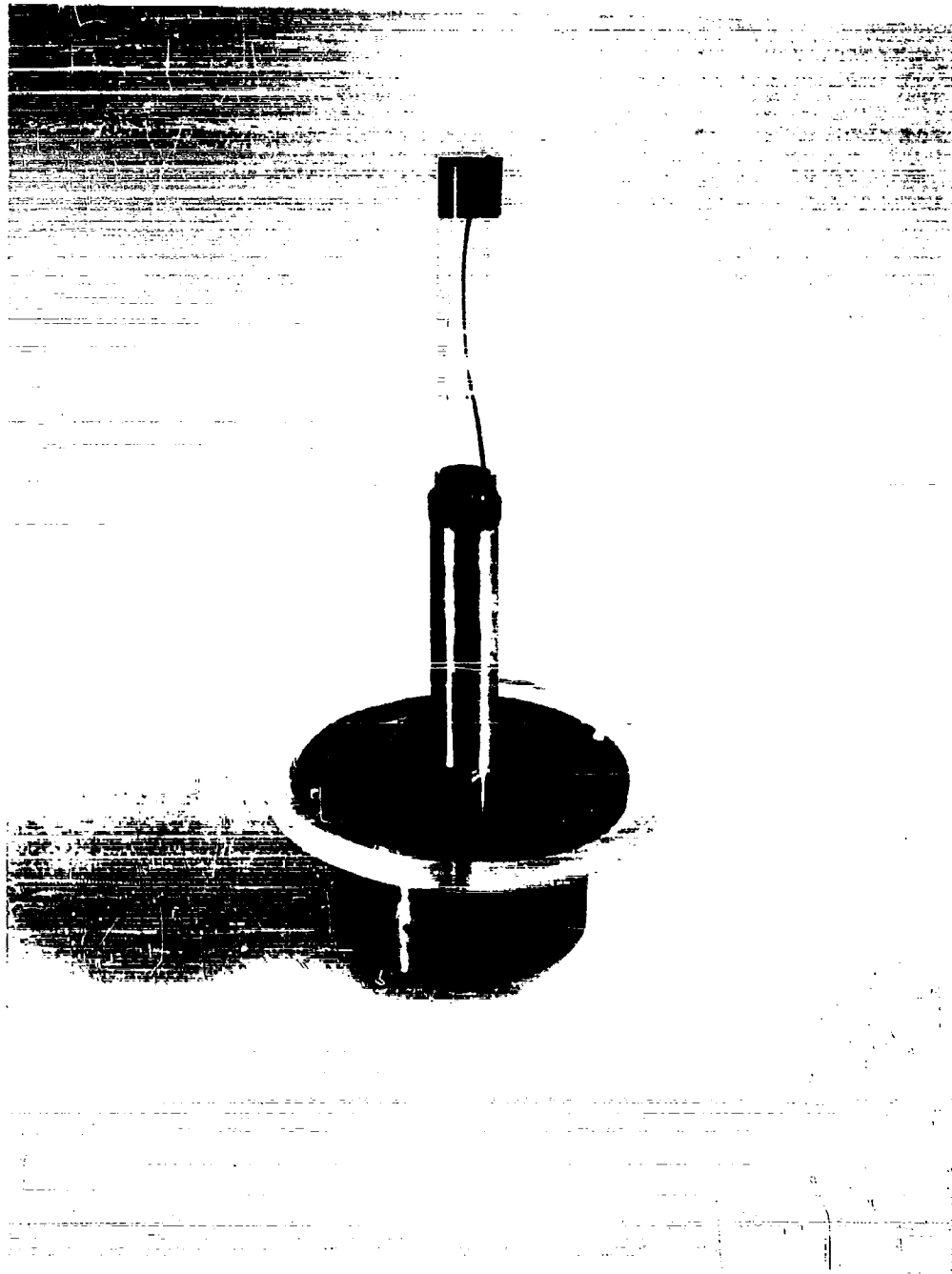


Figure 31. 20mm Diameter Cylindrical Model Showing the Two Thin Film Resistance Thermometers Along the Surface which Becomes the Stagnation Line of the Cylinder



Figure 32. Mounting of the Spherical Model in the Tunnel. Showing also the Pitot Tube for Measuring Test Section Total Pressure

The technique of thin film resistance thermometry is quite well known and very adequately covered in the literature. In essence, the thermometer measures the surface temperature history of the material on which it resides. This measured temperature history is converted to a heat transfer rate by the use of one-dimensional heat conduction theory and one basic calibration of the thermometer. The basic calibration is generally done by the pulsing technique in which a known heat flux, produced by a current step pulse through the resistance thermometer, is applied to the gauge. The calibration is used to determine the lumped thermal properties of the substrate of the thin film, $\sqrt{\pi \rho C k}$, where ρ , C , and k are the density, specific heat, and conductivity of the substrate. The thermal coefficient of resistance of the film is determined by measuring the resistance at the freezing and boiling points of water.

The equation relating the heat transfer rate (\dot{Q}) to the model along with the temperature history of the model surface ($\Delta T/\sqrt{t}$) is given as

$$\dot{Q} = \frac{\sqrt{\pi \rho C k}}{2} \left\{ 1 + \frac{b}{K_0} \left[\left(1 + \frac{\Delta T}{T_0} \right) \left(\frac{T_0}{\Delta T} \right) \log_{10} \left(1 + \frac{\Delta T}{T_0} \right) - .434 \right] \right\} \frac{\Delta T}{\sqrt{t}} \quad (127)$$

T is the temperature change of the surface and T_0 is the initial temperature of the surface. The quantity in the braces $\left\{ \right\}$ represents the correction to the heat transfer rate which must be included in order to account for the change in the thermal properties of the substrate when the surface temperature becomes large in comparison with the calibration temperature.³⁵ b/k_0 is a function of the material, which for Pyrex is 4.73.

Measurements were made in the shock tunnel of the heat transfer rates to cylinders 3mm, 10mm, and 20mm in diameter and to spheres 10 and 20mm in diameter. Reservoir stagnation conditions ranged from 2800 to 3000°K with pressures of 28 to 29 atm and 220 to 240 atm. Mach numbers in the test section varied from 10 to 23, but most of the data was in the range of 13 to 16.

4. Results

In calculating the value of Re_t , the Reynolds number based on leading edge diameter, the value of the viscosity is determined according to the results of the study of oxygen recently reported by Hartunian and Marrone.³⁶ This study indicates that the Sutherland viscosity values based on kinetic theory and hard spherical molecules are as much as 50% too low for temperatures up to 3000°K. This modified value of μ_t also was used to determine the theoretical value of Q_0 , according to Fay and Riddell.²

The experimental values of the reservoir conditions, the flow Mach numbers and the heat transfer rates are tabulated in Table I. Values of $Q_0 Re_t / \frac{1}{2} \rho U^3$ as a function of Re_t are plotted in Fig. 30a and 30b, along with the theoretical curves. The results for the cylinder seem to follow the boundary layer theory right on down to the free molecule flow regime with only a slight increase at Reynolds numbers less than 20. The considerable scatter in the data makes a definitive determination of the best theory impossible.

The experimental data for the axisymmetric probe (sphere) are even more scattered, and therefore, inconclusive.

Some remarks on the accuracy of these experiments should be made. The shock Mach number can be measured to $\pm 1\%$ and this is about the error expected in the reservoir conditions. The total pressure can be measured to within $\pm 10\%$ and this should be the expected error in p . As a result, the theoretical curve which is plotted from the experimentally obtained values for the tunnel conditions could have a width of $\pm 10\%$. The heat transfer measurements have a possible error of between $\pm 5\%$ and $\pm 18\%$, depending on the smoothness and clarity of the heat transfer record. An example of a typically adequate record is shown in Fig. 33 for a flow Mach number of 16.5 and reservoir conditions of 243 atm and 3100°K.

No explanation is immediately available for the greater amount of scatter in the sphere data. Since the spheres were blown from Pyrex tubing some irregularities existed in their radii. However, the heat transfer

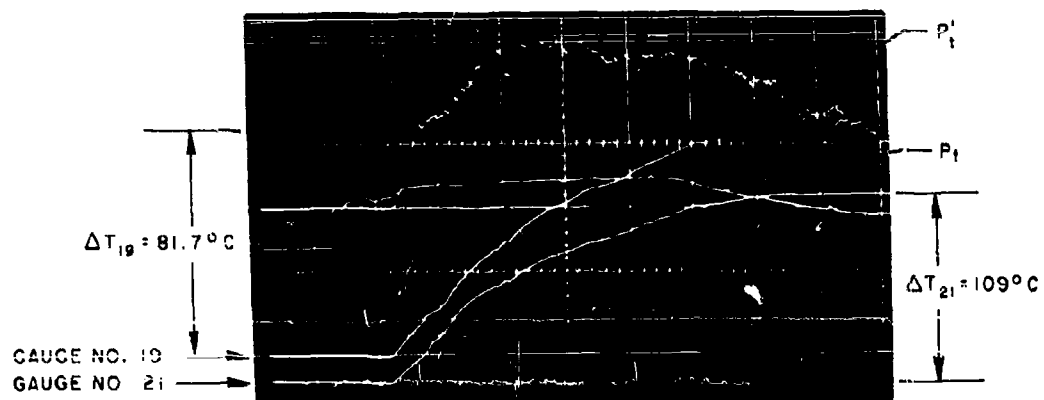


Figure 33. Typical Temperature History for the Stagnation Point of a Cylindrical Model

$$P_t = 222 \text{ atm}$$

$$T_t = 2980^{\circ}\text{K}$$

$$M = 16.0$$

rate varies inversely as the square root of the body radius, and hence, irregularities in the radii should not give significant effects. The much smaller gauge on the spheres could limit the accuracy of the results.

5. Conclusions

The heat transfer rates to cylinders and spheres, as measured in the shock tunnel, are adequately predicted by the theory of Fay and Riddell² down to $Re_t \approx 20$. At this point, the heat transfer rate increases somewhat, as predicted by Probstein and Kemp,³⁴ reaching the free molecule flow heat transfer rate at a value of Re_t between 2 and 3.

Table I - Rate Constants For Chemical Processes

Reaction	Catalyst: M	Rate Constant
$O_2 + M + 5.1 \text{ ev} \xrightleftharpoons[k_R]{k_D} O + O + M$	Ar, N, N ₂ , NO	$k_D^1 = \frac{3.6 \times 10^{18}}{T} \exp(-9373/T) \text{ cm}^3/\text{mole sec}$
	O ₂	$k_D^2 = \frac{3.2 \times 10^{19}}{T} \exp(-9373/T) \text{ cm}^3/\text{mole sec}$
	O	$k_D^3 = \frac{8.9 \times 10^{19}}{T} \exp(-9373/T) \text{ cm}^3/\text{mole sec}$
$N_2 + M + 9.8 \text{ ev} \xrightleftharpoons[k_R]{k_D} N + N + M$	Ar, O, O ₂ , NO	$k_R^1 = 1.7 \times 10^{14} \times (T/4.00)^{-1.5} \text{ cm}^6/\text{mole}^2 \text{ sec}$
	N ₂	$k_R^2 = 5 \times 10^{14} \times (T/450)^{-1.5} \text{ cm}^6/\text{mole}^2 \text{ sec}$
	N	$k_R^3 = 1 \times 10^{16} \times (T/450)^{-1.5} \text{ cm}^6/\text{mole}^2 \text{ sec}$
$NO + M + 6.5 \text{ ev} \xrightleftharpoons[k_R]{k_D} N + O + M$	Ar, O ₂ , N ₂	$k_R^4 = 3.3 \times 10^{14} \times (T/4.00)^{-1.5} \text{ cm}^6/\text{mole}^2 \text{ sec}$
	NO, O, N	$k_R^5 = 6.7 \times 10^{15} \times (T/4.00)^{-1.5} \text{ cm}^6/\text{mole}^2 \text{ sec}$
$NO + O + 1.4 \text{ ev} \xrightleftharpoons[k_2]{k_1} O_2 + N$ $N_2 + O + 3.3 \text{ ev} \xrightleftharpoons[k_2]{k_1} NO + N$ $N_2 + O_2 + 1.9 \text{ ev} \xrightleftharpoons[k_2]{k_1} NO + NO$	$k_2^1 = 1 \times 10^{12} T^{0.5} \exp(-3120/T) \text{ cm}^3/\text{mole sec}$	
	$k_2^2 = 1.3 \times 10^{13}$	$\text{cm}^3/\text{mole sec}$
	$k_2^3 = 2.6 \times 10^{23} \times T^{-2.5} \exp(-43030/T) \text{ cm}^3/\text{mole sec}$	

B. Electron Beam Densitometer Studies

1. General

When an electron beam is projected through a space containing molecules of a gas, the electrons are scattered due to both elastic and inelastic collisions with gas molecules. The incident electron loses energy and causes the parent beam to become diffuse and inhomogeneous. Electron scattering in a gas is a function of electron energy, particle density, molecular cross sections, and path length. It is possible to measure the molecular number density for a known gas by electron scattering.

A high energy beam of electrons was utilized to measure gas density in the flow field of the low density wind tunnel at Berkeley.³⁷ This is a continuous-run tunnel operating at Mach 2 with free stream pressures of about 0.1 millimeters mercury. The Berkeley electron beam apparatus was entirely contained within the large diameter test section of the tunnel.

Perturbation of the flow, and limitations of response time and sensitivity preclude the use of more conventional pressure sensors in a hypersonic low density shock tunnel. The electron beam probe is thus a theoretically ideal sensor since electrons are effectively massless compared to the free stream flow, and have a high order of sensitivity and response speed.

2. Electron Beam Attenuation in a Gas

When an electron beam is projected into a gas, a fraction of the initial beam will survive the passage without deflection and its path is a continuation of the original ballistic trajectory. If only the unscattered electrons are accepted by a suitable means of detection, Lambert's law of absorption will hold for the loss of beam intensity along its path:

$$\frac{dI}{dx} = -\mu I \quad (128)$$

Where I is the beam intensity, x is the path length, ρ is the gas density, and μ is an absorption coefficient.

The absorption coefficient, μ , is related to the effective scattering cross section of the gas. The cross section $Q(\Phi)$ is defined as the probability per scattering center that an electron will be deflected by an interaction with a gas molecule into a cone of half angle Φ which is greater than the effective angle subtended by the detector aperture measured from the point of scattering. If there are n molecules of gas in the volume occupied by the electron beam, the total probability of an electron interaction with a gas molecule is nQ , or over an increment of path length dx , is $nQdx$, and the loss of beam intensity becomes:

$$\frac{dI}{dx} = -nQI \quad (129)$$

$$\text{Integration of Eq. (129) yields } I(x) = I_0 e^{-nQx} \quad (130)$$

Markevitch and Huribut³⁸ have shown that the experimental value of $Q(\pi)$ for high energy electrons in air is close to the theoretical value based on elastic collisions. This value is energy dependent and has been found to have the relation

$$Q(\pi) = \frac{3.6 \times 10^{-13}}{V} \text{ cm}^2 \quad (131)$$

where V is in volts.

Taking Avogadro's number, $N = 6.025 \times 10^{23}/\text{mol.}$, and the standard volume, $V_0 = 22.4146 \times 10^3 \text{ cm}^3/\text{mol.}$, then at a pressure of one micron there are 3.537×10^{13} molecules per cubic centimeter of a perfect gas. Then $n = 3.537 \times 10^{13} \text{ p}$, and $\mu p = nQ = 3.537 \times 10^{13} \text{ p}Q$, from which

$$Q = 2.827 \times 10^{-14} \frac{\mu p}{p} \quad (132)$$

This quantity Q is the total collision cross section of the gas, and has the same significance as the sense of $Q(\pi)$ in Eq. (131); that is, it represents the total cross section which was determined from scattering into a cone or half angle π radians.

We may now obtain the absorption coefficient μ by combining Eq. (131) and (132):

$$\mu p = 12.73 \frac{p}{V} \quad (133)$$

for air, where p is in microns and V is in volts.

The equation for the intensity of an electron beam in air at a constant pressure p microns is then

$$I(x) = I_0 E^{-12.73 \frac{px}{V}} \quad (134)$$

where $I(x)$ is measured in centimeters from the point of origin and I_0 is the incident beam current of an energy V electron-volts.

Equation (134) is plotted on logarithmic coordinates in Figs. 34 and 35.

3. Electron Beam Absorption in an Axially Symmetric Flow Field

The electron beam densitometer will be used to obtain free stream density measurements in the flow field of the hypersonic shock tunnel and the variation of free stream density in the direction normal to the flow. Consider a uniform beam of electrons injected into an axially symmetric flow field where the gas density is a function of r , the radial distance from the central flow axis, as in Fig. 36. It will be required to find the gas density, ρ , as a function of r . Consider a uniform beam of electrons of intensity I_0 originating outside the flow region and directed in the positive x direction.

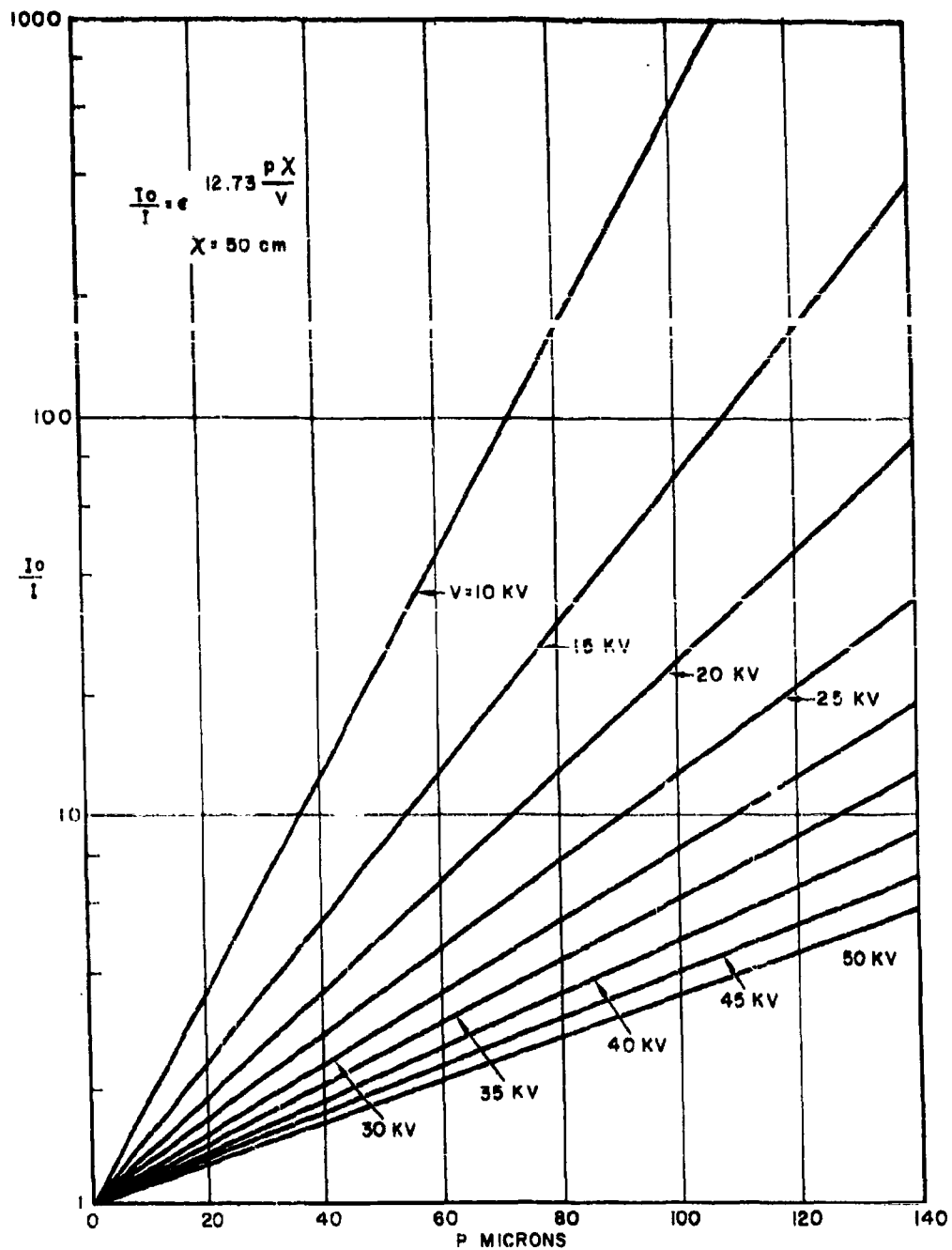


Figure 34. Current Ratio as a Function of Pressure for Constant Path Length

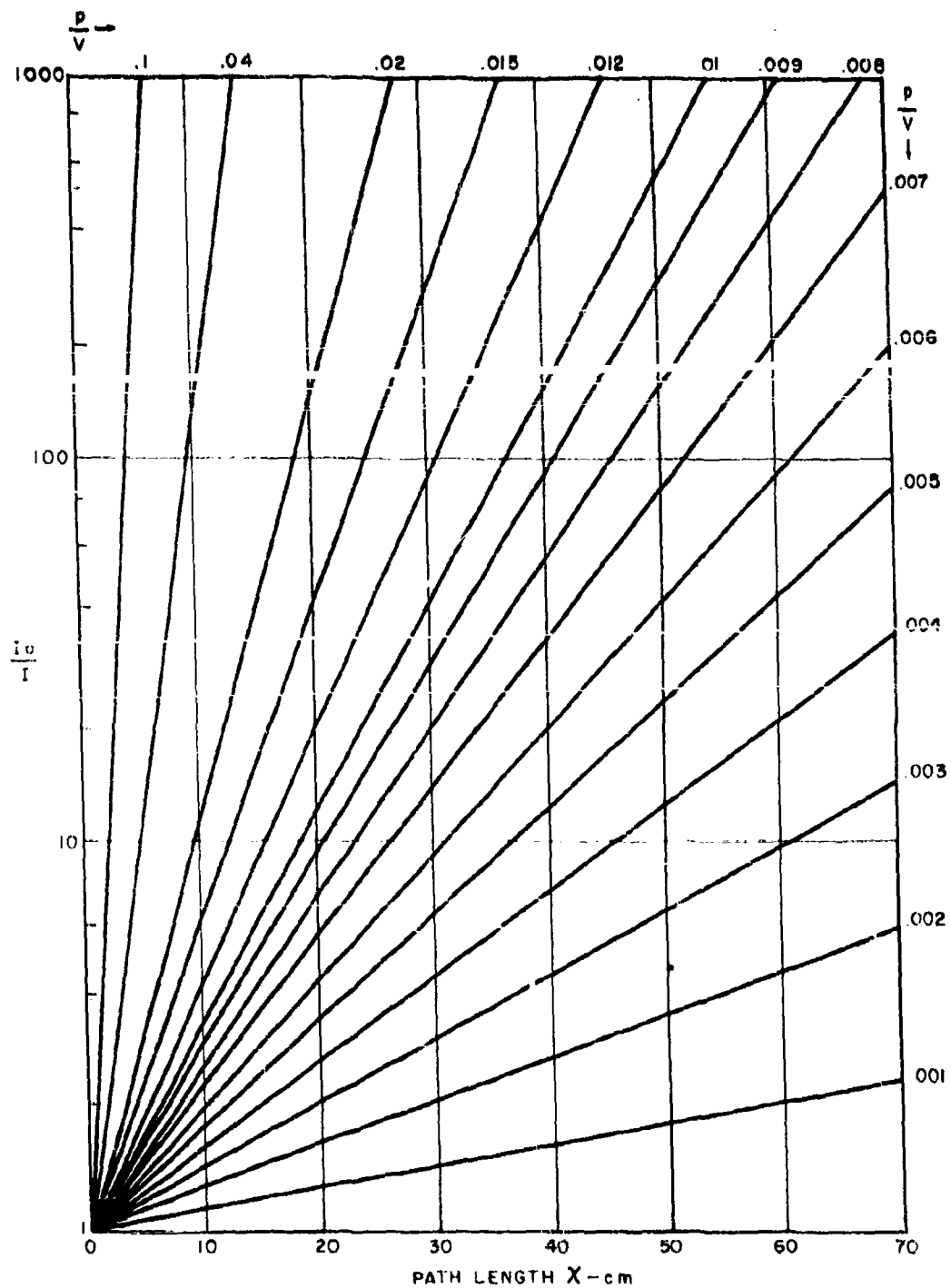


Figure 35. Current Ratio as a Function of Path Length for Constant Pressure-Voltage Ratio

Lambert's law of absorption holds as a partial derivative since the beam attenuation is a function of x and y .

$$\frac{\delta I}{\delta x} = -\mu \rho I \quad (135)$$

which has a solution

$$\ln I(y) - \ln I_0 = -2\mu \int_0^{\bar{x}} \rho dx - \mu \rho_1 (L - 2\bar{x}) = F(y) \quad (136)$$

where $\rho = f(r)$ and ρ_1 is a constant.

From the geometry of Fig. 36, $r^2 = x^2 + y^2$, and for constant y , $rdr = xdx = \sqrt{r^2 - y^2} dx$. Also, when $x = 0$, $r = y$, and when $x = \bar{x}$, $r = R$ then Eq. (136) becomes

$$F(y) = -2\mu \int_y^R \rho(r) \frac{rdr}{\sqrt{r^2 - y^2}} - \mu \rho_1 (L - 2\bar{x}) \quad (137)$$

A second change of variables is made by putting $S = R^2 - r^2$ and $g(s) = \rho(r)$. Now $dS = -2rdr$, and at $r = y$, $s = R^2 - y^2$ and at $r = R$, $S = 0$. Then Eq. (137) becomes

$$F(y) = \mu \int_{R^2 - y^2}^0 g(s) \frac{ds}{\sqrt{R^2 - y^2 - S}} - \mu \rho_1 (L - 2\bar{x}) \quad (138)$$

This may be simplified by substitution of $t = R^2 - y^2$, then

$$F(y) = -\mu \int_0^t \frac{g(s)ds}{\sqrt{t - s}} - \mu \rho_1 (L - 2\bar{x}) \quad (139)$$

and define

$$f(y) = G(t) = -\mu \int_0^t \frac{g(s) ds}{\sqrt{t-s}} \quad (140)$$

then

$$f'(y) = F(y) + \mu \rho_1 (L - 2\bar{x}) \quad (141)$$

Equation (140) is of the Abel type with unknown $g(s)$ and has the solution

$$g(s) = \frac{-1}{\pi\mu} \frac{d}{ds} \int_0^s \frac{G(t) dt}{\sqrt{s-t}} \quad (142)$$

To integrate by parts, choose $U = G(t)$ and

$$dV = \frac{dt}{\sqrt{s-t}}$$

Equation (142) becomes

$$g(s) = \frac{-1}{\pi\mu} \frac{G(0)}{\sqrt{s}} + \frac{1}{\pi\mu} \int_0^s \frac{G'(t) dt}{\sqrt{s-t}} \quad (143)$$

From Eq. (140) $G(0) = 0$ and

$$G'(t) = f'(y) = \frac{d}{dy} f(y)$$

so that

$$g(s) = \frac{1}{\pi\mu} \int_0^s \frac{f'(y) dt}{s-t} \quad (144)$$

We now change variables by the substitutions $t = R^2 - y^2$ and $S = R^2 - r^2$. Note that when $y = R$, $t = 0$ and when $y = r$, $t = s$, then

$$g(s) = \rho(r) = \frac{1}{\pi\mu} \int_r^R \frac{f'(y) dy}{\sqrt{y^2 - r^2}} \quad (145)$$

By differentiation of Eq. (141),

$$f'(y) = \frac{d}{dy} \ln I(y) - 2\mu\rho \frac{y}{\sqrt{R^2 - y^2}} \quad (146)$$

and substitution into Eq. 145,

$$\rho(r) = \frac{1}{\pi\mu} \int_r^R \frac{d}{dy} \ln I(y) \frac{dy}{y^2 - r^2} - \frac{2\rho_1}{\pi} \int_r^R \frac{y dy}{\sqrt{y^2 - r^2} \sqrt{R^2 - y^2}} \quad (147)$$

which leads to

$$\rho(r) = \frac{1}{\pi\mu} \int_r^R \frac{d}{dy} \ln I(y) \frac{dy}{y^2 - r^2} + \rho_1 \quad (148)$$

$I(y)$ may be obtained by measuring segments of the core flow under identical tunnel conditions and $\rho(r)$ is evaluated numerically. A preferred technique is to incorporate a series of detectors and a rapid sweep on the electron beam to measure all segments during a single run.

4. Instrumentation

The electron beam densitometer consists of two major systems: the electron source or gun, with the associated high voltage accelerator, heaters, bias and deflection power supplies, and the detector, with its associated power, bias, and deflection supplies. Oil diffusion pumps supply the high vacuum environment for the electron gun and the detector.

A stage of differential pumping separates the test chamber from the electron gun. The electron gun generates a narrow, slightly convergent beam of electrons in the energy range from 15 to 50 Kev, at a beam current up to 10^{-3} amperes. The electron source is a triode gun using a 10 mil diameter tungsten hairpin filament, emission aperture, Wehnelt aperture and anode aperture. It was adapted from the gun used at Berkeley. A similar gun, probably the original of this type, was designed by K. H. Steigerwald³⁹ for use with the Zeiss EM8 electron microscope, designated the K2 far-focus cathode system. A similar gun is being used by Hamilton-Electrona in their electron beam welding, milling, and hole drilling machines. The Aerospace electron gun is shown in Figs. 37, 38, and 39.

Collimation of the beam is done with apertures of small diameter. These apertures also separate the scavenging chambers required to provide differential pumping (gas molecules escaping from the test chamber are pumped out to prevent degrading the vacuum in the electron gun).

The detector uses a Faraday cup electron collector which may be biased at a positive voltage with respect to ground. An internal shield biased negatively with respect to the collector insures suppression of secondary electrons.

A general view of the densitometer is shown in Fig. 40.

Preliminary tests have been made of the apparatus with satisfactory detection of the scattered beam achieved in a test gas. Evaluation of the preliminary data is now underway to establish feasibility and implementation of this technique to the combustion-driven shock tunnel.

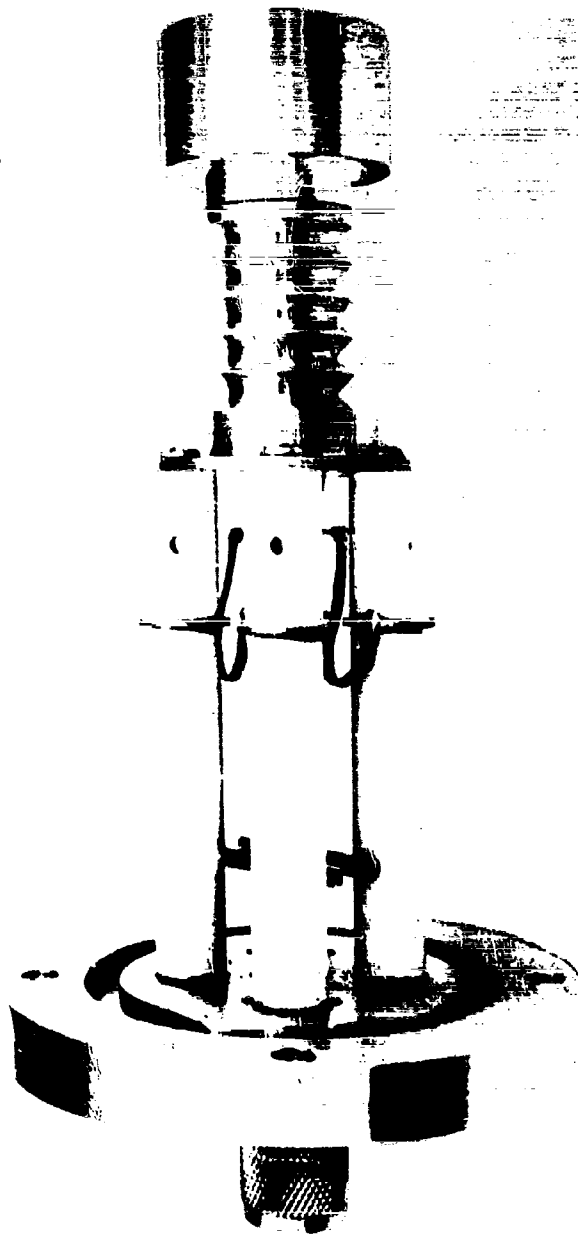


Figure 37. Electron Gun, Assembled View

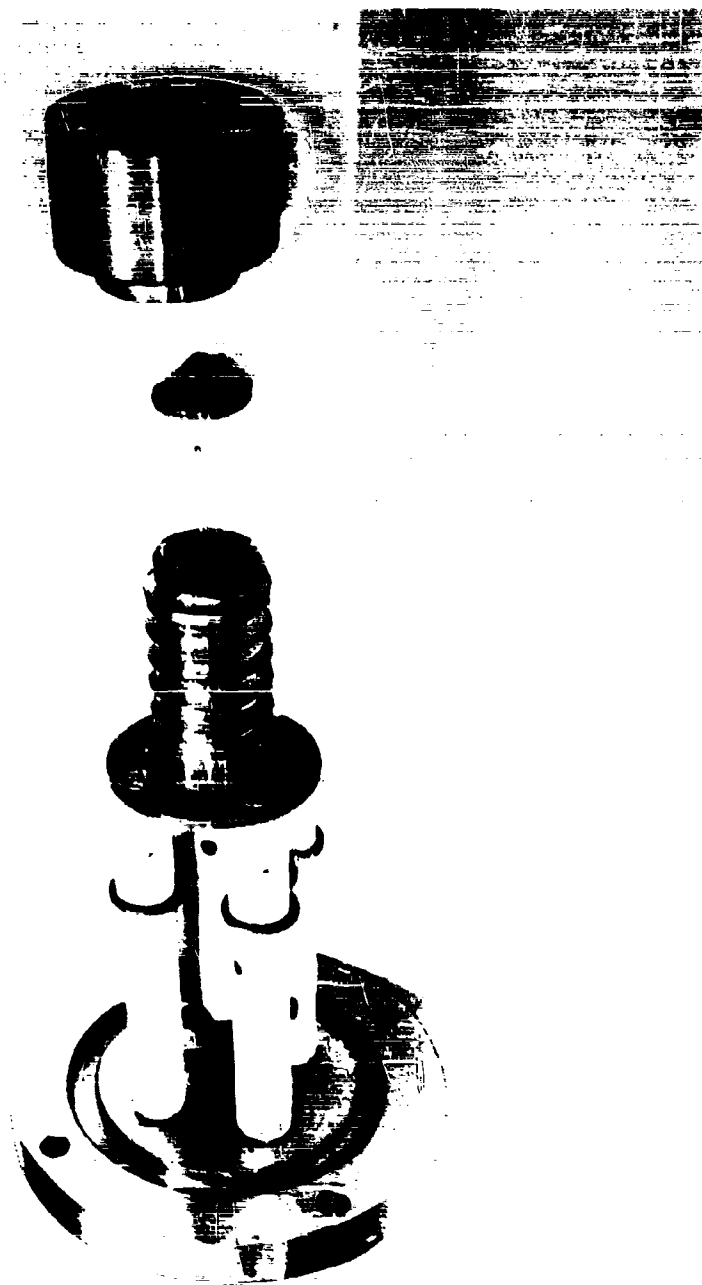


Figure 38. Electron Gun, Exploded View

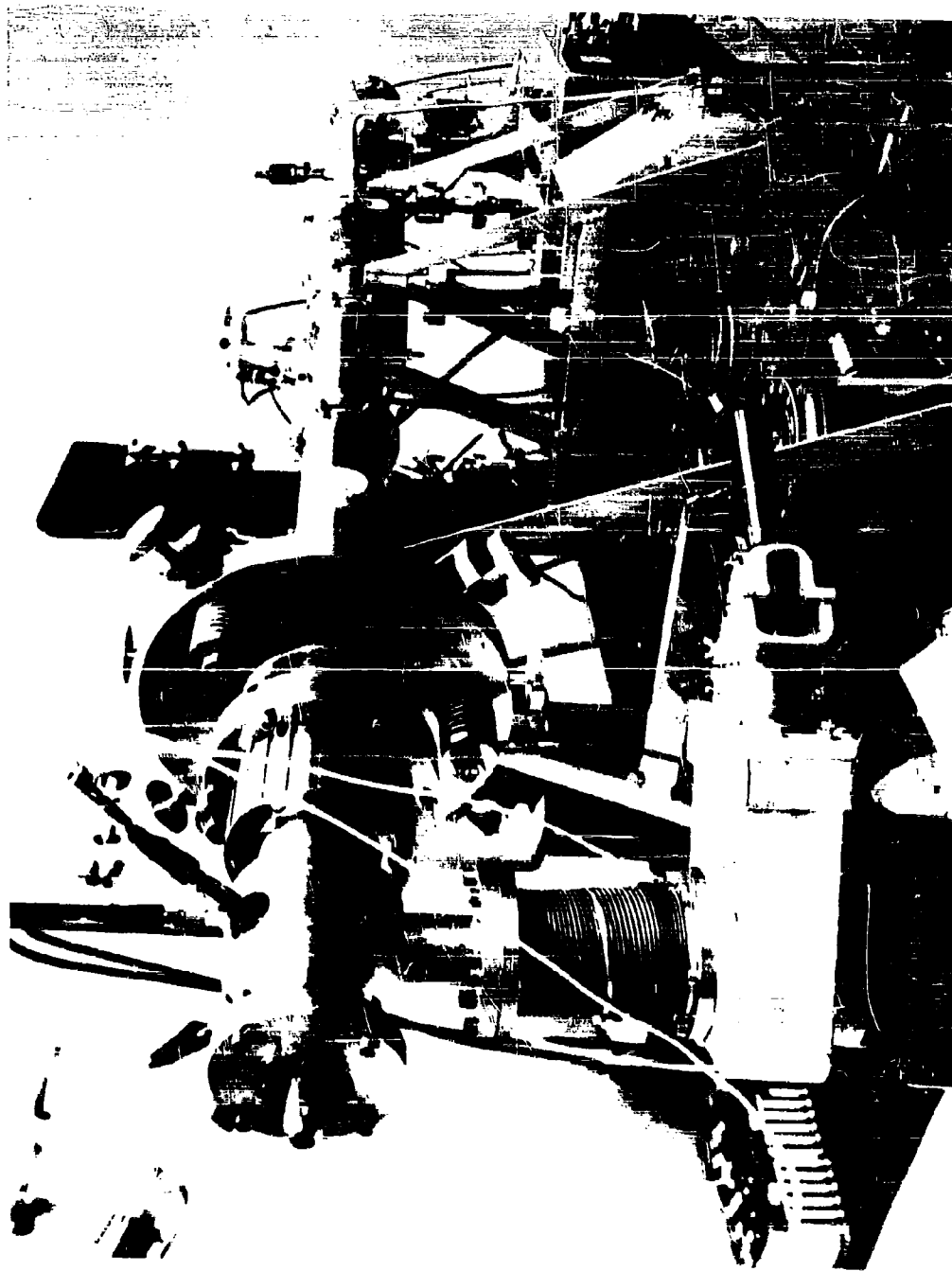


Figure 39. Electron Beam Gun and Tilting Mechanism

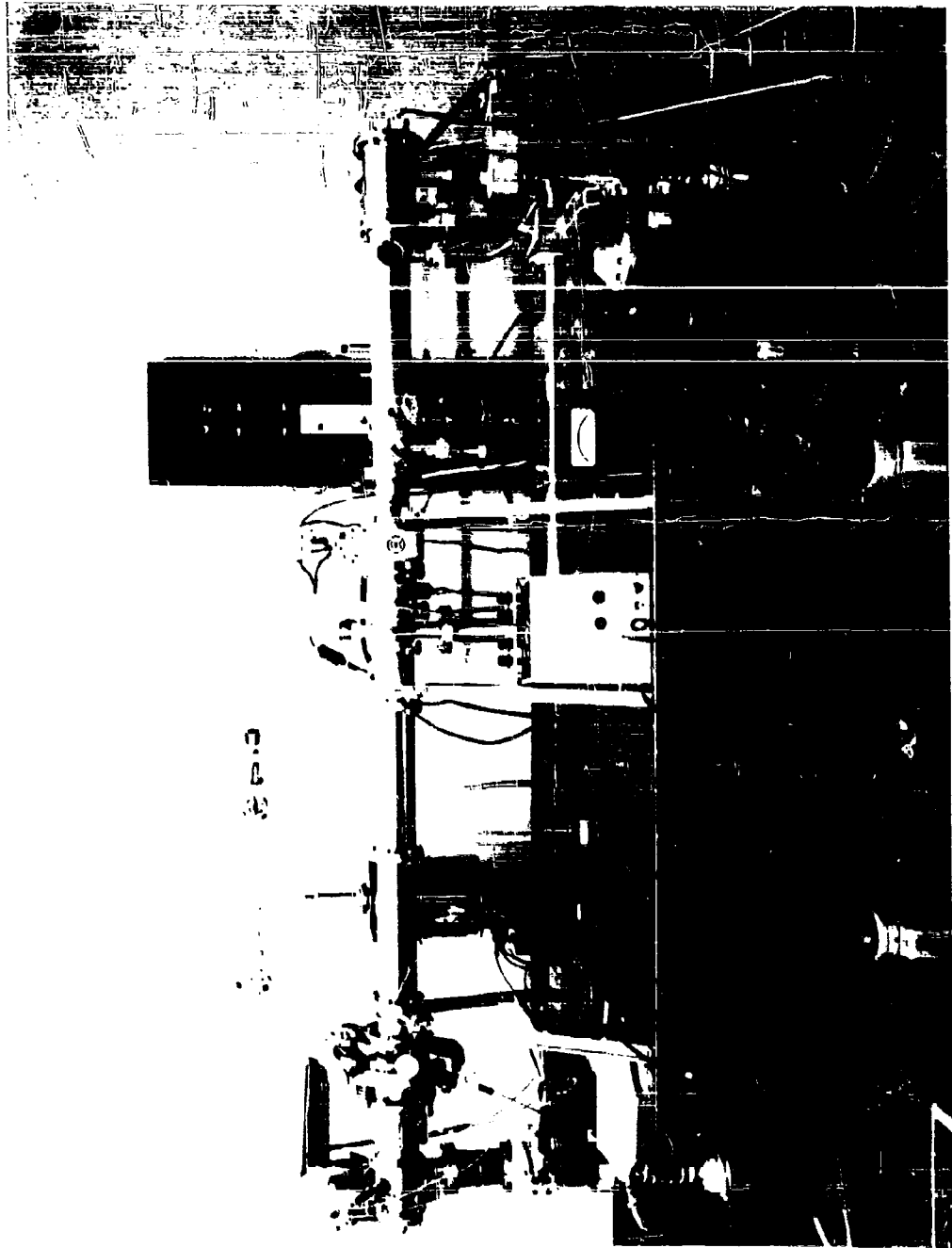


Figure 40. General View of the Apparatus

C. High Enthalpy Combustion-Driven Hypersonic Shock Tunnel Design

1. General Requirements

The requirements for extending the performance capability of the existing helium-driven hypersonic shock tunnel may be most easily observed by examining re-entry vehicle simulation requirements by means of similitude considerations. If the flight envelope for future lifting and non-lifting re-entry vehicles is taken as that shown in Fig. 41, then the simulation requirements for each regime may be examined. These requirements will be examined for both slender bodies, typical of high lift-drag ratio vehicles, and blunt bodies, typical of ballistic re-entry vehicles

a. Slender-Body Simulation Considerations

Regime I:

In this regime as a result of viscous non-equilibrium considerations, complete thermodynamic velocity, and model size simulation are required. It is possible in this regime to relax the above requirements for the inviscid flow, i. e. the actual model length need not be duplicated. Here model scaling can be made by simulating the local residence time of a particle U_∞/L . In this case the inviscid similitude is given by⁵

$$\left. \begin{array}{l} P/P_\infty \\ \rho/\rho_\infty \\ T/T_\infty \\ M_\infty^2 C_L \\ M_\infty^2 C_M \\ M_\infty^3 C_D \\ M_\infty^3 C_q \end{array} \right\} = \pi \left(M_\infty^2, M_\infty \frac{3+\nu}{1+\nu}, k \frac{1}{1+\nu} \frac{d}{L}, \chi, P_r, U_\infty/L, \frac{H_w}{H_\infty}, 0, P_\infty, \rho_\infty, a_\infty \right) \quad (149)$$

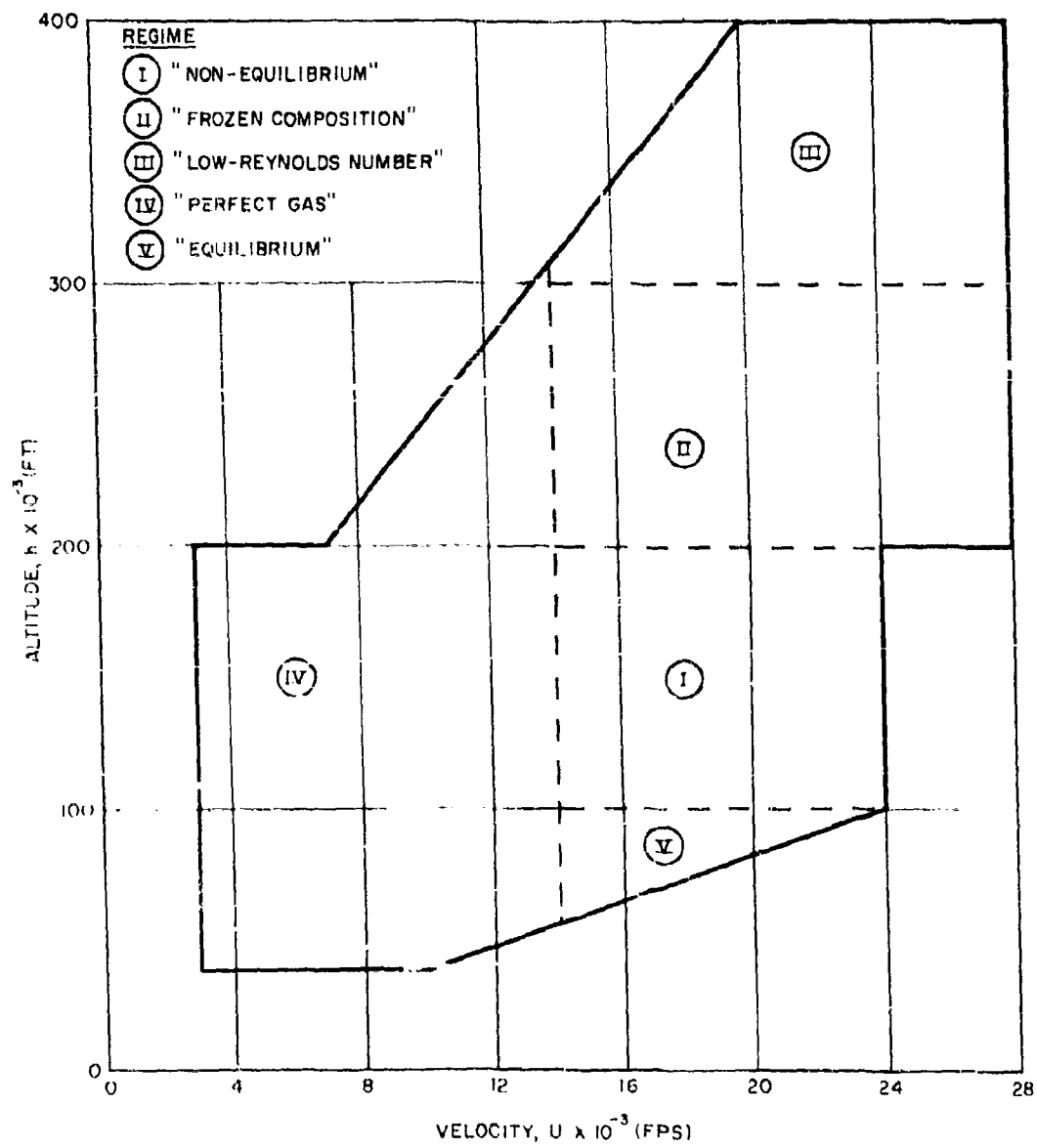


Figure 41. Hypervelocity Simulation Requirements (Slender Body)

Since this regime occurs below an altitude of approximately 200,000 ft (Fig. 41), the low Reynolds number phenomena associated with slender bodies may not be too significant, and therefore, the influence on the inviscid external flow can be considered small. Reference 5 quantitatively indicates the region, in terms of the hypersonic interaction parameter χ , where the interaction of the boundary layer with the external inviscid flow field may be ignored. Therefore, if these effects were to be considered small, the only need for reproducing model length in this case would be for skin friction and heat transfer measurements. If the surface of the vehicle were to be catalytic, present theoretical considerations indicate that non-equilibrium phenomena would not significantly influence either the skin friction or heat transfer, thus offering the possibility of relaxing model length simulation requirements.

All of the above remarks for the altitude bounds indicated in Fig. 41 necessarily must be made on the basis of assumed air dissociation-recombination rates and, therefore, only can be considered quantitative within the accuracy with which these rates are known. There is also some question as to the importance of simulating the ambient free-stream thermodynamic environment ($P_\infty, \rho_\infty, a_\infty$). Since the attainment in practice of exact simulation of these thermodynamic parameters represents one of the most difficult simulation problems for any facility, it would certainly be desirable to relax these requirements if possible. If it was found that, for example, the free-stream temperature simulation (within certain limits) did not significantly influence the aerodynamic or heating characteristics measured on a model, then it might be possible to simulate the non-equilibrium effects by means of simulation of the recombination rate parameter, C_i .⁵ Unfortunately, this type of information is not available either theoretically or experimentally and one must, at this time, be directed by the rigorous mathematical similitude requirements; i. e., complete thermodynamic, velocity, and model length simulation.

Regime II - Frozen Composition

In this regime the chemical reaction rates are considered slow compared to either the rate of convection along stream lines or the rate of diffusion along stream lines. A quantitative delineation of this regime as well as the dissociation non-equilibrium regime is shown in Fig. 41. Mathematically, the similitude requirements in this case may be specified as

$$\left. \begin{array}{l} P/P_{\infty} \\ \rho/\rho_{\infty} \\ T/T_{\infty} \\ M_{\infty}^2 C_L \\ M_{\infty}^2 C_M \\ M_{\infty}^3 C_D \\ M_{\infty}^3 C_q \end{array} \right\} = \pi \left(M_{\infty}, \tau, M_{\infty}^{\frac{3+\nu}{1+\nu}} k^{\frac{1}{1+\nu}} \frac{d}{L}, \chi, P_r, \frac{H_w}{H_{\infty}} \sim 0, C_i \ll 1, P_{\infty}, \rho_{\infty}, a_{\infty} \right) \quad (150)$$

It can be noted, according to the above similitude, that freedom in the choice of both model length and possibly free-stream velocity exists. If, however, we deviate from the mathematical formulation and examine the practical aspect of the simulation requirements, we can then observe that we indeed do not have freedom in the choice of free-stream velocity or model length. In this regime, we are interested in determining the influence of large amounts of energy distributed in the inert degrees of freedom (particularly dissociation). With this consideration in mind, coupled with the free-stream thermodynamic simulation requirement, it is felt that the proper total specific enthalpy level must be simulated. This requirement dictates simulation of free-stream velocity. We would, therefore, conclude that we have freedom only in model length, but this is not so since concurrent simulation of $P_{\infty}, \rho_{\infty}, a_{\infty}, \chi$, dictates reproduction of model length.

Therefore, while the frozen composition model initially indicates some simplifications in terms of facility simulation requirements, these simplifications cannot be considered realistic which means we must revert back to complete thermodynamic, velocity, and model simulation.

In addition, the above remarks are based on the assumption that the dissociation process comes to equilibrium immediately behind the shock envelope. If the rate of equilibration of the forward dissociation process is considered, then at some point in the frozen flow regime, we again encounter non-equilibrium phenomena. Furthermore, since these non-equilibrium effects occur at high altitudes, where the viscous effects are important these considerations (viscous non-equilibrium) further dictate the need for complete thermodynamic velocity and model size simulation.

It should be emphasized again that the importance of complete thermodynamic simulation must be examined; however our present lack of any experimental or theoretical understanding of this flow regime does not permit any relaxation of this requirement at the present time.

Regime III - Low Reynolds Number

This regime also requires complete thermodynamic, velocity and model length simulation but this particular item is separated from Regime I for two reasons: (a) For the most optimistic case this regime is observed to be governed as a minimum by the complete Navier-Stokes equations; and (b) as in the previous regime the problem of the time to dissociate is present thus yielding viscous non-equilibrium simulation requirements. As a result of these considerations it is difficult to see how, in the foreseeable future, quantitative theoretical or experimental data will be available to relax any of the complete simulation requirements. Certainly, relaxation of the simulation requirements, as a result of a more quantitative understanding of the flow phenomena, will have to occur first within either Regime I or Regime II before any such understanding can be possible in Regime III.

•

Regime IV - Perfect Gas

This regime is delimited by considering that if we tie-up a relatively small amount of energy in dissociation behind the vehicle shock-envelope, then the influence of any "real gas" phenomena on either the aerodynamic or heat transfer problem should be relatively small. This consideration was made quantitatively for the slender body problem by considering the ratio of the dissociation energy to the free-stream kinetic energy, which is taken as the total gas enthalpy for hypersonic flow. The numerical work was carried out for a disturbance strength of 30° . This would correspond to a local inclination of the vehicle surface of 30° with respect to the free-stream velocity vector. With these considerations in mind, this estimate is certainly not valid for the stagnation region; however, it should provide a good estimate for the down-stream region and thus, for the over-all vehicle aerodynamic and heat transfer characteristics. In this region the aerodynamic and heat transfer characteristics should be given to a good approximation by

$$\left. \begin{aligned} P/P_\infty \\ \rho/\rho_\infty \\ T/T_\infty \\ M_\infty^2 C_L \\ M_\infty^2 C_M \\ M_\infty^3 C_D \\ M_\infty^3 C_q \end{aligned} \right\} = \left(M_\infty^2 \tau, M_\infty^2 \frac{3+\nu}{\Gamma+\nu} k \frac{1}{\Gamma+\nu} \frac{d}{L}, \chi \frac{H_w}{H_\infty} \approx 0, P_r, \gamma \right) \quad (151)$$

As would be anticipated, the above similitude is recognized as essentially that for a perfect gas with constant specific heat. The simplification associated with simulation of the above compared to the previous simulation requirements outlined in Regimes I, II, and III can be readily observed.

Here we can relax the requirements on particle velocity, model length, and ambient thermodynamic properties. It is felt the above conditions can be satisfactorily simulated with existing hypervelocity facilities (e. g., shock-tunnels, Ohio State, and University of California) and, therefore, should not be considered too critical at the present time. In fact, except for possibly the very high altitude conditions, they can be considered, for slender body application,* fairly well understood within the framework of continuum fluid mechanics.

Regime V - Equilibrium

This regime is considered to be given by high Reynolds number Reynolds number, chemical equilibrium flow phenomena. It is therefore felt one should be able to employ the information obtained from Regime I to easily extrapolate to Regime V for aerodynamic and heat transfer data.

Finally, it should be noted the above remarks for Regimes I through V are applicable for slender bodies down-stream of the immediate vicinity of the leading edge. Therefore, they should be considered pertinent for slender body aerodynamic and heat transfer characteristics exclusive of the stagnation region. The bounds indicated cannot be considered valid for the stagnation region, particularly when the low Reynolds number and dissociative non-equilibrium phenomena are important. This problem will now be discussed in the ensuing blunt body similitude considerations, where the general remarks will apply for the stagnation region of a slender body with the appropriate dimensional changes.

b. Blunt-Body Simulation Considerations

The remarks in this section will be directed toward low fineness ratio (≤ 5) lifting and non-lifting re-entry vehicles. As remarked previously, these considerations will apply to the slender body stagnation regions also.

* It should be remembered this bound will be different for the blunt-body problem.

Regime I - Non-Equilibrium

The previous remarks made for the slender body problem are applicable here. However, the viscous interaction problem considerations have decreased importance for low fineness configurations. Since we are concerned with blunt inviscid dominated flow fields, one is tempted to examine the possibility of relaxing the velocity simulation requirement by means of particle residence time simulation (i. e., U_{∞}/L). Unfortunately, as in the previous slender body case, the necessity of simulating the re-combination rate parameter does not permit us to take advantage of this possibility. Therefore, we conclude that we must provide complete simulation as in the slender body problem. This regime is particularly important for advanced re-entry vehicles because maneuverability and the associated aerodynamic problems must be considered more carefully than those associated with present non-lifting vehicles.

Regime II - Frozen Composition

Again, the remarks made for the slender body problem apply here. In addition, this regime will be particularly important for advanced re-entry vehicle aerodynamic (maneuvering) and communications black-out phenomena. Decoy aerodynamic design, in order to simulate re-entry observables, will also be important in this regime.

Regime III - Low Reynolds Number

All of the remarks made for the slender body problem in this regime can be applied here.

Regime IV - Perfect Gas

This regime is delimited by considerations similar to those previously discussed for the slender body problem. Since the shock-layer associated with these vehicles will be dominated by streamlines which pass through the near normal shock, this regime must apply to lower velocities than those associated with the slender body case. The bound for the blunt-body problem is indicated in Fig. 42.

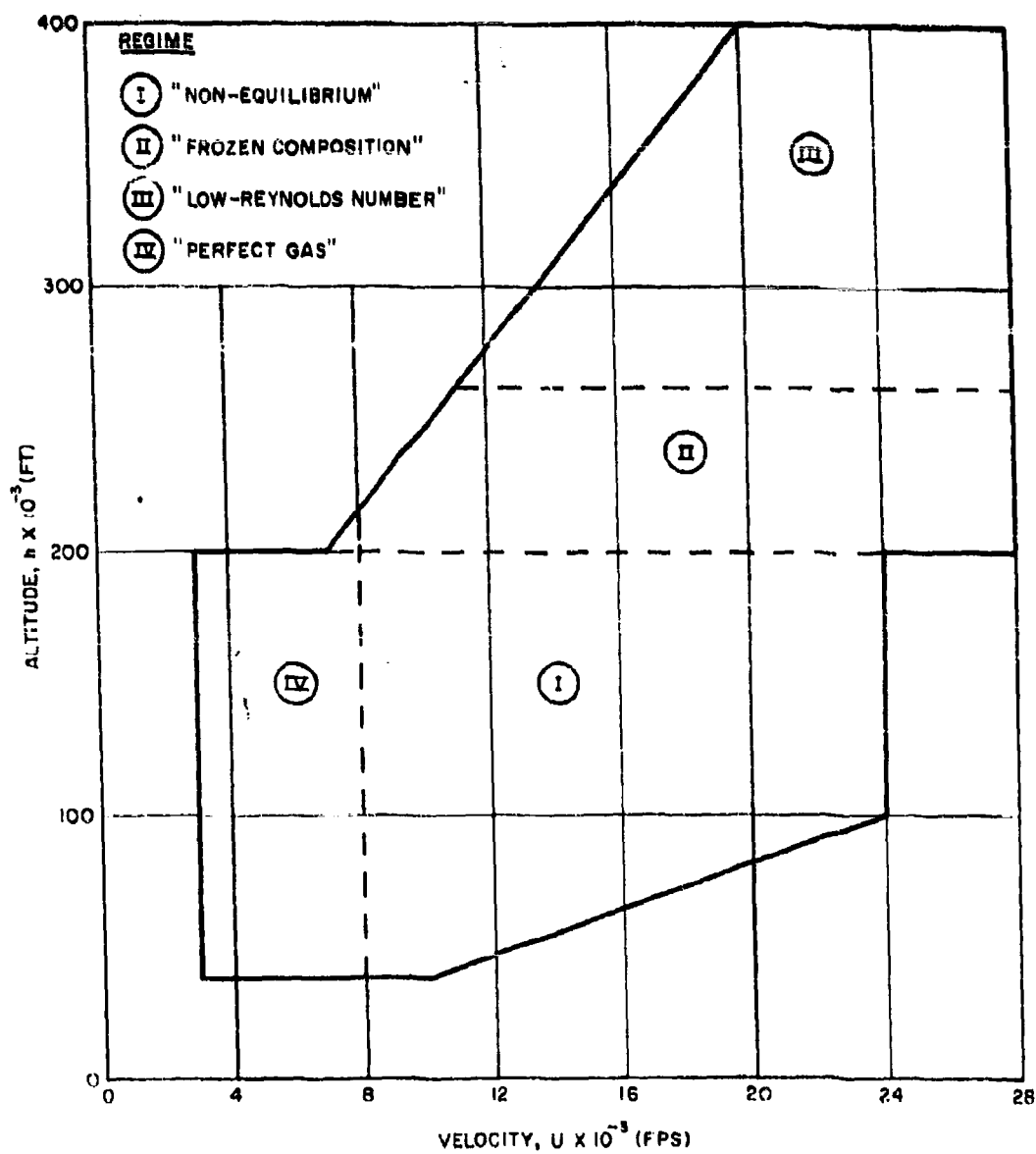


Figure 42. Hypervelocity Simulation Requirements (Blunt Body)

When the use of high-temperature, low-density model testing facilities for non-equilibrium gas flow problems are considered, the nature of the nozzle expansion process must be carefully examined. Indeed, the stagnation conditions required for low-density model testing can give rise to large departures from equilibrium in the nozzle itself. The existence of a departure from equilibrium flow in the nozzle expansion process, and the resultant influence on test section thermodynamic and flow properties, must be quantitatively considered before any meaningful discussion of aerothermodynamic simulation can be made. The influence of dissociative non-equilibrium flow phenomena in a hypersonic nozzle for a stagnation temperature of 8000°K and stagnation pressures between 1 and 1,000 atmospheres was previously discussed and numerical results presented in Figs. 16, 17, and 18. For the more general simulation considerations discussed here, a carpet of the limiting value of the frozen degree of dissociation in the nozzle (α_F) as a function of stagnation temperature and pressure, is shown in Fig. 43.⁵ The range $4000^{\circ}\text{K} \leq T_0 \leq 12,000^{\circ}\text{K}$, $1 \leq P_0 \leq 1,000$ atmospheres, is presented. Therefore, Fig. 43 provides an estimate of the required stagnation conditions to achieve complete equilibrium expansion in the nozzle or to provide a specific frozen degree dissociation for (controlled non-equilibrium expansion) experiments. It can be readily observed from this figure, that the achievement of particle velocity simulation with an equilibrium expansion requires stagnation pressures of the order of 1,000 atmospheres or greater.

With the above simulation and stagnation condition requirements in mind, we will now turn our attention toward consideration of the performance capabilities of the proposed facility.

2. Combustion-Driven Shock Tunnel Performance

The objectives in the proposed design are to attain stagnation pressures greater than 1,000 atmospheres with corresponding stagnation temperatures of $8,000^{\circ}\text{K}$ or higher. This implies that a strong primary shock in the shock tube is required, which can be obtained by using high pressure

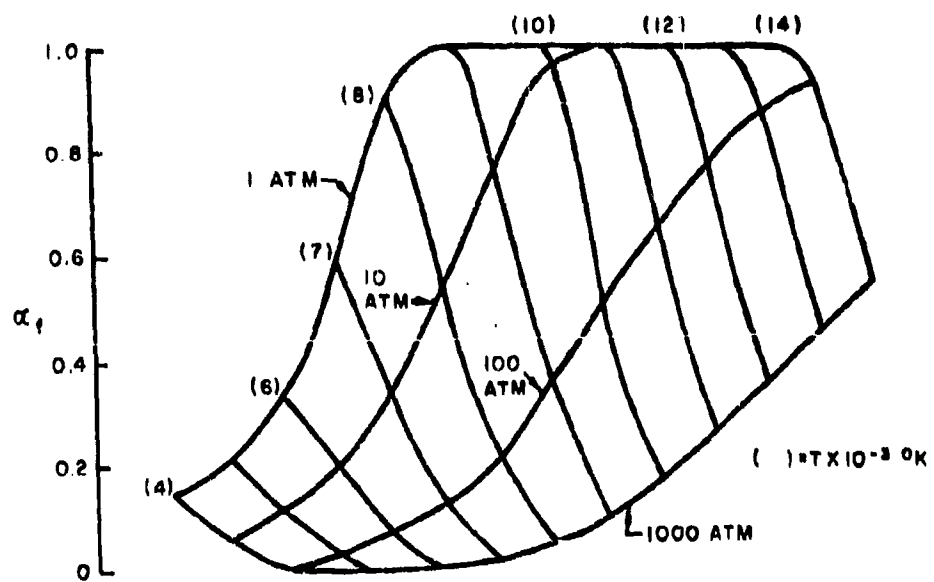


Figure 43. Variation of α_f with Stagnation Conditions: Air

0

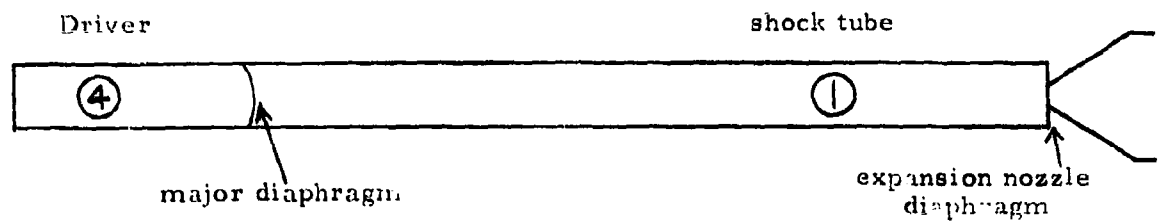
helium in the driver, and a reasonable decrease of driver gas heating. The primary driver gas will then be helium with a stoichiometric mixture of hydrogen and oxygen to supply the energy for heating and to increase the driver gas pressure through a combustion process. In the operation of the combustion driver, however, the helium is regarded as the diluent in suppressing detonation during the combustion process. Thus, a combustion mixture is usually referred to by its helium content in percent of the total volume. Nagamatsu⁴⁰ has performed experiments for hydrogen-oxygen-helium mixtures of various ratios. Detonation was experienced when a 65% helium diluent was used with a stoichiometric mixture of hydrogen and oxygen. Difficulties in igniting the gas were encountered when an 80% helium dilution was used.

In calculating the performance of the shock tunnel, helium is regarded as the driver gas. The product of combustion, vapor of H_2O , is then regarded as the contaminant in the driver gas. Since the water vapor contributes to an appreciable increase in molecular weight of the final gas mixture over that of the pure helium, its effects cannot be ignored completely in the calculations. A detailed study of the combustion process would give an accurate prediction of the driver gas conditions with regard to temperature, pressure, speed of sound, specific heat ratio, etc. A detailed study of this nature in order to be adequate for our present purposes, should trace the expansion process of the driver gas after the shock formation has been initiated. This implies the necessity for the construction of portions of a Mollier diagram for each mixture ratio under consideration, in order that the regions of interest can be adequately covered. For our present purpose, the equilibrium gas temperature, pressure, and specific heat ratio γ were determined at the time when the combustion process was completed. Isentropic expansion of the driver gas was assumed in order to calculate the conditions behind the interface. Four mixture ratios were considered in calculating the driver gas conditions, and subsequently, the shock tunnel performance with regard to stagnation conditions in the region after the reflected primary shock. It is on this stagnation

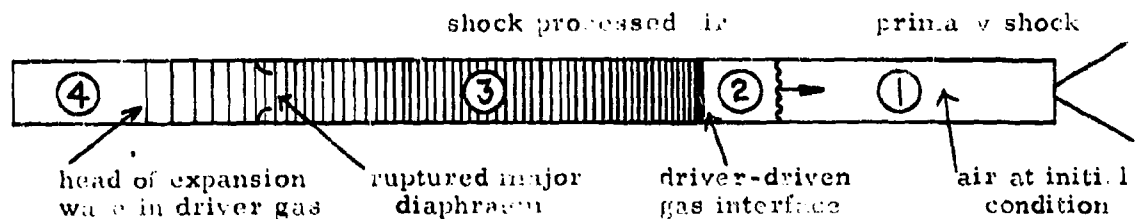
region that our interests will be focused, for this is the reservoir condition to be expanded in a hypersonic nozzle during an experiment.

In the present analysis an ideal shock tube model was chosen for the performance calculation. The following configuration and terminologies are employed:

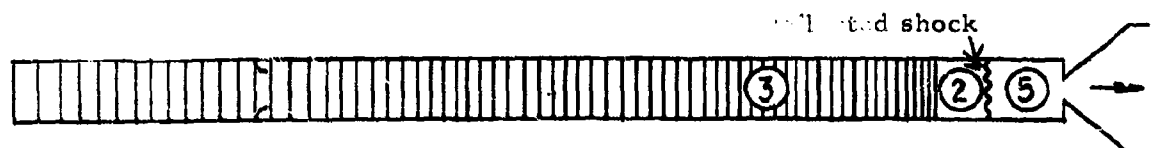
Initial condition



During shock wave propagation



After shock reflection



A brief description of the process involved is in order when formulating the problem. Four mixture ratios were included to cover the possible operating range between no ignition and detonation. A constant volume combustion process was considered. In each case, the driver gas was taken as the gas mixture after complete combustion, assumed homogeneous and at equilibrium. Instant diaphragm removal was considered at a time when the combustion pressure would be at its peak. It was assumed further that the expansion process in the driver gas was isentropic. Using the expression relating the shock tube pressure ratio to the primary shock Mach number we have

$$\frac{p_4}{p_1} = \frac{p_2}{p_1} \left(\frac{p_4}{p_3} \right) = \frac{p_2}{p_1} \left[1 - \frac{\gamma_4}{a} \left(\frac{a_1}{a_4} \right) M_s \left(1 - \frac{p_1}{p_2} \right) \right]^{-a} \quad (152)$$

where

$$a = \frac{2\gamma_4}{\gamma_4 - 1}$$

by taking γ_4 equal to some constant, the pressure ratio can be readily obtained for a given shock Mach number. Figure 44 is a plot of Eq. (152) for the four mixture ratios. During this analysis, extensive use was made of the hypersonic gas dynamic charts for equilibrium air by Feldman.⁴¹

After selecting the shock Mach number, M_s , various parameters with regard to pressure and temperature, etc., can be obtained for different regions in the shock tube. A plot of the reservoir conditions versus shock Mach number is given in Fig. 45. Figure 46 is a graph of the tunnel reservoir conditions for different shock tube initial conditions.

By superimposing the shock tube conditions onto the chart for the non-equilibrium regime, the region of coverage can be obtained. This coverage is presented in Figs. 47 and 48.

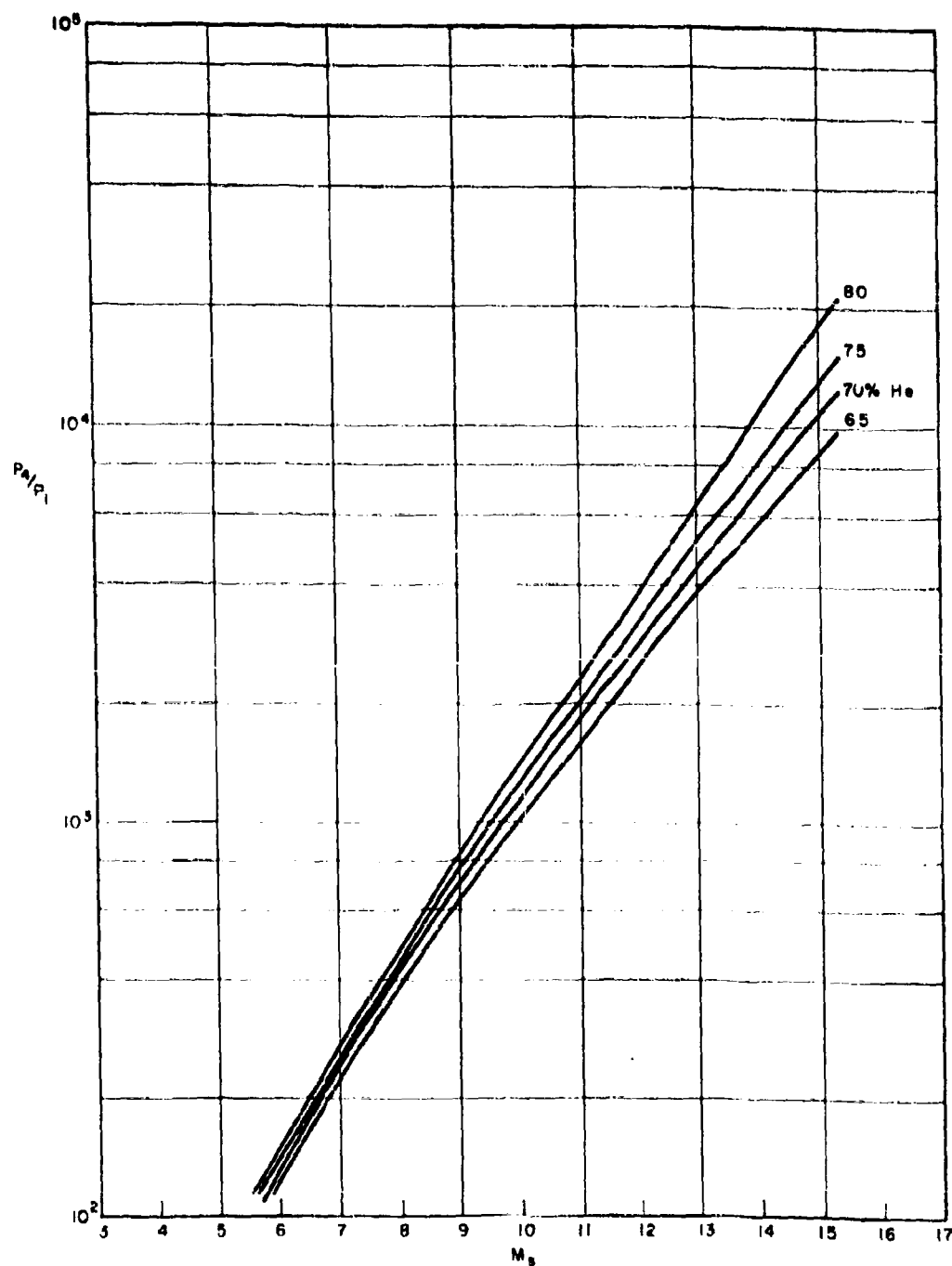


Figure 44. Combustion-Driven Shock Tube Performance as a Function of Percent Helium Diluent in the Stoichiometric Mixture of Hydrogen and Oxygen (plot of Eq. 152)

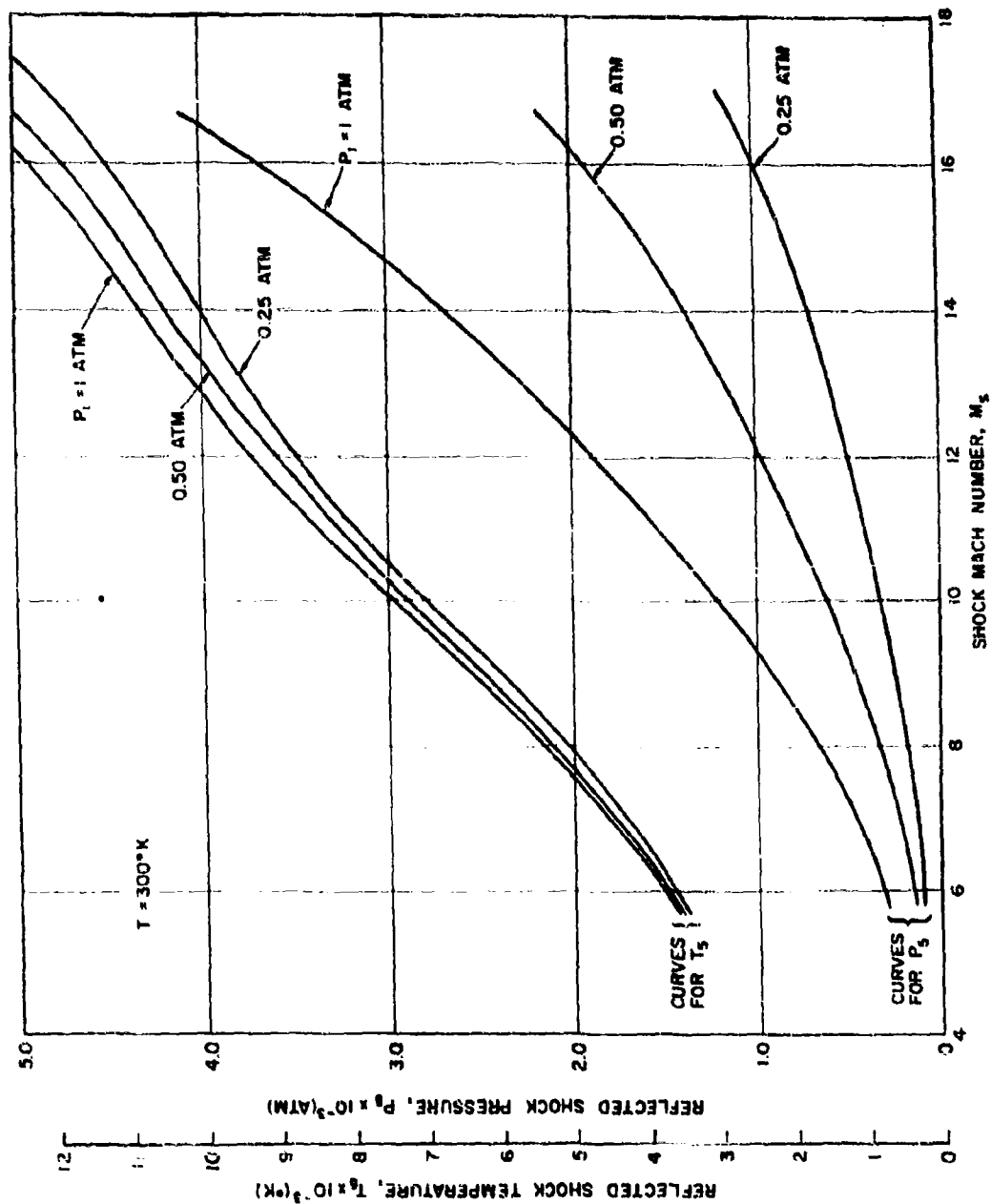


Figure 45. Reservoir Conditions as a Function of Shock Mach Number

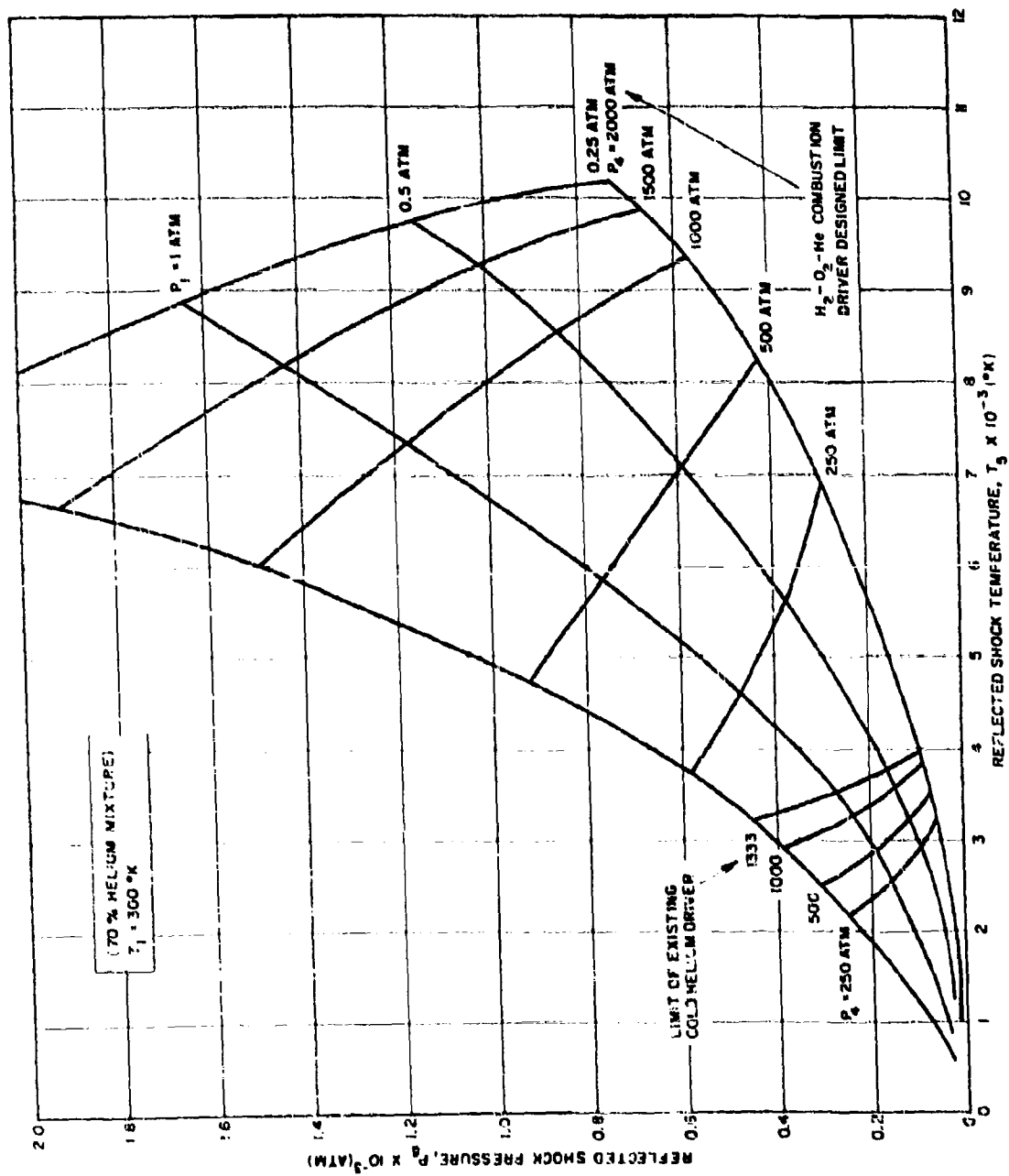


Figure 46. Reservoir Conditions as a Function of Varying Shock Tube Initial Conditions

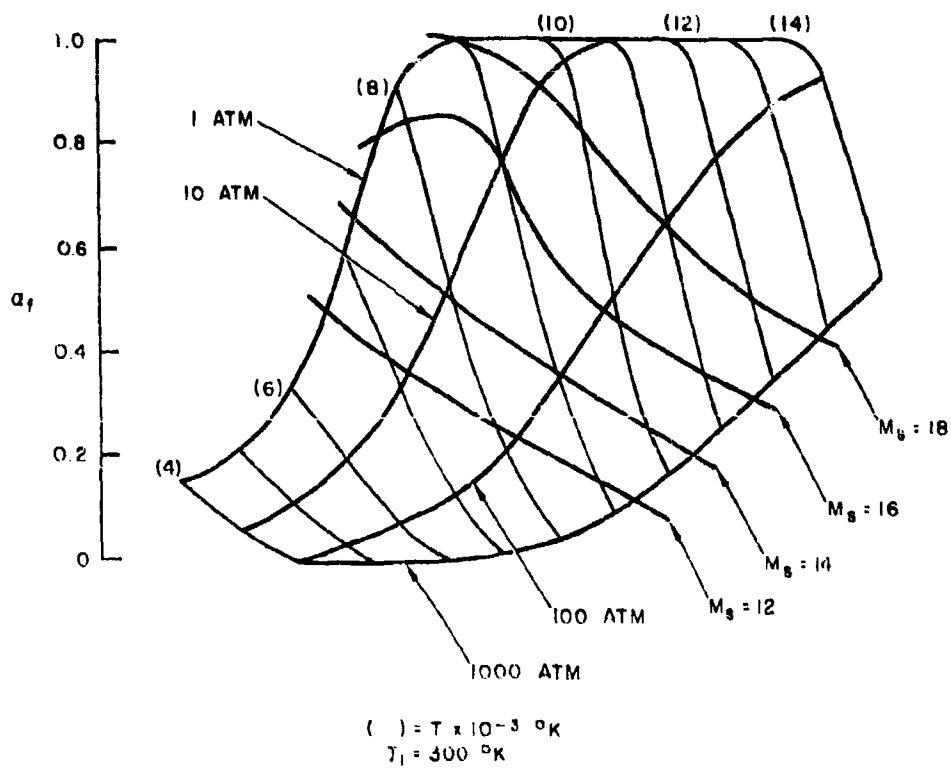


Figure 47. Variation of a_f with Stagnation Conditions for Air
 Showing Region of Coverage with Shock Mach Numbers
 Attainable in the Shock Tube

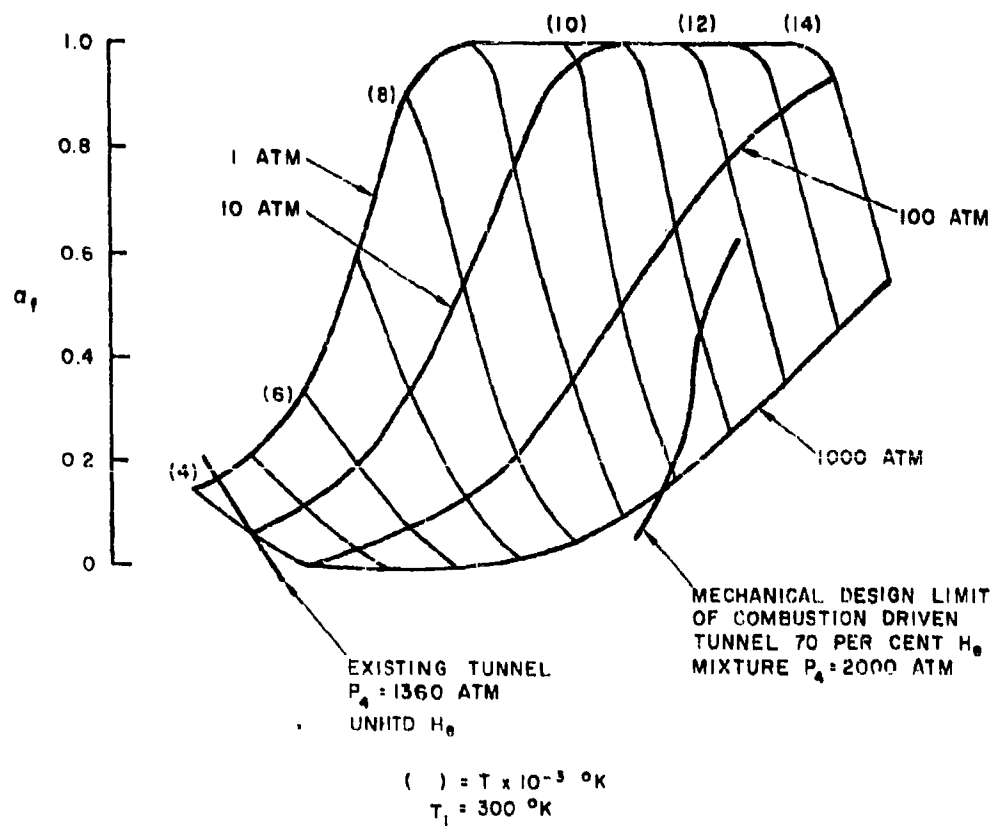


Figure 48. Variation of a_r with Stagnation Conditions for Air Showing Limit of Combustion-Driven Shock Tunnel

Calculations for a shock tunnel, using pure hydrogen as the driver gas, is given in Fig. 49 as a comparison. Hydrogen is very efficient for use as a driver gas; however, its inherent dangerous handling characteristics make it unattractive for use in the present facility.

a. Area Ratio Effect in Shock Tunnels

The preceding analysis was appropriate for an ideal shock tube with constant area throughout. For shock tunnels having unequal driver and driven tube diameters and a throat section at the diaphragm location, the performance calculated previously would be modified to compensate for area ratio effect and the restriction at the throat. A shock tube with such a restriction is given schematically (see Fig. 50). The effective pressure ratio for such a configuration would be⁴²

$$\left(\frac{P_4}{P_1}\right) = \frac{P_4}{P_{3a}} \frac{P_{3a}}{P_{3*}} \frac{P_{3*}}{P_{3b}} \frac{P_{3b}}{P_3} \frac{P_3}{P_2} \frac{P_2}{P_1}$$

$$= \frac{1}{g} \frac{P_2}{P_1} \left[1 - \frac{\gamma_4 - 1}{\gamma_1 + 1} \frac{a_1}{a_4} M_3 \left(1 - \frac{P_2}{P_1} \right) g^{-\frac{1}{\alpha}} \right]^{-\alpha} \quad (153)$$

where

$$g = \left[\frac{2 + (\gamma_4 - 1) M_{3a}^2}{2 + (\gamma_4 - 1) M_{3b}^2} \right]^{\frac{\alpha}{2}} \left[\frac{2 + (\gamma_4 - 1) M_{3b}^2}{2 + (\gamma_4 - 1) M_{3a}^2} \right]^{\alpha} \quad (154)$$

is the gain factor modifying the actual pressure ratio to an effective pressure ratio. With the boundary conditions such that $M_{3*} = 1$ and if A_{3a}/A_{3*} is given, then M_{3a} can be obtained by solving the equation

$$\frac{A_{3a}}{A_{3*}} = \left[\frac{2 + (\gamma_4 - 1) M_{3a}^2}{2 + (\gamma_4 - 1) M_{3*}^2} \right]^{\frac{\gamma_4 + 1}{2(\gamma_4 - 1)}} \frac{M_{3*}}{M_{3a}} \quad (155)$$

C

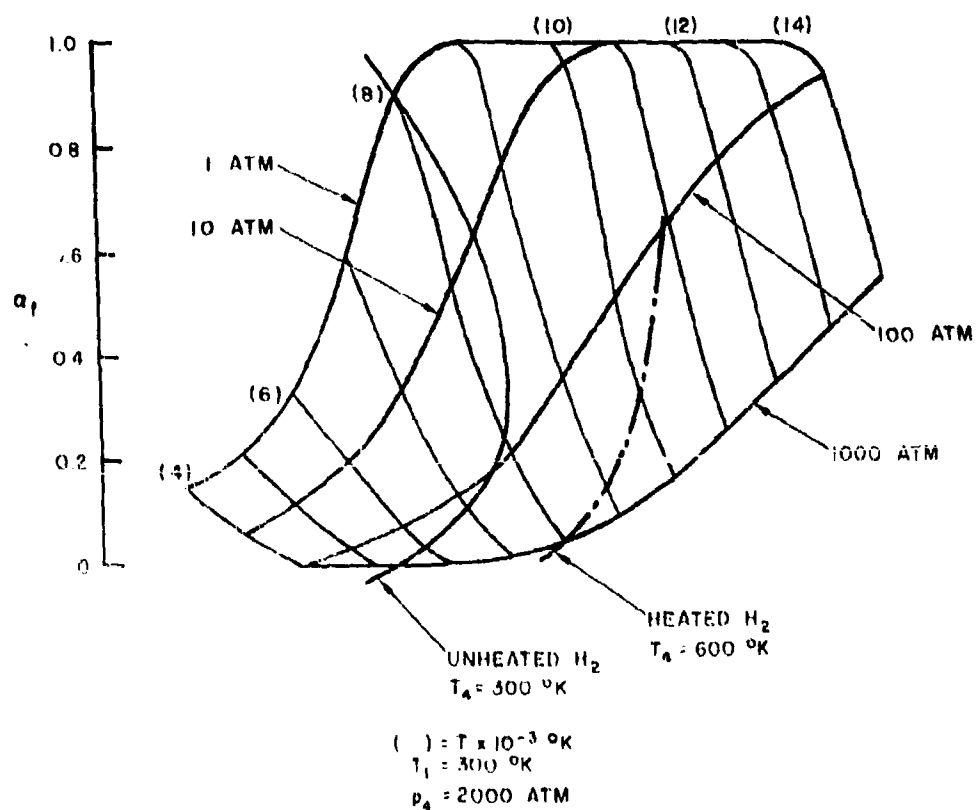


Figure 49. Variation of a_f with Stagnation Conditions for Air.
Region of Coverage Using Pure Hydrogen as the
Driver Gas is Indicated

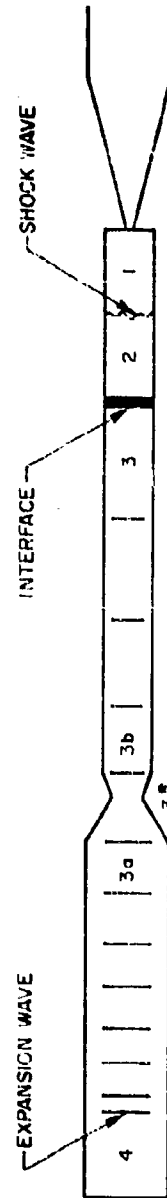


Figure 50. Schematic Diagram of Shock Tunnel with a Converging Divergent Diaphragm Section

Again, M_{3b} can be obtained by solving the following equation:

$$\frac{A_{3*}}{A_1} = \left[\frac{2 + (\gamma_4 - 1)}{2 + (\gamma_4 - 1) M_{3b}^2} \right]^{\frac{\gamma_4 + 1}{2(\gamma_4 - 1)}} M_{3b} \quad (156)$$

A plot of the gain factor g versus diameter d_4 is given in Fig. 51 where a fixed ratio $d_1/d_{3*} = 1.5$ is used (existing configuration for the Aerospace Corp. shock tunnel).

b. Shock Tunnel Testing Time

The testing time for a hypersonic shock tunnel is determined by the length of time that the reservoir pressure remains constant after the primary shock has been reflected from the end of the shock tube. Theoretically, this time interval is the time difference between the primary shock arrival at the end of the shock tube and the reflection of the first reflected shock wave at the interface.

The ideal testing time for a non-tailored shock tunnel is a function of the shock wave speed, shock tube length, and given initial conditions. Figure 52 shows a plot of the testing time as a function of shock Mach number with driven tube length as a parameter. The limit for a different driver length is also indicated. The significance of this limit is that for a given driver section tube length the test time will decrease progressively as the shock Mach number is decreased below the limit. Since ideal conditions will not be encountered in practice, the actual testing time will be some fraction of the ideal testing time. A rough rule of thumb gives this fraction to be approximately 0.5.

Figure 53 shows the regime for tailored operation⁴³ at different reservoir conditions with shock tube initial conditions as parameters. Figure 54 shows the driver pressure versus shock Mach number with the shock tube initial conditions as parameters.

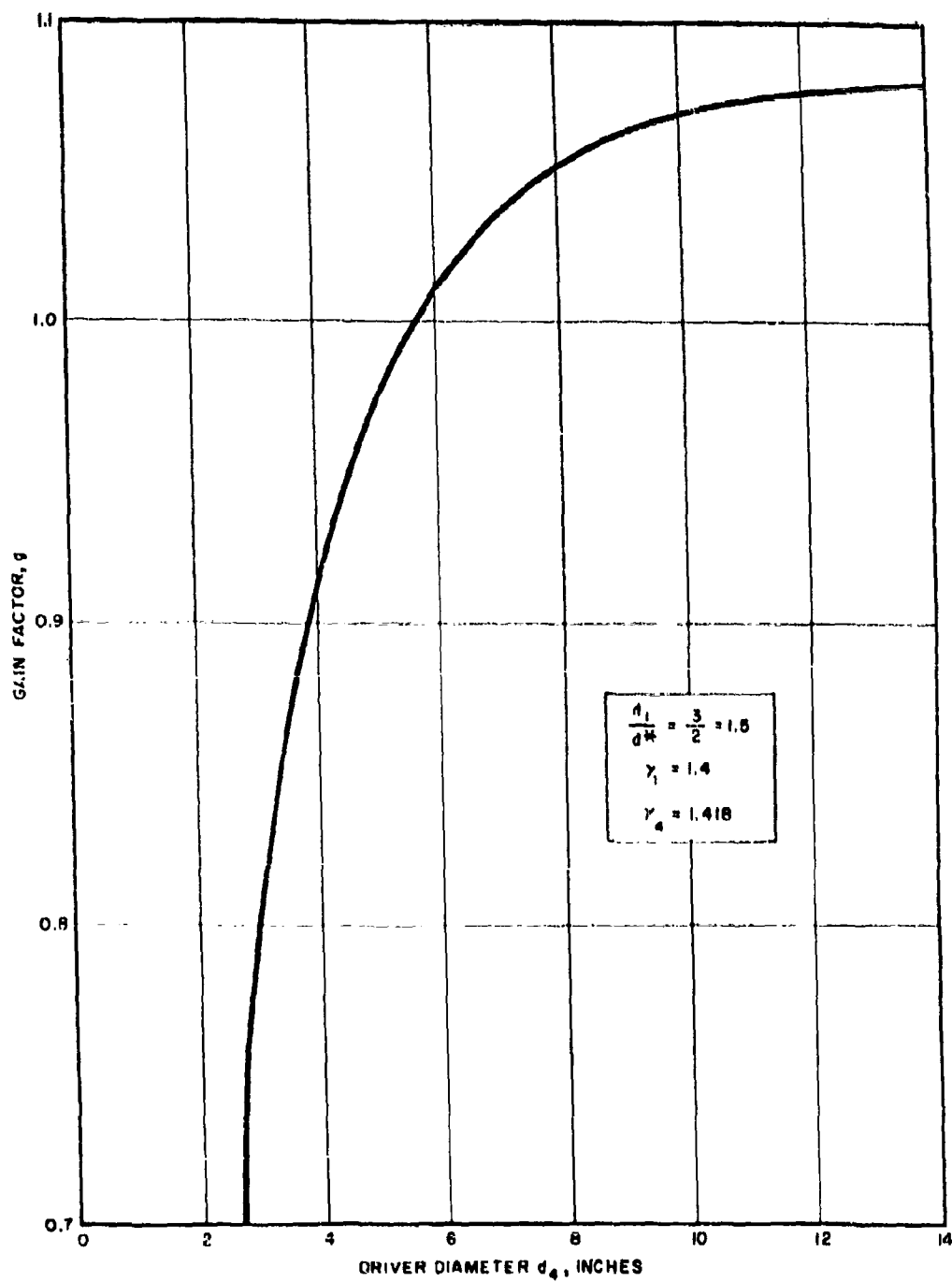


Figure 51. Gain Factor vs Driver Diameter, for Fixed Throat and Driver Tube Diameter (Existing Shock Tunnel)

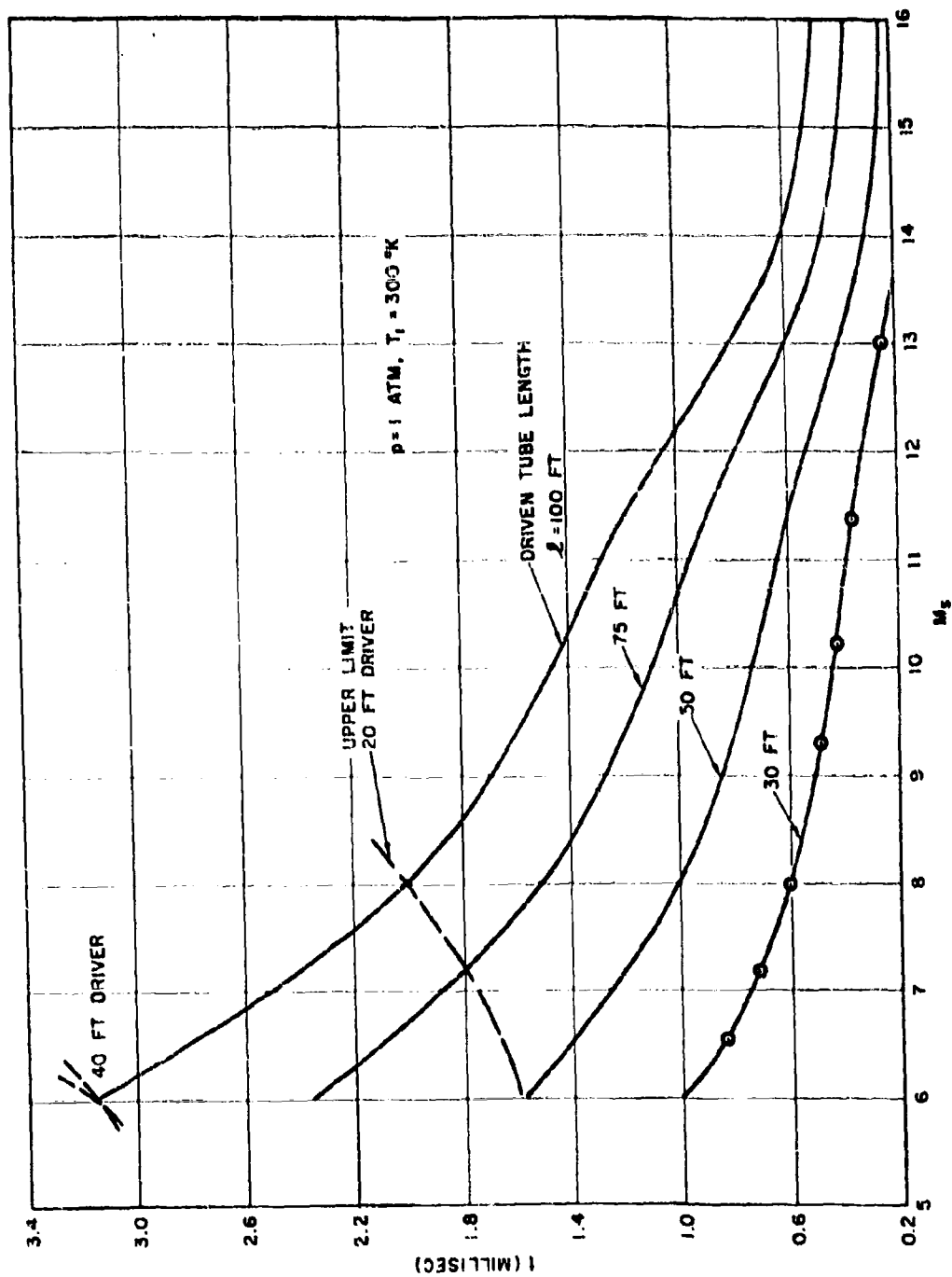


Figure 52. Testing Time for Non-tailored Combustion-Driven Shock Tube, 70% Helium

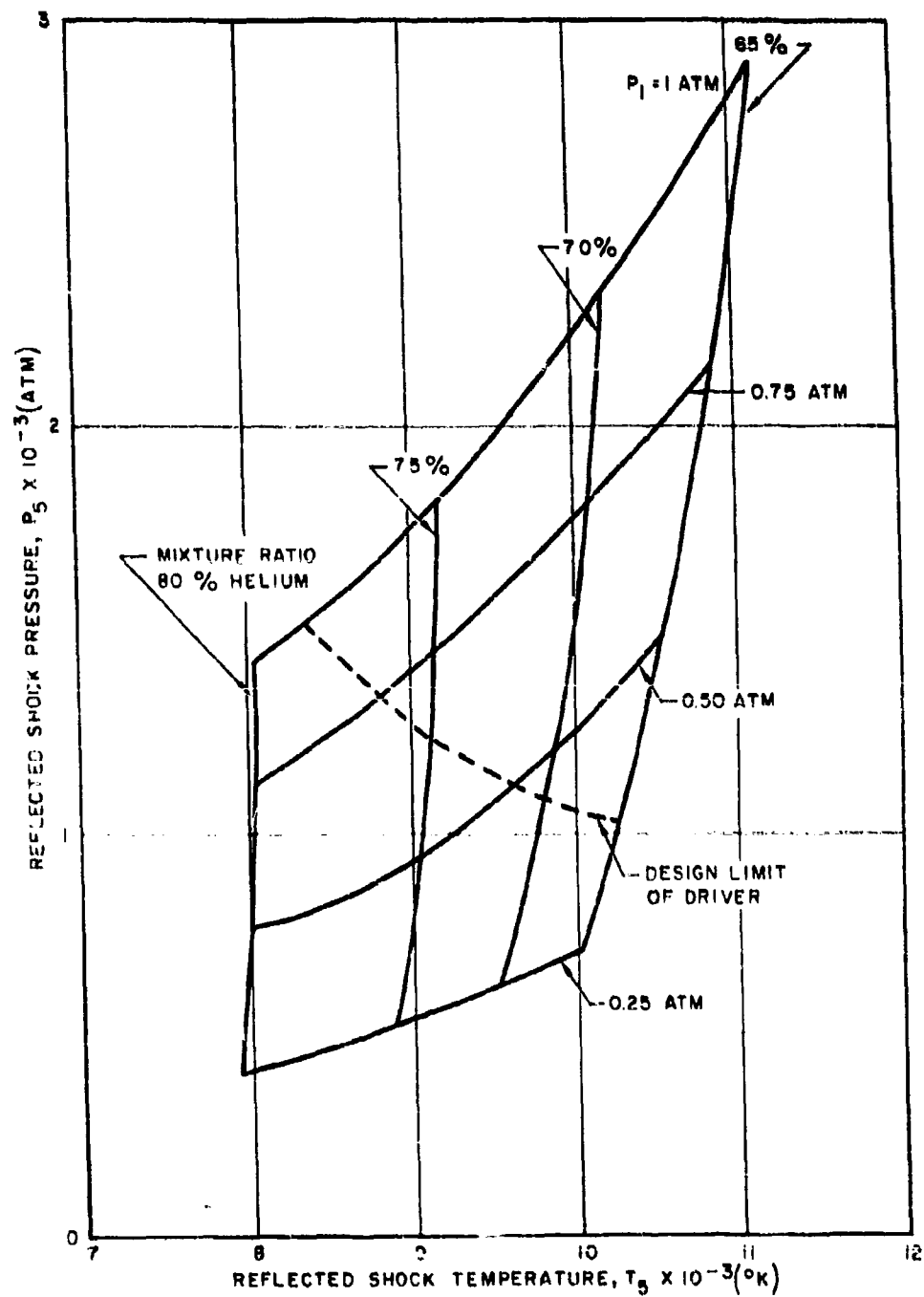


Figure 53. Tailored Interface Operation for the Combustion-Driven Shock Tunnel ($P_s \sim T_s$)

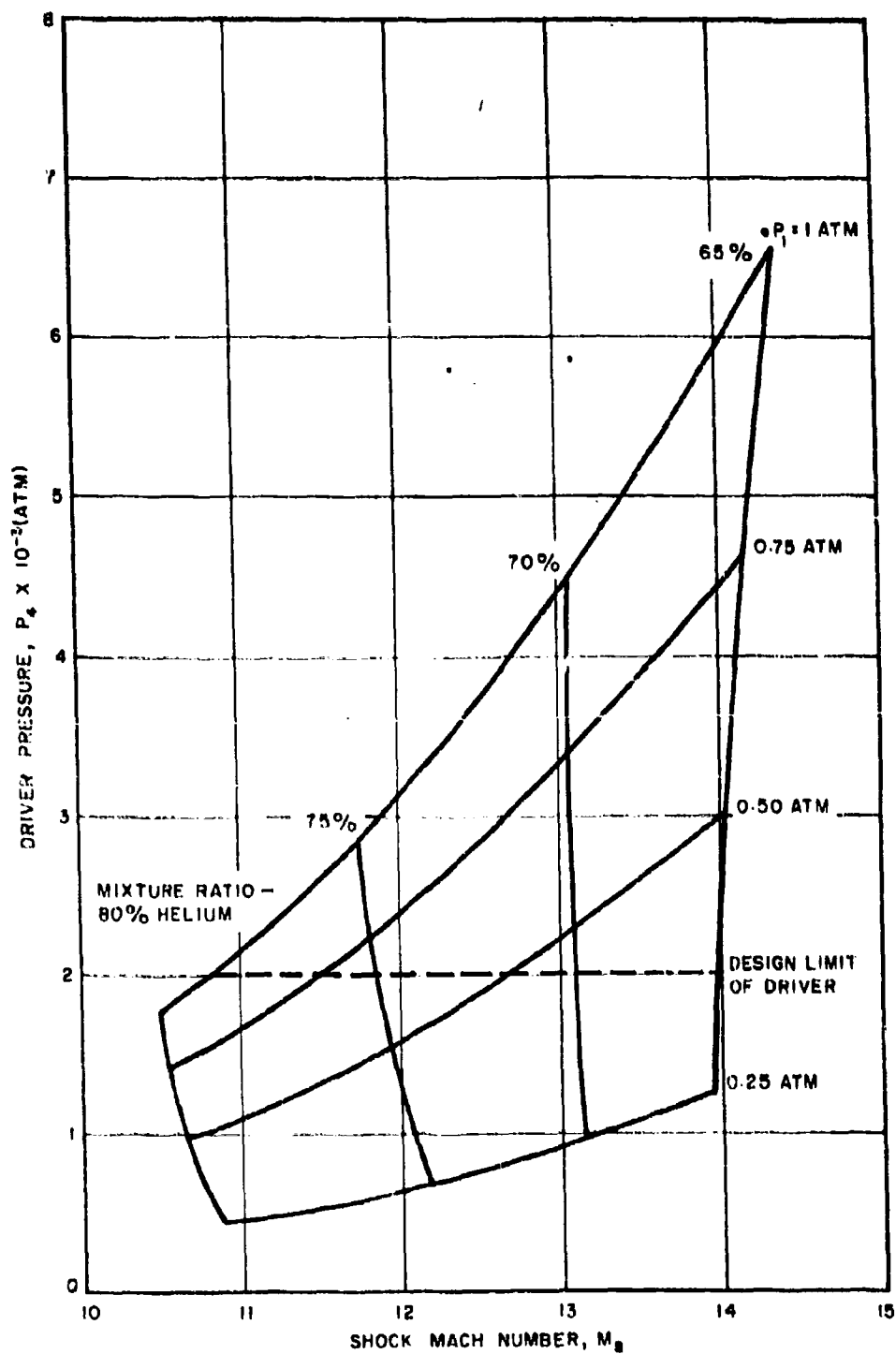


Figure 54. Tailored Interface Operation for the Combustion-Driven Shock Tunnel ($P_4 \sim M_8$)

The calculation so far has been applied to a stoichiometric mixture of hydrogen and oxygen with various percentages of helium diluent. It is theoretically feasible to extend the tailoring regime by adding one or more gases of different molecular weight to the combustible mixture.⁴⁴ Such a possibility can be explored for combustion-driven operation should it be desired.

Figure 55 shows the tailoring regime superimposed on a chart of the reservoir conditions. The upper limits of a non-tailored tunnel operation, having a 1-3/4 millisecond testing time, are indicated for various driven section lengths. Figure 56 is a plot of the theoretical ideal testing time possible for tailored operation, as a function of primary shock Mach number, with driven section tube length as a parameter. The limiting line of zero advantage of tailoring is indicated for a 20-foot driver. This means that tailoring will be useful only above certain shock Mach numbers if the tube length is given. It is also noted that the usefulness of tailoring will be more pronounced for shock tunnels with short driven section tube lengths.

c. Test Section Conditions

Once the conditions behind a reflected shock have been established, the flow parameters, as a function of nozzle expansion ratio, may be determined by means of techniques discussed in II. A. These calculations have been made for reflected shock conditions which may be attained by the combustion driver. All the test conditions possible will not be presented here, but rather, the results for high enthalpy reservoir conditions are presented (Fig. 57). In this figure, the Mach number is presented as a function of nozzle expansion ratio for a stagnation pressure of 1000 atmospheres and a stagnation temperature of 8720°K. The results are presented for both an assumed equilibrium expansion and the non-equilibrium expansion as predicted by the analysis outlined in II. A. The non-equilibrium expansion will freeze out approximately 11 percent of stagnation enthalpy in the nozzle expansion process. From this figure, it can be observed that the Mach number for the assumed equilibrium expansion is approximately

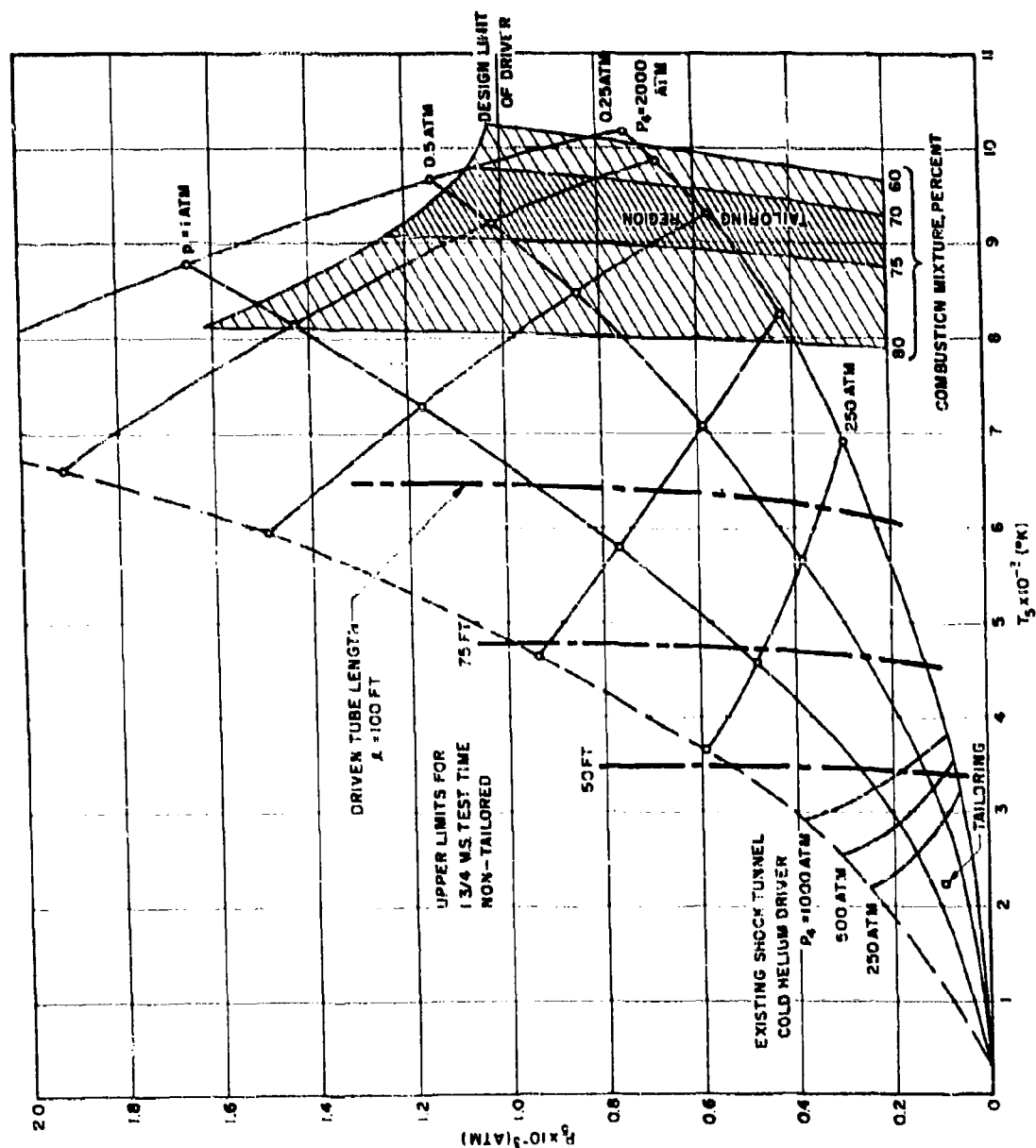


Figure 55. Reservoir Conditions as a Function of Varying Shock Tube Initial Conditions with Tailored Region Superimposed

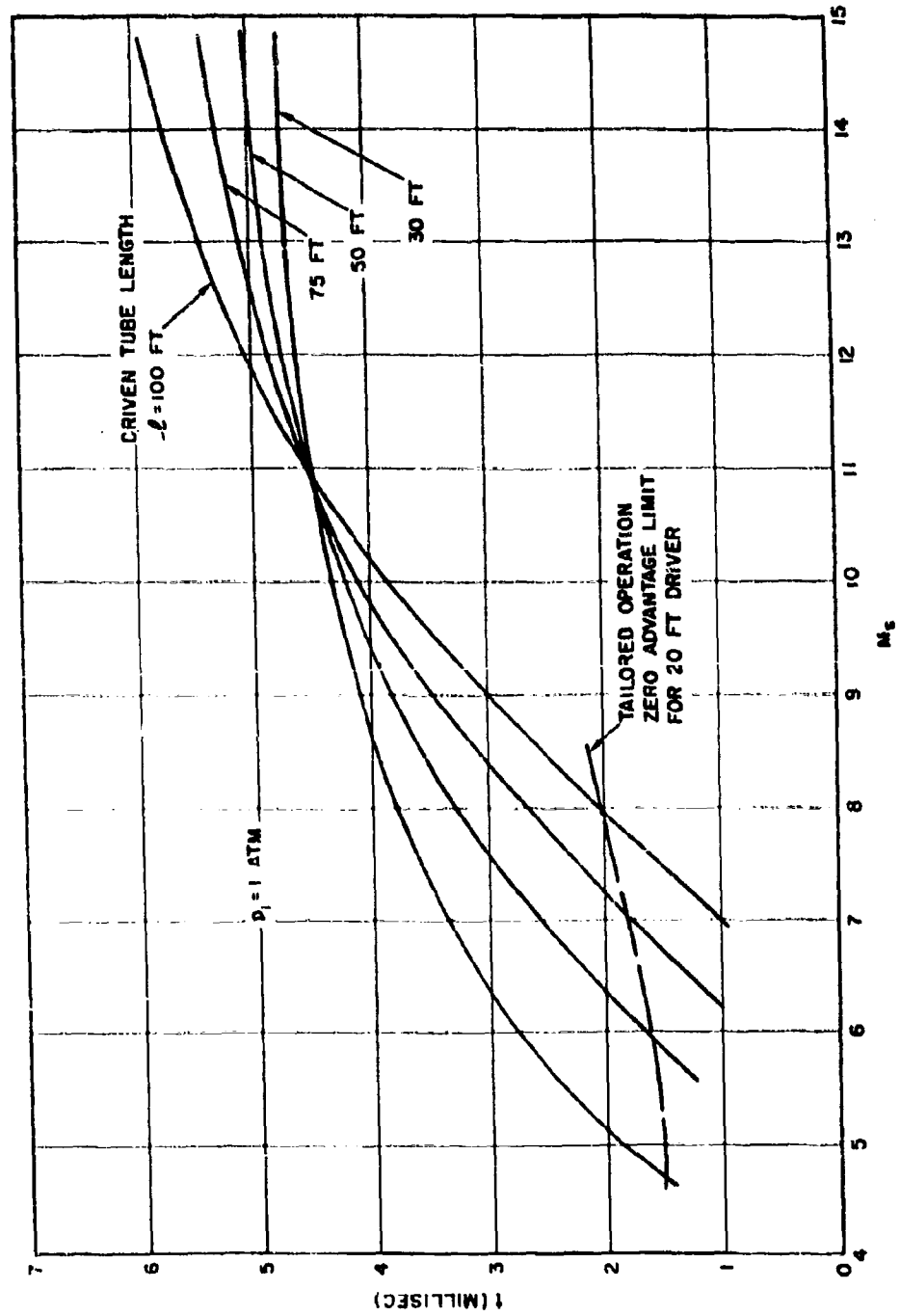


Figure 56. Tailored Shock Tube Testing Time, Combustion Driver, 70% Helium

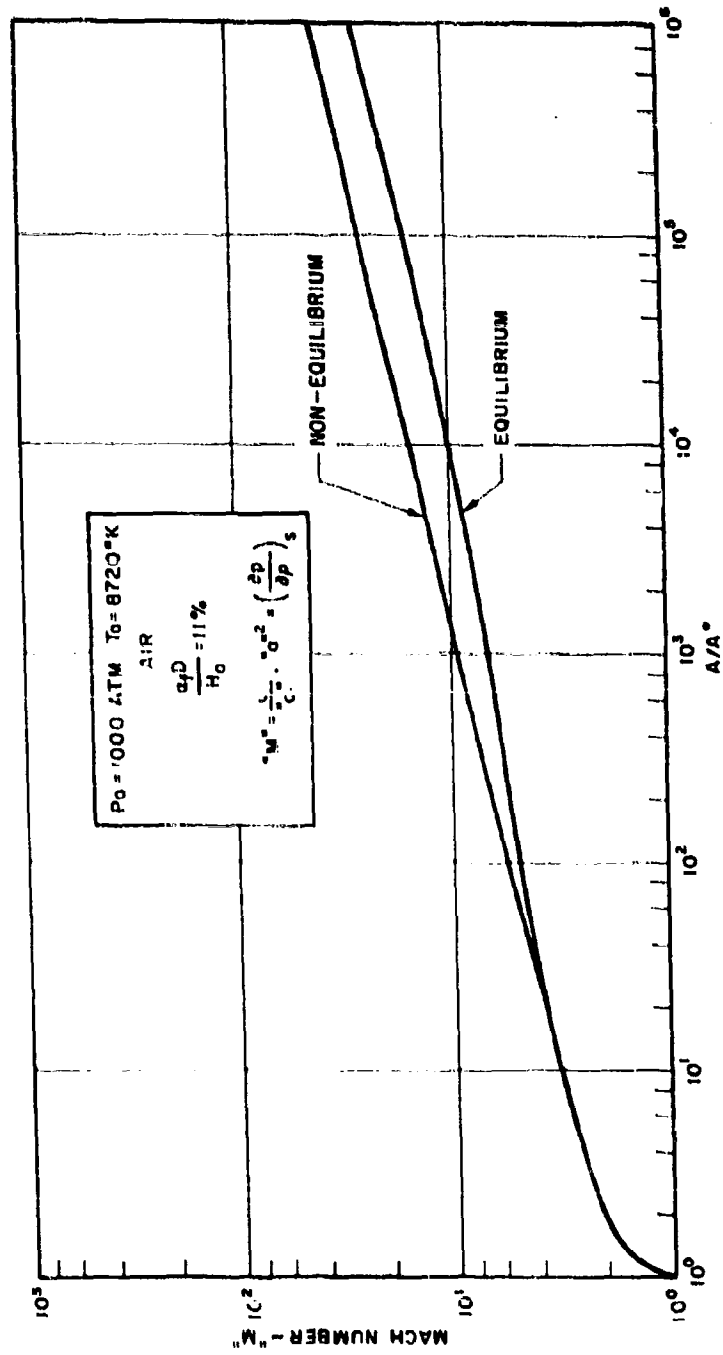


Figure 57. Mach Number vs Area Ratio for Equilibrium and Non-equilibrium Expansion

27 at an expansion ratio of 10^6 , while the corresponding non-equilibrium Mach number is approximately 40. The expansion ratio of 10^6 will be attainable in the modified facility as a result of the inclusion of a six-foot diameter nozzle (the nozzle design and detailed modification is presented in the next section, "Description of Modified Facility"). The performance shown in Fig. 57 will allow experimental investigation of the use of controlled non-equilibrium expansions discussed in II. A. The particle velocity at this condition will be approximately 19,300 feet per second. The Reynolds number and density altitude simulation at this expansion ratio (10^6) corresponds to flight at approximately 300,000 ft. This condition is, therefore, ideal for investigating both low Reynolds number and dissociative non-equilibrium flow phenomena.

d. Design Considerations for the Combustion-Driven Shock Tunnel

In designing the Aerospace Corporation combustion-driven shock tunnel, the foregoing analysis was applied to determine the final configuration. Peripheral factors, however, such as available laboratory space, played important roles in the over-all consideration. Compromises have had to be made with regard to the ultimate in performance as against a more practical design limited by mechanical or economical considerations.

The configuration arrived at is a shock tunnel having a driver section length of 20 feet and a driven section length of 30 feet. While both sections have an inside diameter of three inches, the major diaphragm location has a neck down region with a diameter of two inches.

The advantage in using a smaller diameter on the diaphragm station is apparent when mechanical properties of the diaphragm are taken into consideration, since a larger diameter diaphragm is relatively unreliable, especially at the high pressures under consideration. The present diaphragm, which has been well developed in use, will be retained in the new configuration. From a gasdynamics standpoint, a throat would introduce a local steady flow process which would alleviate, to some extent, the expansion wave propagation from the driver towards the end of the shock

tube. This effect would tend to increase the test time of the shock tunnel. The designed driver operating pressure is 2000 atmospheres, with allowance for a factor of five increase in the operating pressure in the event of detonation. An over-all safety factor of 1.1 is then used to calculate the ultimate yield strength of the driver. The driven section was designed to withstand an internal pressure of 20,000 psi. Since laboratory space is restricted, a 30-foot driven section length was chosen. Tailored operation is employed to obtain adequate testing time for most instrument responses. Maximum use is made of the existing shock tunnel hardware. The intended driver gas mixture ratio to be used is between 70 and 75 percent helium. Within the tailored operation regime the maximum stagnation pressure, after the reflected shock, is approximately 1250 atm. The maximum stagnation temperature is approximately 9800°K, and a theoretical testing time of about four milliseconds is anticipated.

3. Description of Modified Shock Tunnel Facility

a. Introduction

The new tailored combustion-driven shock tunnel is being constructed in order to achieve the high stagnation temperatures and pressures and the required test times specified in Sections III C 1 and III C 2 of this report.

According to the length requirements specified in Section III C 2, a new driver, 20 feet long and three inches in diameter, is to be constructed. The driven section will consist of the three sections of the cold helium driven shock tube (30 feet). A new nozzle and a six-foot test section is to be constructed, utilizing the existing vacuum dump tank. Two cylindrical extensions will be added to the vacuum tank. The nozzle will be fabricated of plastic sections of varying lengths in order to permit flow Mach number variation. The nozzle and test section are enclosed in the dump tank. The design Mach number range is from 16 to 32. A schematic of the shock tunnel facility, as it will be installed in the laboratory building, is shown in Fig. 58. A detailed description of the driver section and gas handling

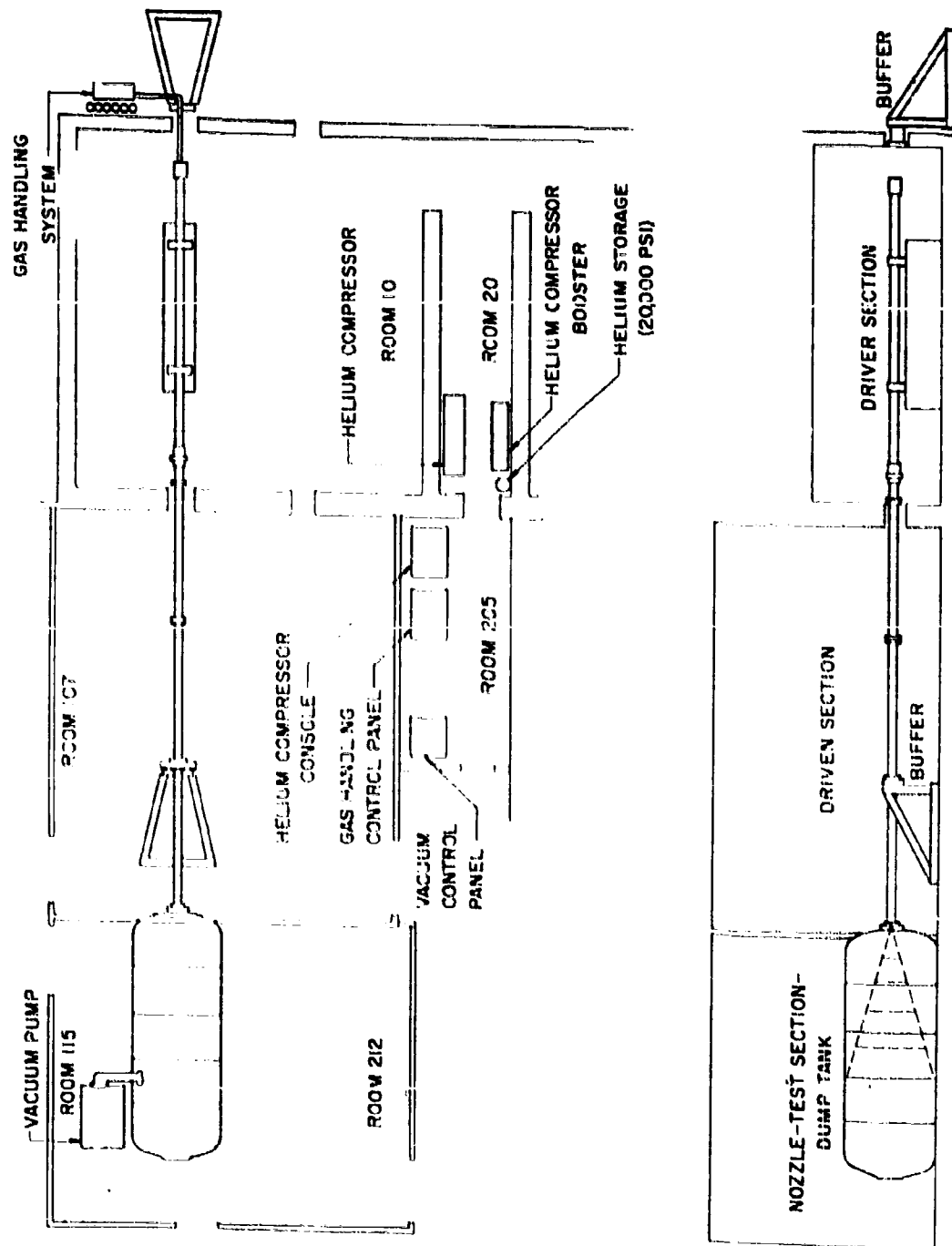


Figure 58. View of Shock Tunnel Showing 12-inch Test Section

system, the driven section, and the nozzle test section dump tank is given below:

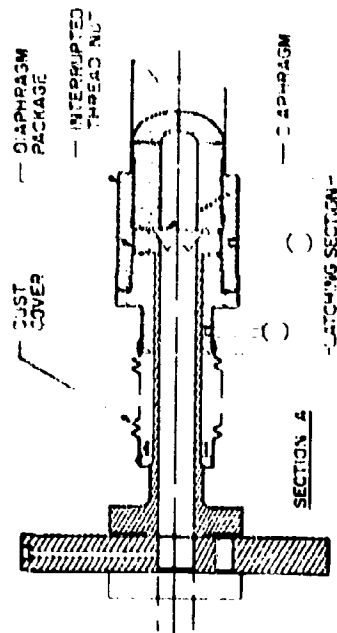
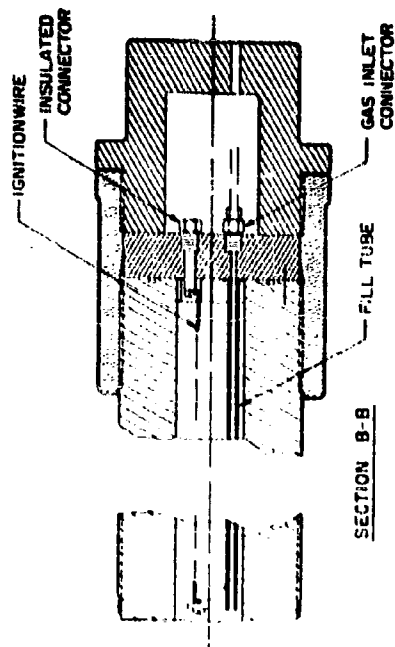
b. Driver Section and Gas Charging System

Due to the possibility of detonation of the combustion mixture, the driver section is designed for an ultimate pressure of 165,000 psi. The working pressure, in general, will not exceed 30,000 psi. The temperature is expected to reach between 2000° and 3000° K, but it is transient, as is the high combustion pressure.

In order to meet these requirements, the driver section and its closely associated fittings will be fabricated from forged 300M steel and heat treated after rough machining to maximize the effectiveness of the heat treating. The vessel, cap hatching mechanism, and diaphragm package are detailed in Fig. 59.

The gas handling system for loading the driver with a combustible mixture of oxygen and hydrogen, diluted with helium, is shown schematically in Fig. 60. A gas accumulator, with a volume equal to that of the driver section, acts as a fast high-pressure hydrogen pump. A stoichiometric mixture of hydrogen and oxygen diluted with 75 percent helium, at a total pressure of 4000 psi before combustion, is used. Oxygen is pumped into the driver section from the storage marked O_2 to a pressure of 330 psi. Helium is then added until a pressure of 3330 psi is reached. Then hydrogen is pumped into the hydrogen accumulator to a pressure of 660 psi. Helium gas then passes into the accumulator behind the piston. As the helium is stored at very high pressures (15,000 - 20,000 psi), it forces the hydrogen into the driver. This sequence of loading never permits a mixture of hydrogen and oxygen to exist in richer concentrations than the mixture to be employed in the test. Hence, the probability of detonation occurring during the filling process is low.

Proper distribution and circulation of the driver charge is obtained by using a long ported stainless steel tube inside the driver to serve as the fill tube. The port area varies exponentially along the tube,



NOTE LATCHING SECTION INCLUDING NUT SLIDES BACK FOR ACCESS TO DIAPHRAGM PACKAGE

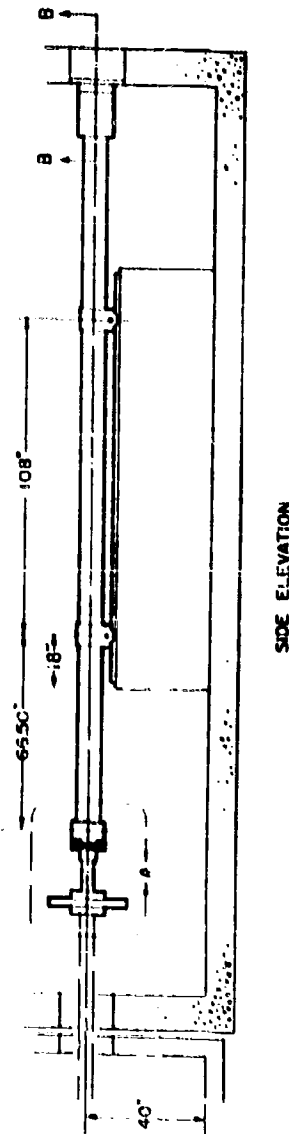


Figure 59. Driver Section Assembly Showing Diaphragm Latch Mechanism, Fill-Circulating Tube and Initiating Wire

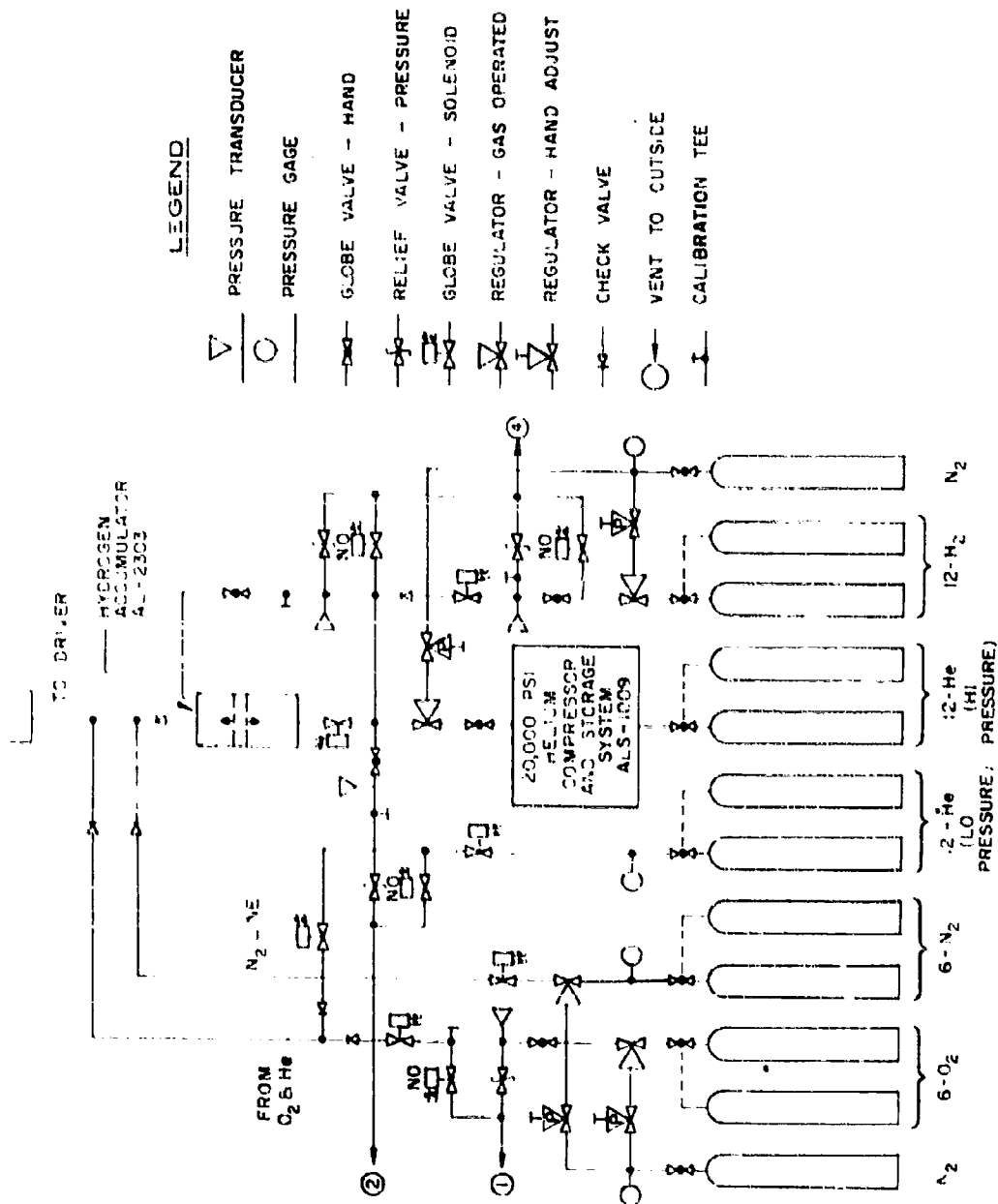


Figure 60. Gas Handling System for Charging the Driver Section

being greatest at the end of fill tube. In this way, the gas enters the driver section uniformly along the entire length. After the driver is charged, the gas is ignited by exploding a long, thin (0.0015 in.) copper wire alloy parallel to and above the fill tube. The insulated high voltage terminal is in the end cap and the fill tube acts as a ground return. The wire is exploded by the discharge of a 5 mfd capacitor charged to 30,000 volts. The exploding wire method was chosen as the most reliable ignition technique. Pilot experiments show that spark plugs fail to operate satisfactorily at the high initial pressure of the driver charge. The driver vessel thus requires no spark plug ports in the side walls, reducing design complexity.

The diaphragm shown in Fig. 61 is inserted into its package and fitted in place against the driver. The locking nut with interrupted threads slides into position on the driver and is rotated into the closed position. The "O" rings around the diaphragm package insure innate sealing. After the diaphragm and ignition wire are installed and the driver charged with gas, the shock tube is ready to fire. When the gas mixture has burned, a mixture of 82 percent helium and 18 percent water vapor forms the driver gas.

c. Driven Section

The new driven section consists of the existing driven section and the existing driver, resulting in a total driven section 30 feet in length. This unit is moved forward six feet to a new position and the main buffer or anchor to fix the position of the shock tube is fastened as shown in Fig. 58. All pressure ports used in the existing shock tube are available for the instrumentation of the drive section with the exception of the last downstream position. This provides the vacuum pump connection for operating the driven section at initial pressures of less than one atmosphere.

d. Tunnel and Test Section

Beyond the buffer plate which immobilizes the driven section, a straight length of shock tube acts as a mechanical transition section for

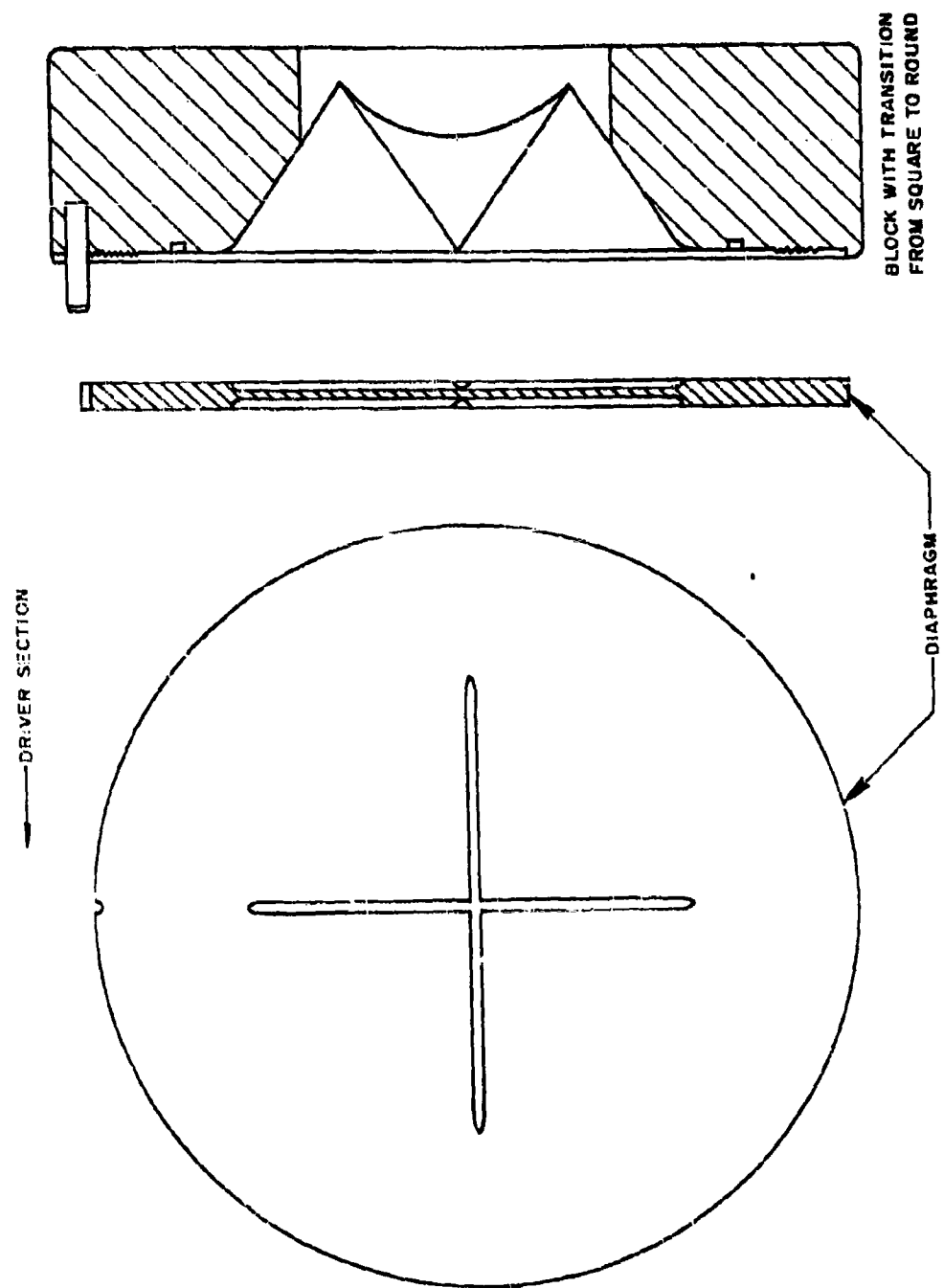


Figure 61. Diaphragm and Diaphragm Package

connecting to the tunnel (Fig. 58). The nozzle consists of a two-inch thick plate containing the throat block which is bolted directly to the dump tank. The conical expansion section and the test section are contained entirely in the vacuum dump tank (Fig. 62). The nozzle sections do not encounter the pressure load of an evacuated chamber.

The 30° conical nozzle is formed by truncated cones of varying lengths. The flow Mach number is thus changed by adding or removing sections. The "test section" is thus the exit of the largest truncated conical section. A reinforced plastic laminate is used to fabricate the nozzle sections. In order to accommodate the nozzle and test section, the dump tank is enlarged by adding two midsections to the dump tank.

The end section of the dump tank is mounted on tracks and permitted to slide open, allowing easy access to the model and internal instrumentation. Ten-inch openings in the dump tank, at points corresponding to the test section of each truncated cone, are provided for schlieren or other observation. The model support enters the dump tank at the first opening downstream of the test section window. The model support is separated from the tunnel structure and sealed by a rubber diaphragm where it enters the dump tank as in the existing shock tunnel.

e. Conclusion

The new hypersonic shock tunnel with the combustion driver will provide the increased capability required to support present and future AF systems. The reservoir stagnation condition will be increased from a maximum of 3200°K and 250 atm to 9800°K and 1600 atm. This corresponds to an increase in the flow velocity at the test section of from 9000 feet per second to 21,000 feet per second. The Mach number which can be achieved in the test section before condensation occurs is increased from 20 to 35. The new six-foot test section will make possible an increase in the model size and the instrumentation capacity of each model.

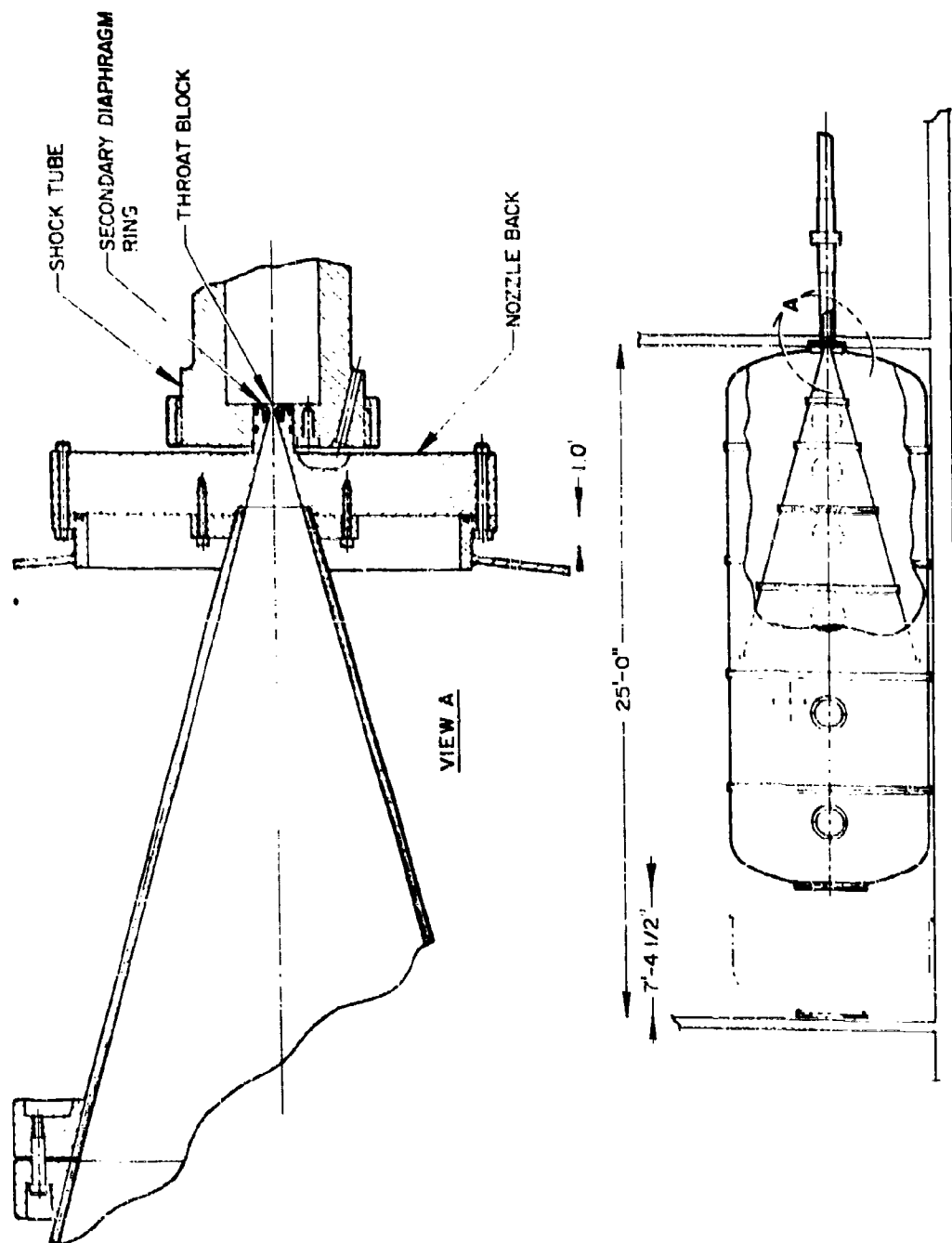


Figure 62. Tunnel and Test Section Arranged in Vacuum Tank

4. Combustion Experiments

The primary modification of the current facility consists of the design and incorporation of a combustion driver. A stoichiometric mixture of oxygen and hydrogen is ignited at high pressure within the driver to heat the primary driver gas (helium). The initial loading pressure of the driver is approximately 4000 psi and the pressure after ignition reaches values as high as 30,000 psi. In order to provide for safe operation of the facility, however, the design point of the driver must be over 150,000 psi to provide sufficient margin in the event of detonation within the driver. Since all of the current facilities employing combustion drivers operate at considerably lower pressures, it was necessary to undertake an experimental investigation of the combustion processes of such a mixture at the pressures of interest as well as methods of uniform ignition of the mixture.

The experimental program undertaken includes the following investigations:

- a. Method of ignition
 - 1. spark plug
 - 2. exploding wire
- b. Combustion processes with regard to
 - 1. mixture ratio
 - 2. effect of loading pressure
 - 3. combustion pressure
 - 4. detonation

Spark plugs have been routinely operated successfully for shock tunnels with a loading pressure in the range 600 to 1200 psi and a corresponding pressure rise after combustion to 6000 - 12,000 psi. This pressure is within the design limitations of commercially available spark plugs. With an increase in loading pressure, the pressure after ignition may exceed the mechanical stress limit of commercial spark plugs.

Another major consideration is the breakdown potential required for the spark to bridge the electrode gap at high pressure in a dominantly helium atmosphere. For minimum achievable electrode spacings, the logarithmic rise of breakdown potential with pressure requires voltages of the order of 100KV at 4000 psi. Extremely small values of electrode spacing limits spark plug life to a single run.

The first method of igniting the gas mixture investigated was a spark plug ignition system, in view of the low pressure operational success with this technique in other facilities. Specially designed plugs were constructed, since commercially available spark plugs are not designed for 4000 psi operation. An assembly drawing of the high-pressure plug is shown in Fig. 63. Figure 64 is a photograph of the finished spark plug. The valve body and the central electrode were made of stainless steel and the ends of the electrode were machined flat. The filler material is teflon. A gas-tight assembly is achieved when the retaining nut is screwed on tightly from the top, compressing the insulating teflon. The 0.010 inch electrode gap is the internal annular area. A ring insert at the tip forms the ground electrode and permits adjustment of the gap distance. The sharp radii of the flat electrodes provide high field strength for initiation of breakdown. The plug was hydraulically tested to a static pressure of 30 000 psi without failure.

Initial combustion tests were made with this spark plug configuration in a specially designed test chamber. Gas charge pressures up to 800 psi were successfully ignited by the spark plug with a potential of 15-20 KV across the electrode gap. Mechanical failures occasionally developed in the electrode insert. Experiences encountered elsewhere show electrode pitting during repeated firing at high pressure, resulting in an increased effective electrode spacing. Gap distance increase by pitting can be sufficient to cause erratic or incomplete breakdown at pressures considerably below 4000 psi.

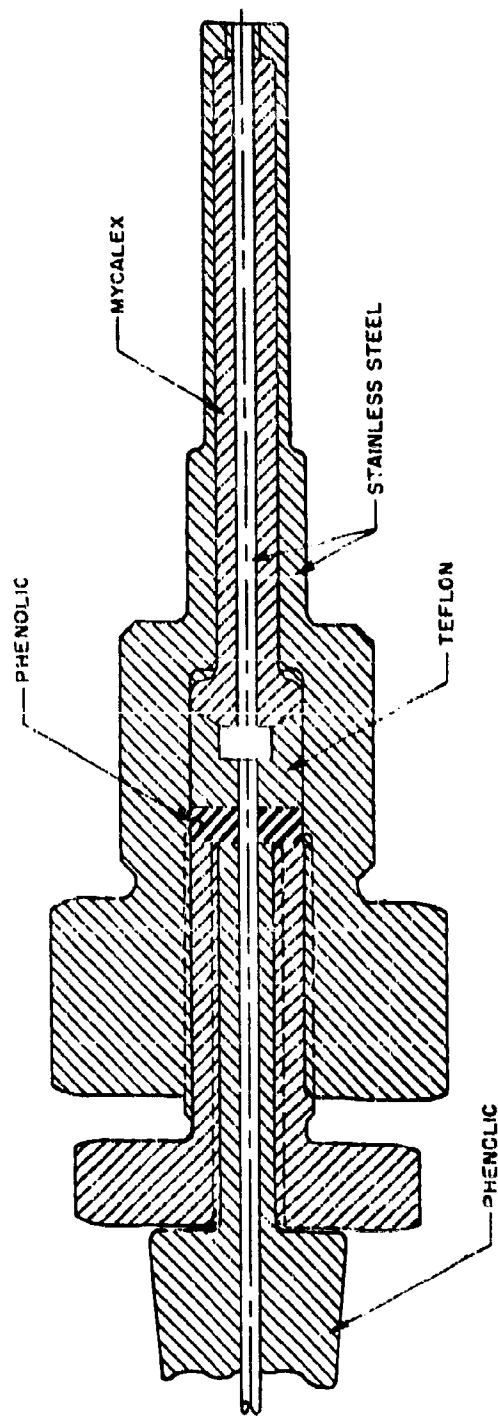


Figure 63. Combustion Driver Spark Plug



Figure 64. High Pressure Spark Plug

For the combustion driver, 18 spark plugs must be used along the length of the driver for uniform combustion. The probability of one or more plugs malfunctioning during any given run is high. This is obviously undesirable as the possibility of induced detonation and erratic performance increases. The problems involved in removing 18 spark plugs with high-pressure fittings for routine checks at regular intervals do not present an attractive picture from an operational standpoint.

Another important design factor is the acute stress problem arising in the mechanical design of the high-pressure driver due to the spark plug holes. These factors presented such difficulties that other ignition techniques were considered for the high-pressure combustion driver.

As a result of these considerations, investigations were undertaken on exploding wire techniques. Successful operation has been obtained in many laboratories using this approach, but at lower gas charge pressures than 4000 psi. The exploding wire considered for use in the Aerospace combustion driver consists of a series of wires spanning the entire length of the driver in order to obtain uniform combustion in both the axial and radial directions. Since initiation of the explosion is a process involving only the wire, there are no problems associated with electrical breakdown of the gas and electrode erosion. The potential required to initiate wire explosion is, for all practical purposes, independent of gas pressure.

The equipment used in the experiment consisted simply of two 3 μ f capacitors connected in series with the wire. The capacitors are rated at 15KV each, and a total capacitance of 1.5 μ f is obtained at 30 KV. The schematic is shown in Fig. 65.

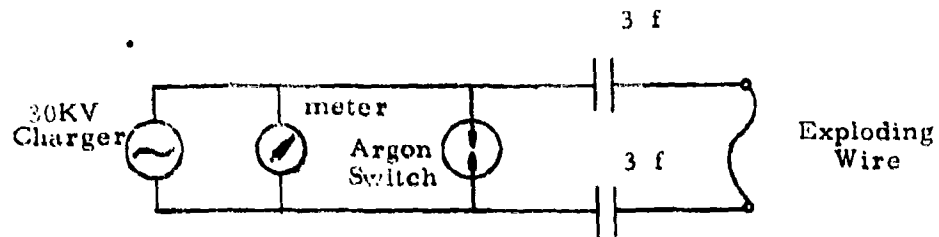


Figure 65. Schematic of Exploding Wire System

With the capacitors charged to the desired potential, argon was allowed to flow into the switch. A minimum potential of 12 KV is required to cause electrical breakdown in the argon for the gap spacing used in the switch (0.5 inch between flat faced rods). The ionized path formed in the argon completes the circuit, discharging the stored energy into the wire, resulting in a violent explosion.

The circuit discharge characteristic, derived from the impedance of the circuit components (including the exploding wire) is critical for a short duration discharge resulting in a strong explosion. When the circuit is completed by ionization at the argon switch, current begins to flow through the wire. Due to the wire resistance, energy dissipation within the wire occurs in the form of joule heating. The amount of current passing through the wire is determined by the total resistance of the wire and the charge potential. Thus, a longer wire requires a higher threshold potential to obtain the required current for a rapid explosion. Changing the wire gauge and material influences the threshold potential. As the wire is raised rapidly to high temperatures, vaporization is initiated. Present theory and experiments show that metal droplets are formed initially, and as further heating occurs, the droplets eventually form vapors and expand radially in the form of a cylindrical shock wave. During the droplet

formation period, the electrical circuit can be interrupted due to physical separation of the conducting material. If, however, the separation of the droplets and sub-droplets is below a critical value, space charge effects will maintain the electrical current, provided the residual potential is high enough. Further heating creates a plasma which continues to conduct current until dissipation due to the radial expansion process quenches the discharge. Each step of these processes occurs in a very short time interval, determined by the material, the length, and the uniformity of the cross section of the wire. The discharge time constant is important in that it must be short or comparable in magnitude to the effective separation time of the droplets or the dissipation time of the plasma.

Experiments have been performed to seek the threshold charge potential required to produce a strong explosion for varying lengths of wire. In addition, different wire gauges and materials were investigated. These included 0.005 inch tungsten, 0.001 inch copper, and 0.0005 inch platinum. The most successful wire found to date is 0.0015 inch copper alloy. Wires of this material are easy to handle and have high mechanical strength. A single wire up to seven feet in length has been successfully exploded with the present power supply. The results of this series of experiments are presented in Fig. 66. A linear relationship is noted between charge potential and wire length. Extrapolating the results to a 20-foot wire indicates a charge potential of about 75KV is required for a strong explosion. This creates a problem in the driver design, since the close spacing within the driver means that arcing to the driver wall is difficult to suppress at this high potential. In addition, the lead wire insulation must withstand high voltage and high pressure simultaneously.

A possible solution is to divide the wire in three sections and connect them in parallel. In this way, the breakdown potential is considerably reduced. The problems associated with simultaneous ignition of multiple wires is now being investigated. The experimental apparatus is shown in Figs. 67 and 68. Preliminary combustion experiments with the exploding wire were conducted by installing a wire on a spark plug modified for the purpose (Fig. 69).

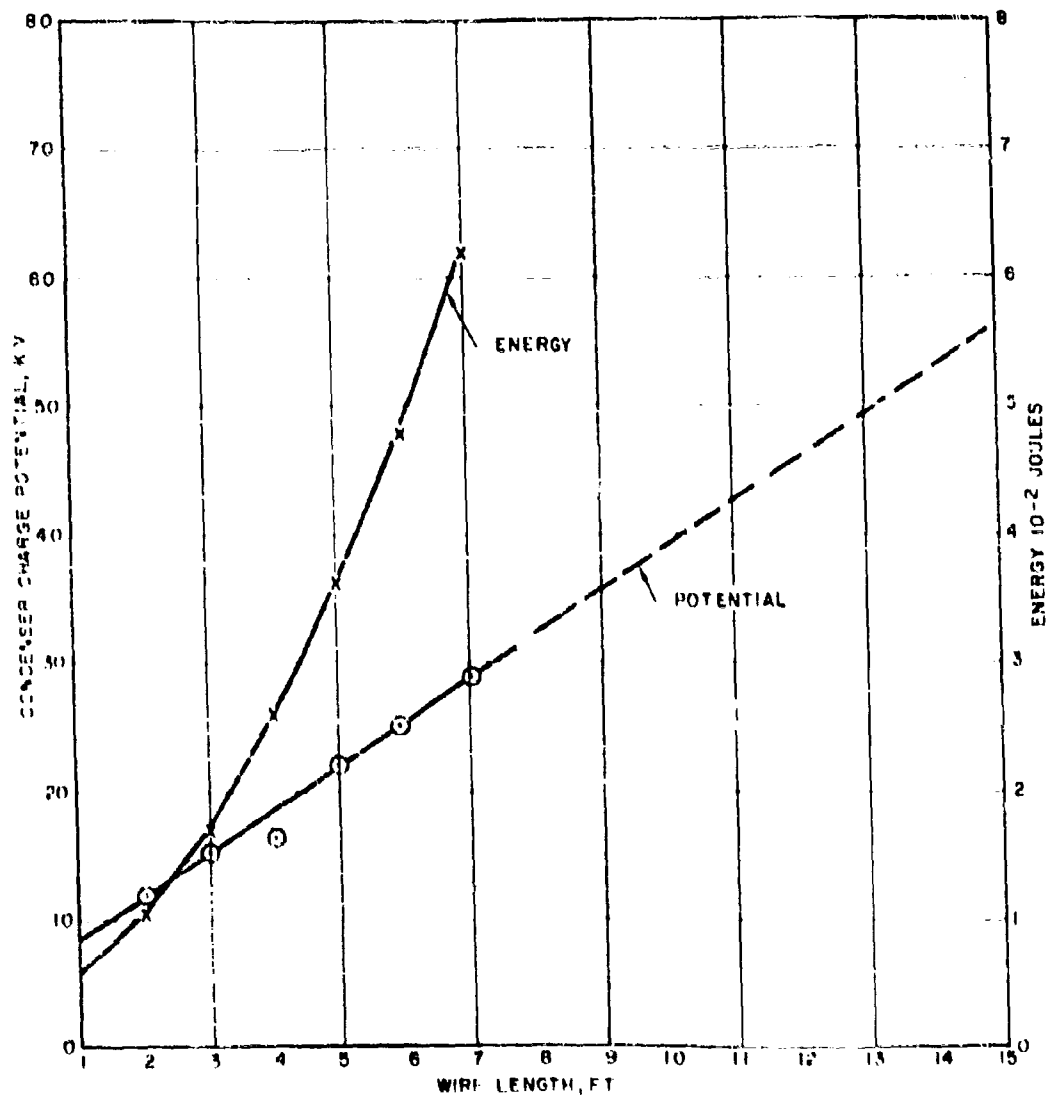


Figure 66. Experimental Threshold Potential for Complete Energy Discharge through Exploding Wire. $C = 1.5 \mu\text{fd}$. Wire is Copper Alloy of .0015-inch Diameter.



Figure 67. Explosion of Three Wires in Parallel

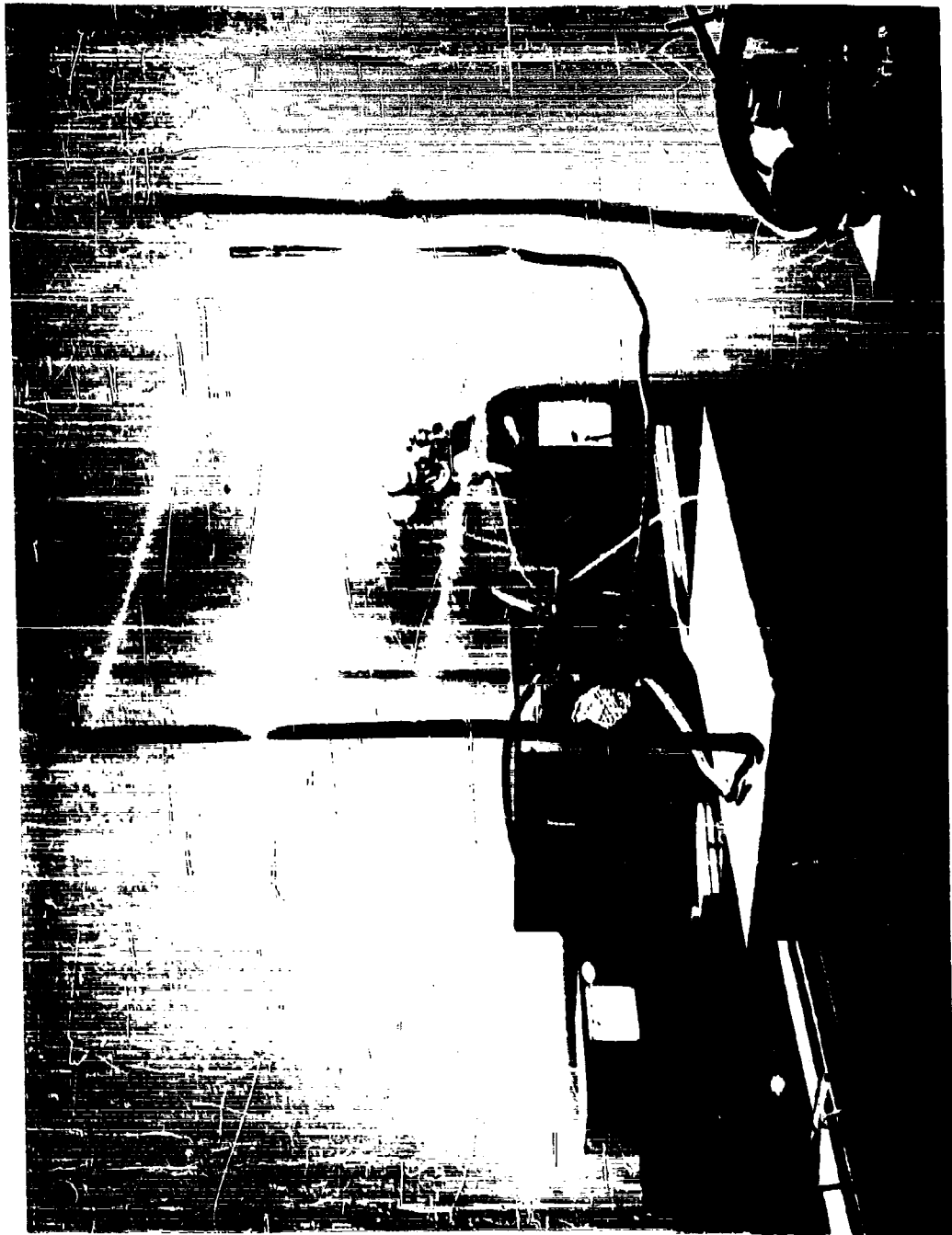


Figure 68. Explosion of Three Parallel Wires with Less than Threshold Energy

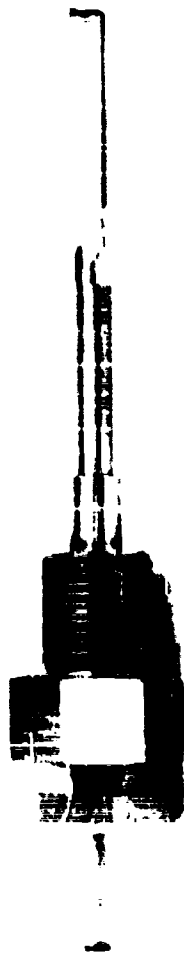


Figure 69. Modification of Spark Plug for "Exploding Wire" Type
Initiation of Combustible Gas Mixture

A strong explosion provides adequate margin for igniting the gas mixture at high pressure and eases ignition problems associated with mixing non-uniformities. A closer study of the ignition problem indicates that complete burning (non-explosive) of the wire may be adequate to ignite a high-pressure gas mixture. Recent reports from other laboratories show that burning of aluminum tape has been used successfully to ignite gas mixtures with pressure levels comparable to the combustion driver.

A specially designed small scale pilot combustion chamber was constructed. The chamber volume is 1.5 cubic inches with a minimum wall thickness of one inch. The cylindrical chamber has a spark plug at one end, and a diaphragm seal at the opposite end of the chamber. The diaphragm is calibrated to break at about 5500 psi. This enables a mixture gas at 4000 psi to be loaded into the chamber. The pressure increase after ignition is such that the diaphragm rupture pressure is exceeded, resulting in diaphragm break and chamber pressure drop.

The combustion chamber is connected to bottles of hydrogen and oxygen. Helium supply is routed from the main reservoir of the present shock tunnel. A schematic of the installation is shown in Fig. 70. The sequence of operations begins with flushing the chamber with oxygen, followed by loading to the desired pressure. Hydrogen is injected next by setting the regulator to the correct pressure and then opening the hand valve. Each hand valve must be closed immediately after loading each component gas in order to prevent feed back of gas mixtures into the component gas lines. Helium from the shock tunnel reservoir is injected last. Difficulty in obtaining the correct mixture ratio in the pilot combustion chamber has been encountered due to the excessive volume in the connecting gas lines. Since a finite length is required to connect the test chamber and the end valves, the connecting line volume must be eliminated or accounted for.

Solenoid valves were installed directly onto the test chamber to eliminate this excess volume. Good results were obtained in this manner

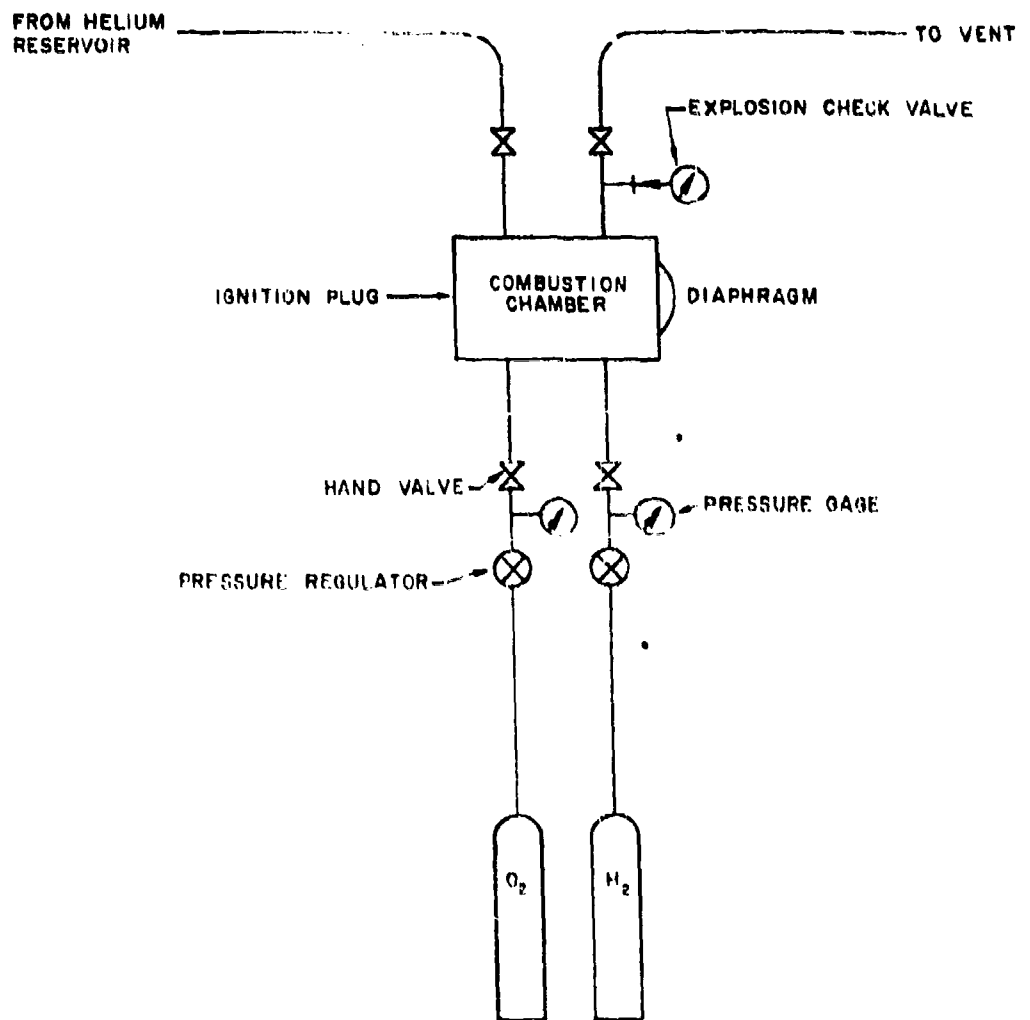


Figure 70. Schematic of Pilot Combustion Test Facility

but the solenoid valves were damaged repeatedly at pressures much below the rated operating pressure. The test combustion chamber volume was enlarged and a well-tested hand valve incorporated to permit operation at the required pressure level. A redesigned combustion chamber with an internal volume of 20 cubic inches was constructed with hand valve seats machined into the wall of the chamber. Combustion experiments are now being initiated in this new test cell.

D. Advanced Instrumentation

1. General

Although any one of a large number of transduction methods could be adapted to shock tunnel testing, initial consideration was restricted to those classed as self-generating; i. e., no external source of electric power is required. This approach was chosen to simplify instrumentation and to eliminate electronic development to accompany the transducer development. Of the self-generating systems, the piezoelectric ceramic transducer appeared to be the most attractive for a reasonably rapid developmental program.

A variety of piezoelectric transducers are commercially available. Most of these are either high-sensitivity types classed as microphones or low-sensitivity devices intended for high-pressure instrumentation. Microphones are generally too large for model instrumentation and not suited to shock tunnel testing for a number of reasons. Some of the high-pressure transducers would be suitable in many respects except for inadequate sensitivity. These transducers usually have a circular cylindrical configuration which is easy to install in models. This shape is a logical consequence of the type of piezoelectric elements usually employed; hollow or solid cylinders operating in compression. Such elements provide a mechanically stiff system with high resonance frequency which limits the ultimate sensitivity attainable with elements of practical dimensions. The higher sensitivity is achieved in microphones in part by the larger size and to a greater degree by the type of piezoelectric element employed. This is usually a composite bar or plate with the output resulting from flexure or torsion of the element. Only flexural (bender) elements can be conveniently made with ceramics. The resonance frequency is usually much lower than that of the cylindrical types, which limits the frequency response of the transducer. Thus the principle objective of the design is to achieve the desired sensitivity with a sufficiently high resonance frequency.

2. Bender Element Transducers

A functional drawing of the conventional bender element transducer is shown in Fig. 71. A positive external pressure causes a downward deflection of the element. This produces tensile stresses in the upper portion of the element and compressive stresses in the lower portion. The element consists of a "sandwich" of two ceramic strips and a shim in the neutral plane of the composite bar. For the most common applications, polarization is such that conducting electrodes on the upper and lower surfaces provide the proper output. Analysis of such a structure is usually made by making use of the electrical analog of the mechanical vibrating system, including the mechanical-to-electrical transduction characteristics.^{45, 46} Figure 72 shows the equivalent circuit of the arrangement shown in Fig. 71. A simplified equivalent circuit for frequencies well below the system resonance is shown in Fig. 73. A cantilever element is shown in Fig. 71 although other crystal support and drive systems are possible without altering the configuration of the equivalent circuit. The values of the components in the equivalent circuit are determined by the type of piezoelectric material, the dimensions of the element, and the material properties and dimensions of the diaphragm. If we assume for the moment that the transducer output is essentially open circuited, the equivalent circuit will yield a solution for the ratio of E to P (volts per unit pressure).

$$\frac{E}{P} = \frac{NA_D}{1 + \frac{C_C}{C_D}}$$

This represents the sensitivity for frequencies well below the system resonance frequency and is independent of frequency. The system resonance frequency is

$$\omega_0^2 = \frac{1}{(M_D + M_C) \frac{C_D C_C}{C_D + C_C}}$$

where ω_0 is the angular resonance frequency and equal to $2\pi f_0$.

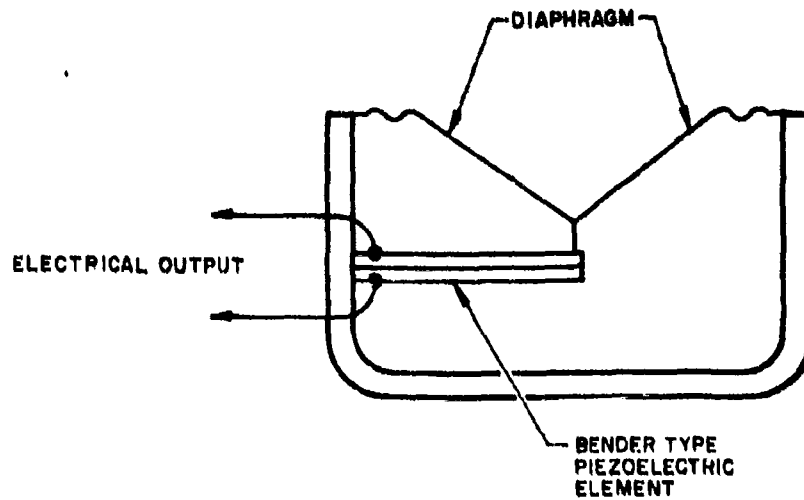
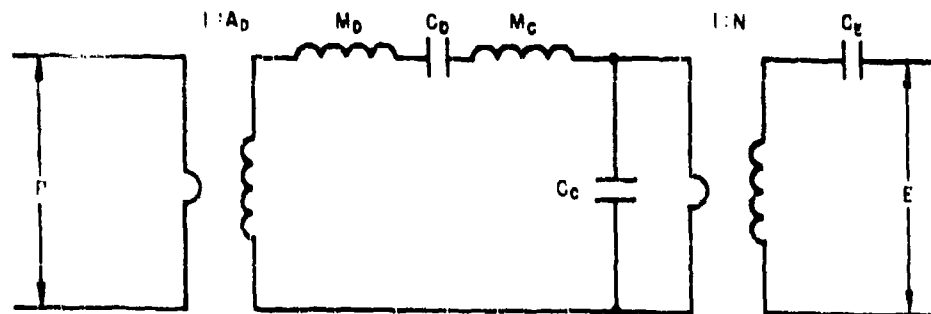


Figure 71. Functional Arrangement of Pressure Transducer Using the Piezoelectric Bender Element



- A_D - DIAPHRAGM EFFECTIVE AREA
- P - FLUCTUATING COMPONENT OF PRESSURE
- M_D - MASS OF DIAPHRAGM
- C_D - COMPLIANCE OF DIAPHRAGM
- M_C - CRYSTAL MASS
- C_C - CRYSTAL COMPLIANCE
- N - ELECTROMECHANICAL TRANSDUCER RATIO
- C_E - BLOCKED ELECTRICAL CAPACITANCE
- E - ELECTRICAL OUTPUT VOLTAGE

Figure 72. Equivalent Circuit for Figure 71

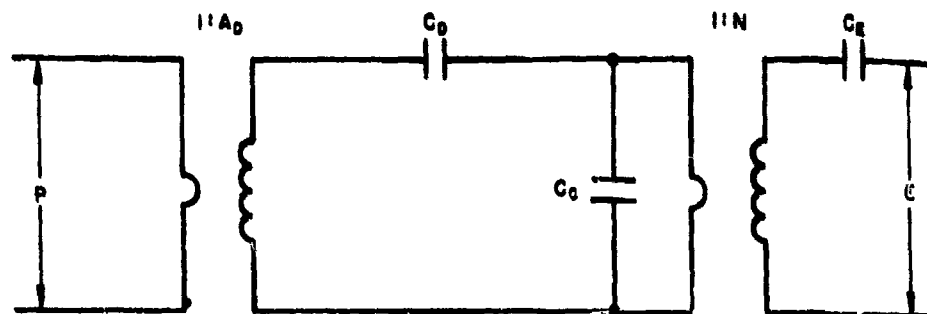


Figure 73. Low Frequency Equivalent Circuit for Figure 71.

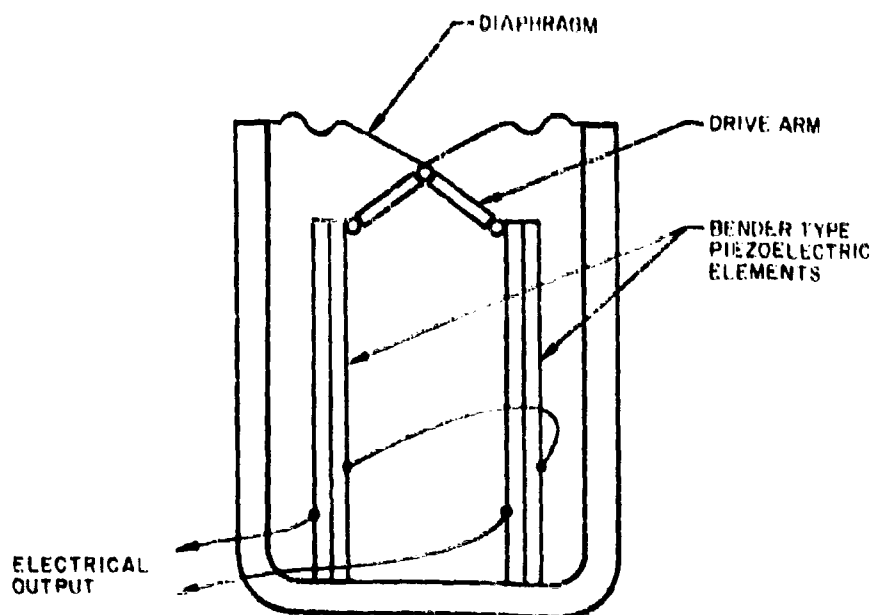


Figure 74. Functional Arrangement of Pressure Transducer with Axial Elements

The relationships given have assumed negligible loading by the external electrical circuit. This will be approximated if the internal electrical impedance is small compared to the load impedance. It is theoretically possible to achieve any sensitivity desired with a given resonance by properly choosing the crystal and diaphragm constants. However, a small structure with very high sensitivity and high resonance will result in an unreasonably high source impedance, and the output will be subject to substantial loading effects. In addition, there are practical limits to the ability to fabricate very small ceramic elements, particularly with respect to thickness.

3. The Axial Element Transducer

Referring to Fig. 71, it is seen that the largest crystal dimension will be of the order of the diaphragm radius if the body diameter is approximately the same as the diaphragm diameter. This puts a severe restriction on element length which can limit sensitivity and source capacitance. This can be overcome by rotating the element 90° so that its longest dimension is parallel to the axis of the cylinder. In order to properly drive an element so positioned, a pivoted drive arm is required. Finally, in order to balance the reaction back on the diaphragm, two elements are used in the configuration shown in Fig. 74. For a downward motion of the diaphragm, both elements are deflected outward. The elements are connected in series and phased so that this type of stressing gives added voltages.

It can be seen that the lateral force available for deflecting the elements is not the same as the force transmitted by the diaphragm, but is some function of the drive angle. Figure 75 shows the relationship between the forces and displacements for the angled drive. If we define mechanical compliance as

$$C_x = \frac{\Delta X}{\Delta F_x}$$

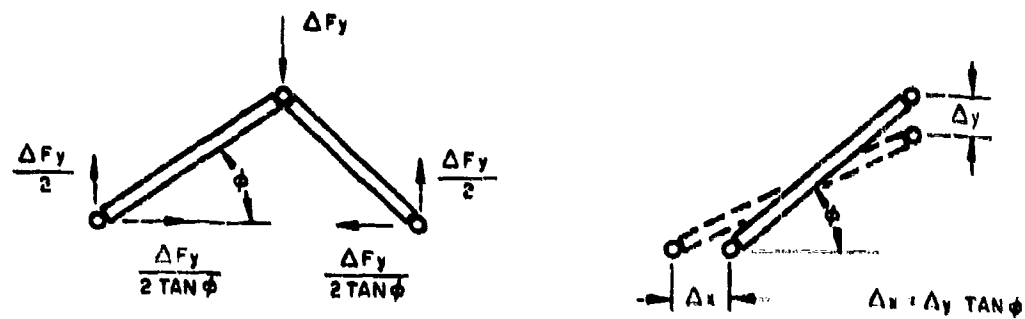


Figure 75. Force and Displacement Relationships in the Axial Element Drive System

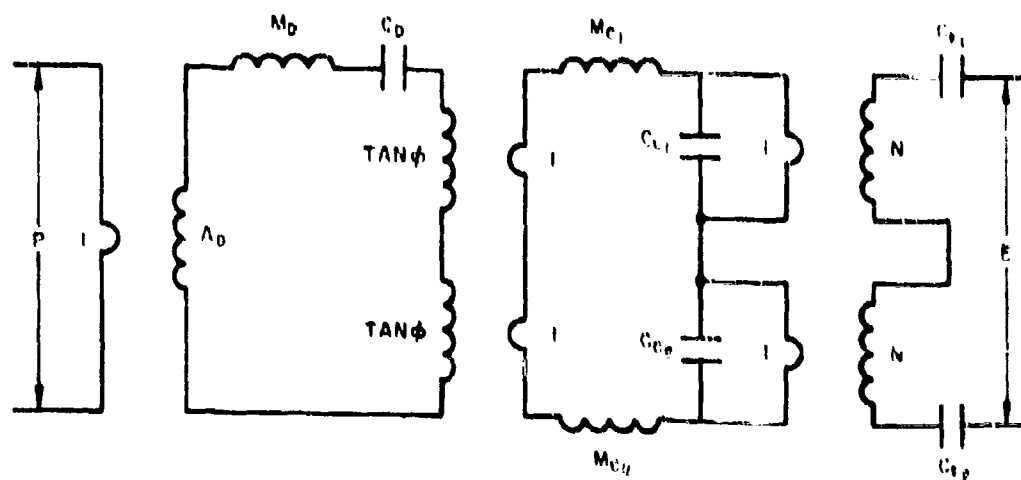


Figure 76. Equivalent Circuit for Axial Element Transducer

for each of the two elements

$$C_y = \frac{\frac{\Delta Y}{\Delta F_y}}{2}$$

$$C_y = \frac{\frac{\frac{\Delta X}{\tan \phi}}{2 \Delta F_x \tan \phi}}{2} = \frac{C_x}{\tan^2 \phi}$$

It can be shown that the angled drive system is equivalent to a mechanical transformer with a "turns ratio" of $\tan \phi / 1$. This satisfies the conditions derived for force, displacement and impedance. The equivalent circuit for this configuration is given in Fig. 76. It is seen that for $\phi = 45^\circ$ the turns ratio becomes unity and the performance becomes identical to that of Fig. 71 except for the fact that the single bender element has been replaced by two with the same aggregate dimensions and mechanical characteristics. This configuration can always be employed with a resultant doubling of the output voltage but since the internal source capacitance is reduced to 1/4 of the single element value it is not often used.

As with the conventional structure, we can derive the low frequency sensitivity. This is found to be

$$\frac{E}{P} = \frac{N A_D}{\tan \phi + \frac{C_C}{2 C_D \tan \phi}}$$

The factor "2" appears in the denominator because C_C refers to each element of the two element system. It can be seen that for a given set of diaphragm and crystal constants there is an optimum angle which gives maximum output. This relationship is

$$\tan \phi = \frac{C_C}{2 C_D} \text{ for } \max \frac{E}{P}$$

The increase in sensitivity which can be achieved by making ϕ optimum in comparison with $\phi = 45^\circ$ is shown in Fig. 77. It can be seen that great increases are possible only where there is a large disparity between the crystal and the diaphragm compliances. At the same time, optimum sensitivity might not always be desired since lower sensitivity transducers would be necessary for measurement of pressures close to stagnation. The drive arm angle could be a convenient means for sensitivity control.

In addition to sensitivity and shape, the factor of acceleration sensitivity is of consequence when employing pressure transducers. The important parameter here is the mass of the transducer moving system. Referring to Fig. 74, it can be seen that axial acceleration acts on the diaphragm mass, but not on the elements. Acceleration in the flexural plane of the elements produces opposing voltages in each of the elements so that a degree of acceleration compensation is provided in this structure.

Drawings for the initial version of the transducer have been submitted to the Laboratory Shop. Its principle design characteristics are as follows:

Body Diameter	.5 in.
Body Length (not including terminals)	.9 in.
Sensitivity	14 volts/psi or -74 db re 1 volt per dyne/cm ²
Internal Capacitance	250 mmf
Principle Resonance	8.5 kcs
Diaphragm Active Diameter	.3 in.
Optimum Drive Angle	60°
Element Dimensions	$\frac{1}{2} \times .060 \times .024$ in.

The above figures are based on an approximate calculation of the diaphragm characteristics for which an exact solution is not possible, and

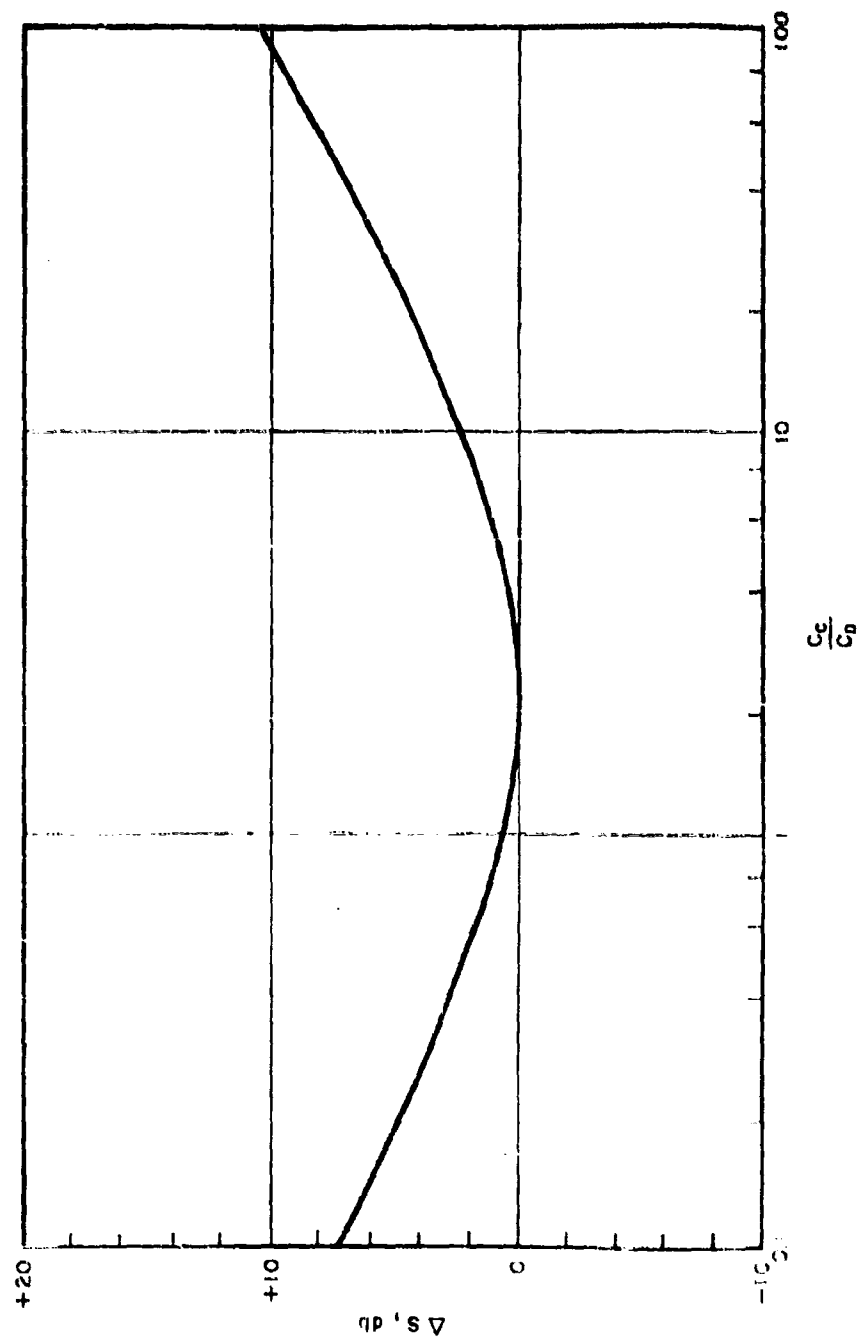


Figure 77. Increase in Sensitivity for Optimum Angle ϕ as a Function of C_c/C_n

are subject to modification when experimental data become available. The design internal capacitance is sufficient for developmental purposes, but too low for operational transducers. Final units will use modified ceramic elements which will give four times the internal capacitance but only half the output voltage.

Complete analysis requires taking into account a number of additional factors. Some of these may be easily assessed without adding to the equivalent circuit and the over-all analysis. These include the mass of the drive arm, the acoustic stiffness of the internal cavity, and the acoustic leak required to equalize for ambient pressure changes. Other factors may require some experimental evidence in order to determine their importance. Included in this class is the effectiveness of the drive arm in transmitting the diaphragm forces and unanticipated diaphragm modes. Coupling of the transducer to the medium is usually made through a small diameter hole leading to a cavity in front of the diaphragm. This can constitute a Helmholtz resonator with substantial effect on the transient response. This can best be avoided by insuring that the resonator frequency is well above the highest frequency of interest. Future consideration will be given to acoustical or mechanical damping in order to improve the transient response of the transducer.

IV. FUTURE PROGRAM

During the next program period, the following investigations will be undertaken:

A. Theoretical Investigations

1. Inviscid three-dimensional hypersonic flows. Analysis of inviscid subsonic and transonic regions in general three-dimensional flows. In particular, the flow fields about zero angle of attack, non-axisymmetric, and angle-of-attack axisymmetric blunt bodies in hypersonic flow. The analyses to be initiated may be divided into three separate general methods:

a. An inverse method of integration from an assumed three-dimensional shock chosen as a constant value in a spheroidal coordinate system.

b. Direct Dorodnitsyn-Betolserkovskii procedure for a three-dimensional body of a constant value spheroidal coordinate surface.

c. Perturbation analysis along basic flow streamlines. Perturbation equations will be solved in series form with coefficients depending only on the axisymmetric or non-axisymmetric basic flow and appropriate boundary conditions.

2. Kinetic theory approach for a sharp leading-edge flat plate in hypersonic flow. A four-stream Maxwellian distribution is employed instead of Lees' and Mott-Smith's two-stream Maxwellian which is inadequate for the flat plate problem.

3. Numerical solution of the non-equilibrium blunt body equations (II. B) for selected flight conditions and vehicle geometries.

4. Theoretical predictions of the non-equilibrium flow about selected geometries in the presence of the frozen ambient gas streams associated with the combustion-driven shock tunnel.

5. Prediction of shock layer characteristics downstream of the stagnation region employing the Navier-Stokes model.

6. Analysis of shock-boundary layer interaction associated with control surface deflection in the presence of thick boundary layers. Prediction of upstream separation and propagation as a function of shock strength, Mach number, Reynolds number, and leading edge bluntness.

B. Experimental Investigations

1. Installation and assembly of combustion driver and six-foot nozzle.
2. Calibration of combustion-driven shock tunnel
 - a. Probe static pressure measurements
 - b. Langmuir probes
 - c. Total head and test-wedge measurements
3. Incorporation of electron beam densitometer into combustion-driven shock tunnel.
4. Control surface effectiveness at high altitudes. Vary ratio of local boundary flap dimension between 10^{-1} to 1. Vary leading-edge bluntness so as to determine influence of blast wave phenomena. Correlate with theoretical investigation (II. A. 6).
5. Pressure distribution and heat transfer about blunt and sharp leading-edge flat plates in order to experimentally determine influence of non-equilibrium flow phenomena. Langmuir probe measurements in the shock layer. Correlate with theoretical investigations (II. A. 3 and II. A. 4).
6. Langmuir probe: Base and wake electron concentration measurements.
7. Pressure and heat transfer measurements on a sharp leading edge ($Kn > 1$) flat plate in the range $5 \leq \chi \leq 1000$. Correlate with theoretical investigations (II. A. 2 and II. A. 5)

V. REFERENCES

1. Cheng, H. K., J. G. Gall, T. C. Golian, and A. Hertzberg. "Boundary-Layer Displacement and Leading-Edge Bluntness Effects in High Temperature Hypersonic Flow." Paper Presented at the IAS 28th Annual Meeting, January 1960.
2. Fay, J. A., and F. R. Riddell. "Theory of Stagnation Point Heat Transfer in Dissociated Air." Avco Research Report 1, April 1957.
3. Byron, S. R. "Interferometric Measurement of the Rate of Dissociation of Oxygen Heated by Strong Shock Waves." Cornell University Report.
4. Cheng, H. K., and A. J. Pallone. "Inviscid Leading Edge Effect in Hypersonic Flow." Reader's Forum, J. Aero. Sci., Vol. 23, No. 7, p. 700, July 1956.
5. Whalen, R. J., K. Pearce, and S. Samet. "Similarity Studies for Dissociating Gases in Hypersonic Low Density Flow." WADD TR 60-341, January 1961.
6. Taylor, G. I. "The Formation of a Blast Wave by a Very Intense Explosion," Pt. I, Theoretical Discussion, Proc. Roy. Soc. (A), Vol. 201, No. 1065, p. 159, March 1950.
7. Sakurai, A. "On the Propagation and Structure of the Blast Wave." Part I, J. Phys. Soc. of Japan, Vol. 9, No. 2, p. 256, March-April 1954.
8. Lees, L., and T. Kubota. "Inviscid Hypersonic Flow over Blunt-Nosed Slender Bodies." J. Aero. Sci., Vol. 24, No. 3, pp. 185-202, March 1957.
9. Whalen, R. J. "Boundary-Layer Interaction on a Yawed Infinite Wing in Hypersonic Flow." Readers' Forum, J. Aero. Sci., Vol. 26, No. 12, p. 889, December 1959.
10. Lin, S. C. "Cylindrical Shock Wave Produced by Instantaneous Energy Release." J. Appl. Phys., Vol. 25, No. 1, p. 54, January 1954.
11. Douglas Aircraft Co. "Normal and Oblique Shock Characteristics at Hypersonic Speeds." Engineering Report No. LB-25599, December 1957.

REFERENCES (continued)

12. Bertram, M. H., and A. Henderson, Jr. "Effects of Boundary Layer Displacement and Leading Edge Bluntness on Pressure Distribution, Skin Friction, and Heat Transfer of Bodies at Hypersonic Speeds." NACA TN 4301, July 1958.
13. Lees, L. "Influence of the Leading-Edge Shock Wave on the Laminar Boundary Layer at Hypersonic Speeds." J. Aero. Sci., Vol. 23, No. 6, p. 594, 1956.
14. Bray, K. N. C. "Departure from Dissociation Equilibrium in a Hypersonic Nozzle," A. R. C. 19, 983, March 1958.
15. Hall, J. G. "Studies of Chemical Non-equilibrium in Hypersonic Nozzle Flows." Cornell Aeronautical Laboratory Report AD-1118-A-6, November 1959.
16. Whalen, R. J., and K. Pearce. "Low Temperature Plasma Phenomena." Presented at the Third Biennial Gas Dynamics Symposium of the ARS, August 1959.
17. Nagamatsu, H. T., J. B. Workman, and R. E. Sheer. "Hypersonic Nozzle Expansion with Air Atom Recombination Present." General Electric Report No. 60-RI-2342C January 1960.
18. Bethe, H. A., and E. Teller. "Deviation from Thermal Equilibrium in Shock Waves." Cornell Ballistic Research Laboratory Report.
19. Cheng, H. K. "Similarity of Hypersonic Real Gas Flows over Slender Bodies with Blunted Noses." J. Aero. Sci. Vol. 26 No. 9, p. 575, September 1959.
20. Lin, C. C., and S. I. Rubinov. "On the Flow Behind Curved Shocks." J. Math. Phys. Vol. 27, pp. 105-129 (1948).
21. Lin, C. C., and S. F. Shen. "An Analytic Determination of the Flow Behind a Symmetrical Curved Shock in a Uniform Stream." NACA TN 2506 (1951).
22. Cabannes, H. "Détermination théorique de l'écoulement d'un fluide derrière une onde de choc détachée." O. N. E. R. A. Note tech. no. 5 (1951).
23. Van Dyke, M. D. "The Supersonic Blunt Body Problem--Review and Extensions." J. Aero/Space Sci., Vol. 25, pp. 485-496 (1958).

REFERENCES (continued)

24. Zlotnick, M., and D. J. Newman. "Theoretical Calculation of the Flow on Blunt-Nosed Axisymmetric Bodies in a Hypersonic Stream." TR No. 2-57-29, Research and Advanced Development Division, Avco Mfg. Corp., Lawrence, Mass., 1957.
25. Mangler, K. W., and M. E. Evans. "The Calculation of the Inviscid Flow Between a Detached Bow Wave and a Body." Tech. Note No. Aero 2536, Roy. Aircraft Est., Farnborough, 1957.
26. Garabedian, P. R., and H. M. Lieberstein. "On the Numerical Calculation of Detached Bow Shock Waves in Hypersonic Flow," J. Aero. Sci., Vol. 25, pp. 109-118 (1958).
27. Vaglio-Laurin R., and A. Ferri. "Theoretical Investigation of the Flow Field About Blunt-Nosed Bodies in Supersonic Flight," J. Aero/Space Sci., Vol. 25, pp. 761-770 (1958).
28. Hayes, W. D., and R. F. Probstein. Hypersonic Flow Theory. Academic Press New York 1959.
29. Li, Y. T. "Recent Advances in Non-equilibrium Dissociating Gasdynamics," ARS J., Vol. 31, no. 2, p. 170, February 1961.
30. Lack, W. "Inviscid Flow of a Reacting Mixture of Gases Around a Blunt Body," J. of Fluid Mech., Vol. 7, p. 128, 1960.
31. Penner, S. S. Chemistry Problems in Jet Propulsion. Pergamon Press New York 1957.
32. Keck, J. C. "Statistical Theory of Chemical Reaction Rates," J. Chem. Phys., Vol. 29, p. 410, 1958. Also Review of Research Program Contract AF 04(647)-278 Avco March 1961.
33. Zinman, W. G. "Recent Advances in Chemical Kinetics of Homogeneous Reactions in Dissociated Air," ARS J., Vol. 30, p. 233, March 1960.
34. Probstein, R. F. and N. H. Kemp. "Viscous Aerodynamic Characteristics in Hypersonic Rarefied Gas Flow," J. Aero/Space Sci., Vol. 27, No. 3, pp. 174-192, 1960.
35. Hartunian, R. A. and R. L. Varwig. "A Correction to Thin-Film Heat Transfer Measurements," Aerospace Report No. TDR-594(1217-01)TN-2, 1961.

REFERENCES (continued)

36. Hartunian, R. A. and P. V. Marrone. "Determination of Viscosity of Dissociated Gases from Shock-Tube Heat-Transfer Measurements." The Physics of Fluids, Vol. 4, No. 5, pp. 535-543, 1961.
37. Hurlbut, F. C. "An Electron Beam Density Probe for Measurements in Rarefied Gas Flows." U. of C. Tech. Report HE-150-149.
38. Markevitch, B. V. and F. C. Hurlbut. "The Study of Electron Beam Attenuation in Air." U. of C. Tech. Report HE-150-142.
39. Stoigerwald, K. H. "A Newly Developed Emission System for Electron Microscope." Optik 5, Vol. 8/9, 1949 (in German).
40. Nagamatsu, H. T. and E. D. Martin. "Combustion Investigation in the Hypersonic Shock Tunnel Driver Section." J. Appl. Phys. Vol. 30, No. 7, July 1959.
41. Feldman, S. "Hypersonic Gas Dynamic Charts for Equilibrium Air." Avco Research Report No. 40, January 1957.
42. Alpher, R. A. and D. R. White. "Ideal Theory of Shock Tubes with Area Change Near Diaphragm." G. E. Report No. 57-RL-1664, January 1957.
43. Wittliff, C. E., M. R. Wilson and A. Hertzberg. "The Tailored Interface Hypersonic Shock Tunnel." J. Aero/Space Sci. Vol. 26, No. 4, April 1959.
44. Weisblatt, H. and R. F. Flegg. "Experimental Technique for Tailored Operation of a Combustion Driven Shock Tunnel." Presented at the 4th Shock Tube Symposium. Aberdeen, Maryland, April 1961.
45. Piezotronic Technical Data, 1953. Brush Electronics Company (Clevite Corporation), Cleveland, Ohio.
46. Bauer, B. B. "Transformer Analogs of Diaphragms." J. Acous. Soc. Vol. 23, No. 6, November 1951.

UNCLASSIFIED

Aerospace Corporation, El Segundo, California.
HIGH MACH NUMBER AND MATERIALS
RESEARCH PROGRAM; PHASE I, AEROPHYSICS
RESEARCH STUDIES, Semiannual Technical
Report, compiled by R. J. Whalen, 1 January -
1 June 1961, 201p, incl. illus, table (Report No.
TDR-594(1206-02)STR) (Contract AF 04(647)-594).
Unclassified Report

During the last program period, September 1960
to 1 July 1961, theoretical and experimental in-
vestigations of high speed gas dynamics were
carried out under this program.

The experimental investigations included stagna-
tion point heat transfer measurements in low
Reynolds number flows in the existing helium-
driven shock tunnel. Electron beam densitometer
studies were continued. Modification of the exist-
ing hypersonic shock tunnel to incorporate a
(cont)

UNCLASSIFIED

UNCLASSIFIED

Aerospace Corporation, El Segundo, California.
HIGH MACH NUMBER AND MATERIALS
RESEARCH PROGRAM; PHASE I, AEROPHYSICS
RESEARCH STUDIES, Semiannual Technical
Report, compiled by R. J. Whalen, 1 January -
1 June 1961, 201p, incl. illus, table (Report No.
TDR-594(1206-02)STR) (Contract AF 04(647)-594).
Unclassified Report

During the last program period, September 1960
to 1 July 1961, theoretical and experimental in-
vestigations of high speed gas dynamics were
carried out under this program.

The experimental investigations included stagna-
tion point heat transfer measurements in low
Reynolds number flows in the existing helium-
driven shock tunnel. Electron beam densitometer
studies were continued. Modification of the exist-
ing hypersonic shock tunnel to incorporate a
(cont)

UNCLASSIFIED

UNCLASSIFIED

Aerospace Corporation, El Segundo, California.
HIGH MACH NUMBER AND MATERIALS
RESEARCH PROGRAM; PHASE I, AEROPHYSICS
RESEARCH STUDIES, Semiannual Technical
Report, compiled by R. J. Whalen, 1 January -
1 June 1961, 201p, incl. illus, table (Report No.
TDR-594(1206-02)STR) (Contract AF 04(647)-594).
Unclassified Report

During the last program period, September 1960
to 1 July 1961, theoretical and experimental in-
vestigations of high speed gas dynamics were
carried out under this program.

The experimental investigations included stagna-
tion point heat transfer measurements in low
Reynolds number flows in the existing helium-
driven shock tunnel. Electron beam densitometer
studies were continued. Modification of the exist-
ing hypersonic shock tunnel to incorporate a
(cont)

UNCLASSIFIED

UNCLASSIFIED

Aerospace Corporation, El Segundo, California.
HIGH MACH NUMBER AND MATERIALS
RESEARCH PROGRAM; PHASE I, AEROPHYSICS
RESEARCH STUDIES, Semiannual Technical
Report, compiled by R. J. Whalen, 1 January -
1 June 1961, 201p, incl. illus, table (Report No.
TDR-594(1206-02)STR) (Contract AF 04(647)-594).
Unclassified Report

During the last program period, September 1960
to 1 July 1961, theoretical and experimental in-
vestigations of high speed gas dynamics were
carried out under this program.

The experimental investigations included stagna-
tion point heat transfer measurements in low
Reynolds number flows in the existing helium-
driven shock tunnel. Electron beam densitometer
studies were continued. Modification of the exist-
ing hypersonic shock tunnel to incorporate a
(cont)

UNCLASSIFIED

Just Available Copy

UNCLASSIFIED

combustion driver and a six-foot diameter nozzle was initiated. This modification will allow an increased performance up to a Mach number equal to 30 and density altitudes to 300,000 feet. This modification will be completed by January 1962.

The theoretical investigations included a study of viscous and inviscid non-equilibrium hypersonic flows about blunt and sharp leading edge slender bodies. A numerical program to determine the non-equilibrium flow about a blunt body in the vicinity of the stagnation region was also initiated. A study of the hypersonic wake about blunt re-entry bodies was completed.

UNCLASSIFIED

combustion driver and a six-foot diameter nozzle was initiated. This modification will allow an increased performance up to a Mach number equal to 30 and density altitudes to 300,000 feet. This modification will be completed by January 1962.

The theoretical investigations included a study of viscous and inviscid non-equilibrium hypersonic flows about blunt and sharp leading edge slender bodies. A numerical program to determine the non-equilibrium flow about a blunt body in the vicinity of the stagnation region was also initiated. A study of the hypersonic wake about blunt re-entry bodies was completed.

UNCLASSIFIED

UNCLASSIFIED

combustion driver and a six-foot diameter nozzle was initiated. This modification will allow an increased performance up to a Mach number equal to 30 and density altitudes to 300,000 feet. This modification will be completed by January 1962.

The theoretical investigations included a study of viscous and inviscid non-equilibrium hypersonic flows about blunt and sharp leading edge slender bodies. A numerical program to determine the non-equilibrium flow about a blunt body in the vicinity of the stagnation region was also initiated. A study of the hypersonic wake about blunt re-entry bodies was completed.

UNCLASSIFIED

UNCLASSIFIED

combustion driver and a six-foot diameter nozzle was initiated. This modification will allow an increased performance up to a Mach number equal to 30 and density altitudes to 300,000 feet. This modification will be completed by January 1962.

The theoretical investigations included a study of viscous and inviscid non-equilibrium hypersonic flows about blunt and sharp leading edge slender bodies. A numerical program to determine the non-equilibrium flow about a blunt body in the vicinity of the stagnation region was also initiated. A study of the hypersonic wake about blunt re-entry bodies was completed.

UNCLASSIFIED

Best Available Copy

ERRATA

HIGH MACH NUMBER AND
MATERIALS RESEARCH PROGRAM

Phase I, Aerophysics Research Studies

Subsequent to the publication of this document the need for several changes became apparent. The attached pages incorporate these changes and should therefore replace the obsolete pages in existing copies of the document. The affected pages are as follows:

65	86	104
66	87	105
67	88	106
68	89	107
69	90	108
70	91	110
71	92	111
72	93	115
73	94	116
74	95	117
76	96	134
79	97	142
80	98	147
81	99	148
82	100	149
83	101	157
84	102	184
85	103	

NOTE: Do not return
to [redacted] Destroy
according to applicable
security regulations.

ASTIA

100-100

A

technique establishes the partial derivatives along this new boundary. In turn, the partial derivatives normal to this boundary are determined from the governing flow equations. Successive applications of this scheme allows the computation to be extended to the unknown body surface which will be established as a part of the solutions based upon the consideration of flow continuity.

The equations of motion, in terms of the shock-oriented curvilinear coordinates may be written (Fig. 24),

$$\frac{u}{1 + Ky} \frac{\partial a_i}{\partial x} + v \frac{\partial a_i}{\partial y} = \frac{\omega_i}{\rho} \quad (60)$$

$$\frac{\partial}{\partial x} (\rho u r) + \frac{\partial}{\partial y} [\rho v r (1 + Ky)] = 0 \quad (61)$$

$$u \frac{\partial u}{\partial x} + K u v + (1 + Ky) v \frac{\partial u}{\partial y} = - \frac{1}{\rho} \frac{\partial p}{\partial x} \quad (62)$$

$$u \frac{\partial v}{\partial x} + (1 + Ky) v \frac{\partial v}{\partial y} - K u^2 = - \frac{1 + Ky}{\rho} \frac{\partial p}{\partial y} \quad (63)$$

$$d \left(\sum_i h_i a_i \right) + u du + v dv = 0 \quad (64)$$

The equation of state is written as

$$p = (R/\overline{m}) \rho T \quad (65)$$

Where R is the universal gas constant, and \overline{m} is the molecular weight,

$$\frac{1}{\overline{m}} = \sum_{i=1}^n \left(\frac{a_i}{\overline{m}_i} \right)$$

n denotes the total number of chemical components in the system. The above system of (n plus 5) equations will be used for the determination of a_i , T , ρ , p , u , and v , which completely describe the flow field.

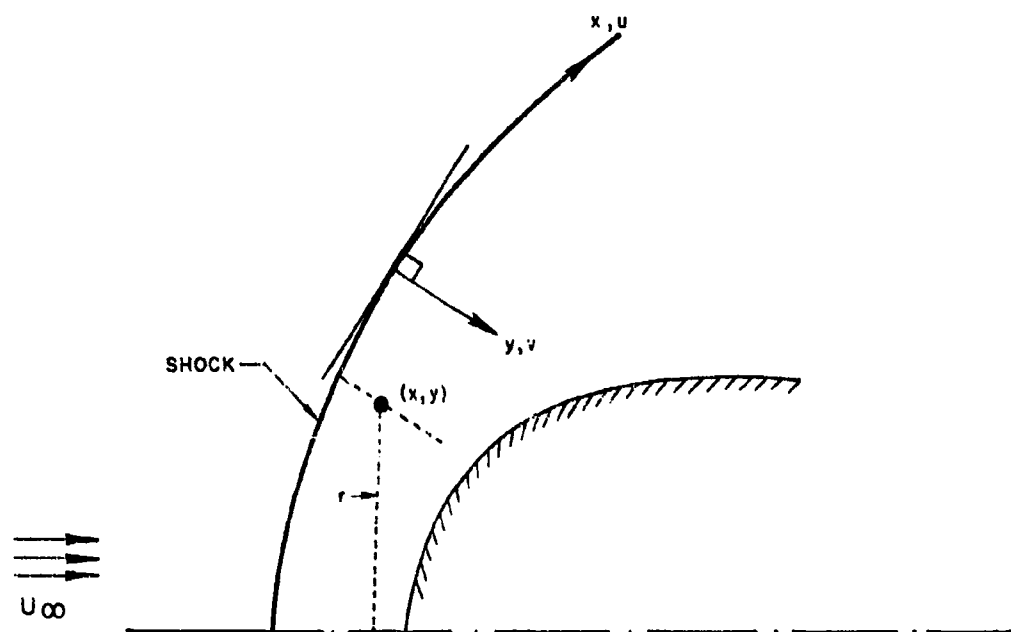


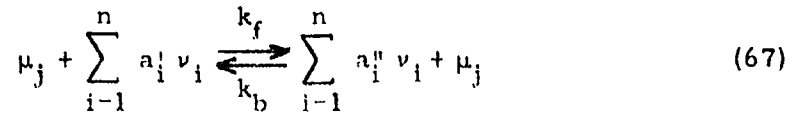
Figure 24. Shock-Oriented Curvilinear Coordinates

In Eq. (60) the mass rate of production of the component by chemical reactions, ω_i , is given by

$$\omega_i = \frac{M_i}{A} \frac{dv_i}{dt} \quad (66)$$

where A is the Avogadro's number, v_i is the number of particles of the i^{th} component per unit volume, (particle/cm³).

In general, chemical reactions can proceed in both forward and backward directions. A set of opposing chemical reactions may be represented by (Ref. 31),



where a_i' and a_i'' are stoichiometric constants.

In these representations, any "third body" chemical species, μ_j , which acts as an energy source or sink in a chemical reaction but is otherwise unchanged, is included.

The net rate of production of i^{th} species is then given by

$$\frac{dv_i}{dt} = (a_i'' - a_i') k_f \prod_{i=1}^n (v_i)^{a_i'} \mu_j + (a_i' - a_i'') k_b \prod_{i=1}^n (v_i)^{a_i''} \mu_j \quad (68)$$

At thermodynamic equilibrium there is no net change in composition, therefore, the rate constants k_b and k_f must be related through the equilibrium constant, \tilde{K} . That is,

$$(k_f/k_b) = \tilde{K} \equiv \prod_{i=1}^n (v_i, c)^{a_i'' - a_i'} \quad (69)$$

When multiple chemical reactions are involved, the net rate production of i th species can be obtained by summing Eq. (68) over all the chemical reactions in the system. Where \bar{K} is the equilibrium constant in the unit of (particle/cm³) while the rate constant, k , has the unit of [cm⁶/(sec particle²)]. In the case of atmospheric air the dominant chemical reactions with their respective rate constants are listed in Table 1.

The rate constants for all the chemical reactions with various "third bodies" used in this analysis are those given by AVCO.³² It should be understood that these numerical values of the reaction constants are to be considered as recommended estimates only. Modifications can readily be introduced when better experimental data become available. Related discussion on chemical kinetics may be found in Ref. 33.

Combining Eqs. (60), (66), (68), and (69) on the basis of chemical reactions and their rate constants given in Table 1, the following set of five equations may be obtained in place of Eq. (60):

$$\begin{aligned} \frac{\partial a_{O_2}}{\partial \bar{y}} = & \frac{L p_r \bar{m}_{O_2}}{\bar{m}_r u_r} \frac{\bar{p}}{\bar{v}} \left\{ k_D^1 \left[\frac{p_r}{K_{O_2}^{O_2}} \frac{\bar{p}}{\bar{T}} \frac{a_{O_2}^2}{\bar{m}_{O_2}^2} - \frac{a_{O_2}}{\bar{m}_{O_2}} \right] \left[\frac{a_N}{\bar{m}_N} + \frac{a_{N_2}}{\bar{m}_{N_2}} + \frac{a_{NO}}{\bar{m}_{NO}} \right] \right. \\ & + \frac{k_D^2}{k_1} \frac{a_{O_2}}{\bar{m}_{O_2}} + \frac{k_D^3}{k_D} \frac{a_O}{\bar{m}_O} \left. + k_2^1 \left[\frac{1}{K_{O_2, N}} \frac{a_{NO} a_O}{\bar{m}_{NO} \bar{m}_O} \right. \right. \\ & \left. \left. - \frac{a_{O_2} a_N}{\bar{m}_{O_2} \bar{m}_N} \right] + k_2^3 \left[\frac{a_{NO}^2}{\bar{m}_{NO}^2} - \frac{K_{O_2}^{O_2} K_P^{N_2}}{(K_P^{NO})^2} \frac{a_{N_2} a_{O_2}}{\bar{m}_{N_2} \bar{m}_{O_2}} \right] \right\} \\ & - \frac{\bar{u}}{\bar{v} (1 + \bar{K} \bar{y})} \frac{\partial a_{O_2}}{\partial \bar{x}} \end{aligned} \quad (70)$$

$$\begin{aligned}
\frac{\partial a_{N_2}}{\partial \bar{y}} = & \frac{L \rho_r^2 \bar{m}_{N_2}}{\bar{m}_r^2 u_r} \frac{\bar{p}}{\bar{v}} \left\{ k_R^1 \left[\frac{a_N^2}{\bar{m}_N^2 \bar{p}} - \frac{K_{N_2}^{N_2} a_{N_2}}{p_r \bar{m}_{N_2}} \frac{1}{\bar{T}} \right] \left[\frac{a_O}{\bar{m}_O} + \frac{a_{O_2}}{\bar{m}_{O_2}} \right. \right. \\
& \left. \left. + \frac{a_{NO}}{\bar{m}_{NO}} + \frac{k_R^2 a_{N_2}}{k_R^1 \bar{m}_{N_2}} + \frac{k_R^3 a_N}{k_R^1 \bar{m}_N} \right] \right\} \\
& + \frac{L \rho_r \bar{m}_{N_2}}{\bar{m}_r u_r} \frac{\bar{p}}{\bar{v}} \left\{ k_2^2 \left[\frac{a_{NO} a_N}{\bar{m}_{NO} \bar{m}_N} - \frac{1}{K_{N_2, O}} \frac{a_{N_2} a_O}{\bar{m}_{N_2} \bar{m}_O} \right] + k_2^3 \left[\frac{a_{NO}^2}{\bar{m}_{NO}^2} \right. \right. \\
& \left. \left. - \frac{K_{O_2}^{O_2} K_P^{N_2} a_{O_2} a_{N_2}}{\left[K_{NO}^P \right]^2 \bar{m}_{O_2} \bar{m}_{N_2}} \right] \right\} - \frac{\bar{u}}{\bar{v}(1 + \bar{K}\bar{y})} \frac{\partial a_{N_2}}{\partial \bar{x}} \quad (71)
\end{aligned}$$

$$\begin{aligned}
\frac{\partial a_{NO}}{\partial \bar{y}} = & \frac{L \rho_r^2 \bar{m}_{NO}}{\bar{m}_r^2 u_r} \frac{\bar{p}}{\bar{v}} \left\{ k_R^4 \left[\frac{a_N a_O}{\bar{m}_N \bar{m}_O} \bar{p} - \frac{K_P^{NO} a_{NO}}{p_r \bar{m}_{NO}} \frac{1}{\bar{T}} \right] \left[\frac{a_{O_2}}{\bar{m}_{O_2}} + \frac{a_{N_2}}{\bar{m}_{N_2}} \right. \right. \\
& \left. \left. + \frac{k_R^5}{k_R^4} \left(\frac{a_{NO}}{\bar{m}_{NO}} + \frac{a_O}{\bar{m}_O} + \frac{a_N}{\bar{m}_N} \right) \right] \right\} \\
& + \frac{L \rho_r}{\bar{m}_r u_r} \frac{\bar{m}_{NO} \bar{p}}{\bar{v}} \left\{ k_2^1 \left[\frac{a_{O_2} a_N}{\bar{m}_{O_2} \bar{m}_N} - \frac{1}{K_{O_2, N}} \frac{a_{NO} a_O}{\bar{m}_{NO} \bar{m}_O} \right] - k_2^2 \left[\frac{a_{NO} a_N}{\bar{m}_{NO} \bar{m}_O} \right. \right. \\
& \left. \left. - \frac{1}{K_{N_2, O}} \frac{a_{N_2} a_O}{\bar{m}_{N_2} \bar{m}_O} \right] - 2k_2^3 \left[\frac{a_{NO}^2}{\bar{m}_{NO}^2} \right. \right. \\
& \left. \left. - \frac{K_{O_2}^{O_2} K_P^{N_2} a_{O_2} a_{N_2}}{\left[K_{NO}^P \right]^2 \bar{m}_{O_2} \bar{m}_{N_2}} \right] \right\} - \frac{\bar{u}}{\bar{v}(1 + \bar{K}\bar{y})} \frac{\partial a_{NO}}{\partial \bar{x}} \quad (72)
\end{aligned}$$

$$\begin{aligned}
\frac{\partial a_O}{\partial \bar{y}} = & \frac{L p_r \bar{m}_O}{m_r u_r} \frac{\bar{p}}{\bar{v}} \left\{ 2k_D^1 \left[\frac{a_{O_2}}{\bar{m}_{O_2}} - \frac{p_r}{K_{P_{O_2}}} \frac{\bar{p}}{\bar{T}} \frac{a_{O_2}^2}{\bar{m}_O^2} \right] \left[\frac{a_N}{\bar{m}_N} + \frac{a_{N_2}}{\bar{m}_{N_2}} \right. \right. \\
& \left. \left. + \frac{a_{NO}}{\bar{m}_{NO}} + \frac{k_D^2}{k_D^1} \frac{a_{O_2}}{\bar{m}_{O_2}} + \frac{k_D^3}{k_D^1} \frac{a_O}{\bar{m}_O} \right] \right\} \\
& + \frac{L p_r^2 \bar{m}_O}{m_r^2 u_r} \frac{\bar{p}}{\bar{v}} \left\{ k_R^4 \left[\frac{K_P^{NO}}{p_r} \frac{a_{NO}}{\bar{m}_{NO}} \frac{1}{\bar{T}} - \frac{a_O a_N}{\bar{m}_O \bar{m}_N} \bar{p} \right] \left[\frac{a_{O_2}}{\bar{m}_{O_2}} \frac{a_{N_2}}{\bar{m}_{N_2}} \right. \right. \\
& \left. \left. + \frac{k_R^5}{k_R^4} \left(\frac{a_{NO}}{\bar{m}_{NO}} + \frac{a_O}{\bar{m}_O} + \frac{a_N}{\bar{m}_N} \right) \right] \right\} \\
& + \frac{L p_r \bar{m}_O}{m_r u_r} \frac{\bar{p}}{\bar{v}} \left\{ k_2^1 \left[\frac{a_{O_2} a_N}{\bar{m}_{O_2} \bar{m}_N} - \frac{1}{K_{O_2, N}} \frac{a_{NO} a_O}{\bar{m}_{NO} \bar{m}_O} \right] + k_2^2 \left[\frac{a_{NO} a_N}{\bar{m}_{NO} \bar{m}_N} \right. \right. \\
& \left. \left. - \frac{1}{K_{N_2, O}} \frac{a_{N_2} a_O}{\bar{m}_{N_2} \bar{m}_O} \right] \right\} - \frac{\bar{u}}{\bar{v}(1 + K\bar{y})} \frac{\partial a_O}{\partial \bar{x}} \quad (73)
\end{aligned}$$

$$\begin{aligned}
\frac{\partial a_N}{\partial \bar{y}} = & \frac{L p_r^2 \bar{m}_N}{m_r^2 u_r} \frac{\bar{p}}{\bar{v}} \left\{ 2k_R^1 \left(\frac{K_P^{N_2}}{p_r} \frac{a_{N_2}}{\bar{m}_{N_2}} \frac{1}{\bar{T}} - \frac{a_N^2}{\bar{m}_N^2} \bar{p} \right) \left[\frac{a_O}{\bar{m}_O} + \frac{a_{O_2}}{\bar{m}_{O_2}} \right. \right. \\
& \left. \left. + \frac{a_{NO}}{\bar{m}_{NO}} + \frac{k_R^2}{k_R^1} \frac{a_{N_2}}{\bar{m}_{N_2}} + \frac{k_R^3}{k_R^1} \frac{a_N}{\bar{m}_N} \right] \right\}
\end{aligned}$$

I

$$\begin{aligned}
& + \frac{L p_r^2 \bar{m}_N}{\bar{m}_r^2 u_r} \frac{\bar{p}}{\bar{v}} \left\{ k_R^4 \left[\frac{K_p^{NO}}{p_r} \frac{a_{NO}}{\bar{m}_{NO}} \frac{1}{T} - \frac{a_O a_N}{\bar{m}_O \bar{m}_N} \bar{p} \right] \left[\frac{a_{O_2}}{\bar{m}_{O_2}} + \frac{a_{N_2}}{\bar{m}_{N_2}} \right. \right. \\
& \quad \left. \left. + \frac{k_R^3}{k_R^4} \left(\frac{a_{NO}}{\bar{m}_{NO}} + \frac{a_O}{\bar{m}_O} + \frac{a_N}{\bar{m}_N} \right) \right] \right\} \\
& + \frac{L p_r \bar{m}_N}{\bar{m}_r u_r} \frac{\bar{p}}{\bar{v}} \left\{ k_2^1 \left[\frac{1}{K_{O_2, N}} \frac{a_{NO} a_O}{\bar{m}_{NO} \bar{m}_O} - \frac{a_{O_2} a_N}{\bar{m}_{O_2} \bar{m}_N} \right] \right. \\
& \quad \left. + k_2^2 \left[\frac{1}{K_{N_2, O}} \frac{a_{N_2} a_O}{\bar{m}_{N_2} \bar{m}_O} - \frac{a_{NO} a_N}{\bar{m}_{NO} \bar{m}_N} \right] \right\} \\
& - \frac{\bar{u}}{\bar{v}(1 + \bar{K} \bar{y})} \frac{\partial a_N}{\partial \bar{x}}
\end{aligned} \tag{74}$$

where

$$\begin{aligned}
\rho_i &= (\bar{m}_i v_i / A) \quad , \\
K_p^{O_2} &\equiv \frac{(p_O)^2}{p_{O_2}} \quad , \quad K_p^{N_2} \equiv \frac{(p_N)^2}{p_{N_2}} \quad , \quad K_p^{NO} \equiv \frac{p_O p_N}{p_{NO}} \\
K_{O_2, N} &\equiv \frac{p_{NO} p_O}{p_{O_2} p_N} \quad , \quad K_{N_2, O} \equiv \frac{p_O p_{N_2}}{p_{NO} p_N}
\end{aligned} \tag{75}$$

In obtaining the above equations, proper care has been taken to convert the rate constants k_f , k_b , in the unit of (cm³/particle sec) to k_D^j ,

k_R^j, k_1^j in the units given in Table 1. Furthermore, the following non-dimensional quantities have been introduced:

$$\begin{aligned}\bar{x} &= \frac{x}{L}, & \bar{y} &= \frac{y}{L}, & \bar{p} &= \frac{p}{p_r}, & \bar{\rho} &= \frac{\rho}{\rho_r} \\ \bar{T} &= \frac{T}{T_r}, & \bar{m}_i &= \frac{m_i}{m_r}, & \bar{u} &= \frac{u}{u_r}, & \bar{v} &= \frac{v}{u_r}, & \bar{K} &= K/L\end{aligned}\quad (76)$$

where $L, p_r, \rho_r, T_r, m_r, u_r$ are chosen reference quantities

$$u_r \equiv \sqrt{p_r/\rho_r}, \quad p_r = \rho_r \left(\frac{R}{m_r} \right) T_r. \quad (77)$$

In terms of these same non-dimensional quantities, Eq. (62) may be rewritten as:

$$\frac{\partial \bar{u}}{\partial \bar{y}} = \frac{-1}{\bar{v}(1 + \bar{K}\bar{y})} \left[\frac{1}{\bar{\rho}} \frac{\partial \bar{p}}{\partial \bar{x}} + \bar{K} \bar{u} \bar{v} + \bar{u} \frac{\partial \bar{u}}{\partial \bar{x}} \right] \quad (78)$$

Eq. (63) may be rewritten as:

$$\frac{\partial \bar{p}}{\partial \bar{y}} = \frac{-\bar{p}}{(1 + \bar{K}\bar{y})} \left[\bar{u} \frac{\partial \bar{v}}{\partial \bar{x}} + (1 + \bar{K}\bar{y}) \bar{v} \frac{\partial \bar{v}}{\partial \bar{y}} - \bar{K} \bar{u}^2 \right] \quad (79)$$

Eq. (61) may be rewritten as:

$$\begin{aligned}\frac{\partial \bar{p}}{\partial \bar{y}} &= \frac{-\bar{p}}{\bar{v}(1 + \bar{K}\bar{y})} \left[(1 + \bar{K}\bar{y}) \frac{\partial \bar{v}}{\partial \bar{y}} + \frac{\partial \bar{u}}{\partial \bar{x}} + \frac{\bar{u}}{\bar{\rho}} \frac{\partial \bar{p}}{\partial \bar{x}} \right. \\ &\quad \left. + (1 + \bar{K}\bar{y}) \frac{\bar{v}}{\bar{r}} \frac{\partial \bar{r}}{\partial \bar{y}} + \bar{v} \bar{K} + \frac{\bar{u}}{\bar{r}} \frac{\partial \bar{r}}{\partial \bar{x}} \right] \quad (80)\end{aligned}$$

Differentiating the equation of state, Eq. (65), with respect to y , we have,

$$\frac{1}{T} \frac{\partial T}{\partial y} = \frac{1}{p} \frac{\partial p}{\partial y} + \frac{1}{M} \frac{\partial M}{\partial y} - \frac{1}{\rho} \frac{\partial \rho}{\partial y} \quad (81)$$

where

$$\frac{\partial(1/M)}{\partial y} = - \sum_i \left[\frac{1}{M_i} \left(\frac{\partial a_i}{\partial y} \right) \right]$$

Dividing the partial differential form of the energy equation, Eq. (64), by the absolute temperature, we obtain,

$$\frac{1}{T} \frac{\partial T}{\partial y} \sum_i \left(a_i \frac{dh_i}{dT} \right) + \frac{1}{T} \sum_i \left(h_i \frac{\partial a_i}{\partial y} \right) + \frac{u}{T} \frac{\partial u}{\partial y} + \frac{v}{T} \frac{\partial v}{\partial y} = 0 \quad (82)$$

Substitution of (81) into (82) yields,

$$\sum_i \left(a_i \frac{dh_i}{dT} \right) \left[\frac{1}{p} \frac{\partial p}{\partial y} - M \sum_i \left(\frac{1}{M_i} \frac{\partial a_i}{\partial y} \right) - \frac{1}{\rho} \frac{\partial \rho}{\partial y} \right] + \frac{1}{T} \sum_i \left(h_i \frac{\partial a_i}{\partial y} \right) + \frac{u}{T} \frac{\partial u}{\partial y} + \frac{v}{T} \frac{\partial v}{\partial y} = 0 \quad (83)$$

Eliminating $(\partial p/\partial y)$ and $(\partial \rho/\partial y)$ from Eq. (83) by using Eq. (63) and Eq. (61) respectively, we obtain

$$\begin{aligned} & \left[\sum_i \left(a_i \frac{dh_i}{dT} \right) \left(\frac{M}{RT} v - \frac{1}{v} \right) - \frac{v}{T} \frac{\partial v}{\partial y} \right] = \left\{ \sum_i \left(a_i \frac{dh_i}{dT} \right) \frac{M}{RT(1+Ky)} \left(Ku^2 - u \frac{\partial v}{\partial x} \right) \right. \\ & - \left[\sum_i \left(a_i \frac{dh_i}{dT} \right) M \left[\sum_i \left(\frac{1}{M_i} \frac{\partial a_i}{\partial y} \right) \right] + \frac{1}{T} \sum_i \left(h_i \frac{\partial a_i}{\partial y} \right) + \frac{u}{T} \frac{\partial u}{\partial y} \right. \\ & \left. \left. + \frac{\sum_i \left(a_i \frac{dh_i}{dT} \right)}{v(1+Ky)} \left[\frac{\partial u}{\partial x} + \frac{u}{\rho} \frac{\partial \rho}{\partial x} + (1+Ky) \frac{v}{r} \frac{\partial r}{\partial y} + vK + \frac{u}{r} \frac{\partial r}{\partial x} \right] \right\} \quad (84) \end{aligned}$$

The non-dimensional form of Eq. (84) reads,

$$\begin{aligned} \left[\sum_i \left(a_i \frac{d\bar{h}_i}{dT} \right) \left(\bar{M} \frac{\bar{v}}{\bar{T}} - \frac{1}{\bar{v}} \right) - \frac{\bar{v}}{\bar{T}} \right] \frac{\partial \bar{v}}{\partial y} = & \left\{ \sum_i \left(a_i \frac{d\bar{h}_i}{dT} \right) \frac{\bar{M}}{\bar{T}(1 + \bar{K}_y)} \left(\bar{K} \bar{u}^2 - \bar{u} \frac{\partial \bar{v}}{\partial x} \right) \right. \\ & - \bar{M} \left[\sum_i \left(a_i \frac{d\bar{h}_i}{dT} \right) \right] \left[\sum_i \left(\frac{1}{\bar{M}_i} \frac{\partial a_i}{\partial y} \right) \right] + \frac{1}{\bar{T}} \sum_i \left(\bar{h}_i \frac{\partial a_i}{\partial y} \right) + \frac{\bar{u}}{\bar{T}} \frac{\partial \bar{u}}{\partial y} \\ & \left. + \frac{1}{\bar{v}(1 + \bar{K}_y)} \left[\sum_i \left(a_i \frac{d\bar{h}_i}{dT} \right) \right] \left[\frac{\partial \bar{u}}{\partial x} + \frac{\bar{u}}{\bar{p}} \frac{\partial \bar{p}}{\partial x} + (1 + \bar{K}_y) \frac{\bar{v}}{r} \frac{\partial \bar{r}}{\partial y} + \bar{K} \bar{v} + \frac{\bar{u}}{r} \frac{\partial \bar{r}}{\partial x} \right] \right\} \quad (85) \end{aligned}$$

where

$$\bar{h}_i = h_i / u_r^2 = \left[h_i / \left(\frac{p_r}{\rho_r} \right) \right]$$

The equation of state may be rewritten as,

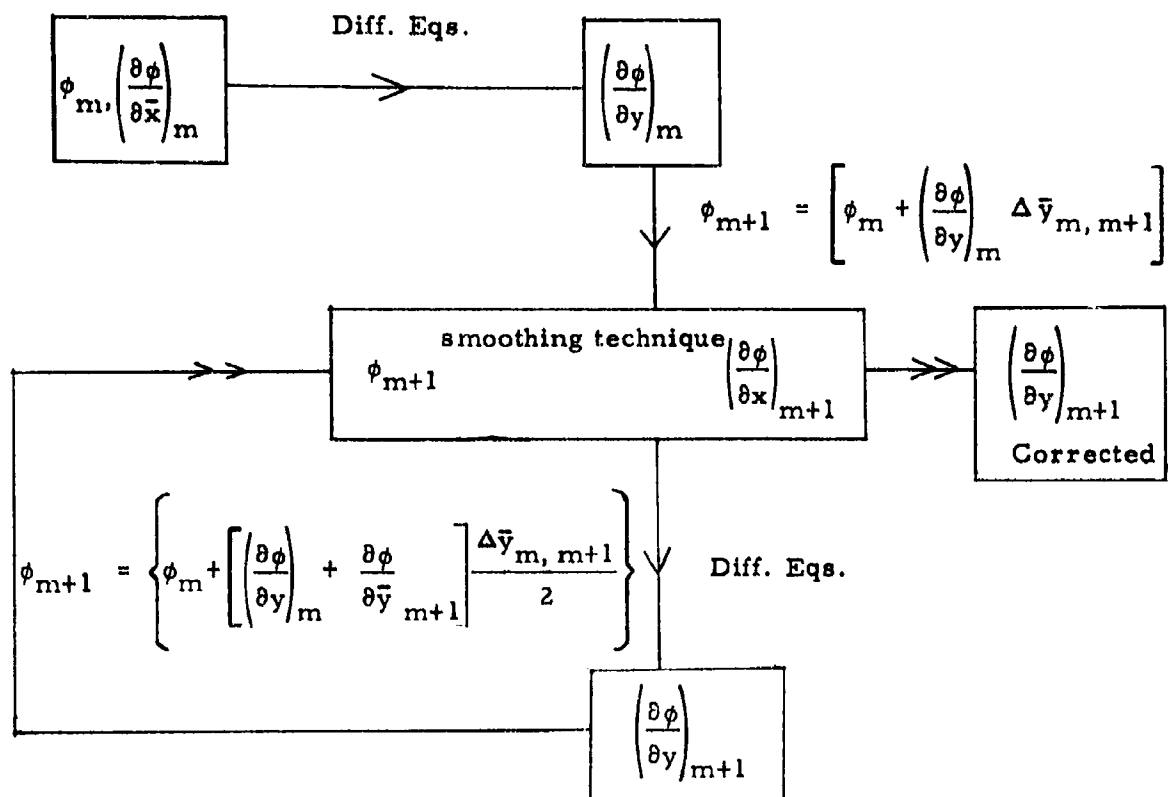
$$\left[\sum_i \left(\frac{a_i}{\bar{M}_i} \right) \right]^{-1} \bar{p} = \bar{p} \bar{T}$$

that is,

$$\left(\frac{a_O}{\bar{M}_O} + \frac{a_N}{\bar{M}_N} + \frac{a_{NO}}{\bar{M}_{NO}} + \frac{a_{O_2}}{\bar{M}_{O_2}} + \frac{a_{N_2}}{\bar{M}_{N_2}} \right)^{-1} \bar{p} = \bar{p} \bar{T} \quad (86)$$

Now the reacting flow field inside the shock layer is governed by the differential system consisting of Eqs. (70, 71, 72, 73, 74, 78, 79, 80, 85, 81, or 86). There are ten equations for the ten unknown quantities

$$a_O, a_N, a_{O_2}, a_{N_2}, a_{NO}, \bar{u}, \bar{v}, \bar{p}, \bar{p}, \bar{T}$$



Where ϕ denotes any of the dependent variables ϕ_m is the value of ϕ at the m th step. The values of $\phi_0, (\partial\phi/\partial\bar{x})_0$ are initially obtained from the oblique shock calculations. The computations are carried out by applying this scheme successively until the body streamline is established from continuity consideration.

Consider a streamline crossing the curved shock at an arbitrary point, B (Fig. 25). The amount of fluid enclosed between this streamline AB and the streamline along the axis of symmetry must be equal to the amount that crosses the section BC inside the shock layer. It should be understood that for the axisymmetric flow, the control surfaces will be obtained by revolving AB and BC about the axis of symmetry. The above mentioned physical condition may be represented by the following equation:

$$\pi r_s^2 \rho_\infty U_\infty = 2\pi \int_0^{y_w} r \rho u dy \quad . \quad (87)$$

Table I - Rate Constants For Chemical Processes

Reaction	Catalyst M	Rate Constant
$O_2 + M + 5.1 \text{ ev} \xrightleftharpoons[k_R]{k_D} O + O + M$	Ar, N, N ₂ , NO	$k_D^1 = \frac{3.6 \times 10^{18}}{T} \exp(-59373/T) \text{ cm}^3/\text{mole sec}$
	O ₂	$k_D^2 = \frac{3.2 \times 10^{19}}{T} \exp(-59373/T) \text{ cm}^3/\text{mole sec}$
	O	$k_D^3 = \frac{8.9 \times 10^{19}}{T} \exp(-59373/T) \text{ cm}^3/\text{mole sec}$
$N_2 + M + 9.8 \text{ ev} \xrightleftharpoons[k_R]{k_D} N + N + M$	Ar, O, O ₂ , NO	$k_R^1 = 1.7 \times 10^{14} \times (T/4500)^{-1.5} \text{ cm}^6/\text{mole}^2 \text{ sec}$
	N ₂	$k_R^2 = 5 \times 10^{14} \times (T/4500)^{-1.5} \text{ cm}^6/\text{mole}^2 \text{ sec}$
	N	$k_R^3 = 1 \times 10^{16} \times (T/4500)^{-1.5} \text{ cm}^6/\text{mole}^2 \text{ sec}$
$NO + M + 6.5 \text{ ev} \xrightleftharpoons[k_R]{k_D} N + O + M$	Ar, O ₂ , N ₂	$k_R^4 = 3.3 \times 10^{14} \times (T/4500)^{-1.5} \text{ cm}^6/\text{mole}^2 \text{ sec}$
	NO, O, N	$k_R^5 = 6.7 \times 10^{15} \times (T/4500)^{-1.5} \text{ cm}^6/\text{mole}^2 \text{ sec}$
$NO + O + 1.4 \text{ ev} \xrightleftharpoons[k_2]{k_1} O_2 + N$	$k_2^1 = 1 \times 10^{12} T^{0.5} \exp(-3120/T)$	$\text{cm}^3/\text{mole sec}$
$N_2 + O + 3.3 \text{ ev} \xrightleftharpoons[k_2]{k_1} NO + N$	$k_2^2 = 1.3 \times 10^{13}$	$\text{cm}^3/\text{mole sec}$
$N_2 + O_2 + 1.9 \text{ ev} \xrightleftharpoons[k_2]{k_1} NO + NO$	$k_2^3 = 2.6 \times 10^{23} \times T^{-2.5} \exp(-43030/T)$	$\text{cm}^3/\text{mole sec}$

SYMBOLS (Section II. B)

A	Avogadro number
h	specific enthalpy
\bar{h}	$= h/h_r$ where $h_r = (p_\infty/p_\infty)$
k	reaction rate constant, $\text{cm}^6/[\text{sec} (\text{particles})^2]$
k_D^j	dissociation rate constant, $[\text{cm}^3/(\text{mole sec})]$, see Table I
k_R^j	resombination rate constant, $[\text{cm}^6/(\text{mole}^2 \text{ sec})]$, see Table I
k_i^j	reaction rate constant, $[\text{cm}^3/(\text{mole sec})]$, see Table I
K	curvature
\bar{K}	$= K L = K \Omega_0$
\tilde{K}	Equilibrium constant, $\text{particles}/\text{cm}^3$
$K_p^{O_2}$	Equilibrium constant, $= (p_O^2/p_{O_2})$
$K_p^{N_2}$	Equilibrium constant, $= (p_N^2/p_{N_2})$
$K_{O_2, N}$	Equilibrium constant, $= [(p_{NO} p_O)/(p_{O_2} p_N)]$
$K_{N_2, O}$	Equilibrium constant, $= [(p_{N_2} p_O)/(p_{NO} p_N)]$
L	reference length, $= \Omega_0$
M	Mach number
\mathcal{M}	molecular weight
p	pressure
\bar{p}	$= (p/p_r)$, where $p_r = p_\infty$
r	radial distance from the axis of symmetry
\bar{r}	$= (r/\Omega_0)$

SYMBOLS (Continued)

R	Universal gas constant
t	time, sec
T	temperature, °K
\bar{T}	$= (T/T_r)$, where $T_r = T_\infty$
u	velocity component along the x direction
\bar{u}	$= u/u_r$, where $u_r = \sqrt{p_\infty/\rho_\infty}$
V_∞	free stream velocity
v	velocity component along the y-direction
\bar{v}	$= v/u_r$, where $u_r = \sqrt{p_\infty/\rho_\infty}$
x	coordinate distance along the shock surface
\bar{x}	$= x/\Omega_0$
y	coordinate distance normal to the shock surface
\bar{y}	$= y/\Omega_0$
α_i	$= \rho_i/\rho$
γ	= specific heats ratio for perfect gas
ν	= number density (particle/cm ³)
μ	= number density of "third body" species (particle/cm ³)
ρ	= density
σ	= shock angle
ϕ	= arbitrary function
Ω	= radius of curvature
Ω_0	= radius of curvature of shock wave at stagnation streamline

SYMBOLS (Continued)

Subscripts:

i	ith species or arbitrary index on rate constants
j	jth species or arbitrary index on rate constants
0	quantities at $x = c$ or sea level standard conditions
r	reference
s	conditions immediately behind the shock
w	wall conditions
∞	free stream

C. Hypersonic Wake Flow Studies

1. Introduction

As a body, such as a nose cone, enters the earth's atmosphere, it leaves a deposit of energy in the form of a trail. The rate at which energy is deposited is equal to the drag energy DU where D is the aerodynamic drag and U is the flight velocity. Part of this energy goes into heating the air and part goes into giving the air directed motion or momentum in the flight direction. It is the heated air that gives rise to observables in the form of an ionized trail and gas radiation.

After the air has passed through the bow shock, around the body, and through the trailing shock system, as shown in Fig. 26, it returns to ambient pressure at some distance x_0 behind the body. At this station a certain velocity and temperature profile would persist downstream if it were not for laminar diffusion, turbulent mixing, and radiation.

The amount of energy radiated from the wake is extremely small compared to the other controlling processes of energy transfer, and, hence, can be neglected in any wake analysis.

Figures 26a and 26b are schematics of what is qualitatively expected in the trail behind a blunt-nosed body and a slender-pointed body, respectively. Both bodies are assumed to have about the same base area and volume. The skin friction or viscous drags of the two bodies will be roughly the same at the same velocity and altitude. This fact is reflected in the temperature and velocity profiles shown in Figures 26a and 26b, and is represented by the small bumps at the center of the profiles. This is a schematic representation only. In reality the momentum defect associated with the bump should include not only skin friction drag, but nose drag in the case of a sharp body with a small nose radii, and the drag associated with the base recompression at the neck. This bump in the velocity profile constitutes the inner core and its spread will be dominated by viscous processes, either laminar or turbulent, if transition has occurred.

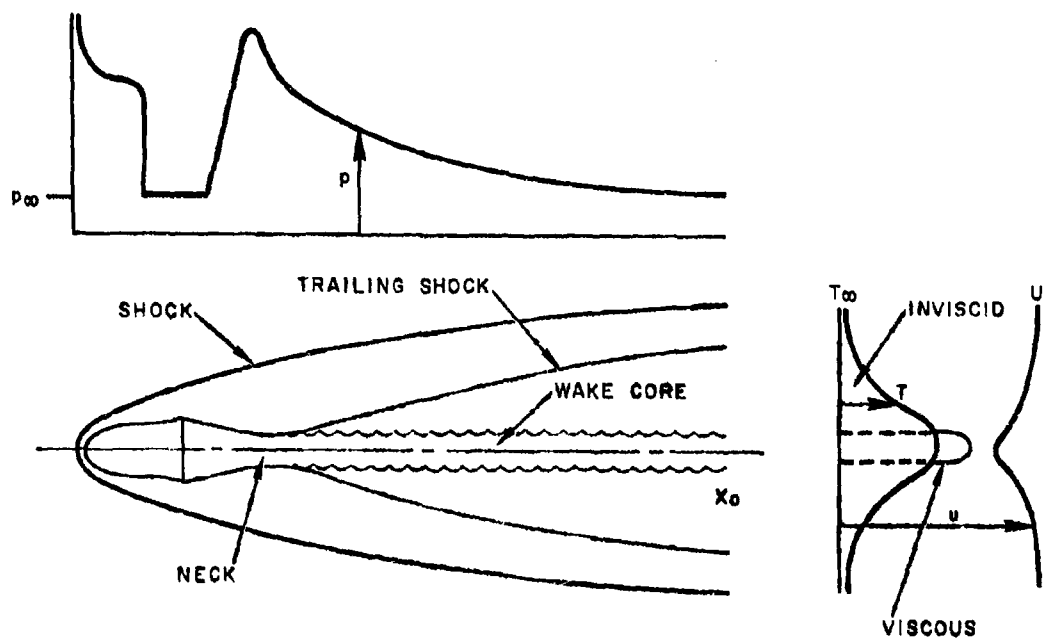


Figure 26a. Schematic of Flow Past a Blunt Body

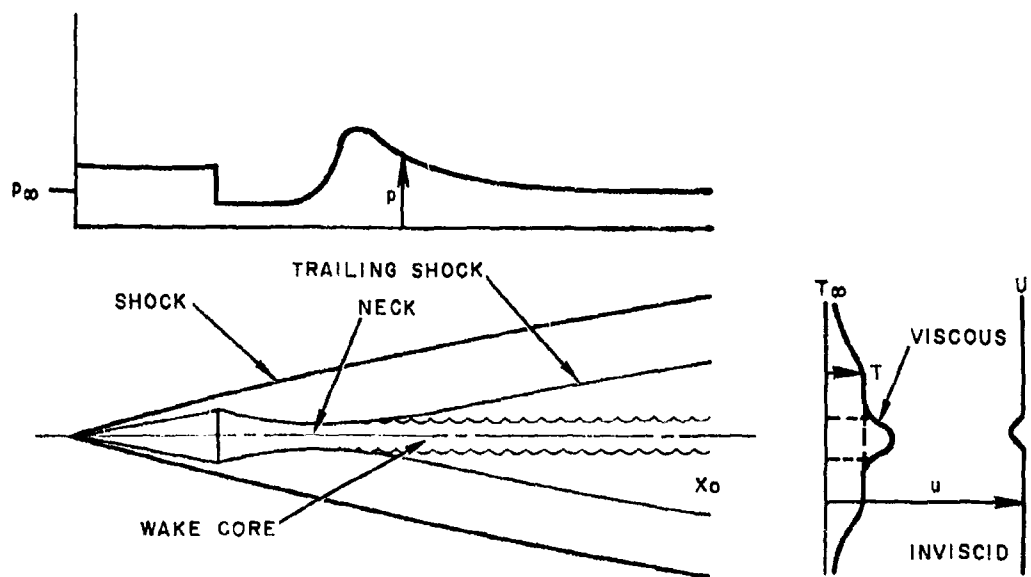


Figure 26b. Schematic of Flow Past a Sharp Body

The associated bump in the temperature or enthalpy profile will reflect, in addition, the heat taken out of the flow by the body, and its peak will, therefore, be much lower than in the case of an insulated body. As will become apparent in the analysis, heat transfer to the body plays a dominant role in erasing observables in the wake of a sharp body which are dependent on the maintenance of a high-temperature environment. Although the heat transfer to the blunt body is of the same order as the heat transfer to the sharp body at the same velocity and altitude, a high-temperature environment is maintained by the high temperature air that has passed through the steep portion of the bow shock and surrounds the viscous core as shown in Fig. 26a, so that in the blunt-body case heat transfer to the body does not play an important role in erasing observables.

2. The Spread of Turbulence in Axisymmetric Wakes

This section presents a simplified analysis of the spread of turbulence in the trail wherein certain simplifying assumptions are made. These assumptions may be summarized:

- a. Equilibrium flow,
- b. Negligible radiation,
- c. Negligible laminar diffusion compared to turbulent mixing,
and
- d. Turbulence originates in the viscous core or on the body and is fully developed and in equilibrium by the time it has reached the 50 radii station.

Turbulence is thus confined to a circular core, the front of which moves out and "swallows up" mass from the outer entropy trail. Eventually the front will have moved out into the outer cool air at the edge of the entropy trail, and the entire trail begins to cool by turbulent mixing. As to how long this process takes (or how far downstream) before the entropy trail produced by the normal portion of the shock of a blunt body is cooled

sufficiently to erase any observables such as electron density, will depend upon certain initial parameters at the station x_0 . These parameters are:

- a. Total drag coefficient,
- b. Ratio of drag associated with the turbulent inner core to the total drag,
- c. Width of the entropy trail, and
- d. Width of turbulent inner core.

3. Basic Equations

We will use the stream function ψ and x as independent variables in this analysis. The stream function is related to the physical radial coordinate r through the formula

$$\psi = 2\pi \int_0^r \rho u r dr \quad (88)$$

and r can be found from the inverse relation

$$r^2 = \frac{1}{\pi} \int_0^\psi \frac{d\psi}{\rho u} \quad (89)$$

Thus the radius R of the stream tube ψ in the free stream up to the bow shock is

$$R^2 = \frac{\psi}{\pi \rho_\infty U_\infty} \quad (90)$$

Let ψ_f be the stream tube which enters the effective front of the inner turbulent core at x and let ψ_{f_0} be the stream tube that enters at x_0 , the origin of calculation. Then from conservation of momentum in the x -direction we have

$$I = \int_0^{\psi_f} u_t d\psi = \int_0^{\psi_{f_0}} u_{t_0} d\psi + \int_{\psi_{f_0}}^{\psi_f} u_i d\psi \quad (91)$$

since there is no x-momentum transported through stream tube boundaries in the outer inviscid flow and the pressure is assumed to be constant.

A second relation is found, the integral relation between the kinetic energy and the dissipation in the turbulent core, viz.

$$\frac{d}{dx} \int_0^{\psi_f} \frac{1}{2} u_t^2 d\psi = \frac{1}{2} u_f^2 \frac{d\psi_f}{dx} - 4\pi^2 \int_0^{\psi_f} \epsilon_t r^2 \rho_t u_t \frac{2u_t^2}{\psi} d\psi \quad (92)$$

By substituting the profile

$$u_t = u_a + (u_f - u_a) \frac{\psi}{\psi_f} \quad (93)$$

into the integral relations (91) and (92) one obtains

$$\frac{1}{2} (u_f + u_a) \psi_f = \frac{1}{2} (u_{f_0} + u_{a_0}) \psi_{f_0} + \int_{\psi_{f_0}}^{\psi_f} u_t d\psi \quad (94)$$

$$\frac{1}{b} (u_f - u_a) \frac{du_a}{dx} \psi_f = 4\pi^2 \int_0^{\psi_f} \epsilon_t r^2 \rho_t u_t (u_f - u_a)^2 \frac{1}{\psi^2} d\psi \quad (95)$$

Where both Eq. (94) and its differential form were used in reducing the left hand side in Eq. (92) to that in Eq. (95). ψ_f , u_a , and u_f are assumed to be purely functions of x with initial values of ψ_{f_0} , u_{a_0} , and u_{f_0} at $x = x_0$. Equation (95) can then be further reduced to

$$\frac{du_a}{dx} = 24\pi^2 \frac{u_f - u_a}{\psi_f^3} \int_0^{\psi_f} \epsilon_t r^2 \rho_t u_t d\psi \quad (96)$$

In order to obtain a simple evaluation of the dissipation integral on the right hand side of Eq. (96) we restrict ourselves to the case where the

variations of velocity and density are small across the core. For this case we make the "incompressible" assumption

$$r^2 = \frac{\psi}{\pi \rho_t u_t} = \frac{\psi}{\pi \rho_f u_f} \quad (97)$$

and approximate ϵ_t by

$$\epsilon_t = K \rho_f r_f |u_f - u_a| = \frac{K}{\sqrt{\pi}} \sqrt{\frac{\psi_f \rho_f}{u_f}} |u_f - u_a| \quad (98)$$

Substituting these into (96) we obtain

$$\frac{du_a}{dx} = 12K \sqrt{\frac{\rho_f}{\psi_f u_f}} |u_f - u_a| (u_f - u_a) \quad (99)$$

Now from the relation (94) we obtain u_a in terms of u_f and an expression for du_a/dx ;

$$u_a = \frac{2}{\psi_f} \int_{\psi_{f0}}^{\psi_f} u_i d\psi + \frac{(u_{f0} + u_{a0}) \psi_{f0}}{\psi_f} - u_f \quad (100)$$

$$\frac{du_a}{dx} = \left[\frac{2u_f}{\psi_f} - \frac{du_f}{d\psi_f} - (u_{f0} + u_{a0}) \frac{\psi_{f0}}{\psi_f^2} - \frac{2}{\psi_f^2} \int_{\psi_{f0}}^{\psi_f} u_i d\psi \right] \frac{d\psi_f}{dx} = \frac{du_a}{d\psi_f} \frac{d\psi_f}{dx} \quad (101)$$

Since u_i is assumed to be known as a function of ψ , it is a simple matter to obtain x as a function of ψ_f by numerical integration of Eq. (99).

We have

$$\int_{\psi_{f0}}^{\psi_f} \frac{\frac{du_a}{d\psi_f}}{|u_f - u_a| (u_f - u_a)} \sqrt{\frac{\psi_f u_f}{\rho_f}} d\psi_f = 12K \sqrt{\pi} (x - x_0) \quad (102)$$

From the graph of x vs ψ_f we can obtain ψ_f vs x and, hence, the flow quantities and equilibrium electron densities as a function of x and ψ and ultimately as a function of x and r through the relation (89).

This formulation is for an arbitrary u_i as a function of ψ . We shall look at the special case where u_i can be approximated by

$$u_i(\psi) = U_\infty (1 - a e^{-b\psi}) \quad (103)$$

This distribution, by the proper choice of a and b , can be made to fit the velocity defect produced by a blunt body fairly well. It gives the bell-shaped nearly Gaussian curve for the outer entropy trail shown in Fig. 26a when plotted in the physical coordinate r . (Note that $\psi \sim r^2$ from Eq. (88).)

At the initial station $x = x_0$ let the drag associated with the inner turbulent core be D_w and let D be the total drag. We then have

$$D_w = \int_0^{\psi_f} (U_\infty - u_t) d\psi = \frac{1}{2} (u_{f_0} - u_{a_0}) \psi_{f_0} \quad (104)$$

$$\begin{aligned} D - D_w &= (U_\infty - u_{f_0}) \psi_{f_0} + \int_{\psi_{f_0}}^{\infty} (U_\infty - u_i) d\psi = (U_\infty - u_{f_0}) \psi_{f_0} \\ &+ \frac{a}{b} U_\infty e^{-b\psi_{f_0}} = \left(\frac{1}{b} + \psi_{f_0} \right) (U_\infty - u_{f_0}) \end{aligned} \quad (105)$$

from which one readily obtains the relation

$$\psi_{f_0} = \frac{2 D_w}{u_{f_0} - u_{a_0}} \quad (106)$$

We shall introduce at this point the dimensionless quantities:

$$u^* = u/U_{\infty} \quad (107)$$

$$\rho^* = \rho/\rho_{\infty} \quad (108)$$

$$T^* = T/T_{\infty} = \rho_{\infty}/\rho = 1/\rho^* \text{ (since } p = \text{const.} = p_{\infty}) \quad (109)$$

$$C_D = D/\frac{1}{2} \rho_{\infty} U_{\infty}^2 A \quad (110)$$

$$C_{D_w} = D_w/\frac{1}{2} \rho_{\infty} U_{\infty}^2 A \quad (111)$$

$$k = C_{D_w}/C_D \quad (112)$$

$$\psi^* = \psi/\psi_b \quad (113)$$

$$\bar{\psi}^* = 1/b\psi_b \quad (114)$$

$$\eta = b\psi_f = \psi_f^*/\bar{\psi}^* \quad (115)$$

$$C_D^* = C_D/\bar{\psi}^* \quad (116)$$

U_{∞} = flight speed

ρ_{∞} = atmospheric density at flight altitude

T_{∞} = absolute temperature at flight altitude

p_{∞} = ambient pressure at flight altitude

A = re-entry body maximum x-sectional area = πr_b^2

r_b = maximum body radius

ψ_b = $\rho_{\infty} U_{\infty} A$ = stream function value of free-stream tube equal to body x-sectional area

D = total drag

D_w = drag contained in turbulent core at the start of calculation

\dot{Q} = total heat transfer rate to the body

\dot{Q}^* = $\dot{Q}/\frac{1}{2} U_{\infty}^2 \psi_b \bar{\psi}^*$ = dimensionless heat transfer rate coefficient.

Equation (101) can then be written in non-dimensional form, viz.

$$\int_{\eta_0}^{\eta} \frac{\frac{du_a^*}{d\eta}}{|u_f^* - u_a^*|(u_f^* - u_a^*)} \eta u_f^* T_f^* d\eta = \frac{12K}{\sqrt{\psi^*}} \left(\frac{x - x_0}{r_b} \right) \quad (117)$$

where

$$u_f^* = 1 - \frac{1}{2} C_D^* \frac{1-k}{1+\eta_0} e^{\eta_0} e^{-\eta}, \quad \left(a = \frac{1}{2} C_D^* \frac{1-k}{1-\eta_0} e^{\eta_0} \right) \quad (118)$$

$$u_a^* = \frac{2}{\eta} \int_{\eta_0}^{\eta} u_f^* d\eta + \frac{\eta_0}{\eta} \left(2 - \frac{k C_D^*}{\eta_0} \right) - u_f^* = 1 - \frac{C_D^*}{\eta} + \frac{1}{2} - \frac{1-k}{1+\eta_0} C_D^* e^{\eta_0} \left(1 + \frac{2}{\eta} \right) e^{-\eta} \quad (119)$$

$$u_f^* - u_a^* = \frac{C_D^*}{\eta} \left[1 - \frac{1-k}{1+\eta_0} e^{\eta_0} (1+\eta) e^{-\eta} \right] \quad (120)$$

$$\frac{du_a^*}{d\eta} = \frac{C_D^*}{\eta^2} \left[1 - \frac{1-k}{1+\eta_0} e^{\eta_0} \left(1 + \eta + \frac{\eta^2}{2} \right) e^{-\eta} \right] \quad (121)$$

$$T_f^* = 1 + \frac{\gamma-1}{2} M_{\infty}^2 \left(1 - u_f^{*2} \right) \quad (122)$$

$$T_a^* = 1 + \frac{\gamma-1}{2} M_{\infty}^2 \left(1 - u_a^{*2} - Q^* \frac{2}{\eta} \right) \quad (123)$$

$$\eta_0 = \frac{k C_D^*}{u_{f_0}^* - u_{a_0}^*} \quad (124)$$

It can be seen immediately that, if Eqs. (120) and (121) are substituted into Eq. (117), a factor $1/C_D^*$ can be pulled out. Thus multiplying Eq. (117) by C_D^* we obtain

$$\int_{\eta_0}^{\eta} F(\dot{Q}^*, M_{\infty}^2, \gamma, k, \eta_0, C_D^*; \eta) d\eta = \frac{12 K C_D^*}{\sqrt{\psi^*}} \frac{x - x_0}{r_b} = \xi \quad (125)$$

with

$$F = \frac{1 - \frac{1-k}{1+\eta_0} e^{\eta_0} \left(1 + \eta + \frac{\gamma^2}{2}\right) e^{-\eta}}{\left| 1 - \frac{1-k}{1+\eta_0} e^{\eta_0} (1+\eta) e^{-\eta} \right| \left[1 - \frac{1-k}{1+\eta_0} e^{\eta_0} (1+\eta) e^{-\eta} \right]} \sqrt{\eta u_f^* T_f^*} \quad (126)$$

4. Discussion and Numerical Examples

Examination of Eq. (125) and (126) reveals that the major parameters that control the spreading of the turbulent core occur only in the combinations

$$C_D^*, \frac{1-k}{1+\eta_0} e^{-\eta_0}, \frac{\gamma-1}{2} M_{\infty}^2, \frac{12 K C_D^*}{\sqrt{\psi^*}}, \frac{k C_D^*}{u_{f_0}^* - u_{a_0}^*} = \eta_0$$

and that $(x - x_0)/r_b$ can be expressed entirely in terms of these parameters. It can further be shown that these parameters can all be expressed in terms of

$$\gamma, M_{\infty}, K, C_D, k, T_{f_0}^*, u_{f_0}^* - u_{a_0}^*$$

Although the exponential variation of velocity given by Eq. (103) was chosen on the basis of a good fit for a blunt body with a spherical nose, the approximation can still be used for sharp bodies, such as a cone, without losing any of the salient features in describing the turbulent core

spreading and temperature on the axis as a function of $(x - x_0)/r_b$. This is due to the fact that, for a sharp body, the radial distribution of velocity and temperature in the inviscid flow is fairly flat and the gradients at the edges are not important. This is demonstrated in the two numerical calculations discussed in the ensuing paragraphs.

Two numerical calculations at 150,000 ft and Mach 20 are presented; one for a typical blunt body such as that shown in Fig. 26a and one for a typical sharp body shown in Fig. 26b. The drag contained in the turbulent core bucket is assumed to be the same, that is, $C_{D_w} = .06$. This, in both cases, includes the skin friction and base drag, plus nose drag in the case of the sharp body. At 150,000 ft, the skin friction coefficient is about 0.03, and using Reynolds analogy, the heat transfer coefficient is $\dot{Q}/\frac{1}{2} \rho_\infty U_\infty^3 A \doteq 0.015$. These values were assumed for both cases. Both calculations were started with the assumption that the velocity on the axis was zero at the beginning which would be the case at the effective rear stagnation point. Each case will now be discussed separately.

a. Blunt Body

A typical pressure drag coefficient for a blunt body is 0.54, giving a total drag coefficient of $C_D = 0.6$ with $k = 0.1$. The results are shown in Fig. 27 where η , T_f^* and T_a^* with and without heat transfer are plotted against $(x - x_0)/r_b$. A measure of how far the front has moved laterally in terms of Gaussian widths of the entropy trail is given by η . It can be seen that in the blunt body case, the front must move many Gaussian widths before the center of the turbulent core begins to cool. This distance is of the order of a hundred body radii. The solid curve for T_a^* is the temperature ratio on the axis for an insulated body, while the dashed curve is for the assumed value of the heat transfer rate. It can be seen that the heat transfer rate to the body has little effect in depressing the temperature except at the very beginning where, for $u_a^* = 0$, T_a^* is about 0.56 times the free stream stagnation temperature (strictly speaking T^* is the enthalpy ratio and not the temperature ratio).

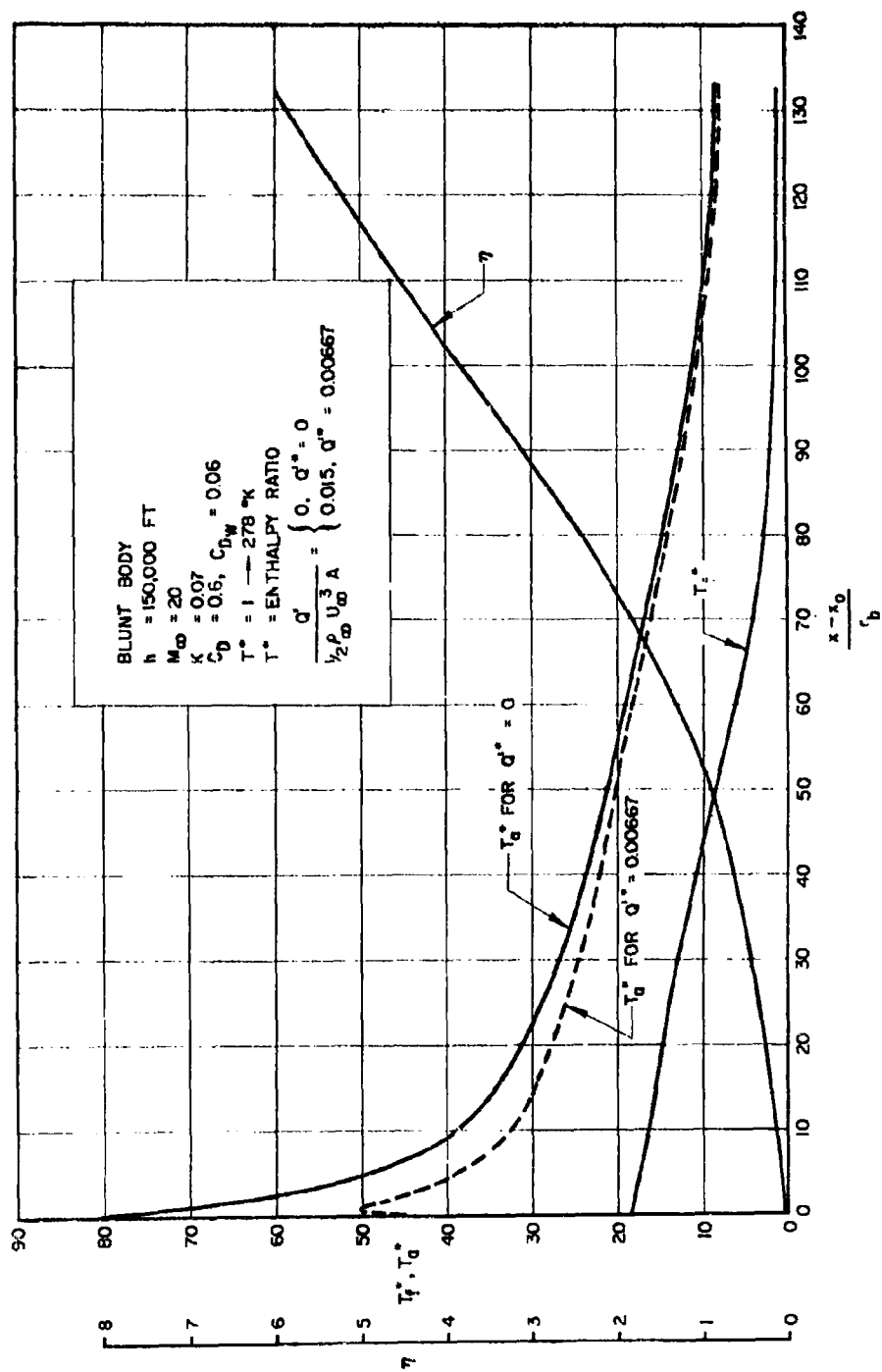


Figure 27. Wake Temperature Decay for Blunt Body in Hypersonic Flow

It can be concluded that for a typical blunt body with a two-foot diameter the temperatures will be sufficiently high to produce large amounts of radiation and sustain high electron concentrations visible to radar. Furthermore, the width of the turbulent core becomes very large for the blunt body case, as evidenced by the large values of η in terms of body radii. When T_a^* has reached roughly half the value of $T_{f_0}^*$, the initial front temperature in the entropy trail, η has the value 5 corresponding to $r_f/r_b = 18.1$ as calculated from Eq. (89), and $(x - x_0)/r_b$ is 117.

b. Sharp Body

A typical pressure drag coefficient for a sharp body, say a 10° half angle cone or an equivalent ogive, is 0.06 giving a total drag coefficient of $C_D = 0.12$ with $k = 0.5$. The results are shown in Fig. 28 where the same quantities are plotted as in the blunt body case. It can be seen that the wake is cooled in a much shorter length than in the blunt body case. The temperature on the axis has reached the value $T_a^* = 9$ at a value of $(x - x_0)/r_b = 33$, with $\eta = 2.1$ for a value of $r_f/r_b = 5.4$.

It can be concluded that for a typical sharp body the dimensions of the high temperature region in the wake are about a factor of three less than for the blunt body case. The heat transfer rate to the body has a more significant effect on the reduction of these dimensions than in the blunt body case.

The values of the parameters chosen for the sharp body are conservative and they tend to make the wake larger than that which might actually be expected at this altitude.

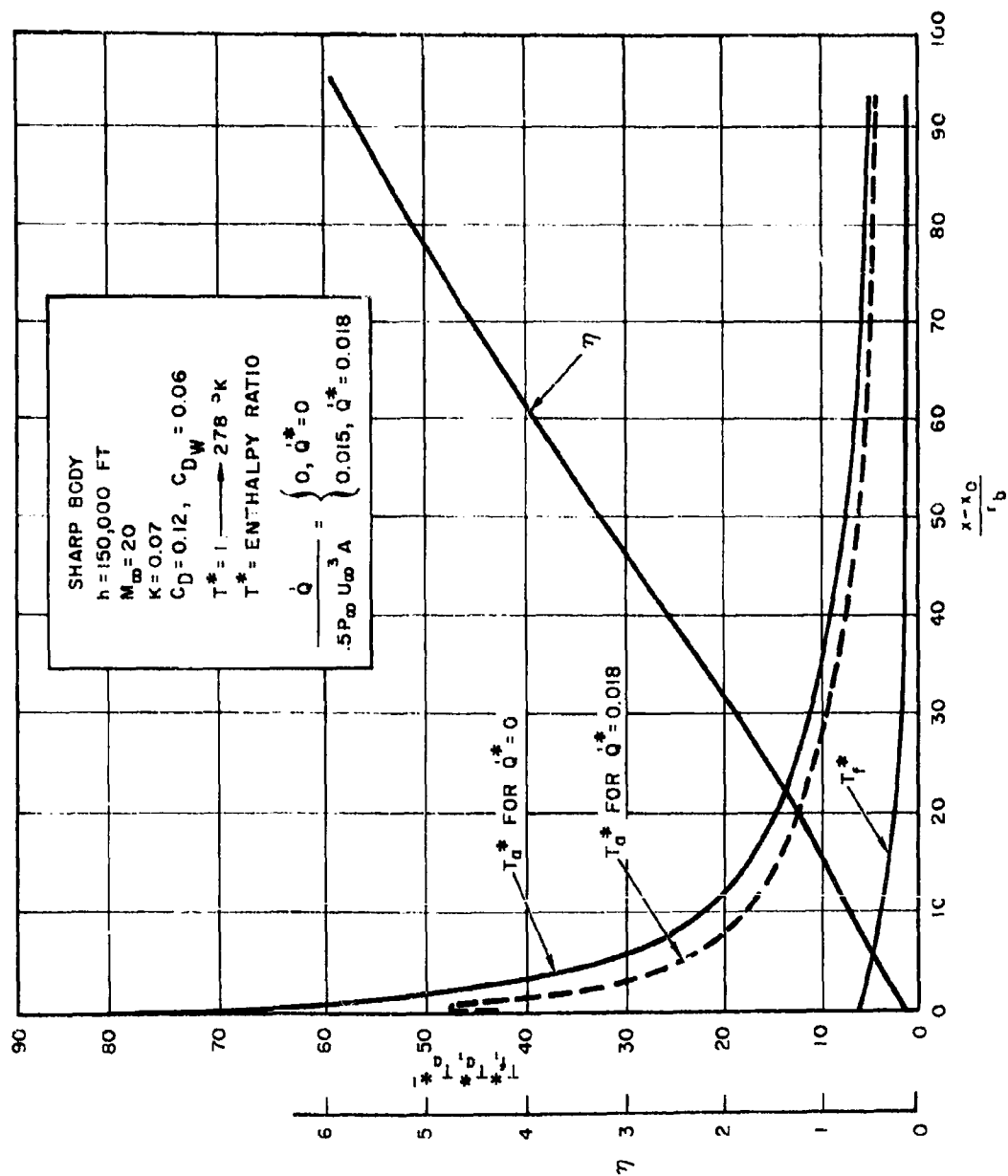


Figure 28. Wake Temperature Decay for Slender Body in Hypersonic Flow

III. EXPERIMENTAL INVESTIGATIONS

A. Stagnation Point Heat Transfer Measurements in Hypersonic Low Reynolds Number Flows

1. Introduction

In determining the point at which protective fairings for delicate payloads should be jettisoned during the launch trajectory of satellites vehicles, free molecule flow heat transfer rates have been assumed. Calculations based on this assumption provide the maximum heat transfer rate predictions, and hence, the maximum payload protective fairing requirements. As a result, the tendency has been to carry the fairings to altitudes which are much beyond optimum because of the uncertainty of the heat transfer rates in the very high atmosphere. These rates were not significant relative to exit and re-entry heat rates and these unknowns were tolerable. Now situations are arising where it is no longer advisable to ignore these uncertainties. Also theoretical analysis³⁴ in the low density regime is, for the most part, unsubstantiated by experiment. It is, therefore, the purpose of this study to attempt to measure the stagnation point heat transfer rates to cylinders and spheres in the hypersonic shock tunnel at flow Mach numbers from 13 to 23. The Reynolds number range to be covered is from 5 to 500, based on leading edge diameter, corresponding to the regime between free molecule flow and the continuum regime.

Because of its high reservoir stagnation temperature, the shock tunnel is an instrument peculiarly suited to making measurements at high Mach numbers and low Reynolds numbers typical of the high altitude portions of the launch trajectory of satellite vehicles. Furthermore, the shock tunnel can yield a variety of stagnation pressures, and hence, Reynolds numbers for a given stagnation temperature. The chief drawback inherent in shock tunnels is the comparatively short time interval during which measurements can be made. As a result, equilibrium conditions between the flow and the measuring instrument usually cannot be obtained and must

be inferred from the transient response of the measuring device. In this report heat transfer rate measurements determined from the transient response of thin film resistance thermometers mounted at the stagnation point of models will be described and the results of the measurements presented. The shock tunnel facility in which these tests were made is shown in Fig. 29.

2. Theoretical Predictions

Probstein and Kemp³⁴ have considered the problem of calculating the aerodynamic heating to be expected in hypersonic rarified gas flows, where the mean free path becomes too large for the use of the inviscid flow-boundary layer approach and too small for the free molecule flow regime to apply. They have solved the Navier stokes equations for two sets of boundary conditions; (1) a "viscous layer" class in which a thin shock wave exists, but the region between the shock and the blunt body is fully viscous, and (2) a "merged layer" class representing a more rarified condition. In the merged layer the shock wave is no longer thin and the Navier stokes equations are used to provide a solution which includes the shock structure and free stream conditions as outer boundary conditions.

From this analysis a deviation is predicted in the stagnation point heat transfer rate from that expected on the basis of extrapolated boundary layer theory. The viscous layer theory predicts higher heat transfer to both spheres and cylinders normal to the flow as the Reynolds number (based on nose diameter) is decreased to the order of 10.

The "incipient merged layer" theory modifies the heat transfer rates to values which are less than in the viscous layer, but greater than in the boundary layer theory. The predicted results for spheres and cylinders are shown in Fig. 30a and 30b. Although an incipient merged layer prediction for the cylinder is not made, it is easy to suppose that it lies between the viscous layer and boundary layer value. These curves were computed on the basis of a density ratio across the shock of 0.1 and a γ for the gas of 11/9.

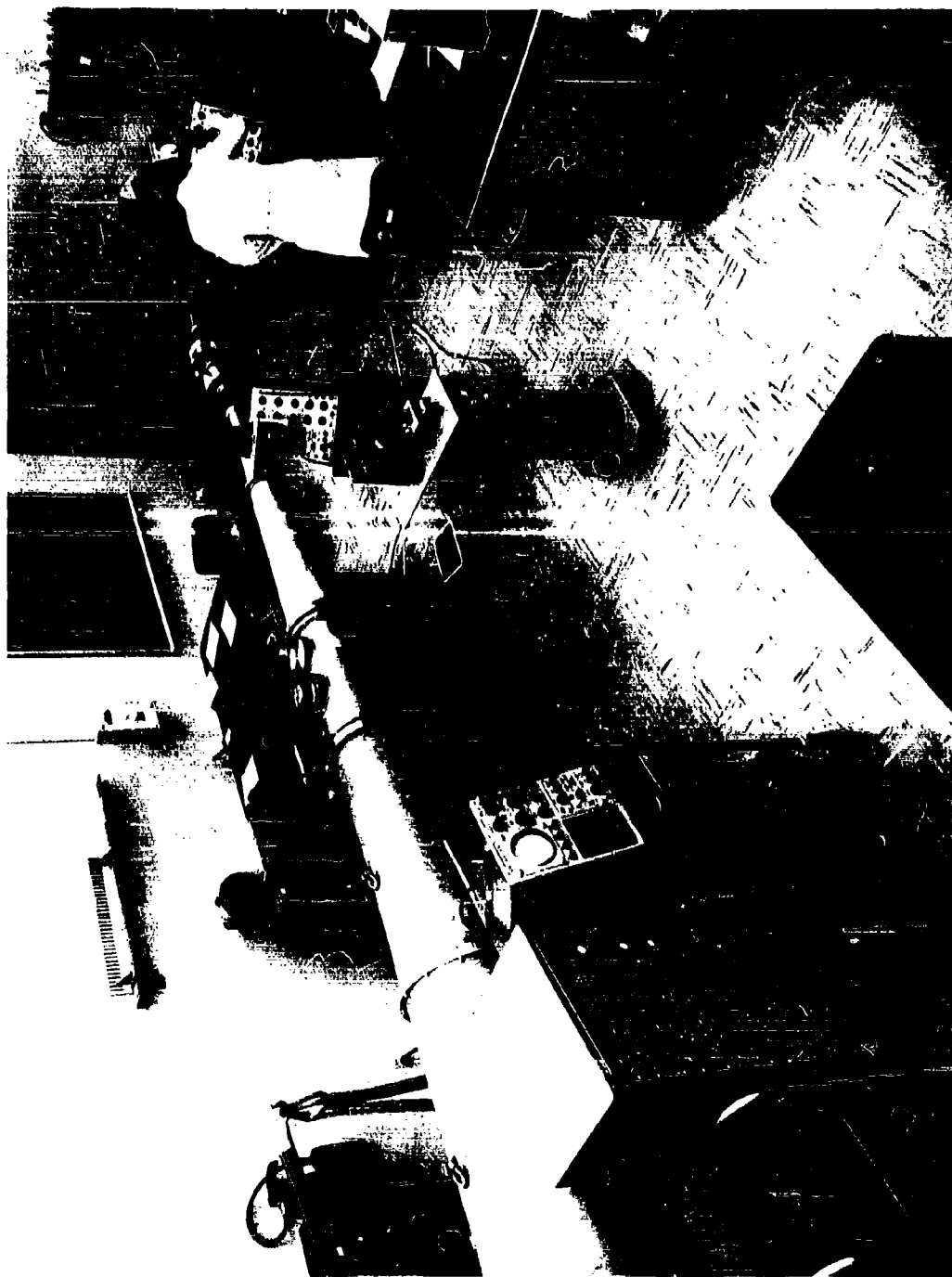


Figure 29. View of Shock Tunnel Showing 12-inch Test Section

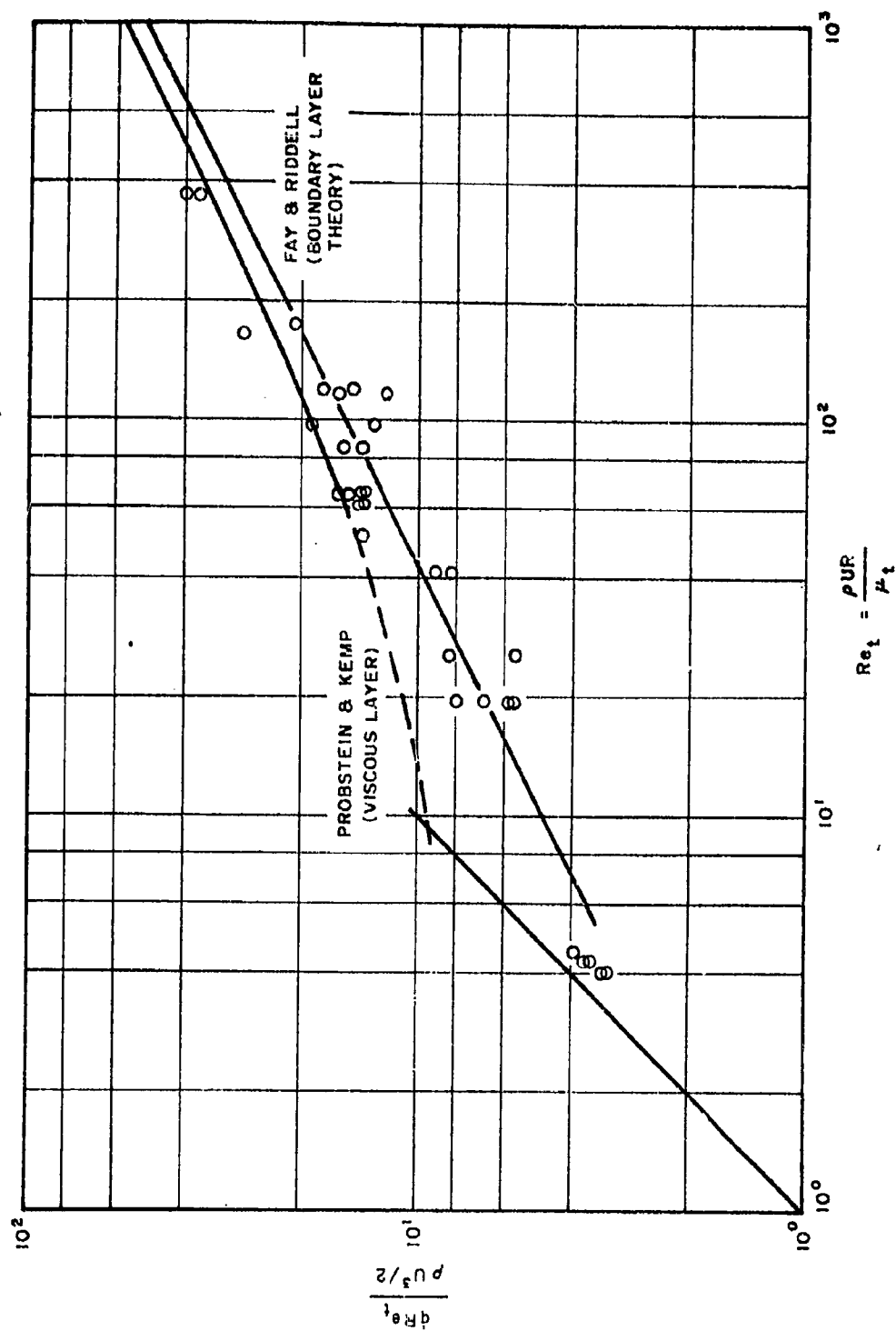


Figure 30a. Heat Transfer Rate to Cylinders Normal to the Flow as a Function of Stagnation Point Reynolds Number

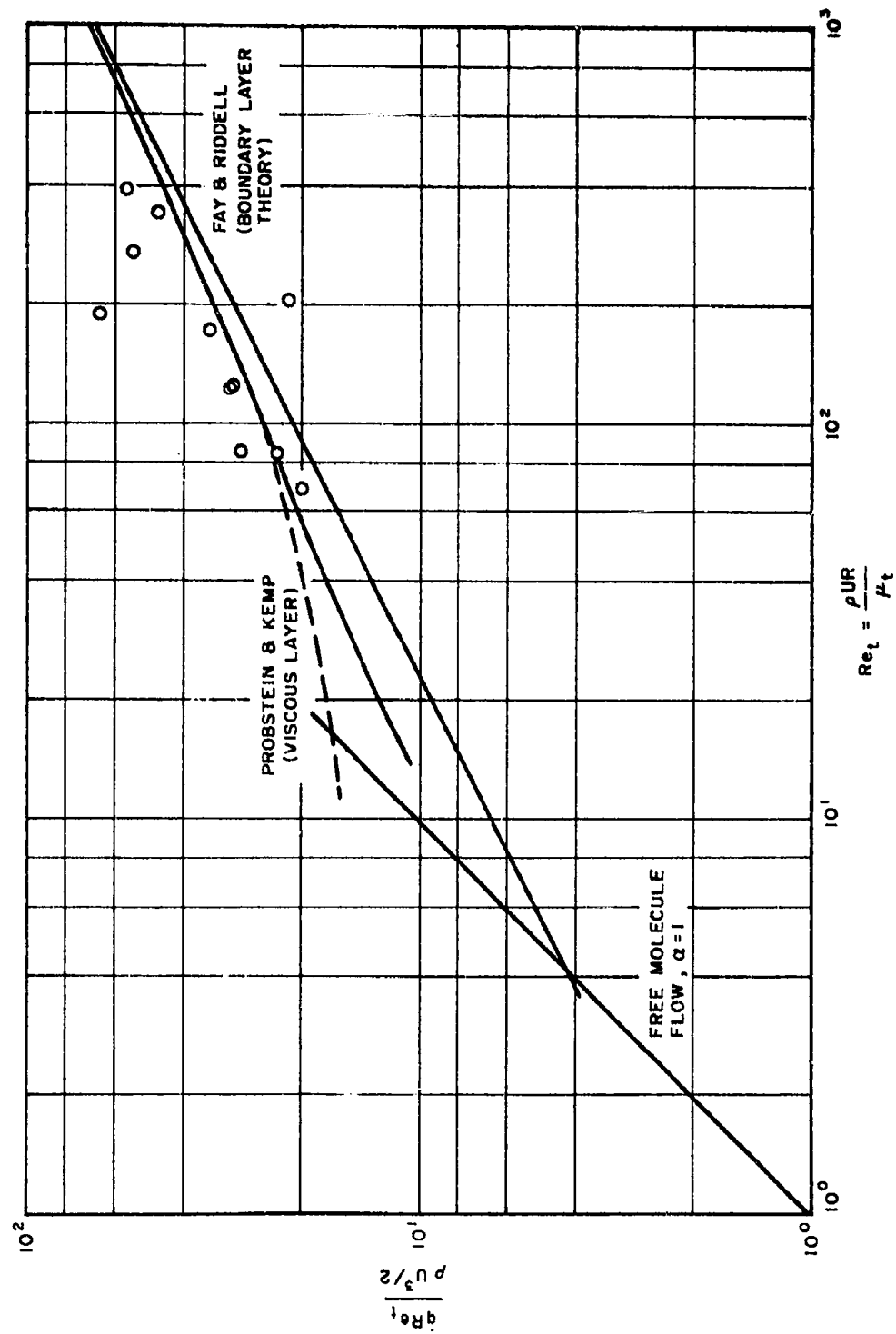


Figure 30b. Heat Transfer Rate to Spheres as a Function of Stagnation Point Reynolds Number

For shock tunnel reservoir conditions of about 240 atmospheres and 2840°K , and test section Mach numbers from 10 to 20, the heat transfer rates, according to Fay and Riddell,² were calculated. These values are plotted in Fig. 30 for comparison with the results of Probst and Kemp. A free molecule flow value for an accommodation coefficient of unity is plotted also.

3. Experiments

In the shock tunnel for shock Mach numbers of 4.5 to 4.7, reservoir test conditions (which remain steady for about 4 millisecon) of between 220 and 240 atm and 2840 and 3000°K are obtained. Using the twelve-inch diameter test section and varying the throat diameter over a range of .04 to .375 inches, Mach numbers from 10 to 23 are achieved. For each test, the shock Mach number (M_s) in the shock tube, and the pitot pressure (P_t) in the test section, are measured. From the shock Mach number, the reservoir conditions (that is, the conditions behind the reflected shock) are ascertained. These conditions, along with the pitot pressure measurement, determine the flow Mach number in the test section.

Spherical and cylindrical shells of Pyrex 7740 glass, ranging in diameter from 3 to 20 mm, were employed as models. Two thin film resistance thermometers were applied at the stagnation point of the cylinder and half an inch on either side of the mid-point of the cylinder. The films were applied by airbrushing Hanovia No. 05X liquid bright platinum paint in a strip 0.5 mm wide and half an inch long and then firing it at 1250°F . Firing silver micro paint in a heavy layer provides low resistance contacts with the measuring circuit. Fig. 31 is a photograph of the cylindrical model. This model was mounted in the test section normal to the flow so that the mid-point of the cylinder corresponded with the axis of the tunnel test section. The cylinder was supported from the wall in cantilever fashion. The spherical model shown in Fig. 32 has a shorter thin film at its stagnation point and is supported from the model stand as illustrated. The pitot pressure gauge location is indicated also in this photograph.

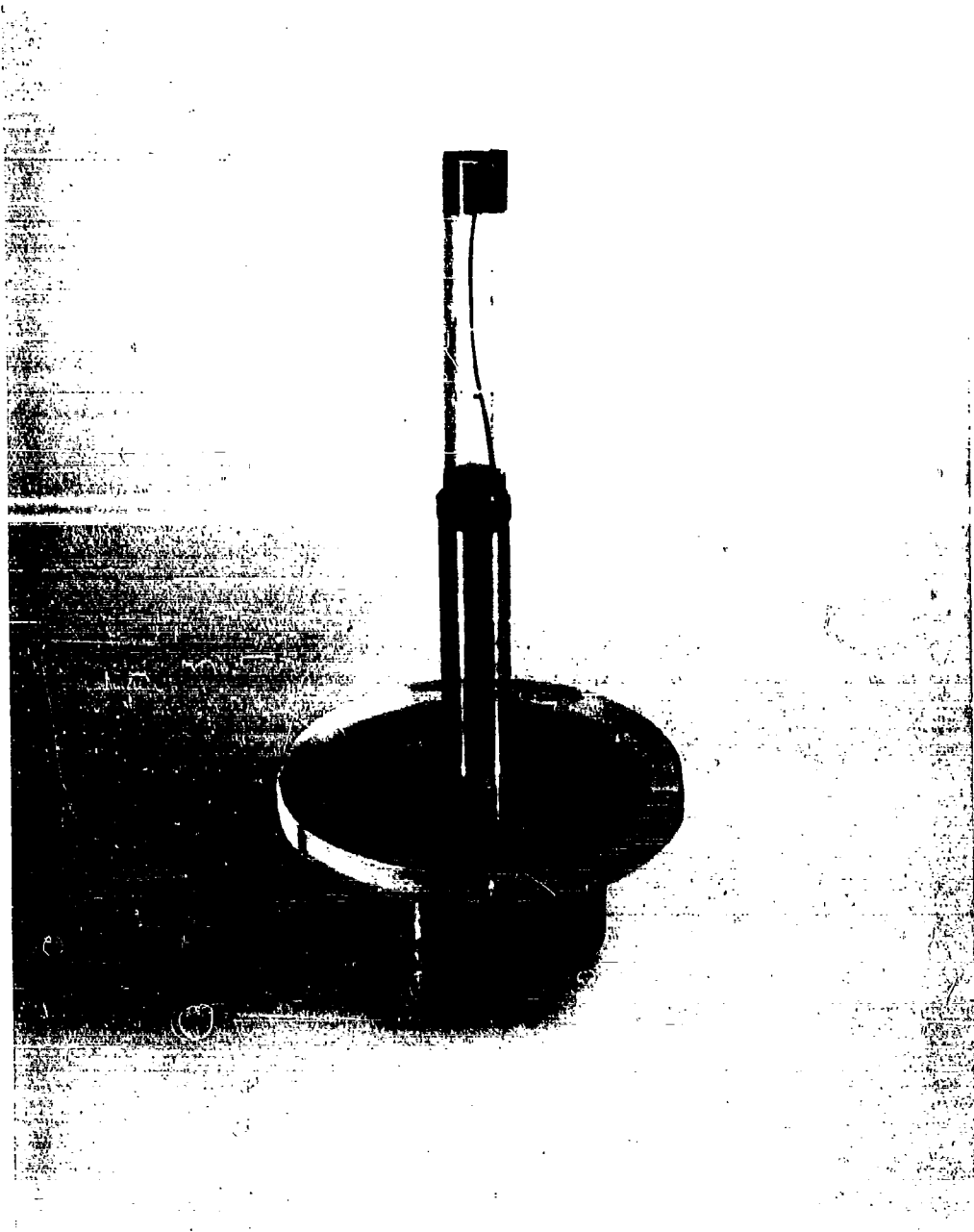


Figure 31. 20mm Diameter Cylindrical Model Showing the Two Thin Film
Resistance Thermometers Along the Surface which Becomes
the Stagnation Line of the Cylinder



Figure 32. Mounting of the Spherical Model in the Tunnel Showing also the Pitot Tube for Measuring Test Section Total Pressure

The technique of thin film resistance thermometry is quite well known and very adequately covered in the literature. In essence, the thermometer measures the surface temperature history of the material on which it resides. This measured temperature history is converted to a heat transfer rate by the use of one-dimensional heat conduction theory and one basic calibration of the thermometer. The basic calibration is generally done by the pulsing technique in which a known heat flux, produced by a current step pulse through the resistance thermometer, is applied to the gauge. The calibration is used to determine the lumped thermal properties of the substrate of the thin film, $\sqrt{\pi \rho C k}$, where ρ , C , and k are the density, specific heat, and conductivity of the substrate. The thermal coefficient of resistance of the film is determined by measuring the resistance at the freezing and boiling points of water.

The equation relating the heat transfer rate (\dot{Q}) to the model along with the temperature history of the model surface ($\Delta T/\sqrt{t}$) is given as

$$\dot{Q} = \frac{\sqrt{\pi \rho C k}}{2} \left\{ 1 + \frac{b}{k_0} \left[\left(1 + \frac{\Delta T}{T_0} \right) \left(\frac{T_0}{\Delta T} \right) \log_{10} \left(1 + \frac{\Delta T}{T_0} \right) - .434 \right] \right\} \frac{\Delta T}{\sqrt{t}} \quad (127)$$

ΔT is the temperature change of the surface and T_0 is the initial temperature of the surface. The quantity in the braces $\left\{ \right\}$ represents the correction to the heat transfer rate which must be included in order to account for the change in the thermal properties of the substrate when the surface temperature becomes large in comparison with the calibration temperature.³⁵ b/k_0 is a function of the material, which for Pyrex is 4.73.

Measurements were made in the shock tunnel of the heat transfer rates to cylinders 3mm, 10mm, and 20mm in diameter and to spheres 10 and 20mm in diameter. Reservoir stagnation conditions ranged from 2800 to 3000°K with pressures of 28 to 29 atm and 220 to 240 atm. Mach numbers in the test section varied from 10 to 23, but most of the data was in the range of 13 to 16.

4. Results

In calculating the value of Re_t , the Reynolds number based on leading edge diameter, the value of the viscosity is determined according to the results of the study of oxygen recently reported by Hartunian and Marrone.³⁶ This study indicates that the Sutherland viscosity values based on kinetic theory and hard spherical molecules are as much as 50% too low for temperatures up to 3000°K. This modified value of μ_t also was used to determine the theoretical value of Q_o , according to Fay and Riddell.²

The experimental values of the reservoir conditions, the flow Mach numbers and the heat transfer rates are tabulated in Table I. Values of $Q_o Re_t / \frac{1}{2} \rho U^3$ as a function of Re_t are plotted in Fig. 30a and 30b, along with the theoretical curves. The results for the cylinder seem to follow the boundary layer theory right on down to the free molecule flow regime with only a slight increase at Reynolds numbers less than 20. The considerable scatter in the data makes a definitive determination of the best theory impossible.

The experimental data for the axisymmetric probe (sphere) are even more scattered, and therefore, inconclusive.

Some remarks on the accuracy of these experiments should be made. The shock Mach number can be measured to $\pm 1\%$ and this is about the error expected in the reservoir conditions. The total pressure can be measured to within $\pm 10\%$ and this should be the expected error in p . As a result, the theoretical curve which is plotted from the experimentally obtained values for the tunnel conditions could have a width of $\pm 10\%$. The heat transfer measurements have a possible error of between $\pm 5\%$ and $\pm 18\%$, depending on the smoothness and clarity of the heat transfer record. An example of a typically adequate record is shown in Fig. 33 for a flow Mach number of 16.5 and reservoir conditions of 243 atm and 3100°K.

No explanation is immediately available for the greater amount of scatter in the sphere data. Since the spheres were blown from Pyrex tubing some irregularities existed in their radii. However, the heat transfer

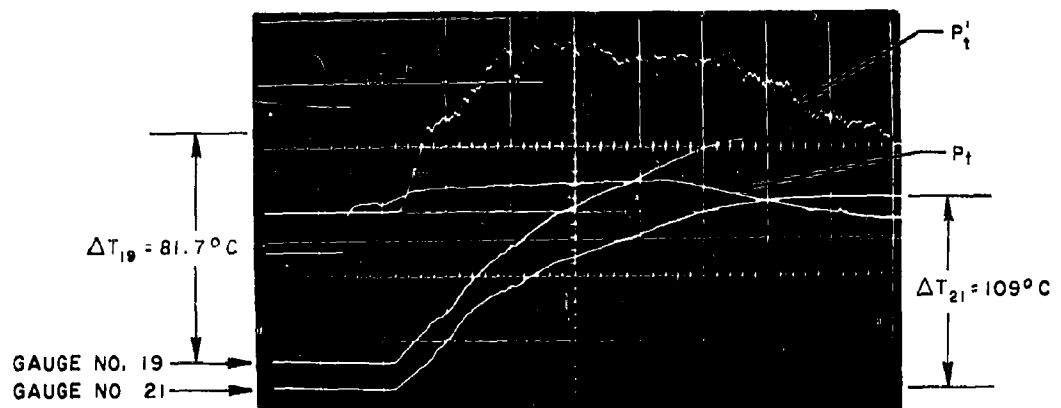


Figure 33. Typical Temperature History for the Stagnation Point of a Cylindrical Model

$$P_t = 222 \text{ atm}$$

$$T_t = 2980^{\circ}\text{K}$$

$$M = 16.0$$

rate varies inversely as the square root of the body radius, and hence, irregularities in the radii should not give significant effects. The much smaller gauge on the spheres could limit the accuracy of the results.

5. Conclusions

The heat transfer rates to cylinders and spheres, as measured in the shock tunnel, are adequately predicted by the theory of Fay and Riddell² down to $Re_t \approx 20$. At this point, the heat transfer rate increases somewhat, as predicted by Probst and Kemp,³⁴ reaching the free molecule flow heat transfer rate at a value of Re_t between 2 and 3.

Where I is the beam intensity, x is the path length, ρ is the gas density, and μ is an absorption coefficient.

The absorption coefficient, μ , is related to the effective scattering cross section of the gas. The cross section $Q(\Phi)$ is defined as the probability per scattering center that an electron will be deflected by an interaction with a gas molecule into a cone of half angle Φ which is greater than the effective angle subtended by the detector aperture measured from the point of scattering. If there are n molecules of gas in the volume occupied by the electron beam, the total probability of an electron interaction with a gas molecule is nQ , or over an increment of path length dx , is $nQdx$, and the loss of beam intensity becomes:

$$\frac{dI}{dx} = -nQI \quad (129)$$

$$\text{Integration of Eq. (129) yields } I(x) = I_0 e^{-nQx} \quad (130)$$

Markevitch and Hurlbut³⁸ have shown that the experimental value of $Q(\pi)$ for high energy electrons in air is close to the theoretical value based on elastic collisions. This value is energy dependent and has been found to have the relation

$$Q(\pi) = \frac{3.6 \times 10^{-13}}{V} \text{ cm}^2 \quad (131)$$

where V is in volts.

Taking Avogadro's number, $N = 6.025 \times 10^{23}/\text{mol.}$, and the standard volume, $V_0 = 22.4146 \times 10^3 \text{ cm}^3/\text{mol.}$, then at a pressure of one micron there are 3.537×10^{13} molecules per cubic centimeter of a perfect gas. Then $n = 3.537 \times 10^{13} \rho$, and $\mu\rho = nQ = 3.537 \times 10^{13} \rho Q$, from which

$$Q = 2.827 \times 10^{-14} \frac{\mu\rho}{\rho} \quad (132)$$

This quantity Q is the total collision cross section of the gas, and has the same significance as the sense of $Q(\pi)$ in Eq. (131); that is, it represents the total cross section which was determined from scattering into a cone or half angle π radians.

We may now obtain the absorption coefficient μ by combining Eq. (131) and (132):

$$\mu p = 12.73 \frac{p}{V} \quad (133)$$

for air, where p is in microns and V is in volts.

The equation for the intensity of an electron beam in air at a constant pressure p microns is then

$$I(x) = I_0 e^{-12.73 \frac{px}{V}} \quad (134)$$

where $I(x)$ is measured in centimeters from the point of origin and I_0 is the incident beam current of an energy V electron-volts.

Equation (134) is plotted on logarithmic coordinates in Figs. 34 and 35.

3. Electron Beam Absorption in an Axially Symmetric Flow Field

The electron beam densitometer will be used to obtain free stream density measurements in the flow field of the hypersonic shock tunnel and the variation of free stream density in the direction normal to the flow. Consider a uniform beam of electrons injected into an axially symmetric flow field where the gas density is a function of r , the radial distance from the central flow axis, as in Fig. 36. It will be required to find the gas density, ρ , as a function of r . Consider a uniform beam of electrons of intensity I_0 originating outside the flow region and directed in the positive x direction.

Lambert's law of absorption holds as a partial derivative since the beam attenuation is a function of x and y .

$$\frac{\delta I}{\delta x} = -\mu \rho I \quad (135)$$

which has a solution

$$\ln I(y) - \ln I_0 = -2\mu \int_0^{\bar{x}} \rho dx - \mu \rho_1 (L - 2\bar{x}) = F(y) \quad (136)$$

where $\rho = f(r)$ and ρ_1 is a constant.

From the geometry of Fig. 36, $r^2 = x^2 + y^2$, and for constant y , $rdr = xdx = \sqrt{r^2 - y^2} dx$. Also, when $x = 0$, $r = y$, and when $x = \bar{x}$, $r = R$ then Eq. (136) becomes

$$F(y) = -2\mu \int_y^R \rho(r) \frac{rdr}{\sqrt{r^2 - y^2}} - \mu \rho_1 (L - 2\bar{x}) \quad (137)$$

A second change of variables is made by putting $s = R^2 - r^2$ and $g(s) = \rho(r)$. Now $ds = -2rdr$, and at $r = y$, $s = R^2 - y^2$ and at $r = R$, $s = 0$. Then Eq. (137) becomes

$$F(y) = \mu \int_{R^2 - y^2}^0 g(s) \frac{ds}{\sqrt{R^2 - y^2 - s}} - \mu \rho_1 (L - 2\bar{x}) \quad (138)$$

This may be simplified by substitution of $t = R^2 - y^2$, then

$$F(y) = -\mu \int_0^t \frac{g(s)ds}{\sqrt{t - s}} - \mu \rho_1 (L - 2\bar{x}) \quad (139)$$

and define

$$f(y) = G(t) = -\mu \int_0^t \frac{g(s) ds}{\sqrt{t-s}} \quad (140)$$

then

$$f(y) = F(y) + \mu \rho_1 (L - 2\bar{x}) \quad (141)$$

Equation (140) is of the Abel type with unknown $g(s)$ and has the solution

$$g(s) = \frac{-1}{\pi\mu} \frac{d}{ds} \int_0^s \frac{G(t) dt}{\sqrt{s-t}} \quad (142)$$

To integrate by parts, choose $U = G(t)$ and

$$dV = \frac{dt}{\sqrt{s-t}}$$

Equation (142) becomes

$$g(s) = \frac{-1}{\pi\mu} \frac{G(0)}{\sqrt{s}} + \frac{1}{\pi\mu} \int_0^s \frac{G'(t) dt}{\sqrt{s-t}} \quad (143)$$

From Eq. (140) $G(0) = 0$ and

$$G'(t) = f'(y) = \frac{d}{dy} f(y)$$

so that

$$g(s) = \frac{1}{\pi\mu} \int_0^s \frac{f'(y) dt}{\sqrt{s-t}} \quad (144)$$

We now change variables by the substitutions $t = R^2 - y^2$ and $s = R^2 - r^2$. Note that when $y = R$, $t = 0$ and when $y = r$, $t = s$, then

$$g(s) = \rho(r) = \frac{1}{\pi\mu} \int_r^R \frac{f'(y) dy}{\sqrt{y^2 - r^2}} \quad (145)$$

By differentiation of Eq. (141),

$$f'(y) = \frac{d}{dy} \ln I(y) - 2\mu\rho \frac{y}{\sqrt{R^2 - y^2}} \quad (146)$$

and substitution into Eq. 145,

$$\rho(r) = \frac{1}{\pi\mu} \int_r^R \frac{d}{dy} \ln I(y) \frac{dy}{\sqrt{y^2 - r^2}} - \frac{2\rho_1}{\pi} \int_r^R \frac{y dy}{\sqrt{y^2 - r^2} \sqrt{R^2 - y^2}} \quad (147)$$

which leads to

$$\rho(r) = \frac{1}{\pi\mu} \int_r^R \frac{d}{dy} \ln I(y) \frac{dy}{\sqrt{y^2 - r^2}} + \rho_1 \quad (148)$$

$I(y)$ may be obtained by measuring segments of the core flow under identical tunnel conditions and $\rho(r)$ is evaluated numerically. A preferred technique is to incorporate a series of detectors and a rapid sweep on the electron beam to measure all segments during a single run.

4 Instrumentation

The electron beam densitometer consists of two major systems: the electron source or gun, with the associated high voltage accelerator, heaters, bias and deflection power supplies, and the detector, with its associated power, bias, and deflection supplies. Oil diffusion pumps supply the high vacuum environment for the electron gun and the detector.

helium in the driver, and a reasonable degree of driver gas heating. The primary driver gas will then be helium with a stoichiometric mixture of hydrogen and oxygen to supply the energy for heating and to increase the driver gas pressure through a combustion process. In the operation of the combustion driver, however, the helium is regarded as the diluent in suppressing detonation during the combustion process. Thus, a combustion mixture is usually referred to by its helium content in percent of the total volume. Nagamatsu⁴⁰ has performed experiments for hydrogen-oxygen-helium mixtures of various ratios. Detonation was experienced when a 65% helium diluent was used with a stoichiometric mixture of hydrogen and oxygen. Difficulties in igniting the gas were encountered when an 80% helium dilution was used.

In calculating the performance of the shock tunnel, helium is regarded as the driver gas. The product of combustion, vapor of H_2O , is then regarded as the contaminant in the driver gas. Since the water vapor contributes to an appreciable increase in molecular weight of the final gas mixture over that of the pure helium, its effects cannot be ignored completely in the calculations. A detailed study of the combustion process would give an accurate prediction of the driver gas conditions with regard to temperature, pressure, speed of sound, specific heat ratio, etc. A detailed study of this nature, in order to be adequate for our present purposes, should trace the expansion process of the driver gas after the shock formation has been initiated. This implies the necessity for the construction of portions of a Mollier diagram for each mixture ratio under consideration, in order that the regions of interest can be adequately covered. For our present purpose, the equilibrium gas temperature, pressure, and specific heat ratio γ were determined at the time when the combustion process was completed. Isentropic expansion of the driver gas was assumed in order to calculate the conditions behind the interface. Four mixture ratios were considered in calculating the driver gas conditions, and subsequently, the shock tunnel performance with regard to stagnation conditions in the region after the reflected primary shock. It is on this stagnation

Calculations for a shock tunnel, using pure hydrogen as the driver gas, is given in Fig. 49 as a comparison. Hydrogen is very efficient for use as a driver gas; however, its inherent dangerous handling characteristics make it unattractive for use in the present facility.

a. Area Ratio Effect in Shock Tunnels

The preceding analysis was appropriate for an ideal shock tube with constant area throughout. For shock tunnels having unequal driver and driven tube diameters and a throat section at the diaphragm location, the performance calculated previously would be modified to compensate for area ratio effect and the restriction at the throat. A shock tube with such a restriction is given schematically (see Fig. 50). The effective pressure ratio for such a configuration would be⁴²

$$\begin{aligned} \left(\frac{P_4}{P_1} \right) &= \frac{P_4}{P_{3a}} \frac{P_{3a}}{P_{3*}} \frac{P_{3*}}{P_{3b}} \frac{P_{3b}}{P_3} \frac{P_3}{P_2} \frac{P_2}{P_1} \\ &= \frac{1}{g} \frac{P_2}{P_1} \left[1 - \frac{\gamma_4 - 1}{\gamma_1 + 1} \frac{A_1}{A_4} M_s \left(1 - \frac{P_2}{P_1} \right) g^{-\frac{1}{\alpha}} \right]^{-\alpha} \end{aligned} \quad (153)$$

where

$$g = \left[\frac{2 + (\gamma_4 - 1) M_{3a}^2}{2 + (\gamma_4 - 1) M_{3b}^2} \right]^{\frac{\alpha}{2}} \left[\frac{2 + (\gamma_4 - 1) M_{3b}^2}{2 + (\gamma_4 - 1) M_{3a}^2} \right]^{\alpha} \quad (154)$$

is the gain factor modifying the actual pressure ratio to an effective pressure ratio. With the boundary conditions such that $M_{3*} = 1$ and if A_{3a}/A_{3*} is given, then M_{3a} can be obtained by solving the equation

$$\frac{A_{3a}}{A_{3*}} = \left[\frac{2 + (\gamma_4 - 1) M_{3a}^2}{2 + (\gamma_4 - 1) M_{3*}^2} \right]^{\frac{\gamma_4 + 1}{2(\gamma_4 - 1)}} \frac{M_{3*}}{M_{3a}} \quad (155)$$

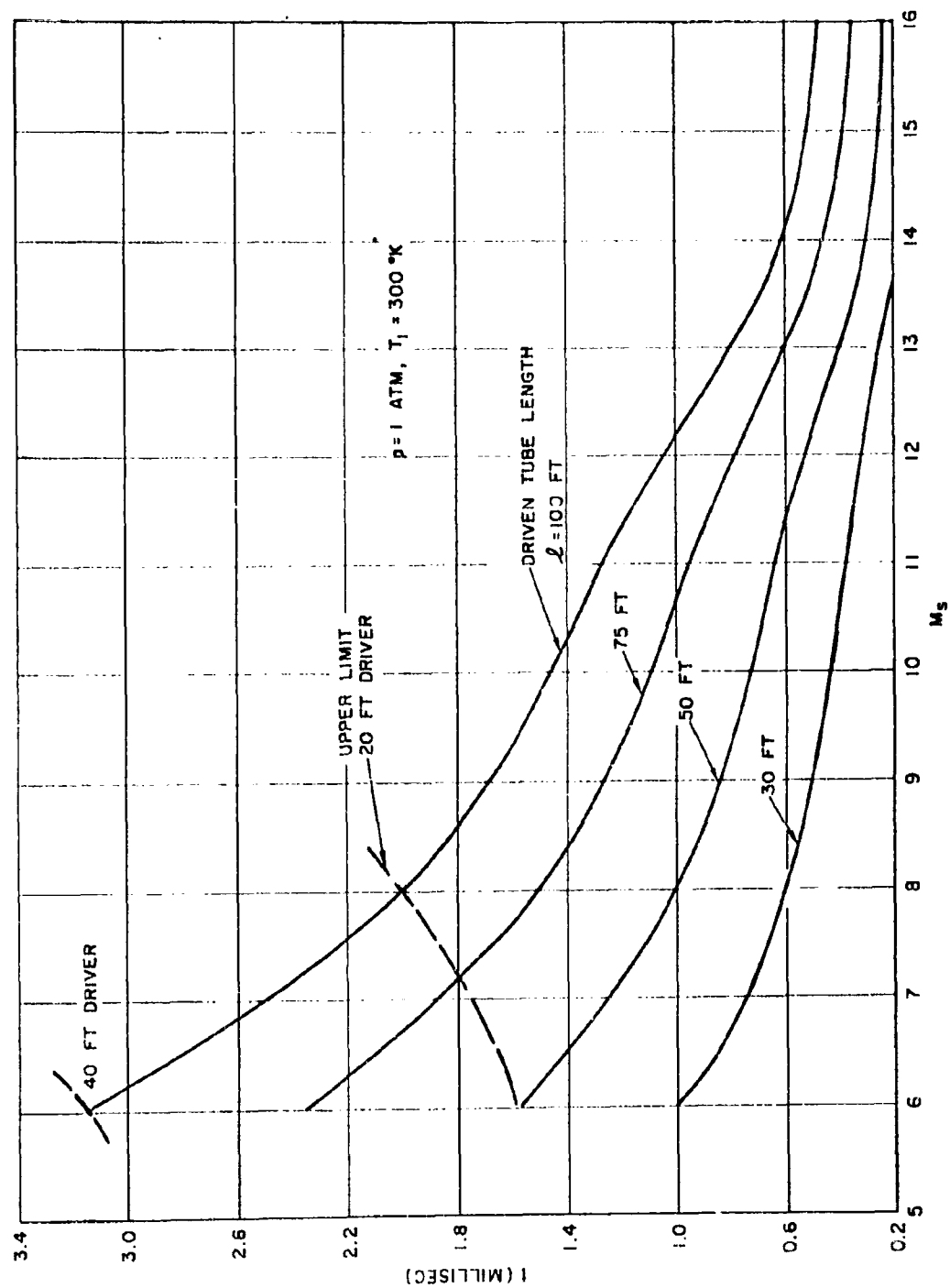


Figure 52. Testing Time for Non-tailored Combustion-Driven Shock Tube, 70% Helium

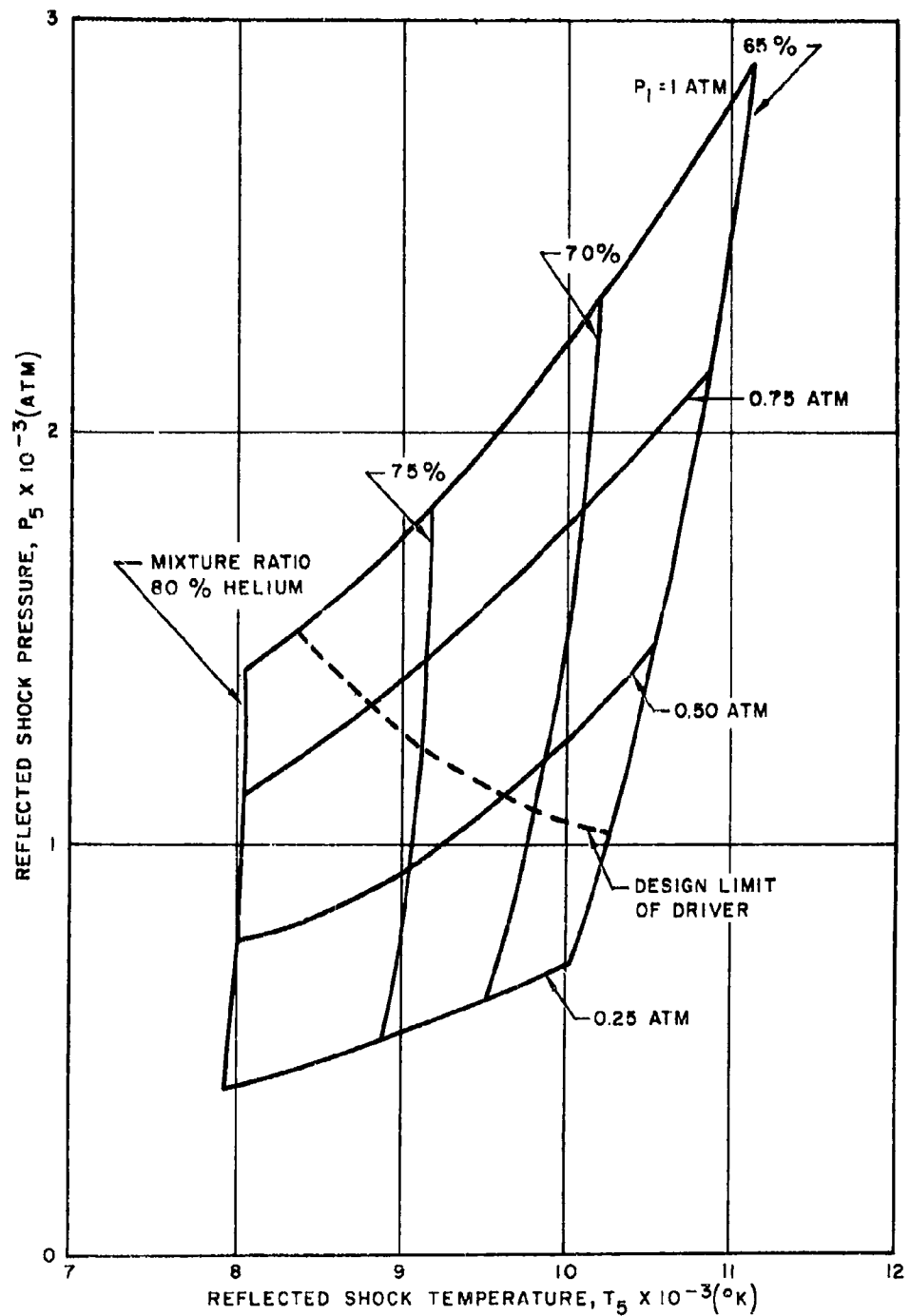


Figure 53. Tailored Interface Operation for the Combustion-Driven Shock Tunnel ($P_5 \sim T_5$)

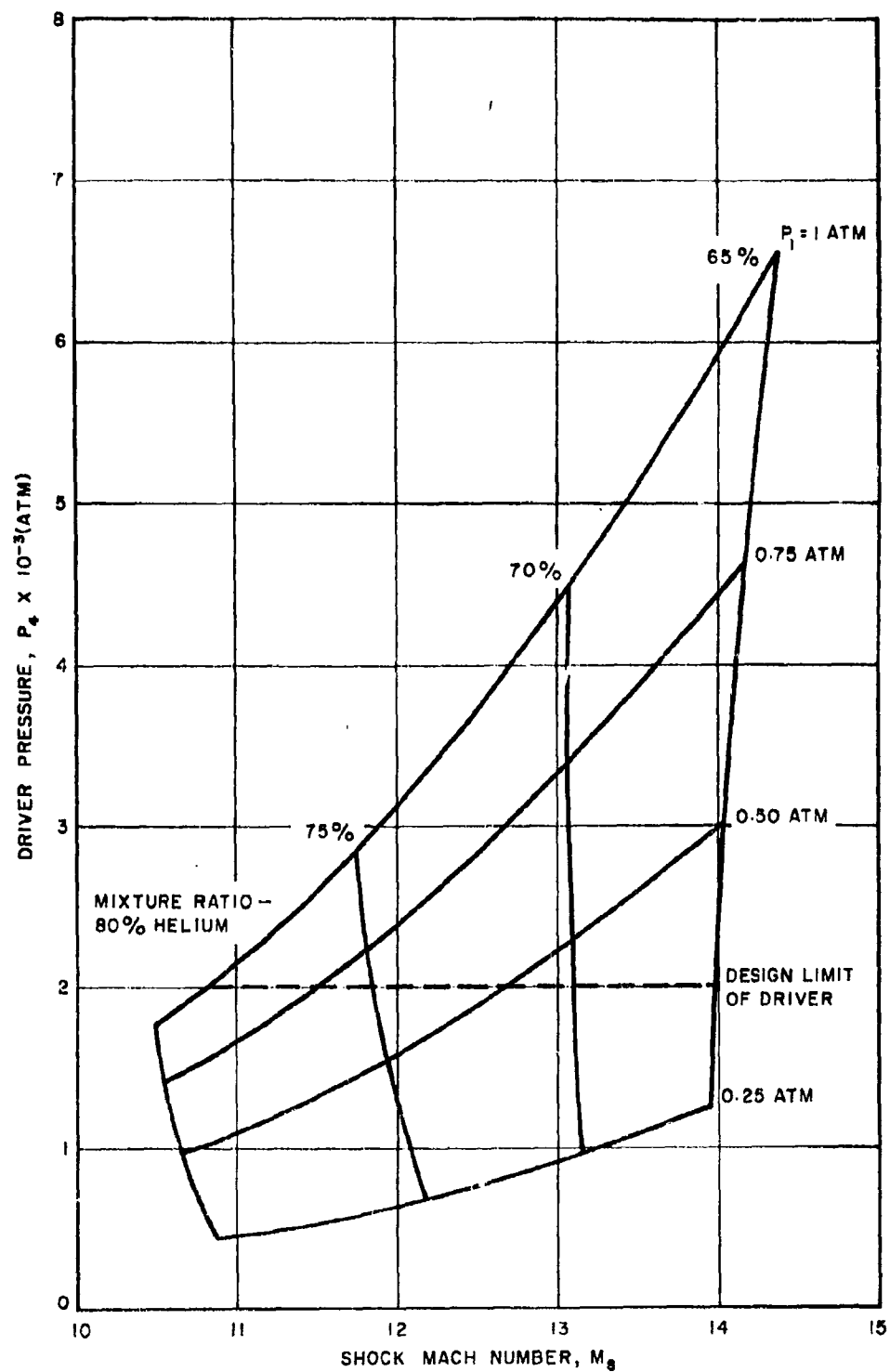


Figure 54. Tailored Interface Operation for the Combustion-Driven Shock Tunnel ($P_4 \sim M_5$)

system, the driven section, and the nozzle test section dump tank is given below:

b. Driver Section and Gas Charging System

Due to the possibility of detonation of the combustion mixture, the driver section is designed for an ultimate pressure of 165,000 psi. The working pressure, in general, will not exceed 30,000 psi. The temperature is expected to reach between 2000° and 3000°K, but it is transient, as is the high combustion pressure.

In order to meet these requirements, the driver section and its closely associated fittings will be fabricated from forged 300M steel and heat treated after rough machining to maximize the effectiveness of the heat treating. The vessel, cap, latching mechanism, and diaphragm package are detailed in Fig. 59.

The gas handling system for loading the driver with a combustible mixture of oxygen and hydrogen, diluted with helium, is shown schematically in Fig. 60. A gas accumulator, with a volume equal to that of the driver section, acts as a fast high-pressure hydrogen pump. A stoichiometric mixture of hydrogen and oxygen diluted with 75 percent helium, at a total pressure of 4000 psi before combustion, is used. Oxygen is pumped into the driver section from the storage marked O₂ to a pressure of 330 psi. Helium is then added until a pressure of 3330 psi is reached. Then hydrogen is pumped into the hydrogen accumulator to a pressure of 660 psi. Helium gas then passes into the accumulator behind the piston. As the helium is stored at very high pressures (15,000 - 20,000 psi), it forces the hydrogen into the driver. This sequence of loading never permits a mixture of hydrogen and oxygen to exist in richer concentrations than the mixture to be employed in the test. Hence, the probability of detonation occurring during the filling process is low.

Proper distribution and circulation of the driver charge is obtained by using a long ported stainless steel tube inside the driver to serve as the fill tube. The port area varies exponentially along the tube,

for each of the two elements

$$C_y = \frac{\Delta Y}{\frac{\Delta F_y}{2}}$$

$$C_y = \frac{\frac{\Delta X}{\tan \phi}}{\frac{2\Delta F_x \tan \phi}{2}} = \frac{C_x}{\tan^2 \phi}$$

It can be shown that the angled drive system is equivalent to a mechanical transformer with a "turns ratio" of $\tan \phi/1$. This satisfies the conditions derived for force, displacement and impedance. The equivalent circuit for this configuration is given in Fig. 76. It is seen that for $\phi = 45^\circ$, the turns ratio becomes unity and the performance becomes identical to that of Fig. 71 except for the fact that the single bender element has been replaced by two with the same aggregate dimensions and mechanical characteristics. This configuration can always be employed with a resultant doubling of the output voltage, but since the internal source capacitance is reduced to 1/4 of the single element value it is not often used.

As with the conventional structure, we can derive the low frequency sensitivity. This is found to be

$$\frac{E}{P} = \frac{N A_D}{\tan \phi + \frac{C_C}{2 C_D \tan \phi}}$$

The factor "2" appears in the denominator because C_C refers to each element of the two element system. It can be seen that for a given set of diaphragm and crystal constants, there is an optimum angle which gives maximum output. This relationship is

$$\tan^2 \phi = \frac{C_C}{2 C_D} \text{ for max } \frac{E}{P}$$